Extragalactic stellar populations in the near and mid-infrared: 1-30 μm emission from evolved populations, young and dusty star forming regions and the earliest stellar populations

by

Erin Mentuch

A thesis submitted in conformity with the requirements
for the degree of Doctor of Philosophy
Graduate Department of Astronomy and Astrophysics
University of Toronto

Abstract

Extragalactic stellar populations in the near and mid-infrared: 1-30 μm emission from evolved populations, young and dusty star forming regions and the earliest stellar populations

Erin Mentuch
Doctor of Philosophy
Graduate Department of Astronomy and Astrophysics
University of Toronto
September 2010

The near- through mid-infrared offers a unique and, as this thesis aims to show, essential view of extragalactic stellar populations both nearby, at intermediate redshifts and at very high redshift. In chapter 2, I demonstrate that rest-frame near-IR photometry obtained by the *Spitzer Space Telescope* provides more robust stellar mass estimates for a spectroscopic sample of $\sim$ 100 galaxies in the redshift desert ($0.5 < z < 2$), and is crucial for modeling galaxies with young star-forming populations. From this analysis, a surprising result emerges in the data. Although the rest-frame light short of 2 μm improves stellar mass estimates, the models and observations disagree beyond 2 μm and emission from non-stellar sources becomes significant. At wavelengths from 1–30 μm, stellar and non-stellar emission contribute equally to a galaxy's global spectral energy distribution. This is unlike visible wavelengths where stellar emission dominates or the far-IR where dust emission provides the bulk of a galaxy's luminosity. Using the sample of high-z galaxies, in chapter 3, I quantify the statistical significance of the excess emission at 2-5 μm and find the emission to correlate with the O II luminosity, suggesting a link between the excess emission and star formation. The origin of the excess emission is not clear, although I explore a number of non-stellar candidates in this chapter. Nearby resolved observations provide a clearer picture of the excess by spatially resolving 68 nearby galaxies. By analyzing the pixel-by-pixel near-IR colours within each galaxy at $\sim$1-5 μm, increasingly red near-IR colors are mapped to spatial regions in chapter 4. For

regions with red NIR colors and high star formation rates, I find the broad near- through mid-IR spectrum is constant, varying only in amplitude as a function of the intensity of star formation, suggesting the infrared emission of a young, dusty stellar populations can be added to stellar population synthesis models as an additional component tied to the star formation rate. In closing the thesis, the focus is moved to the detection of stellar populations in the earliest star-forming galaxies. By $z > 6$, all visible wavelength emission is redshifted into near-IR wavelengths. In chapter 5, I show how a tunable near-IR filter I have helped develop holds promise for finding bright Lyman alpha emitting galaxies at redshifts of $8 < z < 11$.

Do not be too timid and squeamish about your actions. All life is an experiment. The more experiments you make the better.

- Ralph Waldo Emerson

Acknowledgements

Behind every good student is a great mentor. And I have been fortunate enough to have three phenomenal and supportive mentors. Bob Abraham, I thank you the most. Your never ending inspiration and brilliant ideas made me love galaxies and observational cosmology. We spun some crazy ideas in the process, but I still haven't convinced myself we're wrong (and I try daily!). I appreciate your fairness over the years and your ability to supervise me without me feeling as if I was being supervised; although, it was clear you always had ze evil plan in your control. Alan Scott, as your apprentice, you personally taught me optics, software design and electronics; subjects I was happy to be obliviously ignorant about until I had no choice. Working in a lab was very valuable and I will forever be indebted from the support both you personally and COM DEV provided me. Your enthusiasm, whether it was for tunable filters, backyard astronomy or for putting a greenhouse on the moon, was contagious. There is no one path for the astronomer, but learning about your chosen path has helped me find my own. Karl Glazebrook, from day one, I have felt like you are my second supervisor. You taught me so much so quickly and efficiently. Your ability to understand me and the nuances of my analysis made us a great team. You were always one step ahead of me but made sure I kept up and you became a good friend and a great mentor along the way. Your insights and careful critique helped me improve as a scientist and I can safely say I'm a PDLer for life. Behind the curtains, I am forever grateful for the continued support of my friends and family. You helped to keep me sane in my darkest days and were my motivation to finish. Thank you for still being here in my life, especially when I admit there were times that I couldn't be there in yours. And finally, to the woman who birthed me, provided me with constant guidance and convinced me to stay on course, Joan Roberts, I love you and couldn't have been blessed with a better mother.

Contents

1 Introduction **1**
- 1.1 Why the infrared? . . . 2
- 1.2 Stellar population synthesis . . . 5
- 1.3 Stellar populations and dust in the near-infrared . . . 9
  - 1.3.1 Near-infrared excess emission in the Milky Way . . . 10
  - 1.3.2 Near- and mid-infrared emission in nearby galaxies . . . 12
- 1.4 Near-infrared detections of very high redshift galaxies and the earliest stellar populations . . . 15
- 1.5 Scope of thesis . . . 17

2 Spitzer stellar masses in the redshift desert **19**
- 2.1 Abstract . . . 19
- 2.2 Introduction . . . 20
- 2.3 Observations . . . 22
  - 2.3.1 Summary of GDDS observations . . . 22
  - 2.3.2 *Spitzer* IRAC photometry . . . 27
- 2.4 Stellar population synthesis models . . . 34
  - 2.4.1 Additional NIR emission component . . . 35
- 2.5 Photometric SED fitting . . . 36
  - 2.5.1 Measuring the stellar mass from the SED fits . . . 37
- 2.6 Stellar masses . . . 38
  - 2.6.1 The impact of IRAC . . . 39
  - 2.6.2 Single versus composite stellar populations . . . 57
  - 2.6.3 The inclusion of TP-AGB stars . . . 60
- 2.7 Mass function . . . 62
- 2.8 Mass density . . . 68

3 Detection of a NIR excess **71**
- 3.1 Abstract . . . 71
- 3.2 Introduction . . . 72
- 3.3 Observations . . . 76
  - 3.3.1 Summary of GDDS observations . . . 76

3.3.2 *Spitzer* IRAC photometry . . . 77
3.3.3 *Spitzer* 24 μm MIPS photometry . . . 78
3.4 Spectral energy distribution fitting . . . 79
3.4.1 Stellar component . . . 79
3.4.2 Additional dust component . . . 81
3.4.3 Methods . . . 82
3.5 Results . . . 83
3.5.1 SED fitting: the stellar component model . . . 83
3.5.2 SED fitting: additional dust component . . . 84
3.5.3 Quality of fits . . . 88
3.5.4 Greybody temperatures and other limitations of the dust model . . . 88
3.5.5 Model consistency with MIPS photometry . . . 90
3.5.6 Correlation of the near-infrared excess with the star formation rate 93
3.6 Interpretation of the NIR excess emission . . . 94
3.6.1 Non-stellar candidate sources of excess emission . . . 95
3.6.2 Stellar candidate sources of excess emission . . . 98
3.6.3 Conclusions . . . 103

4 The NIR and PAH emission of resolved galaxies 106
4.1 Abstract . . . 106
4.2 Introduction . . . 107
4.3 Sample Selection . . . 110
4.4 Methods . . . 114
4.4.1 Motivation for pixel-by-pixel analysis . . . 114
4.4.2 Image preparation . . . 117
4.4.3 Adaptive smoothing . . . 118
4.5 Results . . . 119
4.5.1 Surface brightness measurements . . . 132
4.5.2 Colour-colour diagrams . . . 135
4.5.3 Galaxies with anomalous NIR colour structures . . . 136
4.6 Discussion . . . 141
4.6.1 The linear scaling of the near/mid-infrared spectrum . . . 141
4.6.2 The NIR excess due to circumstellar (disk) emission . . . 144
4.6.3 AGN activity . . . 145
4.7 Conclusion . . . 145

5 Observing the first stellar populations 148
5.1 Abstract . . . 148
5.2 Introduction . . . 149
5.3 The Flamingos-2 Tandem Tunable Filter (F2T2) . . . 152
5.3.1 Etalon operation . . . 156

5.3.2 Calibration routine . . . 157
5.3.3 Control methodology . . . 157
5.3.4 Spectral analysis . . . 160
5.3.5 First Light at the Mont Megantic 1.6 m Telescope . . . 163
5.4 Gemini Genesis Survey (GGS) observing strategies . . . 165
5.4.1 Converting the power spectrum of the CMB to a Lyman α luminosity function . . . 166
5.4.2 Uncertainties in model predictions . . . 170
5.4.3 Summary . . . 177
5.5 Other high-redshift uses for the F2T2 filter . . . 177
5.5.1 He II emission in the *Hubble* Ultra Deep Field . . . 178
5.5.2 He II emission magnified by gravitational telescopes . . . 179
5.5.3 Observability of H II reionization bubbles . . . 180
5.6 Summary . . . 182

6 Conclusions **184**
6.1 Summary . . . 184
6.2 The bigger picture . . . 186
6.3 Future work . . . 187

Bibliography **190**

List of Figures

2.1 $I - 3.6$ vs. 3.6 colour-magnitude diagram 28
2.2 IRAC colour-colour plot of $3.6 - 4.5$ vs. $5.8 - 8.0$ 29
2.3 Distribution of GDDS stellar masses vs. redshift 40
2.4 Comparison of stellar masses with and without IRAC photometry 44
2.5 Observed to model flux ratios for SED fits with and without IRAC photometry 45
2.6 SED fits and stellar masses with and without the 5.6 and 8.0 wavebands 46
2.7 Photometry and best fit SED for each galaxy 48
2.8 Observed to model band flux ratios with NIR emission model 55
2.9 Stellar masses with NIR emission SED component 56
2.10 Comparison of stellar masses for SPS models with a single or composite star formation history 57
2.11 Comparison of reduced χ^2 for SPS models with a single or composite star formation history 59
2.12 Comparison of stellar masses with a burst stellar population component with a fixed or variable age 61
2.13 Stellar masses with treatment of TP-AGB stellar evolution 63
2.14 GDDS mass function in redshift intervals 66
2.15 Evolution of the GDDS mass function 69
2.16 Evolution of the GDDS mass density function 70

3.1 Rest-frame GDDS photometry and example SED models 74
3.2 IRAC-MIPS colour-colour plot 80
3.3 Observed to model band flux ratios with NIR emission model 85
3.4 SED fitting examples for galaxies with SFRs $> 1\,M_{\odot}$/yr 86
3.5 SED fitting examples for galaxies with SFRs $< 1\,M_{\odot}$/yr 87
3.6 Quality of SED fits with and without NIR component 89
3.7 SED fit examples for objects with MIPS detections 92
3.8 Correlation between the luminosity of the NIR emission component to the OII line luminosity and its resulting star formation rate 93
3.9 JHL(AB) colour-colour plot synthesizing local candidates for the NIR excess 105

4.1 NIR and optical/NIR colour-colour diagrams for integrated galaxy photometry from SINGS and GDDS surveys . . . 110
4.2 Postage stamps and NIR pixel colour-colour diagrams of SINGS galaxies 122
4.3 Linear relationship between the NIR and MIR intensities and the intrinsic Hα intensity . . . 133
4.4 NIR colours and dust exinction . . . 134
4.5 Correlation between NIR and MIR intensities and dust extinction . . . 135
4.6 NIR colour-colour diagrams for colour-selected regions and integrated photometry . . . 137
4.7 Galaxies with compact regions of anomalous NIR colour structures . . . 138
4.8 Galaxies with extended regions of anomalous NIR colour structures . . . 140
4.9 The empirical 1-24 μm spectral energy distribution . . . 143
4.10 The correlation between excess NIR emission and the star formation rate 146

5.1 Tandem Fabry-Perot transmission spectrum . . . 154
5.2 The F2T2 filter with etalon plates exposed . . . 155
5.3 Optical lab design for calibrating the F2T2 Filter . . . 158
5.4 Reflection spectra for the two individual F2T2 etalons . . . 160
5.5 Observed and modeled reflection spectra . . . 161
5.6 Transmission spectra of F2T2 with both etalons in tandem . . . 162
5.7 F2T2 in the filter assembly on the SIMON spectrograph at *OMM* . . . 163
5.8 F2T2 scanning imaging of the Ring Nebula . . . 164
5.9 First science images of NGC 1569 taken with F2T2 in SIMON . . . 164
5.10 Narrow transparent windows for F2T2 observations through the NIR night sky spectrum . . . 167
5.11 The theoretical Lyα luminosity function . . . 169
5.12 Predicted Lyα luminosity function at $z \sim 9$ . . . 171
5.13 Lyα luminosity function at different IGM transparency . . . 174
5.14 Cosmic variance for Lyα emitting galaxies at $z \sim 9$ . . . 176
5.15 The He II luminosity function at $z = 6.5$ . . . 180
5.16 Flux sensitivity required to detect H II regions around sources of *First Light* 181
5.17 Supervisor Roberto Abraham and Erin Mentuch with the F2T2 filter at the Mont Megantic Observatory . . . 183

List of Tables

2.1 GDDS Galaxy Sample 24
2.1 GDDS Galaxy Sample 25
2.1 GDDS Galaxy Sample 26
2.2 GDDS Photometry (AB mags) 30
2.2 GDDS Photometry (AB mags) 31
2.2 GDDS Photometry (AB mags) 32
2.2 GDDS Photometry (AB mags) 33
2.3 Stellar masses and NIR emission luminosity density at 3 μm for different SED fitting methods 41
2.3 Stellar masses and NIR emission luminosity density at 3 μm for different SED fitting methods 42
2.3 Stellar masses and NIR emission luminosity density at 3 μm for different SED fitting methods 43
2.4 GDDS Mass Function 65
2.5 GDDS Mass Density Function ($\log M_\star/M_\odot \gtrsim 10.5$) 68

4.1 Object List 112
4.1 Object List 113
4.2 Colour key for Near-infrared colour criteria 117
4.3 The linear scaling of I_λ with $I_{H\alpha}$ 142

5.1 Key differences between the JWSTs TFI and Geminis F2T2 156
5.2 Model predictions of objects with detectable Lyα emission in a GGS survey of 30 galaxy clusters in $\sim$150 hr of observations. Transmission, T, of Lyα through the IGM is given relative to the transmission at z=6.5. 173
5.3 Specifications of potential deep fields 178
5.4 Predicted HeII line emission flux for objects in the HUDF with detectable Lyα emission. 179

Chapter 1

Introduction

Let's start with the obvious: galaxies are made of stars. Information as to how a galaxy forms and evolves is directly contained in its composite stellar populations. But without a fundamental understanding of stellar populations we can know only very basic properties about a galaxy (observable quantities like bandfluxes or apparent magnitudes, and assuming a luminosity, its distance), and learn very little about the complex and remarkable physical laws that describe their growth. Although individual stars can be complicated, on average their evolution depends mostly on the mass of the star, with some sensitivity to the composition of the birth environment (i.e. metallicity and multiplicity). When we consider a mass of gas converted into stars in a birth cloud, it turns out that the future of all the stars in the cloud is predictable in a statistical sense. Because of this, modeling of a galaxy's stellar populations at visible wavelengths has allowed extragalactic astronomers to draw statistical conclusions on how the universe has assembled its stars and matter into galaxies. These models reasonably describe the visible light of galaxies, but beyond $1 - 2\,\mu$m, the stellar contribution to a galaxy's spectral energy distribution (SED) decreases and other sources of emission begin to contribute to the SED. The nature of galaxies and their composite stellar populations in the near- and mid-infrared is not yet well understood although the wealth of near- and mid-infrared observations now available are set to change this. This thesis is a small effort towards this goal. It includes a broad range of existing observations of galaxies both nearby and at very large distances, corresponding to a time when the universe was just 3 to 6 billion years old. Future observations of even more distant galaxies is an attainable goal for the recent future and a tunable filter, built in Toronto and developed as part of this thesis, hopes to break ground in discovering some of these galaxies. Its development and use is

also presented in this thesis.

The definition of the near-, mid- and far-infrared are loosely defined in the literature, but for the purposes of this thesis, near-infrared (NIR) refers to emission from 0.9-5 μm, mid-infrared (MIR) from 5-30 μm and anything beyond 30 μm is referred to as far-infrared (FIR). Thus, the *Spitzer* observations, which are presented throughout this thesis, contain two NIR bands (at 3.6 and 4.5 μm) and we define the 5.6, 8.0 and 24 μm bands as MIR bands.

1.1 Why the infrared?

Near- and mid-infrared light offers a different view of stellar populations than visible light. Regions of star formation, where dust enshrouds young stars which are too faint to be seen at visible wavelengths, can easily be probed at longer NIR wavelengths where the amount of dust extinction is considerably lower. At wavelengths of 1-2 μm, dust attenuation is a factor $\sim 20-40\times$ less than at visible wavelengths ($\sim$0.5 μm) and is over 3 orders of magnitude less than the extinction at UV wavelengths. In addition, longer-lived, low-mass stars peak in radiative output between 1-2 μm. These stars live longer and are more numerous than more massive, shorter-lived stars which peak in emission at 0.3-0.6 μm. It is the emission from low-mass stars that best represents the build up of stellar material and is used to measure the total stellar mass of a galaxy. Aside from observing the bulk of stellar emission, the NIR and MIR also trace the emission from very small dust grains and small carbonaceous molecules which emit brightly at wavelengths from $\sim$1–30 μm. Their emission is dominantly heated by the stellar populations, and in this thesis, we treat this component as an extension of the stellar population.

Almost every 10 m class observatory is now equipped with a NIR camera and/or spectrograph and many of the major space-based observatories operate in the infrared (e.g. the *AKARI*, *Herschel*, *Spitzer*, *Hubble Space Telescopes* and the upcoming *James Webb Space Telescope*), not to mention other above-atmosphere observatories like the balloon-borne *BLAST* and the airplane-mounted *SOFIA*. This is amazing progress, since it was only 50 years ago that the first infrared photometers were used in astronomy (Johnson, 1962). Astronomical applications of infrared technology developed at such a fast pace because of the fascinating science that could be gained. By the 1970's, cryogenic cooling increased the sensitivity of IR detectors. Interfering photons emitted from the thermal output of surrounding instrumentation were minimized, and new sensitivities

were reached as larger arrays of IR-detectors were developed. With the advent of larger detectors in the 1980's, large volumes of the distant NIR universe were efficiently observed and the evolution of structure in the universe could be mapped.

As NIR detectors became a new standard observing tool, longer infrared wavelengths were also explored. In 1983, the *Infrared Astronomy Satellite* (IRAS) was launched into space to observe the entire night sky at wavelengths of 12, 25, 60 and 100 μm. *IRAS* detected warm dust emitted by circumstellar disks around nearby stars Vega, Formalhaut and Beta Pictoris and found that several nearby galaxies were brighter in the infrared than previously supposed (now recognized to be due to large-scale dust emission). But the resolution on *IRAS* was very low and limited to only a few bright extragalactic objects and did not provide a cohesive data set to the ground based, higher resolution observations in the near-infrared. There was an obvious need for a high resolution, space-based observatory to fill in the gaps of the infrared view of galaxies and stellar populations.

Meanwhile, on the ground, large spectroscopic surveys of galaxies (Broadhurst et al., 1988; Colless et al., 1990; Glazebrook et al., 1995a) were undertaken to measure the evolving luminosity function of galaxies. But it soon became apparent that these B-band ($\sim$0.45 μm) selected surveys were inherently biased towards selecting galaxies with the highest star formation rates. Surveys that were selected by reaching a defined I-band (Lilly et al., 1995) and K-band (Glazebrook et al., 1995b; Cole et al., 2001) limit were preferred. These infrared bands probe the longer-lived stars and are a better proxy of a galaxy's stellar mass. At the turn of the century, larger telescopes probed fainter galaxies and deeper redshift surveys (Dickinson et al., 2003; Fontana et al., 2003; Abraham et al., 2004) revealed how stellar mass was built up out to $z \sim 3$. But as higher redshifts were probed, the NIR light which best probes the stellar mass of a galaxy, is redshifted to longer wavelengths, no longer accessible from ground-based NIR bands. To probe higher redshifts, a space-based observatory covering the NIR and MIR beyond 2 μm was needed.

The *Spitzer Space Telescope*, launched in 2003 (and still operating as of 2010 at 3.6 and 4.5 μm, where cryogenic cooling is not necessary), offered higher resolution and deeper sensitivity than any previous infrared observatory. With it, stellar mass functions were measured out to $z = 4$ (Fontana et al., 2006; Pérez-González et al., 2008) using rest-frame NIR colour selection. The mass function is a measure of the number density of galaxies as a function of a galaxy's stellar mass. It reveals how luminous matter is distributed among galaxies of different masses just as the initial mass function describes the distribution of

stellar material in different sized stars in a birth cloud. The evolution of the mass function with redshift reveals how the distribution of luminous matter changes as the universe ages and how galaxies build up their stellar populations. For example, recent *Spitzer* observations of the deepest galactic fields show that by $z \sim 1$ approximately half of the local stellar mass density was already formed and at least another 40% assembled between $z = 1$ and $z = 4$ (Pérez-González et al., 2008). This is consistent with results from previous intermediate-redshift surveys, such as the Canada-France Redshift Survey (Lilly et al., 1995), which showed that by $z \sim 1$, most of the stellar mass in today's galaxies was already assembled, while galaxies observed at $z \sim 3$, contain only 15-20% of today's stellar mass (Shapley et al., 2001; Dickinson et al., 2003).

Beyond $z = 4$, the sensitivity to reach rest-frame K-band light is not possible with *Spitzer* and, in general, other colour selection methods are adopted to detect galaxies at higher redshifts. A largely successful method is the drop-out technique in which two colour bands straddle the redshifted Lyman limit (at $0.092\,\mu$m) of a galaxy. Blueward of the Lyman limit, a galaxy is relatively faint due to neutral hydrogen absorption of stellar radiation. Redward, the photons are unabsorbed and the galaxy is luminous. The Lyman dropout technique has been successful at finding progressively deep galaxies. Another successful method for finding high-redshift galaxies is using a narrowband filter to detected redshifted Lyman-α radiation. Some high-redshift star-forming galaxies are known to be very bright in their Lyα line emission as a result of hydrogen ionization by the stellar radiation field. Unfortunately, narrowband searches are limited to a small redshift range (and thus small spatial volume) due to the relatively narrow bandpass.

The near- and mid-infrared spectrum offers rich insights into galaxies and their stellar populations. Multiwavelength observations which include one or more NIR wavebands are essential for modeling a galaxy's spectral energy distribution. Stellar population synthesis technique, introduced in §1.2 provides the tools to do so. Models produced by these tools are good at describing the stellar emission of a galaxy, but at rest-frame wavelengths $> 2\,\mu$m the models fail to provide an accurate representation of the stellar emission due to a lack in stellar spectral information and stellar evolution at these wavelengths as well as an absence of the contribution from emission due polycyclic aromatic hydrocarbons and dust. These sources of emission and their relation to the underlying stellar populations are introduced in §1.3. The NIR and MIR is also important for stellar populations at high redshift. Rest frame NIR light is required to model the SED of a galaxy, but at $z \gtrsim 1$, the rest-frame NIR is redshifted into the MIR, only accessible from

space. At $z > 7$, all the visible light of a galaxy is redshifted out of the visible into the NIR. And just as the NIR and MIR is essential for studying both evolved and young and dusty stellar populations, it is also essential for the discovery and study of the most distant, early stellar populations. In §1.4, the current efforts to explore the high redshift universe in the NIR is summarized. This thesis, whose scope is presented in §1.5, encompasses a wide range of observations in the near- and mid-infrared of extragalactic stellar populations in the local universe, at moderately high redshifts and at very high redshifts.

1.2 Stellar population synthesis

The evolution of galaxies and the growth of large scale structure in the universe is best quantified by the growth of stellar mass, although band luminosity or apparent magnitudes are often used as a poor substitute. The visible portion of a galaxy, in its barest form, is simply the sum of its stars, and its luminosity is the total sum of the luminosity of each individual star in the galaxy. Aside from a few neighbouring galaxies, individual stars cannot be resolved in most galaxies, and more often than not, astronomers simply draw an aperture encompassing the entire galaxy and measure its total flux in the passband of observation. By identifying the stellar populations that comprise a galaxy as seen in its integrated light, we can gain knowledge of when the galaxy formed the bulk of its stars, how many stars it formed and whether it is still forming stars out of its reservoir of gas.

Stellar Population Synthesis (SPS) provides the tools to do this. SPS aims to describe how a galaxy's integrated colours and luminosity are created from the collection of its stellar populations. Aperture photometry encompasses the light of a galaxy out to a limited radius yielding the galaxy's magnitude in the observed filter. Magnitudes in multiple wavebands describe the galaxy's SED, which itself is a sum of the SEDs of all the stars in the galaxy. The basic building blocks of SPS are *simple stellar populations* (SSPs); populations of stars of the same age and born under the same conditions (a globular cluster, for example). The spectral energy distribution (or flux density) of an SSP, at any time, t, is given for a population of stars at the same metallicity, Z, as:

$$S_\lambda(t, Z) = \int_{M_l}^{M_u} \Phi(M) F_{\star,\lambda}(M, t, Z) dM \tag{1.1}$$

where $\Phi(M_i)$, an externally calibrated initial mass function (IMF, e.g. Salpeter 1955; Kroupa 2001; Baldry & Glazebrook 2003), is assumed to assign how many stars at a given stellar mass, M (or a certain stellar spectral type), are formed. Each star evolves according to externally calibrated pre-main sequence, main-sequence and post-main-sequence evolutionary tracks (such as those provided by Bressan et al. 1993; Althaus & Benvenuto 1997 and Chabrier & Baraffe 1997). The luminous output of the SSP is determined from externally calibrated stellar spectral libraries (Kurucz, 1979; Lejeune et al., 1997; Bessell et al., 1989; Borgne et al., 2003) that describe the radiative output, $F_{\star,\lambda}(M, t, Z)$, of each stellar spectral type at the different phases of its evolution. The total flux of the SSP is integrated over the stellar mass from a lower mass limit, M_l (0.1-1 $\mathrm{M}_\odot$ is commonly used), to an upper mass limit, M_u (usually 120 $\mathrm{M}_\odot$).

Although based on many externally calibrated assumptions, this simple prescription does a good job at replicating the colours and magnitudes of observed SSPs such as globular clusters. Several applications of SPS theory are in use today such as PEGASE.2 (Fioc & Rocca-Volmerange, 1997), STARBURST99 (Leitherer et al., 1999), Bruzual & Charlot (2003) and Maraston (2005) to name a few. To apply SPS techniques to galaxies, which are known to contain stellar populations at different ages, a star formation history (SFH), $\Psi(t - t')$, is assumed to describe how much gas mass is converted into stars at any time, t. The spectral energy distribution of a composite stellar population (CSP; a galaxy for example) is given at age t and initial metallicity Z as:

$$F_\lambda(t, Z) = \int_0^t \Psi(t - t') S_\lambda(t', Z) \exp^{-\tau_\lambda(t')} dt' \tag{1.2}$$

Emission from the CSP can be attenuated by dust absorption in the line of sight to the galaxy, given by the optical depth, $\tau_\lambda(t)$, which varies with wavelength and depends on the age of the CSP as the dust geometry can vary widely from the stellar population's birth to main-sequence evolution. The evolution of the SSP depends on further assumptions such as interstellar winds, metallicity evolution, additional dust attenuation of embedded young stars, supernova ejecta, and stellar binary fraction, to name a few.

As shown in Equation 1.2, a galaxy, referred to as a composite stellar population, is comprised of simple stellar populations. The spectral energy distribution of each SSP is defined according to Equation 1.1. The age of each SSP depends on the star formation history, $\Psi(t - t')$, of the CSP. In the simplest, top-down scenario of galaxy formation, all

of the stars are formed at once at some formation time and simply evolved from there. The evolution of the galaxy's SED is just the evolution of an SSP. But more realistically, a galaxy likely began forming stars at some formation time and continued to do so at a rate defined as the star formation rate (SFR). The SFR can either be constant, but standard practice is to model the change in the SFR as a declining exponential with some timescale. Often this choice of timescale is varied in SPS modeling and is a fitted parameter in the analysis. This form of the rate of change of the SFR, which we call the star formation history (SFH), is motivated by observations. Massive galaxies have low SFRs and have formed the bulk of their stars in the past (at higher SFRs), galaxies with low stellar masses have higher SFRs and are still building up their stellar mass.

In practice, the SPS technique has provided a firm quantitative basis for observational cosmology. Although the input uncertainties are large, in many ways their effects lead to systematic uncertainties that can be quantified and the results from differing SPS techniques are consistent once corrected for systematic uncertainties. For example, assumptions of the IMF, stellar evolution and individual stellar SEDs are inherent to the SPS code and lead to well understood systematic uncertainties. One of the most robust galaxy parameters that can be extracted from an SPS analysis is fortunately one of the most fundamental parameters, namely a galaxy's stellar mass. A stellar mass can be derived in a few ways from SPS modeling. In the most popular approach, and the one used in this thesis, broadband photometry is fit to a library of SEDs generated by an SPS code with a range of varying input parameters such as formation age, star formation history and metallicity. The galaxy model SED that best matches the galaxy's broadband colours is normalized to the distance or redshift of the galaxy in order to obtain the stellar mass using one of two approaches. One approach is to use the stellar mass that is an output of the SPS code, another approach, is to use the galaxy model's luminosity (in a specific passband, ideally as red as possible) and stellar mass to measure the galaxy model's mass-to-light (M/L) ratio. From this, and the measured magnitude, the M/L ratio can be used to measure the galaxy's mass.

The essence of modeling a galaxy through the SPS technique is to compare measurements of light in multiple filters from the ultraviolet to the infrared to predictions from SPS generated SEDs to model the contribution from different aged stellar populations. The contribution of an old SSP will primarily dominate the longer red wavelengths where the longer-lived stars peak in emission. A younger recently formed SSP is comprised of longer-lived, low-mass stars, intermediate mass stars and very short-lived ($< 10\,\mathrm{Myr}$)

massive stars. Since massive stars peak at shorter wavelengths and emit much more light at all wavelengths, these populations can dominate emission in the UV and visible, and observing a galaxy at these wavelengths may provide information about the number of young massive stars in a galaxy (which is consequently direction related to the instantaneous star formation rate), but it does not always accurately probe the stellar mass if a large population of evolved SSPs comprise the galaxy.

The stellar mass is a measure of how much gas is converted into stars. For an older SSP, the mass is either locked up in the longer-lived, low-mass stellar population, or was once in more massive stars that have left the main-sequence and have either blown most of their mass off in mass loss during various post-main-sequence stages or through more dramatic events such as supernova. Only a small fraction of mass remains in stellar remnants (black holes, neutron stars and white dwarves). But by observing the low-mass stellar population, it is possible to extrapolate how much stellar mass was created in formation. On the other hand, younger SSPs will have their stellar mass distributed among the range of stellar masses according to the assumed IMF. In order to segregate the older stellar population from the younger stellar population, it is essential to be able to decompose the galaxy's SED into the different populations. Fortunately, this can be done by observing the galaxy in multiple wavelengths, including observations at longer wavelengths that probe the lower-mass stellar emission.

Multiwavelength observations are also important for constraining the effect of attenuation due to dust on the SED of the stellar populations. Moving blueward along a galaxy's SED, dust increasingly absorbs stellar radiation and the magnitude of the extinction is hard to constrain in a galaxy with minimal wavelength coverage because the extinction can often be mistaken as an older stellar population as its reddening effectively minimizes more of the light from the higher mass stars, mimicking the SED of a more evolved population. However, this degeneracy can be constrained with multiwavelength data. Here, coverage in the blue to UV is essential to constrain the amount of dust extinction.

In the low-z universe, stellar masses can be measured to within a factor of 2 (Kauffmann et al., 2003; Glazebrook et al., 2004) provided there is photometric coverage at rest-frame wavelengths beyond $\sim 0.9\,\mu$m. Because near-infrared light is believed to be the best tracer for stellar mass, K-band limited surveys (e.g. Cole et al. 2001; Dickinson et al. 2003; Fontana et al. 2003; Abraham et al. 2004) were equated to mass-limited surveys. At longer wavelengths, longer-lived stars provide a greater fractional contribution

to the integrated light of a galaxy and the range of possible M/L ratios is smaller than at visible wavelengths (Kauffmann et al., 2003). However, beyond $z \sim 1$ K-band light probes rest-frame optical light which is no longer such a proxy for stellar mass. Rest-frame K-band surveys are desired and the need for deep and longer wavelength data for such surveys would soon be met from space by the launch of the *Spitzer Space Telescope* (Werner et al., 2004).

1.3 Stellar populations and dust in the near-infrared

The launch of larger angular resolution and improved sensitivity IR space observatories such as the *Infrared Space Observatory* (ISO; Kessler et al. 1996), *AKARI* (Murakami et al., 2007) and especially the *Spitzer Space Telescope* (Werner et al., 2004) provided a new view of stellar populations both nearby and at high redshift.

At low-redshift, surveys by Cole et al. (2001) and Dickinson et al. (2003) showed that NIR photometry traced the evolved stellar populations and resulted in more robust stellar mass estimates. But the K-band surveys of higher redshift galaxies such at Fontana et al. (2003) and Dickinson et al. (2003) lacked rest-frame NIR. Nevertheless, stellar mass estimates from these surveys were used to quantify the evolving mass function and stellar mass density. With the launch of *Spitzer*, an obvious new test was to investigate how the photometry from the Infrared Array Camera (IRAC; Fazio et al. 2004), whose MIR capabilities allow for rest-frame NIR coverage, affect the results of these surveys. Stellar mass estimates were recalculated with the additional photometry provided by IRAC covering the rest-frame NIR out to $z \sim$5 in a number of surveys (Papovich et al., 2006; Fontana et al., 2006; Pérez-González et al., 2008; Elsner et al., 2008). And indeed mass-estimates are more precise with estimates being constrained to within a factor of ~ 1.25 (~ 0.1 dex) with the most significant improvement for galaxies beyond $z \sim 2$ (Elsner et al., 2008; Pérez-González et al., 2008). However, the precision in the stellar masses didn't lead to drastic changes in the conclusions of these studies although it did improve the precision of measurements of the evolving mass function and stellar mass density, which are now limited by the SPS models rather than the observations. Recent work by Muzzin et al. (2009) has shown that the choice of SPS code results in more uncertainty (roughly a factor of 1.5) than that gained with the increased photometry.

For nearby galaxies, SPS modeling of stellar populations is poorly constrained at rest wavelengths beyond 2 μm. A complete consensus of spectral libraries at NIR and MIR

wavelengths at a range of stellar masses and evolutionary phases is not feasible from the ground or today's space observatories. The current generation of SPS models generally assume the emission is dominated by the blackbody radiation emitted by stars. But in reality, the infrared stellar emission is expected to be more complicated because (1) stellar atmospheres are not perfect blackbody emitters, (2) the contribution from lower mass stars ($< 0.5\,M_\odot$) which peak at NIR and MIR wavelengths are not included in the SPS models and (3) the evolutionary phases of stars, particularly low-mass stars, are not well understood but can contribute significantly. In addition, emission from dust and/or polycyclic aromatic hydrocarbons (PAHs) becomes significantly more important at wavelengths beyond $2\,\mu$m. Extragalactic observations with *ISO* and *Spitzer* show excess emission compared to the predictions of the SPS models (Lu et al., 2003; Mentuch et al., 2009). This excess continuum emission, peaking at $2 - 5\,\mu$m can be modeled by continuum emission in the form of a greybody with a temperature of $\sim 1000\,$K (da Cunha et al., 2008), whose intensity scales with line emission related to PAHs (Lu et al., 2003) and appears to correlate with the intensity of star formation in the galaxy (Mentuch et al., 2009).

As a result, stellar mass estimates (as measured in Elsner et al. 2008 and Pérez-González et al. 2008) are compared to SPS models excluding any multiwavelength emission beyond rest-frame $2\,\mu$m where SPS models have not been fully calibrated and the contribution from non-stellar emission becomes significant. To account for the latter, the emission component has been shown to be modeled as an additional parameter (da Cunha et al., 2008; Mentuch et al., 2009). But mass estimates could be more precise, and the SEDs of galaxies more constrained, if instead of modeling the NIR emission as an additional parameter, we can determine how the properties of the emission relates to other galaxy parameters such as the optical dust extinction or the stellar and interstellar radiation fields likely heating the emission. In order to do this, we must consider the sources of NIR emission that must be added to the models.

1.3.1 Near-infrared excess emission in the Milky Way

A large number of objects locally show NIR emission in excess of the emission expected from stellar emission. Stars emit at these wavelengths in a very predictable way (according to the rayleigh-jeans tail of the blackbody distribution), and it turns out that the NIR colours resulting from their emission are independent of the age of the stellar

population. One only needs to look at the closest star-forming regions to find a number of sources with NIR excess emission. Reflection nebulae (RNae) around massive O and B-type stars in the Orion Molecular cloud display a smooth continuum feature from 1.25 to 4.8 μm that is characterized by a blackbody with a ~ 1000 K temperature in addition to a narrow emission feature at 3.3 μm (Sellgren et al., 1983, 1996). But its not only the extended regions that comprise the RNae which exhibit NIR dust emission, some of the O and B stars powering the RNae in the study by Sellgren et al. (1996) have larger L-band (3.6 μm) luminosities than their optical luminosities would suggest. Excesses in such massive stars is not unique, $JHKL$ photometry of massive stars in the $\sim 1-3$ Myr old star-forming regions NGC 3576 (Maercker et al., 2006), G305.2+0.2 (Longmore et al., 2007), and 30 Dor in the Large Magellanic Cloud (LMC) (Maercker & Burton, 2005) show L-band (3.5 μm) excesses in more than half of their stars with masses $> 10\,M_{\odot}$. These authors attribute the excess to dust heated in circumstellar disks (Lada & Adams, 1992).

If the excess NIR emission is attributed to circumstellar dust and/or molecular emission, this would require the dust to be located at very close distances to the heating star. For example, an extremely luminous star of 10^5 L$_{\odot}$ will heat dust to sublimation temperatures of 1000-1500 K at a distance of 7.3 AU. The most likely configuration of this circumstellar dust would be in the form of a circumstellar disk. One model for the circumstellar disk with NIR emission is the flared disk model presented by Dullemond et al. (2001). In this particular model, the inner part of the disk is removed out to a radius (6 AU for a B2 star) of the dust evaporation temperature ($T_{evap} = 1500$ K). Unlike the top and bottom surfaces of the flared disk which receive radiation from the star at a grazing angle, the inner edge of the disk receives radiation face-on and has a large covering fraction of the central star. The result is a disk that is substantially heated to temperatures up to T_{evap} and the disk becomes puffed up, increasing the surface area of the inner rim and the NIR emission (see Dullemond et al. 2001 for schematic diagrams). The circumstellar disk model is supported by observations of nearby young, massive stars (see Muzerolle et al. 2003; Monnier et al. 2005; Millan-Gabet et al. 2006 for surveys of Herbig Ae/Be Disks), although some simulations suggest a halo of hot NIR emission better represents the strong NIR excesses observed around young, massive stars (Vinković et al., 2006). Whatever the configuration, dust heated at very close distances to luminous stars is a likely scenario for the NIR excess emission.

Luminous evolved stars also display NIR excess emission. NIR excesses with spectral signatures indicative of hot (~ 1000 K) continuum emission have been observed in post-

asymptotic giant branch (AGB) stars (de Ruyter et al., 2006) and planetary nebulae (Phillips & Ramos-Larios, 2005). Both are the result of stars in their final stages of nuclear burning as they exhaust their final layers of fuel. Strong mass outflows from intermediate mass stars ($4 - 8\,M_{\odot}$) excites both gas and dust surrounding the luminous (100 - $1000\,L_{\odot}$) post-AGB stars for relatively short timescales of 10^4 yrs (de Ruyter et al., 2006). In a study of 51 post-AGB stars, de Ruyter et al. (2006) find that all post-AGB stars contain large IR excesses with dust excess starting near the sublimation temperature, irrespective of the effective temperature of the central star. They argue that in all systems, gravitationally bound dusty disks are present. The disks must be puffed-up to cover a large opening angle for the central star and we argue that the disks have some similarity with the disks detected around young stellar objects.

Excess continuum emission in the NIR may instead come from a non-stellar source such as an active galactic nuclei (AGN) or from cirrus emission from diffuse dust permeating a galaxy. Observations by *Spitzer's* IRAC and the *Cosmic Background Explorer*/Diffuse Infrared Background Explorer *COBE*/DIRBE of the galactic cirrus (Flagey et al., 2006) reveal a continuum component in the NIR whose contribution to the IRAC [3.6 μm]-band is $50\% - 80\%$. In the nuclear region of a galaxy, AGN provide strong ionizing radiation fields that could easily heat dust to its sublimation temperature. However, heating large quantities of hot dust to the required 800 K – 1200 K is likely to be important only for strong AGN (Riffel et al., 2009) and would likely just be relevant at very close distances (< 1 pc) to the nuclear region, insufficient to explain the strong NIR excess seen in the total integrated light of a galaxy.

1.3.2 Near- and mid-infrared emission in nearby galaxies

Large systematics surveys of nearby galaxies in the near-infrared like the *Spitzer* Infrared Nearby Galaxy survey (SINGS; Kennicutt et al. 2003) and the Large Galaxy Atlas survey (LGA; Jarrett et al. 2003) offer an ideal laboratory to study the near-infrared emission of stellar populations for a range of galaxy spectral types and consequently stellar populations. The SINGS sample contains 75 spatially resolved galaxies imaged in all *Spitzer* IRAC and MIPS filters. Ancillary to the infrared observations, are a range of optical ($BVIR$) broadband observations and H_{α} narrowband observations. Near-infrared observations of the sample were obtained as part of the LGA survey. Examining the sample in its multiwavelength light, these observations demonstrate the usefulness of the infrared

as an indicator of star formation, where star formation rate measurements in the past relied on optical indicators innate with uncertainty due to dust extinction. Combined with detailed spectral information at 5-38 μm obtained by *Spitzer's* Infrared Spectrograph (IRS; Houck et al. 2004), the dataset has also revealed constraints on the mid-infrared emission of galaxies dominated by complex emission produced by polycyclic aromatic hydrocarbons (PAHs).

Star formation rate indicators in the optical and infrared generally correlate with each other in select star-forming regions, but the dependence is not linear due to a complex exchange between dust absorption and dust emission, and their subsequent dependency on metallicity. But the dependence is predictable, at least in the mid-infrared. Calzetti et al. (2007) was able to show that 24 μm emission is a good tracer of the total star formation in a galaxy, provided corrections due to metallicity are applied. The lower the metallicity, the lower the dust content and the lower the 24 μm emission. Remarkably, a simple linear combination of the H_α and 24 μm emission can correct for variations in dust processing and the total star formation rate can be measured completely empirically (Kennicutt et al., 2007; Calzetti et al., 2007). Such simple empirical combinations of photometry are not limited to H_α and 24 μm mission, Kennicutt et al. (2009) show that linear combinations of various optical (such as H_α or O II) and infrared (such as 8 μm, 24 μm or total infrared emission), as well as radio star formation indicators are a good representation of the total star formation rate. The infrared emission accounts for the loss of optical emission due to the absorption of dust.

Mid-infrared emission observations from *Spitzer*, abundant with information on the nature of polycyclic aromatic hydrocarbon (PAH) and very small grain (VSG) dust emission for a range of extragalactic conditions, are finally able to constrain models developed in association with studies of PAHs in laboratories on Earth, where replicating the low pressures and vastly varying radiation fields produced in space is difficult. Observations of "unidentified infrared bands" were first observed in 1973 in the spectra of planetary nebula (Gillett et al., 1973) and later observed in a range of astronomical environments such as planetary nebulae, reflection nebulae, H II regions, circumstellar envelopes and disks and external galaxies. The agreement between the features and emission associated with PAHs in laboratory work led to the conclusion (Leger & Puget, 1984) that the emission is due to different stretching, bending and rotational modes of carbonaceous molecules similar in structure to the laboratory PAHs. In general the PAHs are very small, on the order of $\sim 5 - 50$ Å and consist of lattice structures of fifty to several hun-

dred molecules consisting of carbon and hydrogen atoms. Although, the carriers of the NIR and MIR emission are referred to as the broad class of PAHs, we note that, other particles, also consisting of carbon-carbon bonds remain consistent with some aspects of the band's strength, shape, and location (see Li & Draine 2001 for discussion).

Whatever the atomic description for the carriers of NIR and MIR emission, a number of observational properties describe the emission. The emission is found in range of environments. It is short-lived in circumstellar disks as the disk themselves are short-lived, but is found in extended environments around reflection nebula and in the galactic cirrus emission of our own galaxy (Flagey et al., 2006). In a sample of normal star-forming galaxies, observed in the *ISO Key Project on Nearby Galaxies* (Helou et al., 2000), the PAH spectrum is surprisingly consistent over a range of different galaxy environments, with band-to-band variations of at most 15% out to 11 μm (Lu et al., 2003). Luminosity ratios of PAH bands at 6.2, 7.7, 8.6, 11.3, 12.6 and 17 μm are relatively constant, except in galaxies with low-luminosity AGN, where some PAH features are absent, with shorter wavelength emission features progressively destroyed as distance to the nuclear region decreases (Smith et al., 2007). Galaxies with low metallicity also show little variation in their MIR colours, although the absolute strength of the PAH features decreases with decreasing metallicity (Engelbracht et al., 2005; Madden et al., 2006; Draine et al., 2007).

However, in our own Galaxy (e.g., Verstraete et al. 1996; Peeters et al. 2004) and in nearby resolved galaxies like the Small Magellanic Cloud (SMC) (Contursi et al., 2000) and the LMC (Vermeij et al., 2002) the PAH emission spectrum is variable on small scales and can depend sensitively on the local gas density and the incident radiation field. The natural variations found on small scales appear to be smoothed over when a galaxy is viewed in its integrated light. Nearby resolved galaxy surveys, such as the SINGS and the LGA surveys, provide a synergy between the detailed resolved analysis that can be accomplished by analysing localized star formation regions such as the highly studied Orion Molecular Cloud (OMC) region, while at the same time allowing for a spatial average over such photodissociation regions to smooth over the likely time evolution of star formation dust processes evolving dust from circumstellar emission to cirrus emission. It also reveals the interplay between dust emission and the stellar population. As an example, recent mapping of M33 by Verley et al. (2009) revealed the importance of discrete sources to 24 μm emission, and find that VSG emission, as powered by the diffuse ISRF, account for only 10% of the diffuse 24 micron emission, while unresolved AGB stars of intermediate-mass (e.g. carbon stars), through their dusty circumstellar

envelopes can provide most of the diffuse 24 μm emission.

PAHs, VSGs and larger grain dust emission is an important feature of the SED of stellar populations, seen in young star-forming regions, evolving post-main-sequence stars, and the interstellar medium of our own Galaxy and that of other galaxies. It is a feature that can likely be incorporated into SPS models if the relation between the emission and the underlying stellar populations exciting the emission is accurately modeled. Made from heavy elements such as carbon, silicon and oxygen, emission from these molecules and grains is lower in low metallicity environments. For the first generation of stars, often referred to as Population III stellar populations, there would be no emission from dust and PAHs as a consequence of the zero metallicity birth environment they are borne from. Population III stars and the stellar populations responsible for reionizing the Universe, will not have strong rest-frame NIR and MIR emission, but because they are found at such high redshifts, their stellar light (peaking at visible wavelengths) emits at NIR and MIR wavelengths. And just as the NIR and MIR is essential for studying both evolved and young and dusty stellar populations, it is also essential for the discovery and study of the most distant, early stellar populations.

1.4 Near-infrared detections of very high redshift galaxies and the earliest stellar populations

Near-infrared observations probe rest-frame optical light of distant, high-redshift galaxies and are essential for their discovery. As the sensitivity of near-infrared detectors improve, both observatories on the ground and in space are devoting large fractions of their time to discovering the deepest, most distant galaxies. The number of galaxies detected at $3 < z < 6$, when the universe was just $\sim 1 - 2$ billion years old, is now >6000 galaxies (Bouwens et al., 2009). The success of these deep near-infrared photometric surveys is through the use of the drop-out technique where multiple broadband images are efficiently used to detect galaxies whose redshifted emission blue of the Lyman limit results in a non or weak detection in one or more bands, while the near-infrared images reveal detection of the redshifted galaxies visible emission. The success rate of finding true high-z galaxies is ∼75% as verified by large spectroscopic surveys (Steidel et al., 1996; Popesso et al., 2009; Vanzella et al., 2009).

Finding galaxies beyond $z > 7$ is difficult to do with broad-band filters. The dropout

technique at this redshift requires deep observations in the NIR, but beyond 0.9 μm, the night sky is contaminated with a number of narrow emission lines from atmospheric hydroxyl molecules. Because of this high sky noise, it is just not feasible to detect galaxies from the ground with broadband filters on todays 8-10 m class observatories. Deep NIR observations of the *Hubble Ultra Deep Field* (HUDF) from space were successful at detecting ~ 40 candidates at $z \sim 7$ (Bouwens et al., 2004) and a small number of candidates at $z \sim 8$. The numbers have jumped dramatically with recent re-imaging of the HUDF with the *HST's* new WFC3/IR camera, which provides a deeper view of the NIR universe with about $40\times$ increased sensitivity. The analysis of the new data is somewhat controversial, with the number of candidates at $z \sim 8$ ranging from a conservative five candidates (Bouwens et al., 2010) to 15 candidates (Yan et al., 2009). Objects identified as J_{125}-dropouts ($z > 9$) also varies from zero (Bunker et al., 2009) to three (Bouwens et al., 2009) to 20 (Yan et al., 2009). None of these have been spectroscopically confirmed. The most distant object detected to date is a $z = 8.2$ spectroscopically confirmed gamma ray burst (Tanvir et al., 2009).

From the ground, the emission from earth's atmosphere drowns out the signal of faint distant galaxies. This emission is largely due to a forest of hydroxyl emission lines and fortunately in between these emission lines are relatively transparent windows through the atmosphere into space. A few novel techniques can be used to exploit these rather transparent, but narrow, windows. Narrowband filters, with passbands of ~ 10 nm have found a number of candidates at high redshifts of 5.6 (Shimasaku et al., 2006), 6.5 (Kashikawa et al., 2006) and 7.7 (Hibon et al., 2010; Tilvi et al., 2010). But narrowband surveys beyond this redshift have yet to be successful (Willis & Courbin, 2005; Cuby et al., 2007; Sobral et al., 2009), unable to reach the flux sensitivities required to probe the luminosity function of galaxies assuming no evolution from $z \sim 7.7$. Spectroscopic slit surveys, also capable of detecting photons in between the bright OH emission lines, may have had some success where narrow band filters have not (Santos et al., 2004; Stark et al., 2007a). Rather than blindly placing a spectroscopic slit and surveying only a small fraction of the sky, these surveys took advantage of a gain in flux sensitivity by utilizing the magnification gain of intermediate galaxy clusters. A lens model is used to map the lines of critical magnification gain due to gravitational lensing of a galaxy cluster at a specific redshift. The slit is placed on this line and can search for emitters at the redshift corresponding to this maximum magnification gain. The technique provides a gain in flux sensitivity of $10-50\times$. Reports of six promising candidates from Stark et al. (2007a)

have yet to be spectroscopically confirmed.

1.5 Scope of thesis

This thesis encompasses a broad range of existing and potential observations of extragalactic stellar populations in the near- and mid-infrared. Some of the observations in this thesis are of stellar populations that reside in nearby galaxies; while other observations are of those found in massive, star-forming galaxies at intermediate redshifts when the universe formed the bulk of its stars. I also present work on an instrument which holds the potential to detect stellar populations in some of the earliest galaxies to form after the formation of the universe.

In **chapter 2**, I apply the technique of stellar population synthesis to observations of ~ 100 galaxies with spectroscopic redshifts at $z = 0.5 - 2$ from the Gemini Deep Deep Survey (GDDS; Abraham et al. 2004). I test how stellar mass estimates improve when the code is applied to a set of multiwavelength photometry which includes rest-frame NIR photometry as measured by *Spitzer's* Infrared Array Camera at 3.6, 4.5, 5.6 and 8.0 μm. The effect of model input parameters, such as the choice of star formation history model, the inclusion of an NIR emission component and the treatment of TP-AGB stars, on stellar masses is also investigated.

From the analysis presented in chapter 2, a surprising result emerges in the data. Although the rest-frame light short of $2\,\mu$m is a good description of the total emission of a galaxy, the models and observations disagree beyond $2\,\mu$m. In **chapter 3**, I show that relative to the SEDs produced by SPS models, there is a statistically significant component to a galaxy's SED that emits in the NIR above the NIR emission provided by the stellar population alone. In this chapter, I compile a census of local objects with NIR excess emission and calculate how each NIR emitting candidate would stack up when seen as a galactic scaled population.

In **chapter 4**, I measure the pixel-by-pixel near-infrared colours for a sample of 68 nearby galaxies common to the *Spitzer* Infrared Nearby Galaxy survey (SINGS; Kennicutt et al. 2003) and the Large Galaxy Atlas survey (LGA; Jarrett et al. 2003) observed at H_α, 1.25, 3.6, 4.5, 5.6, 8.0 and $24\,\mu$m. Each galaxy is categorized into different regions based on increasingly red near-infrared colours, consisting of colours redder than the near-infrared colours due to stellar emission. The spatial location of stellar populations with very red NIR colours is investigated and I determine whether these regions

are associated with other properties of the resolved stellar populations, such as the star formation rate, dust extinction, and dust and/or PAH emission.

In **chapter 5**, I present the development of the opto-mechanical control of the Flamingos 2 Tandem Tunable (F2T2; Scott et al. 2006; Mentuch et al. 2008) filter. The NIR-optimized, tunable filter is capable of taking a narrowband image at any wavelength within the J-band, scanning from 0.95 to 1.35 μm. The science driver behind the development of the F2T2 filter is to find bright Lyman alpha emitting (LAE) galaxies at redshifts of $8 < z < 11$. In this chapter, the search strategy to be implemented with the filter is presented and number predictions for $8 < z < 11$ candidates are made by evolving the observed LAE luminosity function at $z = 5 - 7$.

Chapter 2

The stellar masses, mass function and mass density of galaxies in the redshift desert with the *Spitzer Space Telescope*

Some of the work in this chapter has been published as:
"A near-infrared excess in the continuum of high-redshift galaxies: a tracer of star formation and circumstellar disks?"
Mentuch, E., Abraham, R. G., Glazebrook, K., McCarthy, P. J., Yan, H., ODonnell, D. V., Borgne, D. L., Savaglio, S., Crampton, D., Murowinski, R., Juneau, S., Carlberg, R. G., Jorgensen, I., Roth, K., Chen, H.-W., & Marzke, R. O. 2009, ApJ, 706, 1020

2.1 Abstract

The stellar populations of ~ 100 galaxies at $z = 0.5 - 2$ from the Gemini Deep Deep Survey (GDDS; Abraham et al. 2004) are modeled using visible through mid-infrared photometry including wavebands from *Spitzer's* Infrared Array Camera. The star formation history of a galaxy is more accurately determined when rest-frame UV through NIR photometry is included in the fitting analysis. The additional photometry, which probes $\lambda_{\rm rest} = 1 - 5\,\mu$m, provides more robust SED fits, modeling both the stellar populations and attenuation due to dust to higher precision. In this chapter, stellar masses, the evolving mass function and the resulting mass density function, previously deter-

mined with $VIz'K_s$ wavebands in Glazebrook et al. (2004), are revisited. Stellar masses for evolved, red ($(U-B)_{\rm rest} > 0.1$) galaxies are consistent with previous estimates, but galaxies with young or mixed stellar populations and bluer colours ($(U-B)_{\rm rest} < 0.1$), have stellar masses on average ∼0.4 dex higher. The largest changes, however, affect lower mass galaxies that contribute less to the resulting mass density and mass functions, and as a result, including the *Spitzer* IRAC stellar masses produces mass functions and mass densities that are consistent with those measured with the $VIz'K_s$ wavebands only. Also in this chapter, the effect of varying a range of model input parameters, such as the choice of star formation history model, the inclusion of an NIR emission component and the treatment of TP-AGB stars, on stellar masses, is investigated.

2.2 Introduction

In large surveys of high-z galaxies, broadband photometry is commonly fit to SEDs produced by stellar population synthesis (SPS) models to determine photometric redshifts, stellar masses, star formation rates (SFRs) and other global quantities of galaxies. Although, the high number of parameters involved in these models leads to large degeneracies in the fitted parameters, the stellar masses are not highly sensitive to the degeneracies and precise (better than ∼0.1 dex) estimates of the stellar masses are possible provided enough wavelength information (Kauffmann et al., 2003; Glazebrook et al., 2004). Near-infrared light at 1-2 μm is a good probe of the total stellar mass, provided the contribution from young and old populations contributing to the emission can be separately identified (Dickinson et al., 2003; Glazebrook et al., 2004). Rest-frame UV and visible-wavelength photometry probes the younger stellar populations and is sensitive to the amount of dust attenuating stellar emission; while near-infrared photometry probes the underlying older stellar populations. But even in the NIR, these evolved populations can be hidden under younger populations due to their higher mass to light ratios. For a given mass, older populations, consisting mostly of low mass stars, give off less light than young stellar populations, consisting of both bright massive stars and low mass stars. In galaxies where both populations contribute strongly to the total SED output, the underlying evolved population can sometimes be missed without rest-frame near-infrared photometry, underestimating the total mass of the galaxy.

Stellar mass is one of the most fundamental parameters we can measure for a galaxy and quantifies how much of a galaxy's gas reservoir has been converted into stars. Recent

Spitzer observations of the deepest galactic fields show that by $z \sim 1$ approximately half of the local stellar mass density was already formed (Dickinson et al., 2003), with about 40% assembled between $z = 1$ and $z = 4$ (Pérez-González et al., 2008). This is consistent with results from intermediate-redshift surveys, such as the Canada-France Redshift Survey (Lilly et al., 1995), which showed that by $z \sim 1$, most of the stellar mass in today's galaxies was already assembled, while galaxies observed at $z \sim 3$, contain only 15-20% of today's stellar mass (Shapley et al., 2001; Dickinson et al., 2003). Complementary to these findings, examination of star formation rates (SFRs) also reveals the way in which mass has assembled in high-redshift galaxies as a function of both redshift and mass via "downsizing" (Cowie et al., 1996). Juneau et al. (2005) demonstrated, using the GDDS sample analyzed in this thesis, that the star-formation rate density (SFRD) in the most massive galaxies ($M > 10^{10.8} M_{\odot}$) was 6 times higher at $z = 2$ than it is today. In contrast, intermediate mass galaxies ($10^{10.2} M_{\odot} < M < 10^{10.8} M_{\odot}$) display a peak in their SFRD around $z = 1.4$.

Generally, near-IR light traces mass, and *Spitzer* IRAC (3-8 μm) observations are desirable for stellar mass measurements beyond $z \sim 1$ where the K-band rest-frame light is redshifted into the IRAC filters. But at longer wavelengths the contribution from polycyclic aromatic hydrocarbons (PAHs) and emission from other non-stellar sources of luminosity are not included in the models. For this reason, band fluxes beyond rest-frame 2 μm are often excluded from stellar population synthesis SED fitting routines (see for example Papovich et al. 2006; Pérez-González et al. 2008; Magnelli et al. 2008). Emission beyond 5 μm is generally associated with PAH emission and there is also evidence that PAH features and other non-stellar sources of luminosity lead to an excess at 2-5 μm and can be a possible source of bias in the estimation of stellar mass. For example, in a survey of 45 normal star-forming galaxies (Lu et al., 2003), near-IR observations reveal a weak excess component of continuum emission in the range of 2-5 μm characterized by a very high colour temperature (~ 1000 K). Therefore, a more ideal approach for modeling SEDs is to include non-stellar sources of emission in the SED models. Although current SPS models do not yet provide components to model infrared emission associated with PAH molecules and dust, a 850 K greybody scaled to match the spectrum of PAH emission has been shown to be a good empirical model for the NIR excess emission (da Cunha et al., 2008).

In this chapter, we test the robustness of stellar mass estimates and the reliability of stellar population synthesis models when rest-frame near-infrared light out to 5 μm is

included in the analysis on a sample of $\sim$ 100 galaxies, described in § 2.3, from a K-band selected (and thus mass-selected) spectroscopic sample from the Gemini Deep Deep Survey (Abraham et al., 2004). We begin by limiting our analysis to the rest-frame light short of 2 μm where non-stellar emission is assumed to be negligible, and the light is a good tracer of the stellar mass. We investigate how varying model ingredients, described in § 2.4, such as one vs. two component star formation histories (SFHs), or the treatment of thermally pulsating asymptotic giant branch (TP-AGB) stars, affects stellar mass estimates. We also consider an SPS model augmented with the hot dust greybody model from (da Cunha et al., 2008), which has been shown to be a good fit to the GDDS mid-infrared photometry (see chapter 3 of this thesis and Mentuch et al. 2009). The impact of these changes in the input modeling and photometry on measured stellar masses are presented in § 2.6. The revised mass function and mass density for the GDDS survey is presented in § 2.7 and 2.8, respectively. Throughout this study, we adopt a concordance cosmology with H_0=70 km s^{-1} Mpc^{-1}, $\Omega_M = 0.3$, and $\Omega_\Lambda = 0.7$. All photometric magnitudes are given in AB magnitudes, unless otherwise noted.

2.3 Observations

2.3.1 Summary of GDDS observations

The Gemini Deep Deep Survey (hereafter GDDS; Abraham et al. 2004) is a spectroscopically-defined colour-selected subset of the 1 deg^2 Las Campanas Infrared Survey (LCIRS; McCarthy et al. 2001). It consists of four 5′.5 × 5′.5 fields chosen from the parent sample to minimize cosmic variance. The sample consists of galaxies with $K_{s,\mathrm{Vega}} < 20.6$ mag and $I_{\mathrm{Vega}} < 24.5$ mag ($K_{s,\mathrm{AB}} < 22.4$ mag and $I_{\mathrm{AB}} < 24.9$ mag) in the redshift interval $0.5 < z < 2.0$. The GDDS multi-band coverage includes $UVBRIz'JHK_s$ broadband photometry in addition to high-resolution Advanced Camera for Surveys (ACS) coverage of $\sim$ 60% of the fields in the F814W filter. For this analysis, we only select objects with high-confidence spectroscopic redshifts and those which are confidently detected in the longest IRAC channel (we required $\Delta[8.0] < 0.3$ mag). This results in 103 galaxies from the 309 objects in the original GDDS sample. A summary of the properties of the sample, such as the GDDS object identification, right ascension, declination, spectroscopic redshift and dust-corrected star formation rates are tabulated in Table 2.1.

All objects are assigned a spectral type classification as outlined in Table 2.1. The

classification is based on three digits that refer to young, intermediate-age, and old stellar populations. Objects showing nearly pure spectral signatures of an evolved stellar population were assigned a GDDS class of "001" in Abraham et al. (2004). In many of the figures in this chapter, we key each galaxy to their galactic spectral type. The evolved "001" galaxies are plotted as red circles. Objects showing a strong-UV continuum dominated by massive stars were classified as "100" and are plotted as blue stars. Objects with intermediate ages (e.g., strong Balmer absorption) were classified as "010" and are plotted as green squares. Some objects consist of both an evolved population plus a younger more recent star formation component. These objects are listed as mixed populations with spectral types of "110" or "101" and are plotted as orange dots in our figures.

Source blending from objects on the edge of our 4″ apertures could potentially add a flux excess. We went through our sample of 103 galaxies by eye (inspecting both our ground-based I-band and *HST* ACS [814W] images) and flagged any object that has a neighbour within a 7″ aperture. We found 15 such objects and identify them as IRAC blend flag = 1 in Table 2.1. We will show that these objects are poorly fit by the SED models in chapter 3 and exclude them from most of our analysis, but are included in the analysis presented in this chapter.

Table 2.1. GDDS Galaxy Sample

Object ID	Sp.T.[a]	R.A	Dec.	z_{spec}	bl. flag[b]	K_{Vega}	$(U-B)_{rest}$	SFR[c] (UV) ($M_\odot$/yr)	SFR[c] (O II) ($M_\odot$/yr)
SA02-0452	011	02:09:49.51	-04:40:24.49	0.828	1	17.87	0.364	...	1.929
SA02-0621	010	02:09:36.80	-04:40:04.24	1.350	0	19.27	0.054	50.635	9.715
SA02-0708	010	02:09:34.81	-04:39:47.79	1.310	1	18.64	0.381	8.555	4.177
SA02-0715	110	02:09:41.43	-04:39:36.81	1.130	0	17.52	0.047	...	1.150
SA02-0725	010	02:09:42.38	-04:39:38.14	1.080	1	18.25	0.270	...	1.885
SA02-0733	110	02:09:43.10	-04:39:41.10	1.080	0	18.77	-0.067	...	12.709
SA02-0744	110	02:09:38.83	-04:39:44.33	1.270	0	19.93	-0.315	8.172	2.930
SA02-0857	001	02:09:48.89	-04:39:19.87	1.050	0	17.95	0.554	...	0.861
SA02-0995	001	02:09:48.09	-04:38:54.39	0.786	0	18.59	0.332	...	0.622
SA02-1011	001	02:09:31.59	-04:38:53.96	1.130	0	19.27	0.397	...	0.291
SA02-1186	001	02:09:49.91	-04:38:19.44	1.050	0	17.56	0.633	...	2.092
SA02-1255	001	02:09:45.60	-04:38:07.19	1.340	0	18.23	0.516	0.538	0.645
SA02-1417	100	02:09:33.32	-04:37:31.15	1.600	0	19.39	-0.267	66.813	7.037
SA02-1636	100	02:09:48.03	-04:35:25.11	1.640	0	20.04	-0.267	12.955	24.610
SA02-1702	110	02:09:48.89	-04:35:46.07	1.050	1	19.52	-0.140	...	4.151
SA02-1724	010	02:09:37.13	-04:36:02.61	0.995	0	17.80	0.269	...	1.897
SA02-1777	010	02:09:40.27	-04:36:02.60	0.981	0	19.09	-0.098	...	3.785
SA02-1785	110	02:09:36.32	-04:36:01.01	1.000	0	20.70	-0.350	...	...
SA02-1842	001	02:09:49.58	-04:36:23.39	1.340	0	18.61	0.405	4.791	0.035
SA02-1935	001	02:09:51.57	-04:36:29.48	0.915	0	17.90	0.509	...	0.447
SA02-2197	001	02:09:32.10	-04:37:16.87	1.130	0	18.45	0.259	...	1.871
SA02-2530	100	02:09:42.94	-04:35:14.29	1.530	0	20.12	-0.326	18.398	20.346
SA12-5175	001	12:05:21.36	-07:24:58.01	0.891	1	19.28	0.118	...	1.863
SA12-5241	100	12:05:28.35	-07:24:57.86	1.360	0	19.74	-0.364	10.883	...
SA12-5337	001	12:05:18.75	-07:24:57.19	0.678	0	17.49	0.097	...	1.778
SA12-5513	001	12:05:16.62	-07:24:43.70	0.611	0	17.58	0.134	...	1.062
SA12-5592	001	12:05:22.13	-07:24:32.64	1.620	0	19.42	-0.041	30.393	2.689
SA12-5722	110	12:05:20.96	-07:24:22.27	0.841	0	18.37	0.119	...	2.638
SA12-5724	010	12:05:28.80	-07:24:27.60	0.880	0	19.00	0.078	...	0.627
SA12-5761	110	12:05:17.63	-07:24:22.35	1.080	0	20.15	-0.394	...	10.313
SA12-5836	011	12:05:19.09	-07:24:15.12	1.340	0	18.95	-0.062	119.028	1.115
SA12-5869	001	12:05:21.55	-07:24:09.44	1.510	0	18.58	0.232	6.066	1.980
SA12-5957	100	12:05:24.33	-07:24:02.84	1.340	0	20.25	0.076	1.662	3.598
SA12-5965	100	12:05:12.11	-07:24:02.06	1.860	0	20.61	-0.232	...	...
SA12-6192	100	12:05:25.32	-07:23:51.27	1.500	1	19.86	-0.251	12.140	7.200
SA12-6301	100	12:05:18.36	-07:23:43.30	1.760	1	19.49	-0.391	17.464	...
SA12-6456	001	12:05:19.15	-07:23:45.64	0.612	0	16.97	0.298	...	0.239
SA12-6619	011	12:05:30.33	-07:23:22.78	1.080	0	18.03	-0.211	...	8.393
SA12-6800	001	12:05:18.14	-07:23:21.97	0.615	0	16.69	0.307	...	0.065
SA12-7045	001	12:05:32.33	-07:22:46.72	1.300	0	19.73	0.154	34.696	0.117
SA12-7099	011	12:05:26.34	-07:22:53.02	0.567	0	17.54	0.051	...	1.111
SA12-7250	100	12:05:32.88	-07:22:32.76	1.900	1	19.94	-0.235	47.465	...

Table 2.1 (cont'd)

Object ID	Sp.T.[a]	R.A	Dec.	z_{spec}	bl. flag[b]	K_{Vega}	$(U-B)_{rest}$	SFR[c] (UV) ($M_\odot$/yr)	SFR[c] (O II) ($M_\odot$/yr)
SA12-7455	011	12:05:28.40	-07:22:24.24	0.829	0	18.87	0.192	...	1.669
SA12-7524	100	12:05:15.33	-07:22:28.05	1.750	0	19.93	-0.060	15.742	...
SA12-7660	110	12:05:26.83	-07:22:07.83	0.790	0	18.53	-0.002	...	4.104
SA12-7852	101	12:05:23.56	-07:20:34.16	0.963	0	19.17	-0.154	...	1.265
SA12-8025	001	12:05:25.40	-07:21:24.46	1.390	0	18.91	0.073	53.502	...
SA12-8037	001	12:05:31.61	-07:20:59.56	1.270	0	19.22	-0.242	75.133	2.075
SA12-8139	011	12:05:13.15	-07:21:05.35	1.190	0	19.29	0.140	...	3.024
SA12-8250	110	12:05:17.24	-07:20:02.97	0.766	0	20.64	-0.129	...	...
SA12-8266	001	12:05:13.90	-07:21:14.25	1.050	0	19.35	0.112	...	1.254
SA12-8668	010	12:05:14.69	-07:21:40.43	0.985	0	19.22	-0.196	...	8.175
SA12-8895	001	12:05:14.33	-07:20:14.53	1.650	0	18.48	0.275	14.271	7.743
SA12-8983	001	12:05:23.29	-07:19:57.99	0.963	0	18.24	0.369	...	0.694
SA12-9127	001	12:05:19.94	-07:20:19.53	1.030	0	19.69	0.056	...	...
SA15-4762	100	15:23:53.27	-00:06:42.04	1.590	1	19.86	0.044	3.426	8.072
SA15-5005	001	15:23:45.96	-00:06:21.28	1.840	0	19.59	0.022	29.903	...
SA15-5348	001	15:23:54.88	-00:06:04.89	0.961	0	17.99	0.536	...	0.477
SA15-6695	011	15:23:47.13	-00:04:49.61	1.630	1	19.59	0.046	...	...
SA15-6846	011	15:23:52.60	-00:04:36.15	0.961	0	18.76	0.335	...	2.073
SA15-6851	011	15:23:38.25	-00:04:37.28	1.120	0	18.77	0.310	...	6.029
SA15-7241	001	15:23:50.01	-00:04:11.06	0.747	0	18.31	0.368	...	0.103
SA15-7543	001	15:23:44.83	-00:03:37.57	1.800	0	19.03	0.229	37.643	...
SA15-7972	001	15:23:41.42	-00:03:12.04	1.360	0	19.12	0.185	60.025	...
SA15-9333	010	15:23:46.14	-00:02:57.74	1.100	1	20.25	-0.114	...	6.417
SA22-0083	011	22:17:42.27	00:12:59.46	0.859	0	19.12	-0.024	...	1.617
SA22-0128	011	22:17:32.59	00:13:13.00	1.020	0	18.90	0.157	...	2.710
SA22-0189	001	22:17:47.59	00:13:27.15	1.490	0	18.05	0.453	4.762	...
SA22-0206	010	22:17:47.23	00:13:31.78	1.010	0	19.91	-0.046	...	1.909
SA22-0281	011	22:17:35.84	00:13:51.9	1.020	0	17.97	0.390	...	2.409
SA22-0299	010	22:17:46.81	00:13:57.87	1.080	0	20.45	-0.111	...	1...
SA22-0315	011	22:17:45.92	00:14:03.71	0.908	0	18.66	0.160	...	3.288
SA22-0331	110	22:17:47.42	00:14:09.00	0.881	0	19.90	-0.337	...	7.107
SA22-0398	100	22:17:42.12	00:14:30.41	1.400	0	19.04	0.327	10.991	...
SA22-0455	011	22:17:49.42	00:14:49.06	1.310	0	19.50	0.288	2.845	1.444
SA22-0510	001	22:17:31.76	00:15:10.86	0.819	0	18.80	0.327	...	0.401
SA22-0554	001	22:17:33.01	00:15:22.70	0.874	0	18.99	0.283	...	0.063
SA22-0563	010	22:17:36.84	00:15:27.22	0.786	0	19.71	-0.363	...	4.802
SA22-0568	100	22:17:50.74	00:15:28.97	1.270	0	19.52	-0.378	...	16.436
SA22-0619	010	22:17:45.85	00:16:42.48	0.671	0	19.37	-0.016	...	0.869
SA22-0630	010	22:17:32.36	00:16:16.28	0.752	0	19.07	-0.066	...	0.866
SA22-0643	010	22:17:38.32	00:16:59.41	0.787	1	20.28	-0.315	...	1.002
SA22-0674	001	22:17:48.63	00:17:05.63	1.490	0	18.77	0.427	2.658	0.598
SA22-0710	001	22:17:44.64	00:16:49.98	0.878	0	18.40	0.431	...	0.072

Table 2.1 (cont'd)

Object ID	Sp.T.[a]	R.A	Dec.	z_{spec}	bl. flag[b]	K_{Vega}	$(U-B)_{rest}$	SFR[c] (UV) ($M_\odot$/yr)	SFR[c] (O II) ($M_\odot$/yr)
SA22-0721	001	22:17:45.77	00:16:36.30	1.480	0	18.35	0.424	...	...
SA22-0758	100	22:17:34.15	00:16:25.59	1.400	0	19.99	0.002	9.514	4.011
SA22-0770	010	22:17:33.83	00:17:03.24	0.874	0	18.69	0.076	...	0.669
SA22-0893	001	22:17:46.92	00:15:48.80	0.874	0	19.11	0.585	...	0.341
SA22-0964	100	22:17:34.59	00:17:54.85	1.510	0	19.43	-0.281	47.861	9.809
SA22-0997	010	22:17:32.25	00:17:41.81	0.643	0	21.00	-0.392	...	...
SA22-1042	100	22:17:37.76	00:17:27.96	1.520	0	19.42	-0.215	18.856	17.162
SA22-1045	110	22:17:32.58	00:17:22.20	1.370	1	19.00	0.174	7.012	6.727
SA22-1055	110	22:17:45.66	00:17:20.18	1.340	1	19.27	-0.290	24.926	6.135
SA22-1559	100	22:17:38.98	00:17:40.78	1.900	0	20.60	-0.249	3.953	...
SA22-1909	100	22:17:48.18	00:16:22.60	1.490	0	20.68	-0.487	...	...
SA22-1923	110	22:17:32.63	00:16:19.02	1.040	1	19.63	-0.377	...	11.264
SA22-1951	110	22:17:48.06	00:16:15.72	1.480	0	20.29	-0.077	6.118	8.975
SA22-1983	001	22:17:48.41	00:16:08.81	1.490	0	19.06	0.130	27.713	0.311
SA22-2045	010	22:17:35.35	00:15:54.33	1.110	0	20.35	0.037	...	2.938
SA22-2172	100	22:17:39.85	00:15:26.42	1.560	0	20.49	-0.526	20.696	20.148
SA22-2196	010	22:17:44.16	00:15:21.56	0.626	0	21.00	-0.186	...	...
SA22-2237	100	22:17:45.58	00:15:13.50	1.450	0	20.52	-0.160	2.373	8.833
SA22-2395	100	22:17:47.21	00:14:32.91	1.490	0	20.40	-0.660	6.172	5.004
SA22-2400	100	22:17:33.54	00:14:31.68	1.970	0	19.93	-0.082	7.113	...
SA22-2541	011	22:17:32.94	00:13:58.92	0.616	0	18.78	-0.110	...	1.061
SA22-2548	011	22:17:35.83	00:13:51.88	1.020	0	17.84	0.407	...	3.523
SA22-2587	001	22:17:45.12	00:13:48.21	1.400	0	19.27	0.379	1.043	0.809
SA22-2703	100	22:17:35.23	00:13:24.19	1.340	0	20.65	-0.408	...	...
SA22-2863	010	22:17:49.17	00:12:57.29	0.918	0	19.25	0.239	...	2.730

[a]Galaxy spectral type (see § 2.3.1)

[b]Possible contamination from source blending from neighbouring objects in the IRAC images

[c]Observed star formation rates from Juneau et al. (2005); UV = SFRs derived from 2000 Å continuum, O II = SFRs derived from the O II line luminosity. The SFRs were corrected for dust-extinction using the extinction corrections measured from the SED fits.

2.3.2 *Spitzer* IRAC photometry

Near-infrared observations are important for determining stellar masses through SED fitting, particularly at high redshifts where the light from evolved stellar populations, which trace the stellar mass of a galaxy, is redshifted out of the visible wavelength regime. In order to determine stellar masses of GDDS galaxies, a total of 10.9 hours of *Spitzer* IRAC observations were obtained for three of the four GDDS fields (Program ID: 3554; McCarthy et al. 2004) yielding 5σ depths of 0.45, 0.9, 6 and 8 μJy in respective IRAC bands. The final field, GDDS-SA22, was observed through an existing GTO-reserved program (Program ID: 30328; Fazio et al. 2006).

Data reduction on the IRAC photometry was performed by Haojing Yan, a post doctoral researcher at the *Spitzer* Science Center. Mosaics were created from the archived Basic Calibration Data (BCD) images using MOPEX (Final Version 18.2), a more current and improved post-BCD mosaicing tool of the *Spitzer* Science Center to achieve better background removal and a spatial resolution of $0.6''$/pixel. The first three short-exposure BCD images were thrown away to correct for the IRAC "first-frame effect". The background was corrected, for each remaining BCD image, by subtracting the peak of a count histogram of the entire image. The resulting [5.8] and [8.0] images displayed noticeable gradients and in addition had to be gradient-corrected. This gradient correction was not performed in the deeper GDDS-SA22 field. The resulting BCD images were background corrected to an AB magnitude zeropoint of 21.85 and drizzle-combined to create the final post-BCD mosaics.

Objects in the post-BCD IRAC mosaics were detected by running SExtractor in dual-image mode, where a weighted-sum of [3.6] and [4.5] images were used as the detection image. A Mexhat filter was used instead of a Gaussian filter to better de-blend and detect objects in these relatively low resolution, but deep, images. Magnitudes were then measured in each IRAC band in $4''$ diameter apertures. To extrapolate the total flux of the galaxy (which is assumed to be a pseudo point source), aperture corrections of 0.317, 0.360, 0.545 and 0.677 mags (adopted by the GOODS science team) were added to the [3.6], [4.5], [5.8], [8.0] magnitudes, respectively. The visible, near-infrared and IRAC photometry used in the SED fitting analysis are summarized in Table 2.2.

The $I - [3.6]$ vs. [3.6] (approximately $B - H$ vs H in the rest-frame for $|z| \sim 1.2$) colour-magnitude diagram presented in Figure 2.1 shows that I-[3.6] colour is a strong function of redshift for our mass-selected sample of galaxies. This dependence is most

pronounced for the brighter galaxies, suggesting that for these galaxies the red sequence is set in place by $z \sim 1.5$. We plot for reference the colour of an evolved galaxy (age=3 Gyr, τ = 500 Myr, A_v=0.25, Z=$Z_\odot$) at each redshift interval. The brightest galaxies are well matched by this evolved population model, while the fainter galaxies are bluer, indicative of younger ages.

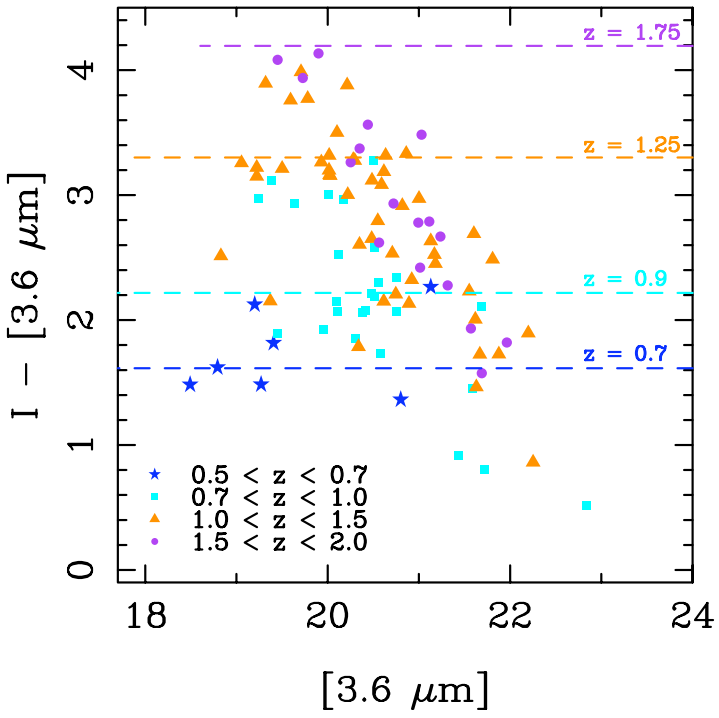

Figure 2.1 $I - [3.6\mu\text{m}]$ vs. [3.6 μm] colour-magnitude (in AB magnitude system) plot. The distribution of GDDS galaxies in this parameter space is redshift dependent. Plotted for reference is the $I - [3.6]$ colour of a 3 Gyr galaxy (τ = 500 Myr, A_v=0.25, Z=$Z_\odot$) at each redshift interval.

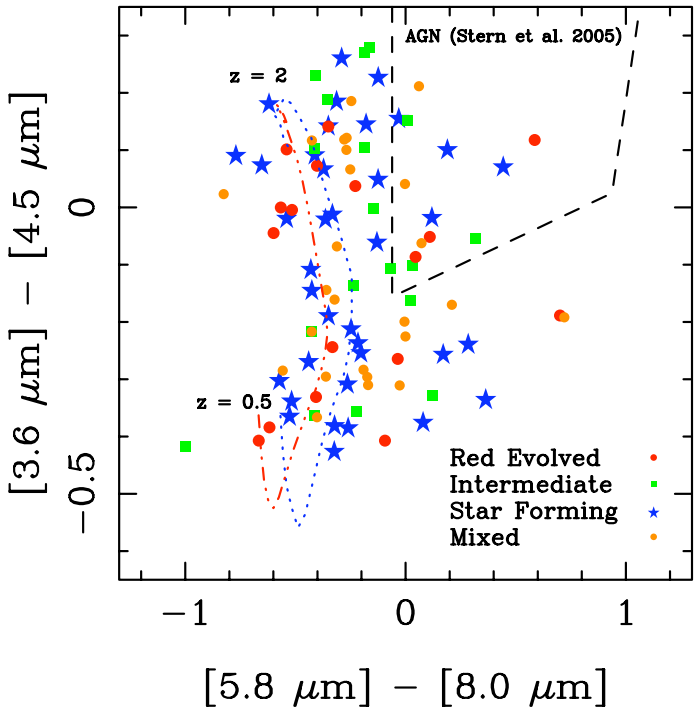

Figure 2.2 IRAC colour-colour plot of [3.6] - [4.5] vs. [5.8] - [8.0] (in AB magnitude system). We plot for reference the evolution of a typical star-forming galaxy (blue dotted line; age=200 Myr, τ = 500 Myr, A_v=1, Z=$Z_\odot$) and evolved galaxy (red dot-dashed line; age=3 Gyr, τ = 500 Myr, A_v=0.25, Z=$Z_\odot$). AGN selection from Stern et al. (2005) (region contained by the dashed line) shows that the sample could contain several of AGNs according to these criteria. However, MIPS photometry presented in the next chapter of this thesis further rules out contamination from strong AGN as seen in Figure 3.2.)

Table 2.2. GDDS Photometry (AB mags)

Object ID	V	I	z'	K_s	[3.6]	[4.5]	[5.6]	[8.0]
SA02-0452	23.796 ± 0.050	21.794 ± 0.032	21.337 ± 0.036	19.681 ± 0.085	19.382 ± 0.043	19.758 ± 0.044	19.914 ± 0.057	19.834 ± 0.116
SA02-0621	25.155 ± 0.124	23.604 ± 0.050	23.157 ± 0.095	21.081 ± 0.173	20.485 ± 0.044	20.504 ± 0.048	20.787 ± 0.110	20.667 ± 0.235
SA02-0708	25.515 ± 0.153	23.674 ± 0.058	23.096 ± 0.085	20.451 ± 0.133	19.861 ± 0.043	19.970 ± 0.044	20.392 ± 0.088	20.822 ± 0.269
SA02-0715	22.535 ± 0.032	21.344 ± 0.032	20.747 ± 0.032	19.331 ± 0.076	18.830 ± 0.043	18.932 ± 0.043	19.364 ± 0.052	19.333 ± 0.081
SA02-0725	24.305 ± 0.067	22.414 ± 0.036	21.727 ± 0.042	20.061 ± 0.104	19.445 ± 0.043	19.508 ± 0.043	19.893 ± 0.061	19.822 ± 0.120
SA02-0733	23.136 ± 0.036	22.124 ± 0.032	21.657 ± 0.042	20.581 ± 0.133	20.338 ± 0.043	20.501 ± 0.046	20.820 ± 0.090	20.797 ± 0.233
SA02-0744	23.776 ± 0.042	23.094 ± 0.042	22.857 ± 0.076	21.741 ± 0.262	21.629 ± 0.062	21.844 ± 0.085	21.665 ± 0.253	21.793 ± 0.648
SA02-0857	25.175 ± 0.124	22.714 ± 0.036	21.747 ± 0.042	19.761 ± 0.095	19.501 ± 0.043	19.786 ± 0.044	20.094 ± 0.060	20.651 ± 0.235
SA02-0995	25.116 ± 0.114	23.134 ± 0.042	22.526 ± 0.058	20.401 ± 0.124	20.169 ± 0.044	20.471 ± 0.047	20.435 ± 0.085	21.007 ± 0.319
SA02-1011	25.645 ± 0.192	23.734 ± 0.050	22.826 ± 0.076	21.081 ± 0.173	20.818 ± 0.044	21.006 ± 0.048	21.731 ± 0.197	21.030 ± 0.232
SA02-1186	25.276 ± 0.124	22.314 ± 0.032	21.506 ± 0.036	19.371 ± 0.076	19.055 ± 0.043	19.268 ± 0.043	19.787 ± 0.063	20.035 ± 0.136
SA02-1255	26.136 ± 0.292	23.354 ± 0.042	22.697 ± 0.058	20.041 ± 0.104	19.593 ± 0.043	19.655 ± 0.044	20.045 ± 0.071	20.175 ± 0.155
SA02-1417	24.386 ± 0.076	23.564 ± 0.050	23.456 ± 0.114	21.201 ± 0.192	20.741 ± 0.045	20.515 ± 0.047	20.291 ± 0.082	20.416 ± 0.188
SA02-1636	24.066 ± 0.050	23.594 ± 0.050	23.436 ± 0.104	21.851 ± 0.272	21.316 ± 0.049	21.104 ± 0.055	21.053 ± 0.147	20.992 ± 0.313
SA02-1702	23.905 ± 0.050	23.054 ± 0.036	22.587 ± 0.058	21.331 ± 0.192	21.218 ± 0.048	21.756 ± 0.080	21.613 ± 0.239	21.698 ± 0.591
SA02-1724	23.235 ± 0.036	21.344 ± 0.032	20.697 ± 0.032	19.611 ± 0.085	19.450 ± 0.043	19.687 ± 0.043	19.942 ± 0.060	20.158 ± 0.088
SA02-1777	24.346 ± 0.058	22.864 ± 0.036	22.387 ± 0.058	20.901 ± 0.163	20.560 ± 0.044	20.896 ± 0.048	21.205 ± 0.168	20.841 ± 0.219
SA02-1785	23.645 ± 0.042	22.874 ± 0.036	22.716 ± 0.067	22.511 ± 9.990	21.661 ± 0.051	21.896 ± 0.059	22.057 ± 0.310	22.082 ± 0.524
SA02-1842	25.375 ± 0.133	23.334 ± 0.042	22.576 ± 0.058	20.421 ± 0.124	20.016 ± 0.043	20.098 ± 0.045	20.579 ± 0.102	21.395 ± 0.444
SA02-1935	24.846 ± 0.095	22.504 ± 0.032	21.857 ± 0.042	19.711 ± 0.085	19.389 ± 0.043	19.643 ± 0.043	19.916 ± 0.058	20.119 ± 0.117
SA02-2197	24.886 ± 0.095	23.184 ± 0.042	22.596 ± 0.058	20.261 ± 0.114	20.020 ± 0.043	20.157 ± 0.045	20.546 ± 0.098	20.784 ± 0.258
SA02-2530	23.785 ± 0.042	23.264 ± 0.042	23.037 ± 0.076	21.931 ± 0.282	21.689 ± 0.059	21.572 ± 0.058	22.114 ± 0.368	21.528 ± 0.364
SA12-5175	24.866 ± 0.076	22.894 ± 0.036	23.026 ± 0.076	21.091 ± 0.182	20.433 ± 0.043	20.924 ± 0.054	21.284 ± 0.113	21.699 ± 0.504
SA12-5241	23.596 ± 0.036	23.024 ± 0.042	23.306 ± 0.095	21.551 ± 0.232	20.891 ± 0.045	20.959 ± 0.053	21.040 ± 0.103	21.804 ± 0.549
SA12-5337	22.465 ± 0.032	20.754 ± 0.030	20.806 ± 0.032	19.301 ± 0.085	19.270 ± 0.043	19.697 ± 0.043	19.873 ± 0.048	20.197 ± 0.099
SA12-5513	23.046 ± 0.032	21.224 ± 0.032	21.276 ± 0.032	19.391 ± 0.085	19.408 ± 0.043	19.747 ± 0.044	19.846 ± 0.052	20.363 ± 0.151
SA12-5592	24.976 ± 0.095	23.654 ± 0.050	24.236 ± 0.222	21.231 ± 0.202	20.721 ± 0.044	20.648 ± 0.048	21.001 ± 0.095	21.403 ± 0.386
SA12-5722	24.495 ± 0.058	22.564 ± 0.032	22.887 ± 0.067	20.181 ± 0.124	19.631 ± 0.043	19.927 ± 0.044	20.036 ± 0.054	20.210 ± 0.137
SA12-5724	24.596 ± 0.058	22.694 ± 0.036	22.936 ± 0.067	20.811 ± 0.163	20.480 ± 0.044	20.791 ± 0.049	21.130 ± 0.133	21.157 ± 0.317

Table 2.2 (cont'd)

Object ID	V	I	z'	K_s	[3.6]	[4.5]	[5.6]	[8.0]
SA12-5761	23.465 ± 0.036	22.764 ± 0.036	23.227 ± 0.085	21.961 ± 0.292	20.614 ± 0.044	20.334 ± 0.045	20.319 ± 0.059	20.481 ± 0.155
SA12-5836	24.625 ± 0.058	22.954 ± 0.036	22.817 ± 0.058	20.761 ± 0.163	20.348 ± 0.043	20.417 ± 0.044	20.844 ± 0.067	21.156 ± 0.218
SA12-5869	25.826 ± 0.143	23.664 ± 0.050	24.276 ± 0.202	20.391 ± 0.133	19.727 ± 0.043	19.605 ± 0.043	19.987 ± 0.062	20.255 ± 0.139
SA12-5957	25.326 ± 0.095	24.294 ± 0.067	24.497 ± 9.990	22.061 ± 0.301	21.807 ± 0.067	21.984 ± 0.081	23.036 ± 0.759	21.691 ± 0.504
SA12-5965	25.645 ± 0.143	24.634 ± 0.124	24.466 ± 0.232	22.421 ± 0.361	21.860 ± 0.050	21.807 ± 0.086	21.778 ± 0.174	21.083 ± 0.282
SA12-6192	23.585 ± 0.036	23.144 ± 0.042	23.677 ± 0.124	21.671 ± 0.252	20.843 ± 0.045	20.788 ± 0.052	21.210 ± 0.144	21.625 ± 0.476
SA12-6301	22.965 ± 0.032	22.664 ± 0.032	23.227 ± 0.085	21.301 ± 0.202	21.074 ± 0.047	20.929 ± 0.052	21.063 ± 0.120	21.242 ± 0.327
SA12-6456	22.526 ± 0.032	20.414 ± 0.030	20.377 ± 0.032	18.781 ± 0.067	18.793 ± 0.043	19.159 ± 0.043	19.432 ± 0.048	19.958 ± 0.092
SA12-6619	22.965 ± 0.032	21.524 ± 0.032	21.497 ± 0.036	19.841 ± 0.104	19.371 ± 0.043	19.532 ± 0.043	19.927 ± 0.056	20.249 ± 0.110
SA12-6800	22.096 ± 0.032	19.974 ± 0.030	19.907 ± 0.030	18.501 ± 0.058	18.492 ± 0.043	18.876 ± 0.043	19.154 ± 0.050	19.771 ± 0.095
SA12-7045	25.986 ± 0.182	23.954 ± 0.058	23.736 ± 0.124	21.541 ± 0.262	20.636 ± 0.045	20.780 ± 0.049	20.942 ± 0.117	21.302 ± 0.341
SA12-7099	22.986 ± 0.032	21.324 ± 0.032	21.377 ± 0.032	19.351 ± 0.085	19.201 ± 0.043	19.465 ± 0.043	19.367 ± 0.047	19.403 ± 0.061
SA12-7250	24.335 ± 0.050	23.624 ± 0.050	24.326 ± 0.202	21.751 ± 0.272	20.730 ± 0.045	20.460 ± 0.046	20.401 ± 0.080	20.588 ± 0.183
SA12-7455	24.235 ± 0.050	22.154 ± 0.032	22.276 ± 0.042	20.681 ± 0.153	20.300 ± 0.044	20.774 ± 0.052	20.937 ± 0.121	21.728 ± 0.509
SA12-7524	24.796 ± 0.058	23.904 ± 0.058	24.497 ± 9.990	21.741 ± 0.252	21.115 ± 0.048	20.876 ± 0.050	20.927 ± 0.113	21.818 ± 0.569
SA12-7660	23.886 ± 0.042	22.174 ± 0.032	22.506 ± 0.050	20.341 ± 0.133	20.104 ± 0.043	20.460 ± 0.046	20.370 ± 0.079	20.594 ± 0.184
SA12-7852	24.276 ± 0.050	22.754 ± 0.036	23.087 ± 0.076	20.981 ± 0.173	20.274 ± 0.044	20.473 ± 0.044	20.949 ± 0.105	20.953 ± 0.178
SA12-8025	25.326 ± 0.095	23.574 ± 0.050	23.477 ± 0.104	20.721 ± 0.153	20.173 ± 0.043	20.186 ± 0.044	20.642 ± 0.086	20.974 ± 0.217
SA12-8037	24.495 ± 0.050	23.134 ± 0.036	23.526 ± 0.104	21.031 ± 0.182	20.482 ± 0.044	20.534 ± 0.045	21.304 ± 0.159	21.194 ± 0.226
SA12-8139	25.375 ± 0.095	23.344 ± 0.042	23.186 ± 0.076	21.101 ± 0.192	20.549 ± 0.044	20.807 ± 0.050	21.220 ± 0.130	21.049 ± 0.259
SA12-8250	24.546 ± 0.058	23.254 ± 0.042	24.497 ± 9.990	22.451 ± 0.371	21.515 ± 0.053	21.821 ± 0.066	22.014 ± 0.293	21.439 ± 0.336
SA12-8266	25.596 ± 0.104	23.244 ± 0.036	23.797 ± 0.133	21.161 ± 0.192	20.709 ± 0.045	20.992 ± 0.049	21.155 ± 0.118	21.346 ± 0.303
SA12-8668	24.076 ± 0.042	22.694 ± 0.036	23.026 ± 0.067	21.031 ± 0.182	20.508 ± 0.044	20.654 ± 0.045	20.733 ± 0.076	21.158 ± 0.221
SA12-8895	24.645 ± 0.058	23.534 ± 0.050	23.447 ± 0.104	20.291 ± 0.124	19.451 ± 0.043	19.262 ± 0.043	19.432 ± 0.057	19.784 ± 0.097
SA12-8983	24.695 ± 0.067	21.974 ± 0.032	22.137 ± 0.042	20.051 ± 0.114	19.656 ± 0.043	19.987 ± 0.043	20.568 ± 0.088	20.974 ± 0.187
SA12-9127	25.335 ± 0.095	23.244 ± 0.042	23.657 ± 0.104	21.501 ± 0.232	20.921 ± 0.046	21.250 ± 0.051	23.015 ± 0.725	21.519 ± 0.363
SA15-4762	24.846 ± 0.067	24.104 ± 0.058	23.997 ± 0.272	21.671 ± 0.153	21.590 ± 0.060	21.600 ± 0.082	21.720 ± 0.328	21.650 ± 0.694
SA15-5005	25.066 ± 0.095	24.004 ± 0.058	23.627 ± 0.212	21.401 ± 0.143	20.440 ± 0.045	20.180 ± 0.045	20.250 ± 0.071	20.540 ± 0.189
SA15-5348	24.905 ± 0.076	22.214 ± 0.032	21.537 ± 0.042	19.801 ± 0.058	19.240 ± 0.042	19.510 ± 0.045	19.760 ± 0.060	20.200 ± 0.148

Table 2.2 (cont'd)

Object ID	V	I	z'	K_s	[3.6]	[4.5]	[5.6]	[8.0]
SA15-6695	24.875 ± 0.076	23.694 ± 0.050	23.427 ± 0.163	21.401 ± 0.133	20.320 ± 0.045	20.090 ± 0.045	20.280 ± 0.082	20.690 ± 0.230
SA15-6846	25.305 ± 0.104	23.014 ± 0.036	22.396 ± 0.067	20.571 ± 0.076	20.010 ± 0.045	20.320 ± 0.045	20.530 ± 0.121	20.700 ± 0.286
SA15-6851	25.596 ± 0.133	23.194 ± 0.036	22.427 ± 0.076	20.581 ± 0.085	19.930 ± 0.045	20.100 ± 0.045	20.660 ± 0.108	20.450 ± 0.189
SA15-7241	23.956 ± 0.050	21.874 ± 0.032	21.477 ± 0.042	20.121 ± 0.067	19.950 ± 0.045	20.410 ± 0.045	20.580 ± 0.108	21.290 ± 0.440
SA15-7543	25.745 ± 0.143	24.034 ± 0.067	23.227 ± 0.124	20.841 ± 0.104	19.900 ± 0.045	19.720 ± 0.045	19.860 ± 0.071	20.480 ± 0.244
SA15-7972	26.125 ± 0.232	23.564 ± 0.085	23.047 ± 0.114	20.931 ± 0.104	20.280 ± 0.045	20.300 ± 0.045	20.520 ± 0.121	21.060 ± 0.342
SA15-9333	24.965 ± 0.085	23.694 ± 0.050	23.596 ± 0.173	22.061 ± 0.262	21.230 ± 0.051	21.130 ± 0.051	21.620 ± 0.314	21.430 ± 0.398
SA22-0083	24.605 ± 0.058	23.094 ± 0.050	22.997 ± 0.114	20.931 ± 0.192	20.510 ± 0.043	20.876 ± 0.044	20.832 ± 0.065	21.235 ± 0.177
SA22-0128	24.995 ± 0.076	23.184 ± 0.050	22.677 ± 0.095	20.711 ± 0.173	20.028 ± 0.043	20.083 ± 0.043	20.489 ± 0.052	20.169 ± 0.067
SA22-0189	25.655 ± 0.133	23.214 ± 0.050	22.736 ± 0.085	19.861 ± 0.114	19.320 ± 0.043	19.217 ± 0.043	19.461 ± 0.044	19.875 ± 0.062
SA22-0206	24.816 ± 0.067	23.624 ± 0.067	23.227 ± 0.124	21.721 ± 0.282	21.618 ± 0.045	21.622 ± 0.048	21.633 ± 0.097	22.149 ± 0.360
SA22-0281	24.855 ± 0.076	22.444 ± 0.042	21.846 ± 0.050	19.781 ± 0.104	19.223 ± 0.043	19.440 ± 0.043	19.804 ± 0.046	20.230 ± 0.075
SA22-0299	24.256 ± 0.042	23.394 ± 0.058	23.017 ± 0.095	22.261 ± 0.371	21.668 ± 0.045	21.860 ± 0.050	22.037 ± 0.123	21.317 ± 0.164
SA22-0315	24.026 ± 0.042	22.444 ± 0.036	21.977 ± 0.050	20.471 ± 0.153	20.384 ± 0.043	20.712 ± 0.044	21.021 ± 0.063	20.898 ± 0.115
SA22-0331	23.366 ± 0.036	22.514 ± 0.036	22.337 ± 0.058	21.711 ± 0.272	21.714 ± 0.045	21.974 ± 0.051	22.445 ± 0.170	22.827 ± 0.629
SA22-0398	25.186 ± 0.095	23.574 ± 0.058	22.497 ± 0.067	20.851 ± 0.182	20.297 ± 0.043	20.196 ± 0.043	20.488 ± 0.054	20.757 ± 0.108
SA22-0455	25.585 ± 0.114	23.764 ± 0.076	22.826 ± 0.095	21.311 ± 0.232	21.131 ± 0.044	21.197 ± 0.045	21.530 ± 0.086	22.745 ± 0.537
SA22-0510	24.546 ± 0.050	22.494 ± 0.036	22.076 ± 0.058	20.611 ± 0.163	20.414 ± 0.043	20.821 ± 0.044	20.938 ± 0.060	21.605 ± 0.234
SA22-0554	24.916 ± 0.067	22.824 ± 0.042	22.567 ± 0.085	20.801 ± 0.173	20.753 ± 0.043	21.139 ± 0.045	21.475 ± 0.085	21.736 ± 0.273
SA22-0563	23.145 ± 0.032	22.354 ± 0.036	22.537 ± 0.067	21.521 ± 0.252	21.438 ± 0.044	21.846 ± 0.052	22.021 ± 0.140	22.115 ± 0.407
SA22-0568	27.476 ± 9.990	22.954 ± 0.042	23.116 ± 0.173	21.331 ± 0.232	20.747 ± 0.043	20.750 ± 0.044	20.897 ± 0.063	21.043 ± 0.130
SA22-0619	24.796 ± 0.067	23.394 ± 0.058	23.267 ± 0.133	21.181 ± 0.212	21.130 ± 0.044	21.236 ± 0.045	21.782 ± 0.096	21.851 ± 0.261
SA22-0630	23.585 ± 0.036	22.314 ± 0.036	22.127 ± 0.050	20.881 ± 0.192	20.578 ± 0.043	20.995 ± 0.045	20.640 ± 0.056	21.641 ± 0.240
SA22-0643	23.925 ± 0.042	23.114 ± 0.050	23.197 ± 0.124	22.091 ± 0.331	22.226 ± 0.048	22.736 ± 0.073	23.973 ± 0.771	22.479 ± 0.510
SA22-0674	25.796 ± 0.124	23.604 ± 0.058	22.846 ± 0.095	20.581 ± 0.163	20.102 ± 0.043	20.029 ± 0.043	20.309 ± 0.050	20.961 ± 0.133
SA22-0710	24.465 ± 0.050	22.244 ± 0.036	21.716 ± 0.042	20.211 ± 0.133	20.095 ± 0.043	20.477 ± 0.043	20.789 ± 0.054	21.112 ± 0.136
SA22-0721	27.476 ± 9.990	23.554 ± 0.058	22.966 ± 0.104	20.161 ± 0.133	19.781 ± 0.043	19.680 ± 0.043	19.991 ± 0.046	20.531 ± 0.088
SA22-0758	24.916 ± 0.067	24.194 ± 0.104	23.716 ± 0.222	21.801 ± 0.292	20.862 ± 0.043	20.813 ± 0.044	21.046 ± 0.069	21.171 ± 0.163
SA22-0770	24.215 ± 0.042	22.644 ± 0.042	22.146 ± 0.058	20.501 ± 0.153	20.120 ± 0.043	20.429 ± 0.043	20.561 ± 0.057	20.825 ± 0.121

Table 2.2 (cont'd)

Object ID	V	I	z'	K_s	[3.6]	[4.5]	[5.6]	[8.0]
SA22-0893	25.995 ± 0.173	23.094 ± 0.050	22.267 ± 0.058	20.921 ± 0.192	20.753 ± 0.043	21.116 ± 0.045	21.374 ± 0.079	21.786 ± 0.247
SA22-0964	24.006 ± 0.042	23.184 ± 0.050	23.037 ± 0.114	21.241 ± 0.222	20.563 ± 0.043	20.409 ± 0.043	20.646 ± 0.060	20.677 ± 0.105
SA22-0997	24.686 ± 0.058	24.084 ± 0.085	23.466 ± 0.163	22.811 ± 9.990	23.091 ± 0.067	23.031 ± 0.088	24.721 ± 1.653	22.548 ± 0.542
SA22-1042	24.186 ± 0.042	23.434 ± 0.058	23.677 ± 0.182	21.231 ± 0.212	21.014 ± 0.044	20.863 ± 0.044	20.947 ± 0.066	20.939 ± 0.129
SA22-1045	23.645 ± 0.036	23.074 ± 0.050	21.396 ± 0.042	20.811 ± 0.173	20.106 ± 0.043	20.127 ± 0.043	20.350 ± 0.053	20.713 ± 0.111
SA22-1055	24.055 ± 0.042	23.194 ± 0.050	23.006 ± 0.124	21.081 ± 0.202	20.847 ± 0.043	20.806 ± 0.044	21.152 ± 0.065	21.155 ± 0.147
SA22-1559	24.206 ± 0.050	24.254 ± 0.104	23.997 ± 9.990	22.411 ± 0.391	22.424 ± 0.050	22.293 ± 0.057	21.936 ± 0.124	22.461 ± 0.468
SA22-1909	23.476 ± 0.036	23.524 ± 0.058	22.907 ± 0.095	22.491 ± 0.441	22.349 ± 0.050	22.331 ± 0.059	22.415 ± 0.184	22.626 ± 0.582
SA22-1923	23.055 ± 0.032	22.494 ± 0.036	22.216 ± 0.058	21.441 ± 0.242	20.663 ± 0.043	20.903 ± 0.044	21.001 ± 0.066	20.717 ± 0.110
SA22-1951	25.006 ± 0.067	24.294 ± 0.114	23.997 ± 9.990	22.101 ± 0.361	21.603 ± 0.045	21.484 ± 0.047	21.787 ± 0.111	22.066 ± 0.349
SA22-1983	25.866 ± 0.133	24.094 ± 0.095	23.776 ± 0.222	20.871 ± 0.192	20.213 ± 0.043	20.146 ± 0.043	20.353 ± 0.051	20.604 ± 0.101
SA22-2045	24.715 ± 0.067	23.784 ± 0.067	22.756 ± 0.085	22.161 ± 0.381	21.552 ± 0.045	21.683 ± 0.049	21.834 ± 0.119	22.244 ± 0.439
SA22-2172	23.756 ± 0.036	23.504 ± 0.067	23.317 ± 0.143	22.301 ± 0.381	21.571 ± 0.045	21.501 ± 0.048	21.785 ± 0.119	21.342 ± 0.201
SA22-2196	24.726 ± 0.058	23.724 ± 0.067	23.997 ± 9.990	22.811 ± 9.990	23.584 ± 0.081	23.798 ± 0.146	23.291 ± 0.382	22.952 ± 0.730
SA22-2237	24.346 ± 0.050	24.094 ± 0.085	23.997 ± 9.990	22.331 ± 0.381	22.199 ± 0.048	22.175 ± 0.053	22.205 ± 0.143	22.736 ± 0.573
SA22-2395	23.035 ± 0.032	23.114 ± 0.050	23.526 ± 0.153	22.211 ± 0.361	22.252 ± 0.048	22.234 ± 0.053	23.557 ± 0.446	23.018 ± 0.700
SA22-2400	23.706 ± 0.042	23.904 ± 0.095	23.657 ± 0.192	21.741 ± 0.292	21.236 ± 0.044	21.170 ± 0.046	21.338 ± 0.084	21.711 ± 0.268
SA22-2541	23.305 ± 0.036	22.164 ± 0.036	22.017 ± 0.050	20.591 ± 0.163	20.801 ± 0.043	21.096 ± 0.045	21.136 ± 0.071	21.498 ± 0.202
SA22-2548	24.765 ± 0.058	22.374 ± 0.036	21.806 ± 0.050	19.651 ± 0.104	19.223 ± 0.043	19.440 ± 0.043	19.804 ± 0.046	20.230 ± 0.075
SA22-2587	26.006 ± 0.182	23.804 ± 0.067	23.997 ± 9.990	21.081 ± 0.202	20.617 ± 0.043	20.594 ± 0.044	21.001 ± 0.066	21.826 ± 0.273
SA22-2703	23.796 ± 0.042	23.454 ± 0.058	23.276 ± 0.143	22.461 ± 0.431	21.757 ± 0.046	21.863 ± 0.050	22.615 ± 0.226	21.812 ± 0.255
SA22-2863	25.715 ± 0.143	23.784 ± 0.067	23.706 ± 0.212	21.061 ± 0.202	20.504 ± 0.043	20.730 ± 0.044	20.789 ± 0.062	20.789 ± 0.118

In Figure 2.2 an IRAC colour-colour plot of [3.6] - [4.5] vs. [5.8] - [8.0] colours for the sample is presented (resulting in rest-frame colours of approximately $H - K_s$ vs $K_l - L$ at $|z| \sim 1.2$) . For reference we plot the evolution of a star-forming and evolved galaxy computed with the PEGASE.2 code (Fioc & Rocca-Volmerange, 1997). The GDDS sample generally traces these tracks, although many galaxies show redder [5.8]-[8.0] colours, possibly indicating an NIR excess at rest-frame 2-5 μm. We plot the IRAC colour-colour selection criteria to pick out any galaxies with a strong active galactic nucleus (AGN) from Stern et al. (2005) as the region contained in the dashed region in Figure 2.2. Only 11% of the objects from the selected GDDS sample fall in this region and most of those are near the selection boundary, showing little contamination from strong AGNs in our sample. We key each galaxy to their galactic spectral type. There is no obvious relationship between a galaxy's location in the colour-colour space and its spectral type.

2.4 Stellar population synthesis models

To test stellar mass estimates and investigate the differences between different stellar population models we generate several sets of model SEDs. We generate three sets of SED libraries from PEGASE.2 software (Fioc & Rocca-Volmerange, 1997) and one from Maraston (2005), whose treatment of thermally pulsating-asymptotic giant branch (TP-AGB) stars is scaled to match photometry of globular clusters in the Magellanic Clouds in the NIR. We apply various star formation history (SFH) treatments to each SPS model as follows:

1. **Single SFH:** an exponentially declining star formation history with PEGASE.2 (Fioc & Rocca-Volmerange, 1997) models.

2. **Single SFH with TP-AGB:** Exponentially declining star formation history with Maraston (2005) models.

3. **Composite SFH**: Exponentially declining star formation history plus a young "burst" stellar population with PEGASE.2 models.

4. **Composite SFH + NIR emission** As above with PEGASE.2 models plus an additional SED component accounting for excess NIR emission likely associated

with hot dust emission modeled as an 850 K greybody (discussed in more detail in chapter 3).

For each model set up, a library of SEDs is generated consisting of the different star formation history prescriptions and spectral components listed above. Our most basic model set consists of a star formation history modeled as a decreasing star formation rate (SFR), SFR $\propto \exp(-t/\tau)$, that exponentially declines on a timescale that can range from $\tau \ \epsilon \ [0.1, 500]$ Gyr. The first approximates an instantaneous starburst and the last a constant SFR. We generate a similar library set to compare to the Maraston (2005) models, but due to small differences in the model parameter choices, the timescale of the exponentially declining SFHs are $\tau\epsilon\,[0.1, 20]$ Gyr.

The composite SFH models include an additional spectral component modeling a "burst" of star formation. The two component stellar model allows for a more robust determination of stellar masses by correctly modeling the light from evolved populations and that from a recent star forming episode. The secondary component is modeled as a short burst of star formation with an exponentially declining SFH with a short 100 Myr timescale. The amplitude of this component is a free parameter and can have a mass between 10^{-4} and 2 times the initial component. This secondary component can occur at any time between z_{form} and z_{obs}.

We opt to use the initial mass function (IMF) from Kroupa (2001) and extinction is added to the spectra ourselves in eleven reddening bins covering $0 \leq A_{\rm V} \leq 2$ mag. We assume that nebular extinction is twice the stellar continuum due to increased dust extinction within stellar birth clouds (Calzetti et al., 1994) and use the Small Magellanic Cloud (SMC) reddening law of Pei (1992) which provides a numerical fit to the global dust attenuation in the SMC. For the PEGASE.2 models, evolution of the stellar population assumes constant metallicity, and does not include effects due to galactic winds, infall or substellar objects. The PEGASE.2 models encompass five possible metallicity values from $0.0004 \leq Z \leq 0.02$, while only solar metallicity is available for the Maraston (2005) models.

2.4.1 Additional NIR emission component

Broadband multi-wavelength (UV, visible, and IR) empirical SED modeling performed by da Cunha et al. (2008) on galaxies from the *Spitzer* Infrared Nearby Galaxies Survey (SINGS; Kennicutt et al. 2003; Dale et al. 2005) show that emission in the NIR (in

excess of stellar emission) from rest-frame 2-5 μm, can be modeled by an additional SED component described by a spectrum of polycyclic aromatic hydrocarbon (PAH) emission superposed on an 850 K greybody modified by λ^{-1} extinction (hereafter written as GB+PAH to identify this as a single parameter SED component). In their model, a PAH template is scaled to match the NIR continuum excess (e.g., the greybody) seen in the star-forming galaxies in Lu et al. (2003) and Dale et al. (2005) and is shown to also match the colours of the galactic cirrus (see Figure 1 of da Cunha et al. 2008). The subject of this additional NIR emission component is the subject of chapter 3 of this thesis. Here we focus on how the addition of this SED component influences the measurement of a stellar mass of a galaxy.

To investigate whether a PAH feature at rest-frame 3.3 μm plus greybody component can explain an IRAC excess in our sample of star-forming galaxies we superpose our model SEDs in our final set of SPS models with an additional component following the results of da Cunha et al. (2008) and fit an 850 K greybody modified by λ^{-1} dust extinction and add the 3.3 μm PAH emission feature using the Lorentzian profile parametrized by Verstraete et al. (2001) as $F_\nu^{\rm Lorentz} = f_{\rm o}[1 + (x - x_{\rm o})^2/\sigma^2]^{-1}$, where $x = 1/\lambda$ is the wavenumber, $x_{\rm o} = 3039.1\,{\rm cm}^{-1}$ is the central wavelength of the feature and $\sigma = 19.4\,{\rm cm}^{-1}$ is its FWHM.

The 3.3 μm PAH feature is scaled to match 2.27 times the continuum emission of the greybody at 4 μm. da Cunha et al. (2008) match the amplitude of the 3.3 μm feature to 0.1 times the amplitude of the 11.3 μm PAH feature, the relative ratio found by Li & Draine (2001). They then approximate the amplitude of the greybody at 4 μm to be 0.11 times the peak amplitude of the 7.7 μm PAH feature as found in Lu et al. (2003). However, because of our spectral coverage, there is no need to account for PAH features at longer wavelengths than rest-frame 4 μm. Instead we use the results of Chan et al. (2001) to relate the the ratio of the longer PAH features as $F^{\rm peak}_{\lambda=11.3\,\mu m}/F^{\rm peak}_{\lambda=7.7\,\mu m} = 0.4$. Thus relating the 3.3 μm PAH feature as 2.27 times the flux of the continuum emission at 4 μm. The contribution of the PAH line to the total PAH+greybody component in an IRAC band is at most 20%.

2.5 Photometric SED fitting

The photometry is fit using least-squares minimization to the modeled photometry at the observed frame wavebands. A grid of apparent AB magnitudes is generated by

redshifting each rest-frame model to the galaxy's spectroscopic redshift and integrate the transmission of the spectrum over the spectral response curves for all observed filters: $VIz'K_s$ and *Spitzer* IRAC [3.6], [4.5], [5.8], [8.0]. The χ^2 for each model is calculated in flux space with the normalization of the SED component computed directly in the minimization procedure. We restrict the age of the model to be less than the age of the Universe at the observed redshift. To estimate errors in the fitted parameters, we consider 20[1] Monte Carlo realizations of the data through a random Poisson distribution of the count rate, thus simulating the detector shot noise.

2.5.1 Measuring the stellar mass from the SED fits

The stellar mass is measured by integrating the star formation rate history over the galaxy's age using the normalization of the SED fit to the photometry. In the case of a composite star formation history, the total mass is the sum of two stellar components, each with their own defined star formation history. In models with an additional NIR emission SED component, we assume the component adds negligible mass to the galaxy. The stellar mass of each component is computed by the sum of the star formation rate from age zero to its current age. The relative contribution of each stellar SED component to the total mass of the galaxy will change as a function of time. We therefore define the ratio between the contribution of each component to the total SED as the ratio of the mass contribution of each component at $t \to \infty$:

$$f = M_{burst}(t \to \infty)/M_{csp}(t \to \infty) \tag{2.1}$$

f is included in the mass-fitting code as a free parameter, ranging from 10^4 to 2, with steps in $\log f$ of 0.48. The contribution of the exponentially declining stellar population (ie. continually forming stellar population, f_{csp}) at any age is given as:

$$M_{csp} = f_{csp} \times \int_0^t \mathrm{SFR}_{csp}\, dt \tag{2.2}$$

where $f_{csp} = 1/(1+f)(M_{total}(t \to \infty))$ and the contribution from the burst stellar population, f_{burst} at any age is given as:

$$M_{burst} = f_{burst} \times \int_0^t \mathrm{SFR}_{burst}\, dt \tag{2.3}$$

[1] A small number, but we find uncertainties converge by this value and are similar to 1000 MC trials

where $f_{burst} = f/(1+f)(M_{total}(t \rightarrow \infty))$.

We fit our photometry to the bandfluxes (derived from the grid of AB magnitudes) to the models using χ^2 minimization. The normalization of the SED component to the photometry is a free parameter. Using this factor, f_{norm}, the total stellar mass is:

$$M_{total} = f_{norm} \times (M_{csp} + M_{burst}) \tag{2.4}$$

For models with only a continually forming stellar population, the total stellar mass is simply:

$$M_{total} = f_{norm} \times M_{csp} \tag{2.5}$$

2.6 Stellar masses

In the previous section, we introduced four separate libraries of SEDs which differed by their star formation history and the inclusion of either TP-AGB stars or an NIR continuum SED component (and thus an additional fitted parameter). In addition to testing the impact of varying SPS input model parameters, we also seek to understand how the impact of rest-frame near-infrared photometry from *Spitzer's* IRAC instrument improves stellar mass estimates and affects the resulting mass density and mass function. Thus, we also seek to compare SED fits to photometry with just visible $VIz'K_s$ information to fits with visible plus IRAC photometry.

However, longer than rest-frame 2 μm, emission from non-stellar sources such as hot dust emission (due to or in addition to PAH emission) can lead to observational discrepancies between the data and models (Mentuch et al., 2009). We thus additionally seek to quantify the impact of fitting the longer wavelength photometry to models that do or do not contain the additional component. As well, we wish to test the importance of the inclusion of the IRAC [3.6], [4.5] channels, which measure the rest-frame 1-2 μm emission, compared to fits to just visible through K-band observed photometry. Thus, we wish to test three different sets of photometry: (1) Visible: $VIz'K_s$, (2) Visible + IRAC (limited to $\lambda_{\rm rest} < 2\,\mu$m): $VIz'K_s$[3.6][4.5] and (3) Visible + ALL IRAC: $VIz'K_s$[3.6][4.5][5.6][8.0].

Our goal is not to explore every possible combination of input model parameters and photometry, rather we wish to see how the major changes in each model set impact the

stellar mass estimated for the whole sample or subsets of the sample (such as those with a large fraction of young stars). In the following sections we will isolate a significant change in the input prescription by keeping as many parameters common and only changing one variable.

2.6.1 The impact of IRAC

In this section, we focus only on the addition of the IRAC photometry, to augment the existing visible through near-infrared (observed K_s-band) photometry. We begin by considering how the addition of the [3.6] and [4.5] wavebands change stellar masses derived for models with a composite star formation history with PEGASE.2. This input model was used in Glazebrook et al. (2004) to measure the mass density of the GDDS sample and is thus the standard we use here to compare our results with. In the first section, the role of including the [3.6] and [4.5] wavebands is tested. We then augment the data set with all IRAC wavebands and compare the stellar masses with previous ones. Discovering, that in general these do not provide very good fits to the photometry, we use the model with the additional NIR emission component and again calculate stellar masses.

We list the stellar masses in Table 2.3 for each of these iterations and show the distribution of stellar masses as a function of wavelength in Figure 2.3. In this plot, stellar masses were calculated with all visible and IRAC photometry and an SPS model with a composite SFH and NIR emission component is used. This model offers the most accurate representation of the photometry and most precise stellar mass measurements. The galaxies are keyed according to their galaxy spectral type. The solid curve shows how the 20.6 mag (Vega) K-flux limit translates into a mass completeness limit for a maximally old simple stellar population, that is a stellar population that forms all its stellar mass at the maximum age of the universe and evolves. The dashed curve shows an example mass limit for bluer objects (SFR=const. model).

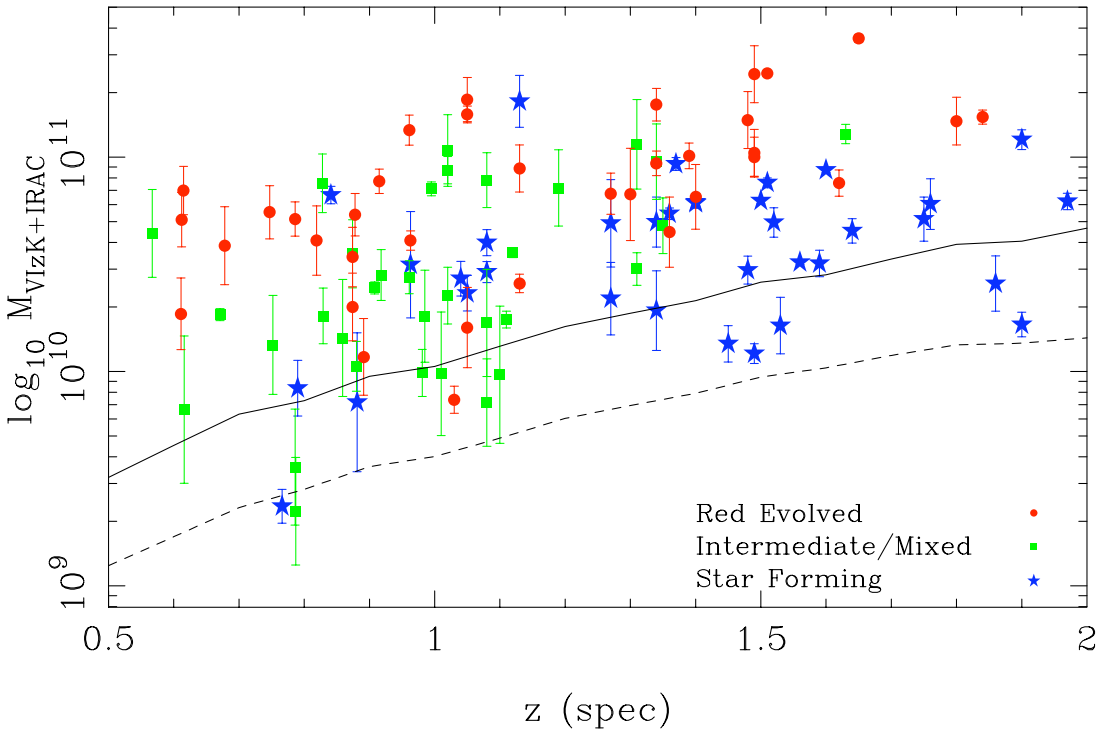

Figure 2.3 Stellar masses for the GDDS sample as a function of redshift, keyed according to their galactic spectral type. The masses are from SED fits for the visible + IRAC [3.6][4.5][5.6][8.0] photometry to the composite star formation history model (consisting of an evolving stellar population and a burst stellar population) with an additional component to account for NIR emission at $\lambda > 2\,\mu$m. The solid curve shows how the 20.6 mag (Vega) K-flux limit translates into a mass completeness limit for a maximally old Simple Stellar Population. The dashed curve shows an example mass limit for bluer objects (SFR=const. model).

Table 2.3. Stellar masses and NIR emission luminosity density at 3 μm for different SED fitting methods

Object ID	$\log \frac{M_\star}{M_\odot}$ (VIzK)	$\log \frac{M_\star}{M_\odot}$ (VIzK12)	$\log \frac{M_\star}{M_\odot}$ (VIzK1234 no NIR emission	$\log \frac{M_\star}{M_\odot}$ (VIzK1234 with NIR emission)	$F_{3\mu m}$ (rest) (ergs/s/Å)
SA02-0452	11.000 ± 0.105	10.972 ± 0.121	10.670 ± 0.072	10.878 ± 0.137	3.98e+31 ± 1.11e+31
SA02-0621	10.700 ± 0.226	10.603 ± 0.123	10.667 ± 0.203	10.680 ± 0.130	5.8e+31 ± 3.24e+31
SA02-0708	11.100 ± 0.197	11.110 ± 0.134	11.055 ± 0.213	11.060 ± 0.209	7.19e+30 ± 1.47e+31
SA02-0715	11.300 ± 0.058	11.256 ± 0.198	11.062 ± 0.157	11.260 ± 0.121	1.96e+32 ± 3.52e+31
SA02-0725	10.900 ± 0.130	10.817 ± 0.081	10.706 ± 0.119	10.893 ± 0.128	1.31e+32 ± 2.18e+31
SA02-0733	10.500 ± 0.127	10.494 ± 0.079	10.423 ± 0.082	10.464 ± 0.049	5.91e+31 ± 1.44e+31
SA02-0744	10.300 ± 0.259	10.226 ± 0.260	10.183 ± 0.280	10.340 ± 0.169	3.32e+31 ± 2.08e+31
SA02-0857	11.200 ± 0.060	11.204 ± 0.030	11.196 ± 0.059	11.199 ± 0.039	3.92e+31 ± 1.79e+31
SA02-0995	10.800 ± 0.065	10.782 ± 0.062	10.719 ± 0.108	10.711 ± 0.080	2.17e+31 ± 5.57e+30
SA02-1011	10.500 ± 0.128	10.416 ± 0.042	10.420 ± 0.053	10.411 ± 0.043	1.31e+31 ± 8.31e+30
SA02-1186	11.400 ± 0.080	11.241 ± 0.089	11.242 ± 0.093	11.269 ± 0.103	2.56e+31 ± 2e+31
SA02-1255	11.200 ± 0.140	11.274 ± 0.080	11.236 ± 0.086	11.245 ± 0.076	6.44e+31 ± 4.08e+31
SA02-1417	10.900 ± 0.139	10.961 ± 0.013	10.965 ± 0.027	10.939 ± 0.012	2.91e+32 ± 5.44e+31
SA02-1636	10.400 ± 0.305	10.650 ± 0.058	10.685 ± 0.047	10.656 ± 0.057	1.84e+32 ± 5.97e+31
SA02-1702	10.400 ± 0.182	10.367 ± 0.067	10.364 ± 0.081	10.365 ± 0.083	1.18e+30 ± 2.83e+30
SA02-1724	10.900 ± 0.093	10.848 ± 0.046	10.862 ± 0.021	10.852 ± 0.032	4.2e+31 ± 1.41e+31
SA02-1777	10.400 ± 0.217	10.018 ± 0.122	10.003 ± 0.105	9.993 ± 0.110	1.6e+31 ± 1.11e+31
SA02-1785	-2.010 ± 11.541	9.711 ± 0.233	9.645 ± 0.260	9.640 ± 0.329	1.6e+31 ± 6.3e+30
SA02-1842	11.000 ± 0.103	10.959 ± 0.091	10.971 ± 0.057	10.971 ± 0.057	5.88e+29 ± 2.69e+30
SA02-1935	11.100 ± 0.073	10.921 ± 0.059	10.917 ± 0.040	10.887 ± 0.057	3.71e+31 ± 1.35e+31
SA02-2197	11.000 ± 0.092	10.942 ± 0.139	10.936 ± 0.131	10.947 ± 0.110	3.31e+31 ± 2.33e+31
SA02-2530	10.200 ± 0.243	10.104 ± 0.161	10.212 ± 0.174	10.214 ± 0.132	4.96e+31 ± 3.83e+31
SA12-5175	10.000 ± 0.078	10.036 ± 0.192	10.066 ± 0.180	10.068 ± 0.179	1.68e+29 ± 5.6e+29
SA12-5241	10.700 ± 0.135	10.727 ± 0.029	10.724 ± 0.022	10.736 ± 0.027	4.68e+31 ± 2.32e+31
SA12-5337	10.400 ± 0.134	10.453 ± 0.200	10.385 ± 0.115	10.587 ± 0.182	1.22e+31 ± 4.17e+30
SA12-5513	10.200 ± 0.155	10.373 ± 0.260	10.222 ± 0.210	10.269 ± 0.167	1.11e+31 ± 4.48e+30
SA12-5592	11.100 ± 0.100	10.877 ± 0.064	10.879 ± 0.061	10.879 ± 0.061	3.05e+30 ± 9.29e+30
SA12-5722	10.700 ± 0.104	10.853 ± 0.031	10.855 ± 0.040	10.823 ± 0.041	4.26e+31 ± 8.31e+30
SA12-5724	9.960 ± 0.124	9.989 ± 0.118	9.969 ± 0.098	10.024 ± 0.116	7.44e+30 ± 7.11e+30
SA12-5761	9.140 ± 0.442	10.711 ± 0.019	10.738 ± 0.037	10.601 ± 0.061	2.06e+32 ± 1.77e+31
SA12-5836	10.700 ± 0.387	11.055 ± 0.095	10.980 ± 0.175	10.979 ± 0.176	7.83e+29 ± 3.47e+30
SA12-5869	11.500 ± 0.059	11.405 ± 0.018	11.392 ± 0.014	11.391 ± 0.014	4.73e+30 ± 9.93e+30
SA12-5957	10.200 ± 0.338	10.348 ± 0.093	10.258 ± 0.190	10.284 ± 0.186	7.13e+30 ± 1.16e+31
SA12-5965	10.200 ± 0.438	10.495 ± 0.094	10.495 ± 0.092	10.410 ± 0.129	1.46e+32 ± 6.1e+31
SA12-6192	10.600 ± 0.120	10.804 ± 0.015	10.801 ± 0.012	10.796 ± 0.014	2.39e+31 ± 2.37e+31
SA12-6301	10.900 ± 0.072	10.783 ± 0.093	10.802 ± 0.121	10.781 ± 0.118	8.42e+31 ± 7.96e+31
SA12-6456	10.700 ± 0.138	10.670 ± 0.085	10.687 ± 0.117	10.708 ± 0.127	8.34e+30 ± 6.99e+30
SA12-6619	10.000 ± 0.251	10.278 ± 0.326	10.266 ± 0.301	10.226 ± 0.250	1.01e+31 ± 1.61e+31
SA12-6800	10.900 ± 0.090	10.831 ± 0.083	10.851 ± 0.116	10.844 ± 0.113	3.27e+30 ± 4.95e+30
SA12-7045	10.200 ± 0.429	10.896 ± 0.218	10.721 ± 0.313	10.826 ± 0.215	3.23e+31 ± 2.16e+31
SA12-7099	10.600 ± 0.080	10.746 ± 0.017	10.944 ± 0.132	10.644 ± 0.205	4.75e+31 ± 3.97e+30

Table 2.3 (cont'd)

Object ID	$\log \frac{M_\star}{M_\odot}$ (VIzK)	$\log \frac{M_\star}{M_\odot}$ (VIzK12)	$\log \frac{M_\star}{M_\odot}$ (VIzK1234 no NIR emission	$\log \frac{M_\star}{M_\odot}$ (VIzK1234 with NIR emission)	$F_{3\mu m}$ (rest) (ergs/s/Å)
SA12-7250	10.800 ± 0.172	11.103 ± 0.042	11.111 ± 0.036	11.081 ± 0.046	2.97e+32 ± 1.38e+32
SA12-7455	10.100 ± 0.081	10.265 ± 0.143	10.280 ± 0.108	10.259 ± 0.130	4.48e+30 ± 5.04e+30
SA12-7524	10.600 ± 0.191	10.733 ± 0.064	10.730 ± 0.103	10.711 ± 0.103	4.89e+31 ± 6.95e+31
SA12-7660	10.500 ± 0.137	9.905 ± 0.136	9.914 ± 0.130	9.922 ± 0.130	2.61e+31 ± 5.54e+30
SA12-7852	9.750 ± 0.248	10.401 ± 0.341	10.557 ± 0.176	10.498 ± 0.248	1.67e+31 ± 8.93e+30
SA12-8025	11.100 ± 0.136	11.015 ± 0.056	11.009 ± 0.060	11.006 ± 0.060	4.14e+30 ± 1.06e+31
SA12-8037	10.800 ± 0.099	10.838 ± 0.096	10.840 ± 0.087	10.829 ± 0.096	1.87e+30 ± 4.73e+30
SA12-8139	10.400 ± 0.293	10.871 ± 0.108	10.849 ± 0.178	10.856 ± 0.178	2.13e+30 ± 7.75e+30
SA12-8250	9.550 ± 0.340	9.506 ± 0.246	9.541 ± 0.161	9.371 ± 0.079	9.93e+30 ± 3.69e+30
SA12-8266	10.400 ± 0.133	10.102 ± 0.150	10.208 ± 0.197	10.205 ± 0.187	1.52e+31 ± 1.32e+31
SA12-8668	9.540 ± 0.267	10.340 ± 0.137	10.432 ± 0.165	10.258 ± 0.215	4.76e+31 ± 7.44e+30
SA12-8895	11.500 ± 0.060	11.552 ± 0.015	11.563 ± 0.019	11.554 ± 0.019	1.84e+32 ± 8.12e+31
SA12-8983	10.700 ± 0.074	10.656 ± 0.040	10.613 ± 0.043	10.611 ± 0.045	4.76e+29 ± 1.76e+30
SA12-9127	9.780 ± 0.140	9.847 ± 0.152	9.868 ± 0.063	9.868 ± 0.063	0 ± 0
SA15-4762	10.700 ± 0.153	10.517 ± 0.055	10.495 ± 0.071	10.504 ± 0.062	3.7e+31 ± 3.41e+31
SA15-5005	10.800 ± 0.156	11.177 ± 0.024	11.189 ± 0.031	11.187 ± 0.033	1.09e+32 ± 9.35e+31
SA15-5348	11.100 ± 0.065	10.937 ± 0.100	10.948 ± 0.060	11.126 ± 0.070	7.85e+31 ± 1.74e+31
SA15-6695	0.000 ± 0.000	11.091 ± 0.065	11.112 ± 0.045	11.108 ± 0.045	6.33e+31 ± 4.5e+31
SA15-6846	10.700 ± 0.100	10.440 ± 0.081	10.472 ± 0.070	10.440 ± 0.077	2.93e+31 ± 1.91e+31
SA15-6851	10.700 ± 0.127	10.557 ± 0.028	10.558 ± 0.021	10.553 ± 0.022	2.32e+31 ± 1.42e+31
SA15-7241	10.700 ± 0.140	10.654 ± 0.212	10.686 ± 0.195	10.743 ± 0.124	8.7e+30 ± 6.57e+30
SA15-7543	11.000 ± 0.122	11.295 ± 0.128	11.169 ± 0.111	11.168 ± 0.111	3.27e+30 ± 1.21e+31
SA15-7972	10.800 ± 0.135	10.676 ± 0.148	10.593 ± 0.168	10.650 ± 0.164	2.71e+31 ± 3.82e+31
SA15-9333	9.520 ± 0.457	10.236 ± 0.201	10.265 ± 0.234	9.985 ± 0.320	5.9e+31 ± 1.62e+31
SA22-0083	10.100 ± 0.290	10.238 ± 0.180	10.238 ± 0.081	10.156 ± 0.273	1.79e+31 ± 4.56e+30
SA22-0128	10.600 ± 0.275	10.465 ± 0.139	10.582 ± 0.096	10.354 ± 0.132	7.92e+31 ± 7.95e+30
SA22-0189	11.500 ± 0.150	11.408 ± 0.128	11.341 ± 0.174	11.387 ± 0.133	7.07e+31 ± 4.46e+31
SA22-0206	9.820 ± 0.477	9.801 ± 0.198	9.873 ± 0.309	9.989 ± 0.288	3.26e+31 ± 5.34e+30
SA22-0281	11.000 ± 0.128	10.939 ± 0.110	10.942 ± 0.053	10.939 ± 0.064	7.08e+30 ± 9.15e+30
SA22-0299	9.740 ± 0.357	9.921 ± 0.238	9.544 ± 0.242	9.855 ± 0.204	3.32e+31 ± 7.41e+30
SA22-0315	10.700 ± 0.100	10.452 ± 0.102	10.453 ± 0.185	10.390 ± 0.028	1.41e+31 ± 4.9e+30
SA22-0331	9.700 ± 0.298	9.922 ± 0.303	9.837 ± 0.309	9.856 ± 0.324	1.99e+30 ± 1.99e+30
SA22-0398	10.800 ± 0.145	10.798 ± 0.018	10.782 ± 0.034	10.790 ± 0.025	5.84e+31 ± 1.96e+31
SA22-0455	10.500 ± 0.118	10.427 ± 0.045	10.479 ± 0.076	10.478 ± 0.076	1.51e+30 ± 2.85e+30
SA22-0510	10.500 ± 0.132	10.546 ± 0.154	10.426 ± 0.161	10.611 ± 0.162	9.6e+30 ± 2.74e+30
SA22-0554	10.200 ± 0.154	10.334 ± 0.136	10.295 ± 0.159	10.301 ± 0.158	2.04e+30 ± 2.83e+30
SA22-0563	9.580 ± 0.211	9.668 ± 0.228	9.613 ± 0.228	9.554 ± 0.271	4.5e+30 ± 2.1e+30
SA22-0568	9.910 ± 0.323	10.706 ± 0.115	10.668 ± 0.089	10.691 ± 0.204	5.86e+31 ± 1.21e+31
SA22-0619	10.100 ± 0.273	10.271 ± 0.044	10.273 ± 0.023	10.265 ± 0.028	1.23e+30 ± 1.18e+30
SA22-0630	9.840 ± 0.265	10.088 ± 0.279	9.726 ± 0.106	10.124 ± 0.231	2.1e+31 ± 4.06e+30
SA22-0643	9.400 ± 0.353	9.538 ± 0.270	9.365 ± 0.246	9.348 ± 0.251	4.76e+29 ± 1.04e+30

Table 2.3 (cont'd)

Object ID	log $\frac{M_\star}{M_\odot}$ (VIzK)	log $\frac{M_\star}{M_\odot}$ (VIzK12)	log $\frac{M_\star}{M_\odot}$ (VIzK1234 no NIR emission	log $\frac{M_\star}{M_\odot}$ (VIzK1234 with NIR emission)	$F_{3\mu m}$ (rest) (ergs/s/Å)
SA22-0674	11.100 ± 0.131	11.019 ± 0.025	10.991 ± 0.099	11.000 ± 0.093	1.13e+31 ± 1.73e+31
SA22-0710	10.800 ± 0.128	10.839 ± 0.092	10.756 ± 0.125	10.731 ± 0.099	7.64e+30 ± 5.04e+30
SA22-0721	11.200 ± 0.115	11.217 ± 0.119	11.139 ± 0.147	11.173 ± 0.133	7.53e+30 ± 1.84e+31
SA22-0758	10.400 ± 0.270	10.793 ± 0.025	10.810 ± 0.022	10.785 ± 0.023	5.05e+31 ± 1.75e+31
SA22-0770	10.700 ± 0.112	10.648 ± 0.179	10.715 ± 0.257	10.549 ± 0.159	2.07e+31 ± 6.02e+30
SA22-0893	10.600 ± 0.182	10.502 ± 0.135	10.494 ± 0.166	10.534 ± 0.139	5.88e+30 ± 4.25e+30
SA22-0964	10.700 ± 0.284	10.878 ± 0.070	10.900 ± 0.015	10.880 ± 0.023	9.68e+31 ± 2.32e+31
SA22-0997	-0.031 ± 11.181	8.695 ± 0.233	8.735 ± 0.184	8.810 ± 0.359	4e+30 ± 1.34e+30
SA22-1042	10.900 ± 0.093	10.732 ± 0.055	10.764 ± 0.053	10.695 ± 0.069	1.2e+32 ± 2.29e+31
SA22-1045	10.600 ± 0.066	10.966 ± 0.030	10.978 ± 0.026	10.968 ± 0.030	6.82e+31 ± 1.95e+31
SA22-1055	10.800 ± 0.174	10.683 ± 0.084	10.702 ± 0.102	10.697 ± 0.117	4.84e+31 ± 1.74e+31
SA22-1559	10.400 ± 0.286	10.254 ± 0.089	10.266 ± 0.056	10.219 ± 0.057	1.09e+32 ± 3.06e+31
SA22-1909	8.820 ± 4.916	9.970 ± 0.156	9.917 ± 0.105	9.990 ± 0.128	3.3e+31 ± 1.87e+31
SA22-1923	10.200 ± 0.276	10.565 ± 0.061	10.526 ± 0.052	10.433 ± 0.081	7.02e+31 ± 8.48e+30
SA22-1951	10.400 ± 0.277	10.454 ± 0.070	10.484 ± 0.054	10.473 ± 0.065	2.1e+31 ± 2.16e+31
SA22-1983	11.100 ± 0.172	11.075 ± 0.119	11.025 ± 0.186	11.020 ± 0.109	6.49e+31 ± 2.05e+31
SA22-2045	9.870 ± 0.421	10.221 ± 0.108	10.148 ± 0.183	10.242 ± 0.039	2.76e+31 ± 1.07e+31
SA22-2172	10.100 ± 0.348	10.525 ± 0.014	10.527 ± 0.017	10.509 ± 0.011	6.14e+31 ± 2.2e+31
SA22-2196	1.230 ± 11.414	8.790 ± 0.149	8.766 ± 0.119	8.720 ± 0.117	1.57e+30 ± 7.55e+29
SA22-2237	10.200 ± 0.434	10.168 ± 0.056	10.146 ± 0.095	10.129 ± 0.085	2.44e+31 ± 1.8e+31
SA22-2395	10.100 ± 0.346	10.097 ± 0.015	10.083 ± 0.046	10.083 ± 0.046	0 ± 0
SA22-2400	10.700 ± 0.291	10.805 ± 0.040	10.797 ± 0.038	10.793 ± 0.038	2.46e+31 ± 3.21e+31
SA22-2541	9.950 ± 0.420	9.750 ± 0.242	9.601 ± 0.239	9.822 ± 0.344	6.57e+30 ± 2.18e+30
SA22-2548	11.000 ± 0.177	10.999 ± 0.122	10.963 ± 0.151	11.031 ± 0.167	1.1e+31 ± 1.09e+31
SA22-2587	10.700 ± 0.151	10.755 ± 0.083	10.814 ± 0.151	10.815 ± 0.151	1.18e+30 ± 3.78e+30
SA22-2703	9.810 ± 0.504	10.264 ± 0.079	10.220 ± 0.085	10.194 ± 0.075	9.4e+30 ± 8.31e+30
SA22-2863	10.300 ± 0.304	10.533 ± 0.104	10.619 ± 0.154	10.450 ± 0.119	3.45e+31 ± 5.57e+30

Stellar masses with 3.6 μm and 4.5 μm from *Spitzer's* IRAC

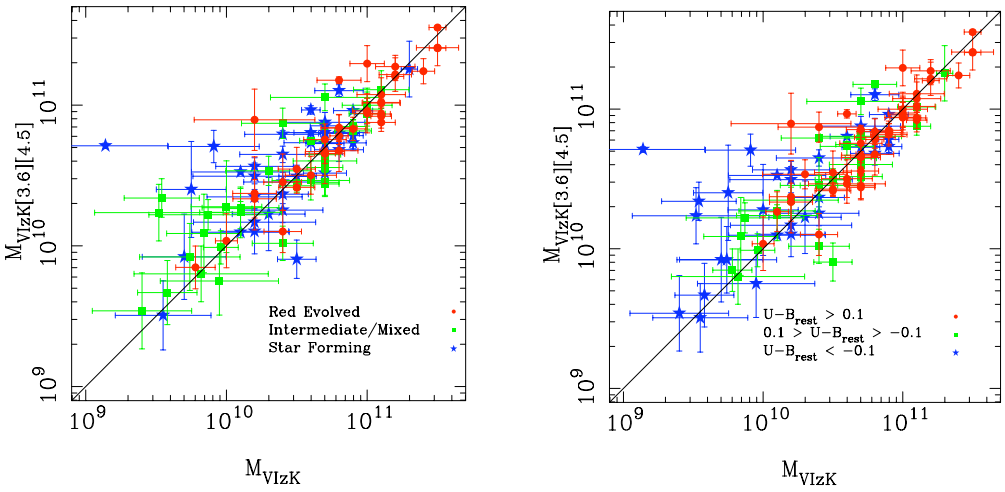

Figure 2.4 A comparison of masses derived from fitting the visible + IRAC [3.6],[4.5] wavebands to fitting to just $VIz'K_s$ photometry. Objects are keyed to galaxy spectral type in the left panel and according to their rest-frame $(U-B)$ colours in the right panel. The scatter is greatest for less massive, star-forming galaxies that have relatively blue $(U-B)_{\rm rest}$ colours.

Stellar masses for the GDDS galaxy survey were measured in Glazebrook et al. (2004) and these values are used to produce some of the results presented in later GDDS papers (e.g. Juneau et al. 2005; Abraham et al. 2007; Damjanov et al. 2009). These stellar masses were fit to $VIz'K_s$ wavebands only, thus probing the SED out to $\lambda_{\rm rest}$ $\sim$1 μm for $z \sim 1$. We compare stellar mass estimates from $VIz'K_s$ wavebands to the mass calculated from fits which also include the IRAC [3.6] and [4.5] wavebands in Figure 2.4. For the entire sample, there is a scatter of 0.3 dex above or below the previous mass estimates, and an increase in the stellar mass of 0.2 dex on average. In the left panel, the galaxies are keyed according to their galaxy spectral type. We can see that for the majority of evolved galaxies (red circles), the change in stellar mass is small. As a sample, these evolved galaxies show a negligible shift in stellar mass of -0.03 dex which is much less than the scatter in the sub-sample $\sigma_{rms} = 0.18$. The intermediate galaxies increase in stellar mass with the revised photometry on average by 0.42 dex and show the most scatter with $\sigma_{rms} = 1.9$. The blue star-forming galaxies are on average about 0.15 dex more massive, with a scatter of $\sigma_{rms} = 0.36$.

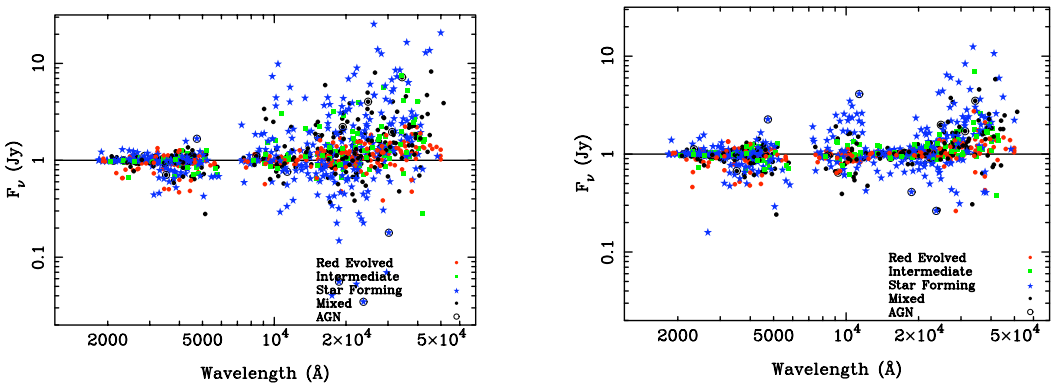

Figure 2.5 Ratio of observed bandfluxes divided by the model band fluxes predicted by SED fitting to the $VIz'K_s$ photometry (left) and $VIz'K_s$[3.6][4.5] photometry (right). The photometry has been blue shifted to the rest-frame. The rest-frame visible photometry (top) is generally well matched to the model SED bandfluxes, but beyond 1 μm, the SED extrapolated photometry can be up to a factor of 10 different from the observed photometry. The agreement at observed wavelengths of 1-2 μm improves when the [3.6] and [4.5] wavebands are used, as seen in the bottom panel, but beyond 2 μm, the observed photometry is greater by up to a factor of 10 than the extrapolated model photometry.

We also divide the sample based on their rest-frame $(U-B)$ colours in the right panel. There are more obvious trends in the different mass estimates in the colour-selected subsets than in the spectral type selected subsets. We see that, in general, mass estimates for objects with $(U-B)_{\rm rest} < -0.1$ increase, by 0.21 dex on average, with the inclusion of IRAC photometry, while mass estimates for objects with $(U-B)_{\rm rest} > 0.1$ generally stay the same (increasing by a negligible 0.005 dex on average) with smaller scatter ($\sigma_{rms} = 0.18$) evident. This shows that while it is not necessary to have rest-frame near-IR SED information for massive, "red and dead" galaxies; galaxies which have large fractions of young stellar populations, indicated by $(U-B)_{\rm rest} < -0.1$, generally have underestimated masses without near-IR SED information. We also see in this figure that the errors in the mass estimates generally decrease, as expected, with the addition of NIR photometric information.

The additional photometry not only provides more precise stellar mass measurements, but also improves the errors in all SED input model parameters so that the number of unique SED models which match the photometry is smaller. *By adding the rest-*

frame NIR photometry using the [3.6] and [4.5] wavebands, the best-fit SED matches the photometry much better. In Figure 2.5 we show the ratio between the observed band fluxes to the model band fluxes measured from the best-fit SED model. The wavelength for each band is blueshifted to the rest-frame using the spectroscopic redshift. In the left panel, the SED model is from a composite SFH model fit to the $VIz'K_s$ photometry, and the right is from SED fits to the $VIz'K_s$[3.6][4.5] wavebands. The scatter is much lower in the right panel where the models are consistent with the photometry short of $\lambda_{\rm rest} = 2\,\mu$m, whose photometry info is used for the fits, but beyond this wavelength, the best fit model does not do a good job at predicting the observed waveband fluxes at [5.6] and [8.0]. Clearly, the [3.6] and [4.5] wavebands alone do not provide unique matches between the observed and model photometry at wavelengths longer than rest-frame $2\,\mu$m.

Stellar masses with 3.6 - 8.0 μm from *Spitzer's* IRAC

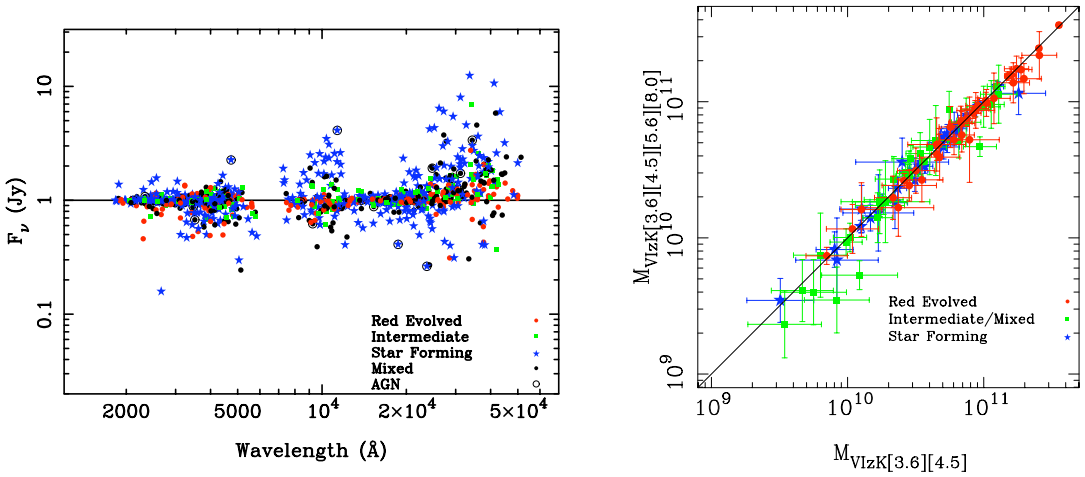

Figure 2.6 On the right, the ratio of observed band fluxes divided by the model band fluxes predicted by SED fitting to the $VIz'K_s$[3.6][4.5][5.6][8.0]. The photometry has been blue shifted to the rest-frame. The rest-frame visible photometry is generally well watched to the model SED bandfluxes, but beyond $2\,\mu$m, the SED underestimates the observed NIR flux.

In the previous section, we showed that the photometry predicted by the SED model fits and observed photometry do not agree at $\lambda_{\rm rest} > 2\,\mu$m. Is this simply because we have not included rest-frame photometry at these wavelengths provided by the IRAC [5.6] and [8.0] wavebands? We test whether we can achieve more robust SED fits that are

consistent with the photometry at rest wavelengths $> 2\,\mu$m by fitting the composite SFH models from PEGASE.2 to the photometry, this time including all IRAC wavebands. However, as we show in the left panel of Figure 2.6, adding the [5.6] and [8.0] wavebands does not improve the quality of fits. The observed to model bandflux ratios disagree. The same scatter is seen between the observed and model photometry as is seen in the right panel of Figure 2.5. The stellar masses are compared to fits without the [5.6] and [8.0] wavebands in the right panel and are shown to be consistent within the errors. The precision of the stellar masses is about the same, with a very small (0.004 dex) *decrease* in precision by adding the longer wavebands. *The stellar population synthesis models do not match the observed [5.6] and [8.0] photometry corresponding to rest-frame wavelengths longer than 2 μm and lead to a decrease in the precision of stellar mass estimates, while the accuracy is just as good to fits which include the [3.6] and [4.5] IRAC channels only.*

Stellar masses with a NIR emission SED model

In the previous section, we showed that the model SEDs generated by composite star formation history models do not match the photometry at rest wavelengths longer than $2\,\mu$m. As discussed in § 2.4.1, emission from non-stellar sources can provide significant luminosity at longer near- and mid-infrared wavelengths. Broadband multi-wavelength (UV, visible, and IR) empirical SED modeling performed by da Cunha et al. (2008) of galaxies from the *Spitzer* Infrared Nearby Galaxies Survey (SINGS; Kennicutt et al. 2003; Dale et al. 2005) show that emission in the NIR, from 2-5 μm, can be modeled by an additional SED component described by a PAH template spectrum superposed on an 850 K greybody modified by λ^{-1} extinction (written as GB+PAH to identify this as a single parameter SED component).

This simplistic model is added as an additional free parameter to the SED fitting routine. For each galaxy, the best-fit SED from this SPS model is plotted with the GDDS $VIz'K_s$[3.6][4.5][5.6][8.0] photometry in Figure 2.7 as a solid line. The stellar contribution to this SED component is plotted in green and the NIR emission component is plotted as a blue dotted curve. Also shown is the best fit SED fit to the $VIz'K_s$ photometry (dashed line). This additional SED component greatly improves the quality of fits as is seen in the flux ratio and residual plots in Figure 2.8. The motivation for this model, its nuances and its interpretation are the topic of the chapter 3 in this thesis. For now we simply compare the stellar masses produced by this composite SFH plus NIR emission component model.

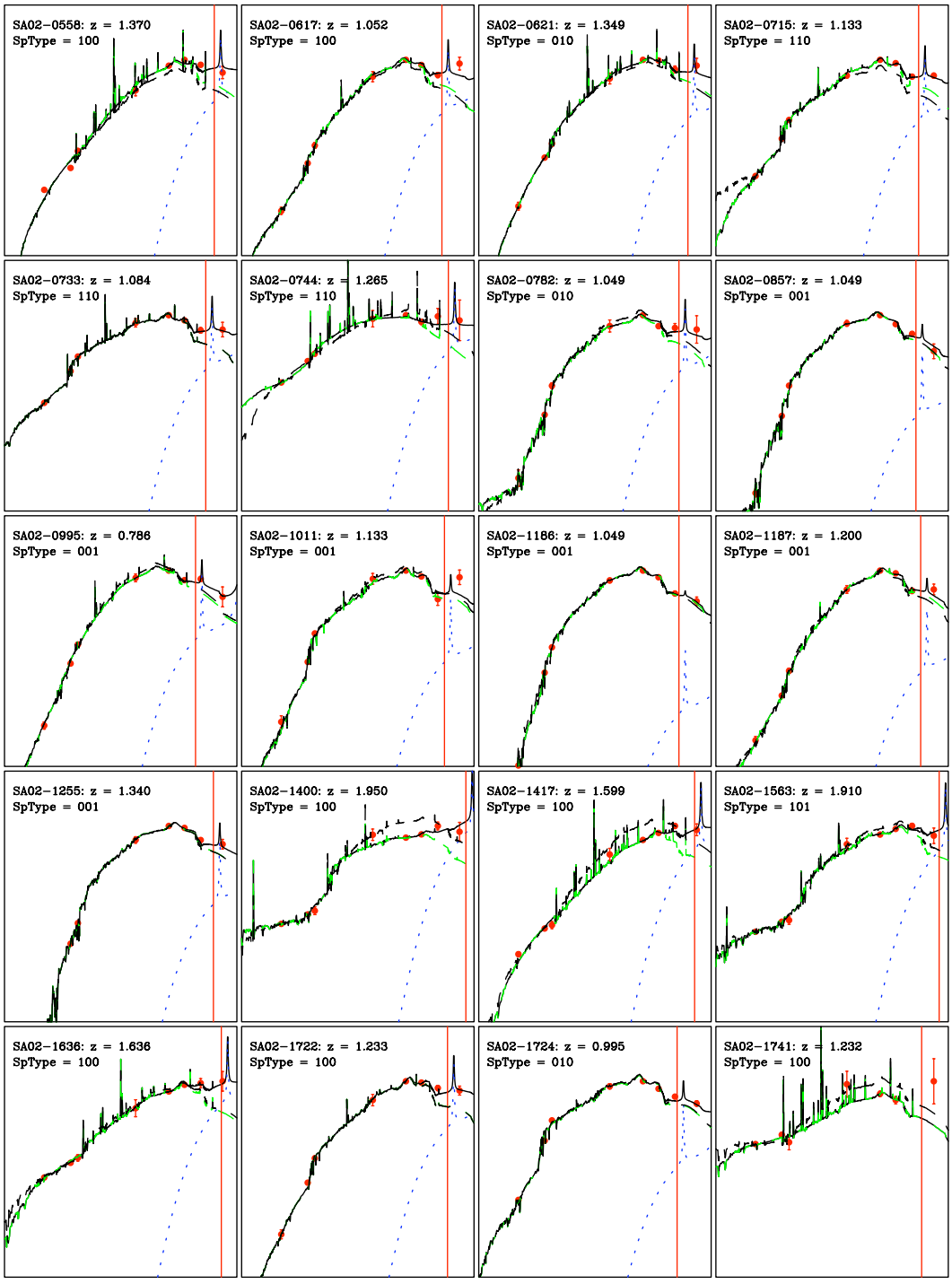

Figure 2.7 SED fit to the photometry (red dots show the $VIzK_s$[3.6][4.5][5.6][8.0] bands) for each galaxy. The SED (solid black line) is composed of both a (2 comp. SFH) stellar component (green dashed) and an NIR emission component consisting a 850 K greybody emission and a PAH spectrum (blue dotted line). The dashed curve is the best fit SED resulting from fits to just the $VIz'K_s$. For reference, $\lambda_{\rm rest} = 3\,\mu$m is plotted as a red vertical line.

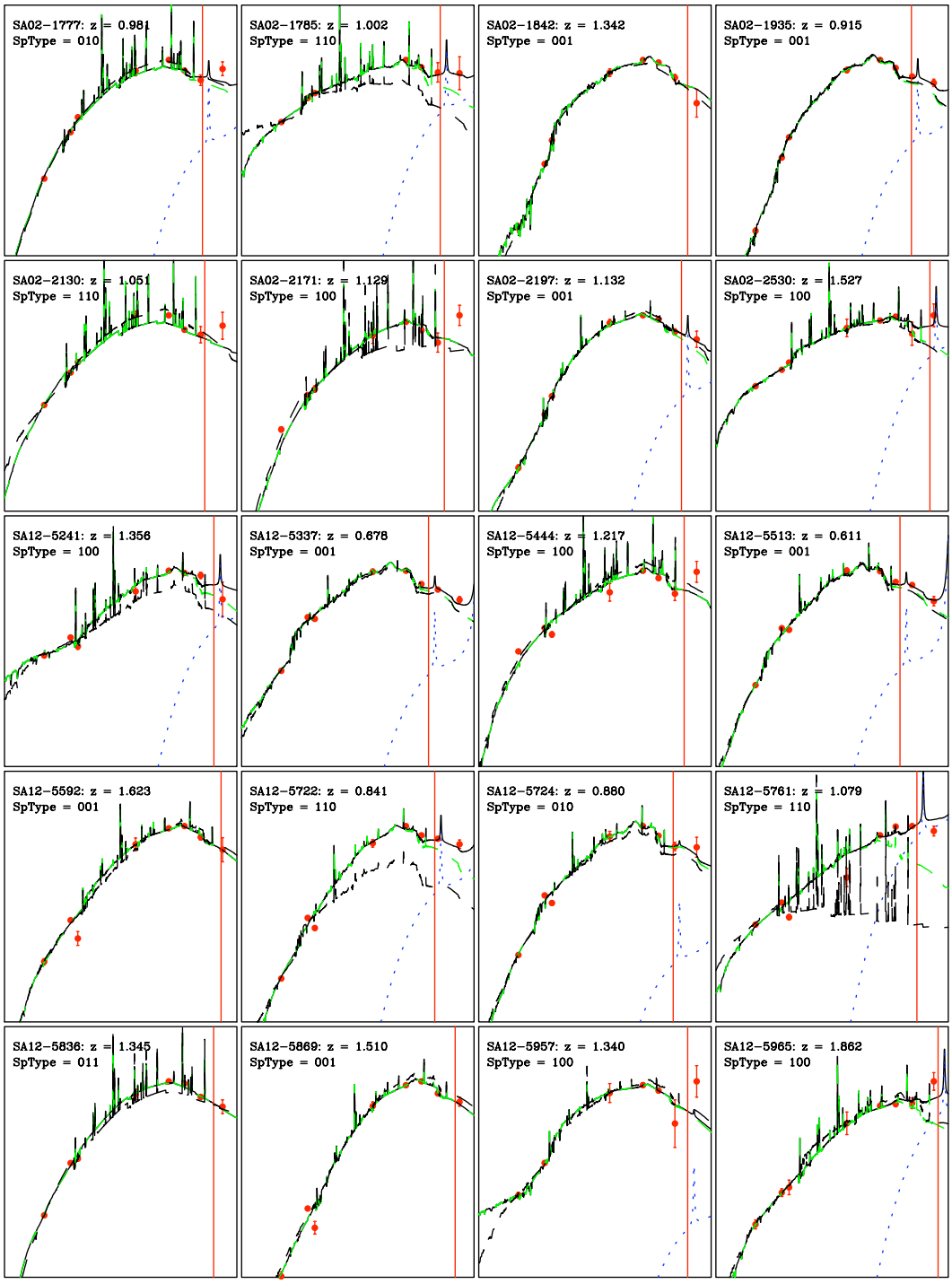

Figure 2.7 – cont'd

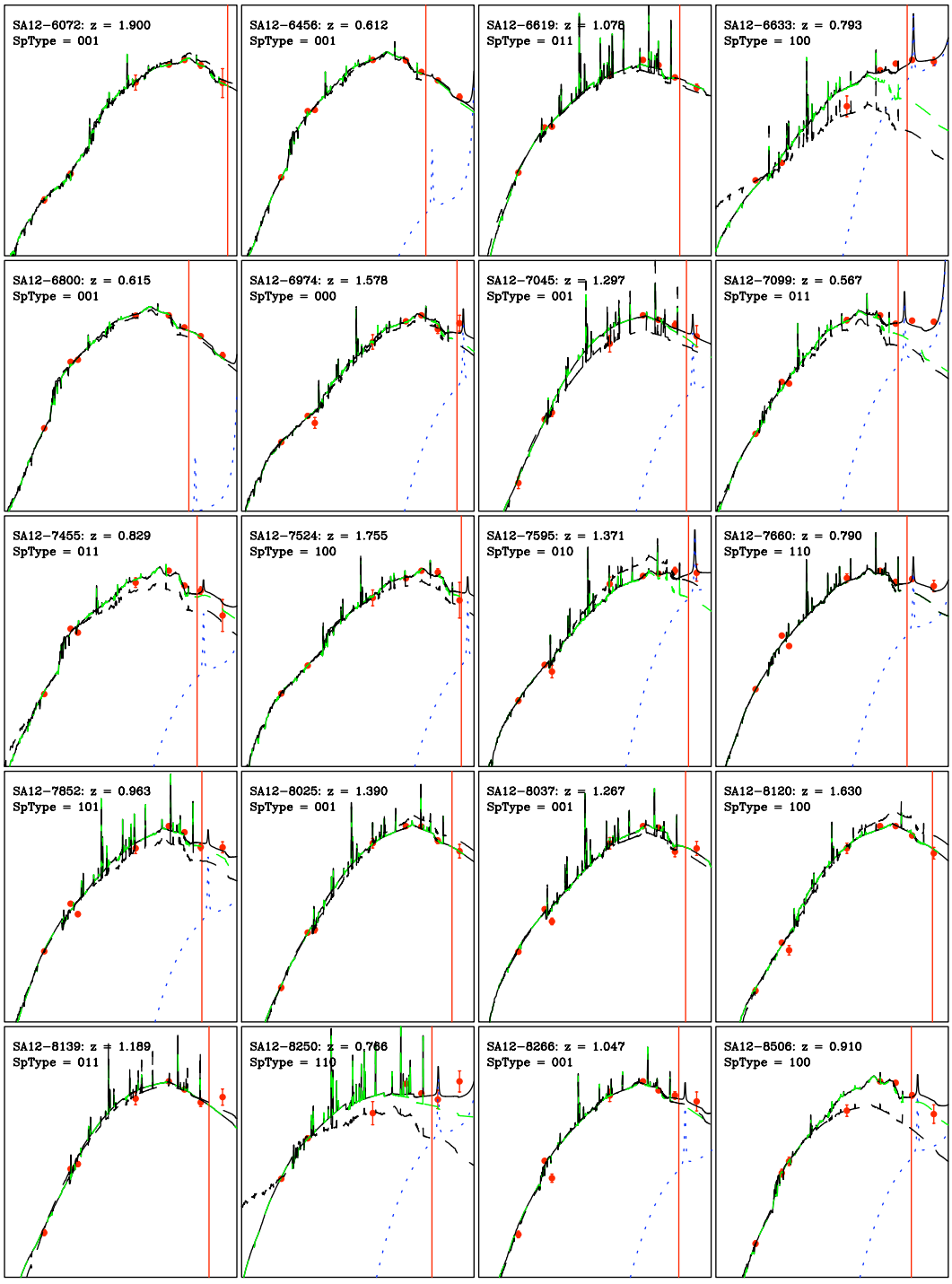

Figure 2.7 – cont'd

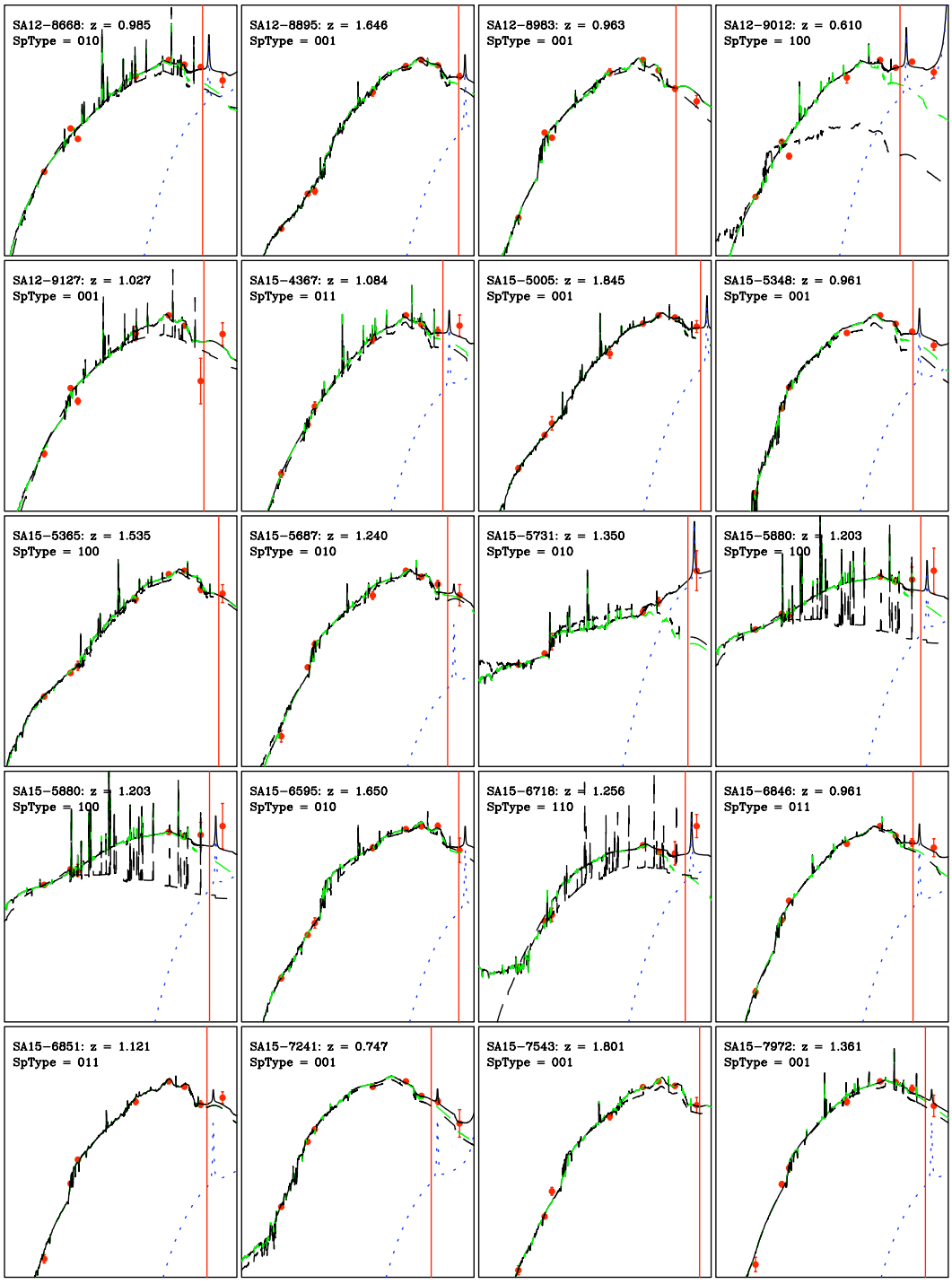

Figure 2.7 – cont'd

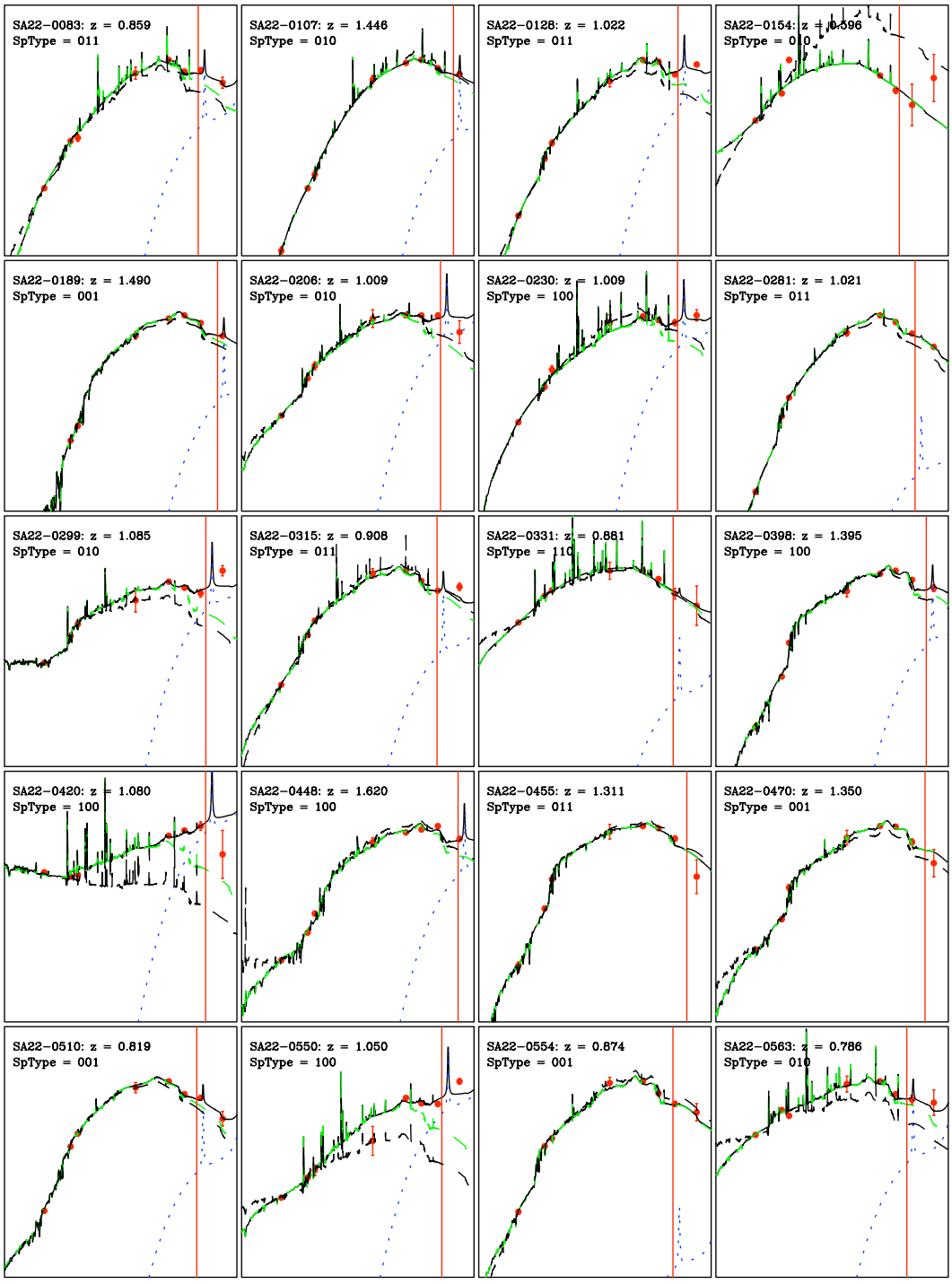

Figure 2.7 – cont'd

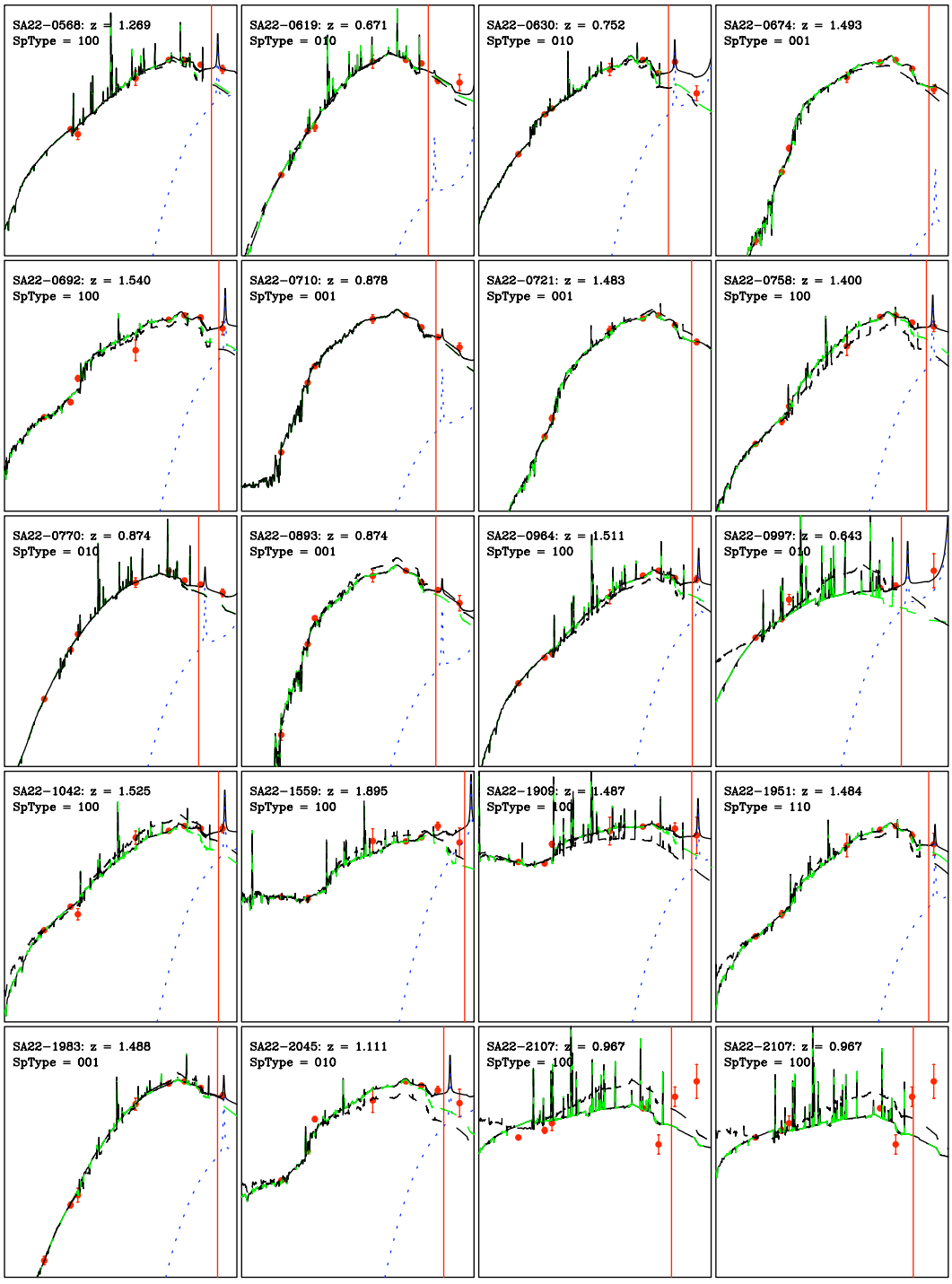

Figure 2.7 – cont'd

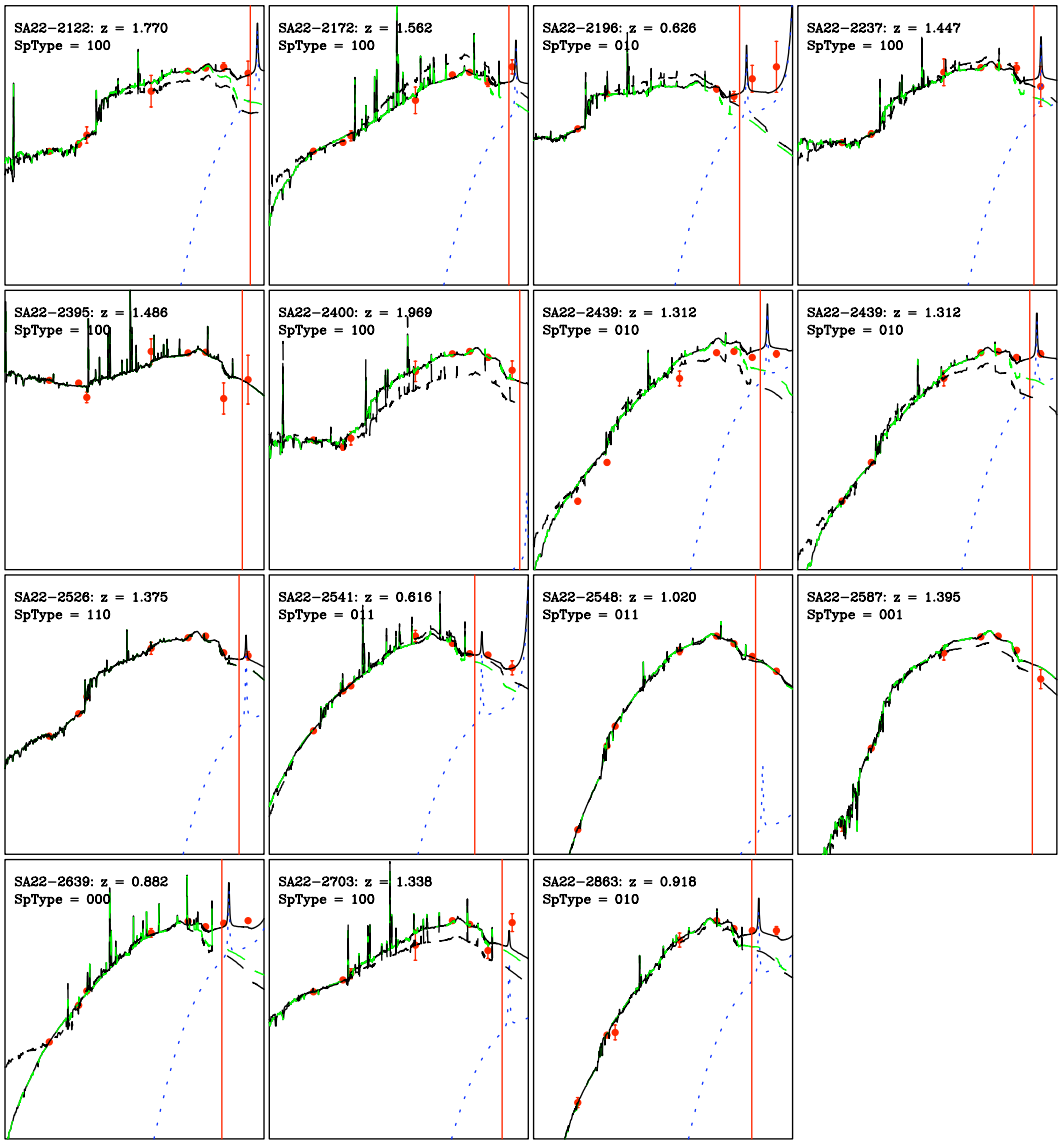

Figure 2.7 – cont'd

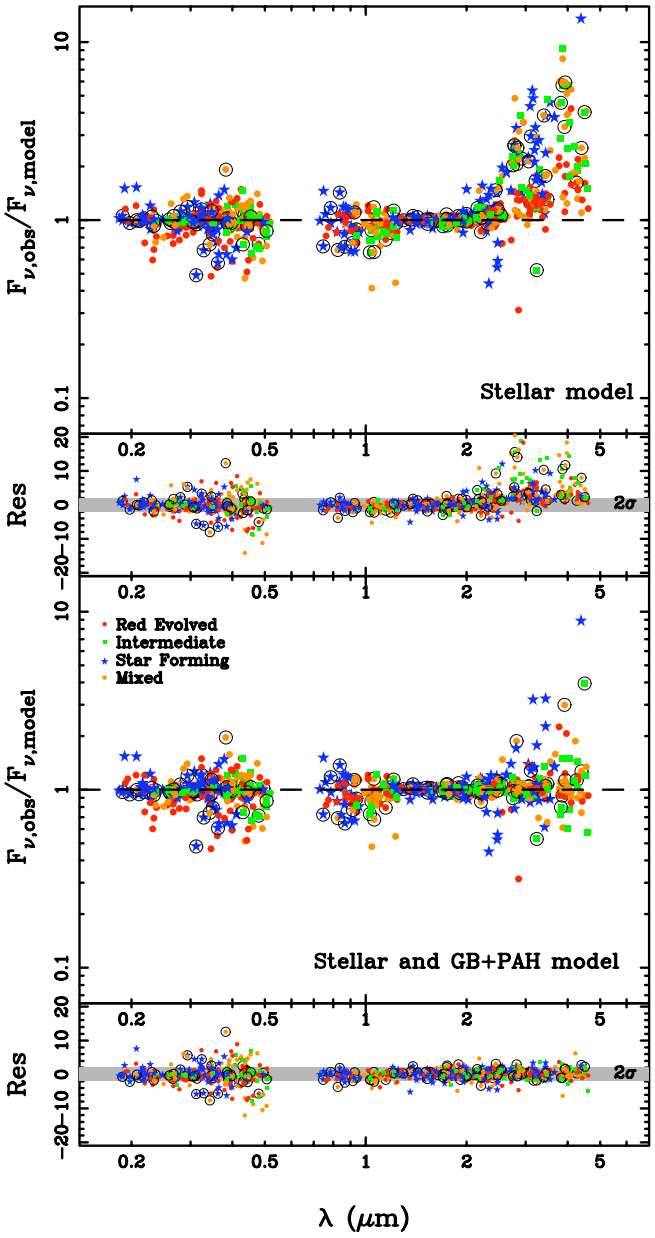

Figure 2.8 Ratios of the observed band fluxes to the best-fitting SED band fluxes for each galaxy in the sample, each blueshifted to the rest-frame wavelength. The residual between observed and model band fluxes are given as $(F_{obs} - F_{model})/\sigma$ under each panel. In both plots, we flag objects with possible contamination in the IRAC channels due to source confusion as thin open circles. *Top*: the visible (VIz'K) and *Spitzer*/IRAC [3.6 μm] and [4.5 μm] bands are fit to a stellar only SED model. *Bottom*: an additional GB+PAH component is added to the SED model as described in Section 2.4.1 and SEDs are fit again using all VIz'K+IRAC bands (with reasonable detections). The two component SED model fits the data much better, except for the objects with known contamination from source blending in the IRAC channels (thin open circles).

These stellar masses are compared to the masses from $VIz'K_s$[3.6][4.5] fits which probes rest-frame photometry shorter than 1 μm, which we assume to have a smaller contribution of the NIR emission adding to the the longer wavelength flux densities and are shown to be more precise and accurate than the stellar masses derived from $VIz'K_s$ fits. Figure 2.9 shows that the stellar masses are consistent for the GDDS sample with a small scatter in the sample of $\sigma_{rms} = 0.07$ dex, which is below the average errors in the mass estimates themselves. The stellar masses are no more accurate using this more complicated model. The average error in the stellar mass estimates decreases by a small amount 0.006 dex. *The NIR emission SED component provides a better match to the observed photometry beyond* $\lambda_{\rm rest}$ *=2*μ*m, but does not improve the accuracy of estimated stellar masses.*

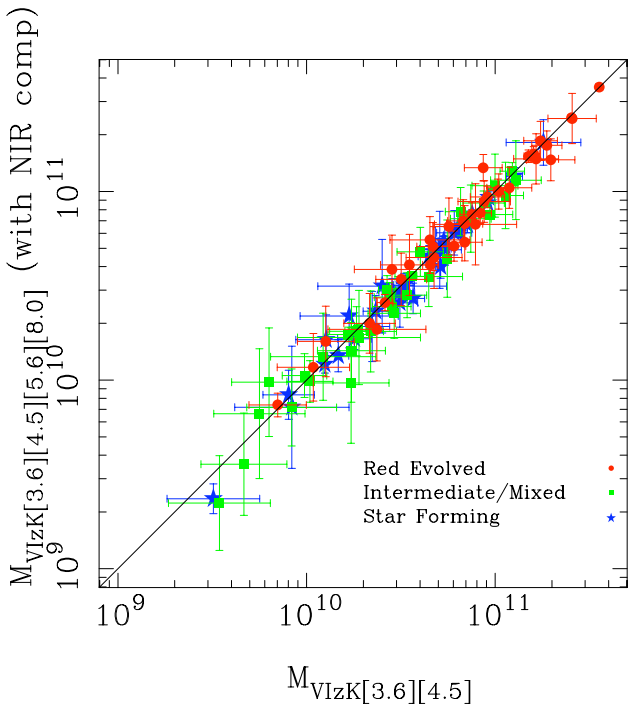

Figure 2.9 A comparison of masses derived from fitting the $VIz'K$[3.6][4.5][5.6][8.0] photometry to a composite SFH model augmented with a NIR emission SED component to stellar masses from fitting $VIz'K_S$[3.6][4.5] wavebands to a composite SFH model (the most precise and accurate stellar mass estimates in this study). Objects are keyed to galaxy spectral type. The estimated stellar masses are consistent with similar precision.

2.6.2 Single versus composite stellar populations

Longer wavelength photometry from *Spitzer's* IRAC instrument at 3.6 and 4.5 μm provides more accurate and precise stellar mass estimates without requiring the need to add an addition NIR emission component. Using a photometric dataset consisting of the $VIz'K_s$[3.6][4.5] wavebands we can now test other input parameters of stellar population models. In the visible, it has been shown that composite star formation history models provide more robust masses and improve the quality of SED fits because the models include a burst component that can model a young stellar population. Young stellar populations have the lowest mass-to-light ratios, particularly in the UV through blue part of the spectrum from the contribution of the short-lived massive stars composing the population (which have very low M/L as they give off much more energy per unit mass compared to lower mass stars). A young population can be much more luminous and as a results it can hide the contribution to the SED from underlying evolved populations A composite SED model is required to disassociate the contribution from a burst population from the underlying evolving stellar populations.

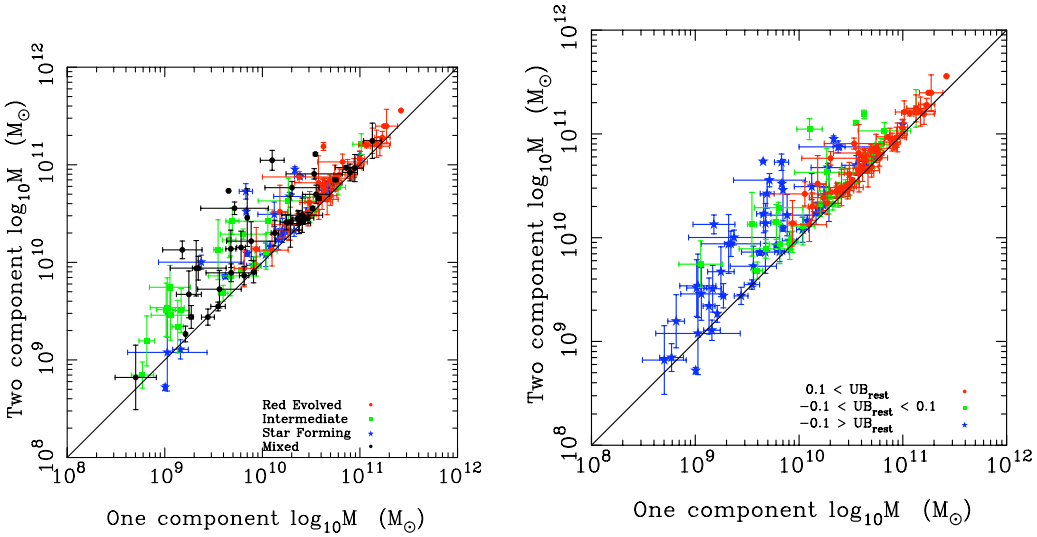

Figure 2.10 Stellar masses with and without secondary burst components calculated with PEGASE.2 models using VIzK+IRAC [3.6 μm],[4.0 μm] photometry. Not including a burst component can lead to an underestimation of stellar masses of up to 0.2 dex. This is most pronounced in mixed, intermediate star-forming galaxies (left panel) and in blue ($(U-B)_{\rm rest} < -0.1$) galaxies (right panel).

In this section, we investigate how stellar mass estimates from single SFH models compare to estimates from 2 component SFH models. Stellar masses are computed for both SFHs with the PEGASE.2 code using the $VIz'K_s$[3.6][4.5] wavebands. The resulting stellar masses are compared in Figure 2.10. In the left panel, the galaxies are keyed according to their galaxy spectral type, in the right panel according to their $(U-B)_{\rm rest}$ colours. The stellar masses of star-forming galaxies are underestimated in the single component model by ~ 0.2 dex. Red, evolved galaxies are underestimated by ~ 0.1 dex, while the mixed and intermediate galaxies are underestimated the most by ~ 0.3 dex on average. We find galaxies with blue rest-frame colours ($(U-B)_{\rm rest} < -0.1$) are underestimated by about 0.3 dex on average, while galaxies with redder rest-frame colours ($(U-B)_{\rm rest} > -0.1$) are underestimated by about 0.15 dex on average, roughly consistent with the stellar mass error. In Figure 2.11, the reduced χ^2 values from each fit are compared. Overall, the models with a 2 component SFH, with the second component modeled as an instantaneous burst, fit as good or better than the single SFH models. The median $\chi^2_{\rm reduced} = 3.2$ for the model with a single SFH and the median $\chi^2_{\rm reduced} = 1.96$ for the two component SFH.

The largest discrepancy is for galaxies with the bluest colours, many of which are mixed and intermediate stellar population galaxies. The star-forming galaxies are affected less than the intermediate and mixed galaxies, which is the result of having a more simplistic star formation history that is sufficiently modeled by a one component SFH with a relatively young age. The galaxies with the largest discrepancies are the mixed stellar populated galaxies, which were identified as having spectral signatures of both young and old populations. A single SFH model fit to these galaxies is driven by the more luminous, younger (but lower mass) population and leads to a lower mass-to-light ratio for the galaxy overall. As is seen in Figure 2.10, a lower mass-to-light ratio in the single SFH model results in an incorrect lower estimated stellar mass given the galaxy's luminosity.

Burst age as a fixed parameter

Stellar masses are often computed with a two component SFH model (Dickinson et al., 2003; Glazebrook et al., 2004) but to save computing time the age of the second component is assumed to be at a fixed age somewhere in the range of 50-200 Myr prior to the age of the galaxy at observed time (see Elsner et al. 2008 for example). Here we test the

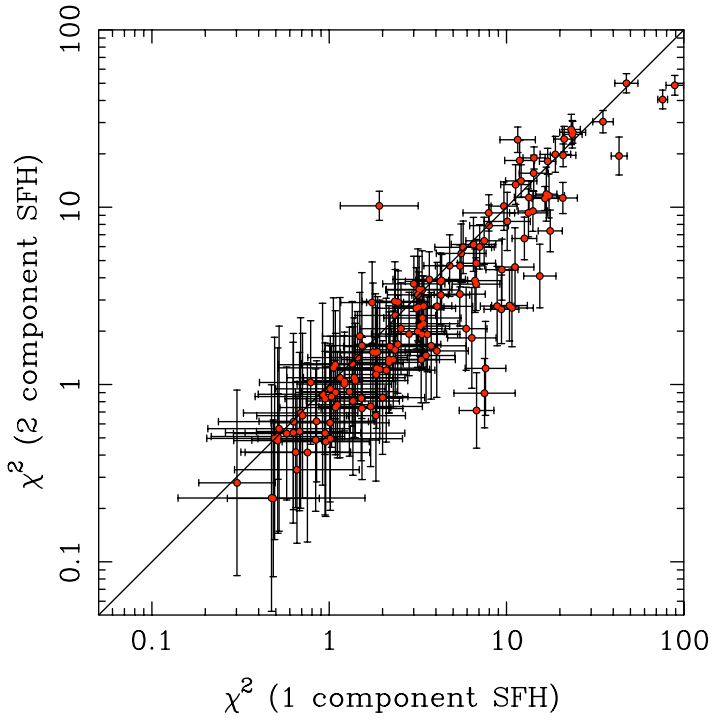

Figure 2.11 The reduced χ^2 values for each fit with and without secondary burst components calculated with PEGASE.2 models using VIzK+IRAC [3.6 μm],[4.0 μm] photometry. The models with a burst component have equal or lower χ^2 values than models with a single SFH component.

validity of this assumption. The left panel of Figure 2.12 compares stellar masses computed with two component SEDs generated from PEGASE models with the secondary component having a fixed age or a variable age. Again $VIz'K_s$[3.6][4.5] photometry is used. Masses derived from a secondary component with a fixed age of 50 Myr are underestimated compared to masses derived from bursts with a variable age. On the right, the difference in stellar masses is shown as a function of the galaxy's age. In both plots, symbols are keyed to $(U-B)_{\rm rest}$.

The burst mass fraction calculated from the fit is smaller in $\sim 90\,\%$ of the fits to the age fixed burst component. This leads to an underestimation of stellar mass of up to $\sim$0.3 dex for galaxies with blue rest-frame colours ($(U-B)_{\rm rest} < -0.1$) and an underestimation of $\sim$0.1 dex for the redder galaxies ($(U-B)_{\rm rest} > -0.1$). The right panel of figure 2.12 shows that the discrepancy in stellar mass is most pronounced for galaxies with older ages. As discussed in previous sections, this is due to the increase in the mass-to-light ratio of a galaxy as it ages. In the fixed burst model, the mass-to-light ratios are lower than any of the variably aged burst models older than 50 Myr. This is demonstrated in our fits; the model with the age of the burst component as a free parameter has an average of 250 ± 130 Myr for the time since the burst. Thus in these models the burst component has a relatively higher mass-to-light ratio and leads to larger stellar mass estimates. *Stellar masses derived from either single star formation history models or composite star formation history models with bursts occurring at a fixed age of 50 Myr provide underestimates in the estimated stellar mass up to $\sim$0.3 dex.* Composite SFH models where the age of both stellar populations is allowed to be a free parameter in the fits provide the most accurate measures of the stellar mass.

2.6.3 The inclusion of TP-AGB stars

The PEGASE.2 models do not include thermally pulsating asymptotic giant branch (TP-AGB) stars which emit brightly in the near-infrared during this evolutionary phase (that can last up to 10 Myr) of evolving intermediate mass red giant stars. The SPS models of Maraston (2005) include TP-AGB stars by matching to the near-IR colours of Magellanic cloud globular clusters and find that the TP-AGB phase of intermediate mass stars (2-3 $M_\odot$) ranging from 200 Myr to 2 Gyr leads to relatively higher near-infrared fluxes and thus lower mass-to-light ratios in the near-infrared. For galaxies dominated by TP-AGB emission in the near-IR, this could potentially lead to an overestimate in the stellar mass

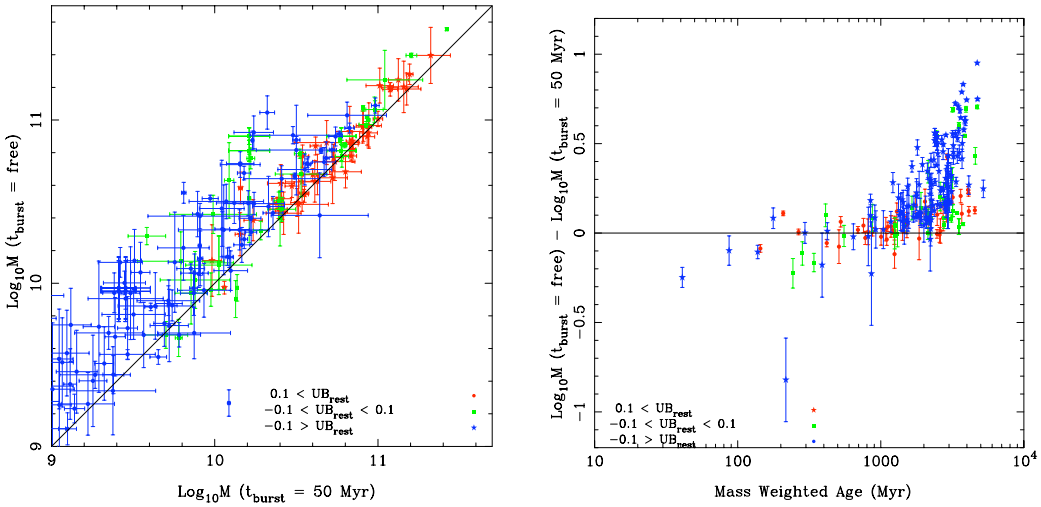

Figure 2.12 Stellar masses computed with two component SEDs generated from PEGASE models. In the left panel, masses computed from a SFH with a secondary burst component that is fixed to an age of 50 Myr are compared to models with a secondary burst component whose age is a free parameter. Masses derived from the fixed age secondary component are underestimated compared to masses derived from bursts with a variable age. On the right, the difference in stellar masses is shown as a function of the galaxy's age. In both plots, symbols are keyed to $(U-B)_{\rm rest}$.

if TP-AGB phase is not properly modeled.

We fit our photometry using the same method described above to publicly available [2] Maraston (2005) models. The models use a slightly different IMF from Kroupa et al. (1993) than the IMF we adopted for our SED fitting (Kroupa, 2001). To convert from masses from Kroupa et al. (1993) to Kroupa (2001) a scaling factor of 0.86 is applied to the masses. In Figure 2.13, stellar masses from single SFH models computed with PEGASE.2 are compared to single SFH models from Maraston (2005). About 10% of the stellar masses are in agreement, but the majority show a large offset of ~ 0.38 dex. The masses computed with PEGASE.2 are larger as a result of higher mass-to-light ratios predicted without the inclusion of TP-AGB stars. In the middle panel, the mass difference is plotted as a function of galaxy age measured in the PEGASE.2 SED fits. At young (< 100 Myr) and old (> 2 Gyr) ages, the two models in some cases estimate consistent stellar masses, but at the ages in between there is a large offset (0.37 ± 0.17 dex) for all of the galaxies as expected because intermediate aged stellar populations have a greater contribution from TP-AGB stars. In the right panel, we compare the estimated galaxy ages from the two SPS models and find that ages are consistent within 3σ for 75% of the galaxies. Those galaxies which disagree tend to be galaxies with young ages and blue colours as predicted by the PEGASE.2 model fits. They are modeled by the Maraston (2005) SPS models as intermediate age (0.8-1.8 Gyr) galaxies.

2.7 Mass function

A number of high-z galaxy surveys, such as those of Fontana et al. (2006) and Pérez-González et al. (2008) have measured the mass function and mass density function out to $z = 4$. In this section, we add to these surveys, and calculate for our spectroscopic sample the galaxy mass function and investigate the impact of the *Spitzer* augmented photometry. We consider the following four sets of analysis: $VIz'K_s$, $VIz'K_s$[3.6][4.5] and $VIz'K_s$[3.6][4.5][5.6][8.0] fit to composite SFH models from PEGASE.2 and $VIz'K_s$[3.6][4.5][5.6][8.0] fit to composite SFH models from PEGASE.2 augmented with a NIR emission SED component. Recall that these stellar masses are all listed in Table 2.3.

In order to construct the stellar mass density from our sample, a number of biases must be corrected for. Cosmic variance can lead to large errors in number density mea-

[2] http://www-astro.physics.ox.ac.uk/~maraston/Claudia's_Stellar_Population_Models.html

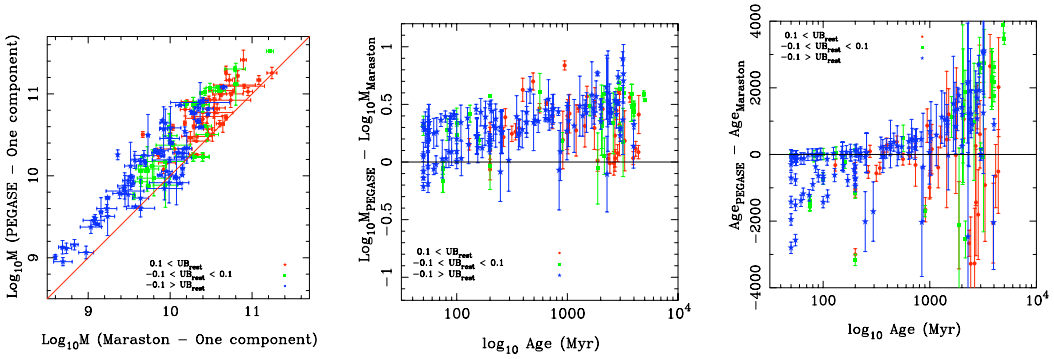

Figure 2.13 On the left, a comparison of masses calculated with PEGASE.2 and Maraston 2005 models. The mass difference as a function of age (from PEGASE.2 SED fits) and the age difference as a function of age is shown in the middle and right plots respectively. The Maraston 2005 models, which include modeling of TP-AGB stars, underestimate stellar masses compared to the PEGASE.2 fits.

surements, which the mass function is based upon. The GDDS survey design consists of four relatively small fields (1.21 arcmin^2) so that we can assume that any density inhomogeneities due to cosmic variance are averaged out over the fields. In addition, since we have a selected sample of the LCIR survey, we also need to consider the ratio of the galaxies chosen to obtain spectrscopic redshifts compared to those known in the field but not selected. The latter has already been addressed in the first paper of the GDDS (Abraham et al., 2004) by using weights for each galaxy. The weight, w_i, is defined as the fraction of galaxies in a given bin in the selected colour-magnitude space that have spectrscopic redshifts out of the total number of galaxies detected in the field in that colour-magnitude space from the LCIR survey.

We also need to consider the mass-completeness of the survey as less massive galaxies at higher redshifts are not detected in the survey due to our magnitude limit. We correct for this bias using the V_{max} formalism of Schmidt (1968). V_{max} is the volume corresponding to the highest redshift, z_{max}, at which the given galaxy would still appear brighter than the $K_{\rm Vega} = 20.6$ magnitude limit of the GDDS survey. We compute this using the best-fit SED for each galaxy. This SED is redshifted from $z = 0$ until the observed $K_{\rm Vega}$ band equals 20.6 (or $K_{\rm AB} = 22.4$), the redshift at which the apparent K-magnitude exceeds this limit is z_{max}.

We can also consider for the sample what the overall mass completeness is by con-

sidering a generic SED model. In Figure 2.3, in which the distribution of stellar masses for the sample is plotted against redshift, the solid curve indicates our mass detection limit, given the K_{Vega} limit of 20.6 mag, for a maximally old simple stellar population (SSP); a galaxy that formed all of its stars at once at the beginning of the universe. The dashed curve shows the same mass detection limit for a galaxy with a constant SFR, which better represents bluer galaxies. The sample is mass complete out to $z = 2$ for galaxies with $\log M_\star/M_\odot \gtrsim 10.5$.

The mass function, $\phi(M)$, is calculated for a given redshift bin:

$$\phi(M)\ dM = \sum \frac{1}{w_i V_{i,max}} dM \tag{2.6}$$

where dM is the width of the mass bin the mass function and V_{max} is given by

$$V^i_{max} = \int_{z_{low}}^{z_{high}} \frac{dV}{dz} dz \tag{2.7}$$

where the limits are given by z_{low}, the minimum redshift in a given bin and the $z_{high} = min(z_{high}, z_{max})$, where z_{high} is the maximum redshift in a given bin and z_{max} is the redshift detection limit for our K-band limited sample. The comoving volume is calculated from

$$\frac{dV}{dz} = A \frac{cD_L^2}{(1+z)^5 H(z)} \tag{2.8}$$

where c is the speed of light, D_L is the luminosity distance, and H(z) is the evolving *Hubble* function.

We compute the likelihood of the mass function for a given set of redshift bins through bootstrap error analysis as we can assume our data set of stellar mass values is independent and identically distributed. The sample is mass complete out to $z = 2$ for stellar masses of $\log M_\star/M_\odot > 10.5$. Only 59 of our 103 sample of galaxies with spectroscopic redshifts have masses that satisfy this criterium. Error bars are quite large given that the

Table 2.4. GDDS Mass Function

z	$\log \frac{M_\star}{M_\odot}$	ϕ (VIzK) (n/Mpc^3)	ϕ (VIzK12) (n/Mpc^3)	ϕ (VIzK1234) (n/Mpc^3)	ϕ (VIzK1234+GB) (n/Mpc^3)
0.70-1.00	9.00-9.25	...	...	...	...
0.70-1.00	9.25-9.50	3.057e-03 ± 2.164e-03	...	1.590e-03 ± 1.590e-03	1.590e-03 ± 1.590e-03
0.70-1.00	9.50-9.75	...	3.057e-03 ± 2.164e-03	2.052e-03 ± 1.580e-03	1.467e-03 ± 1.467e-03
0.70-1.00	9.75-10.00	3.273e-03 ± 1.536e-03	1.946e-03 ± 1.334e-03	1.946e-03 ± 1.334e-03	1.946e-03 ± 1.334e-03
0.70-1.00	10.00-10.25	1.523e-03 ± 7.446e-04	1.273e-03 ± 7.200e-04	6.881e-04 ± 4.198e-04	1.273e-03 ± 7.200e-04
0.70-1.00	10.25-10.50	...	2.012e-03 ± 8.894e-04	2.240e-03 ± 9.279e-04	2.087e-03 ± 8.926e-04
0.70-1.00	10.50-10.75	2.865e-03 ± 1.360e-03	2.369e-03 ± 1.291e-03	2.746e-03 ± 1.346e-03	2.865e-03 ± 1.360e-03
0.70-1.00	10.75-11.00	1.959e-03 ± 1.086e-03	2.085e-03 ± 1.089e-03	1.480e-03 ± 9.861e-04	1.450e-03 ± 9.976e-04
0.70-1.00	11.00-11.25	6.277e-05 ± 6.277e-05	...	...	6.277e-05 ± 6.277e-05
0.70-1.00	11.25-11.50	...	...	...	...
0.70-1.00	11.50-11.75	...	...	...	...
1.00-1.50	9.00-9.25	4.567e-04 ± 4.567e-04	...	...	...
1.00-1.50	9.25-9.50	...	...	...	...
1.00-1.50	9.50-9.75	...	...	1.071e-03 ± 1.071e-03	...
1.00-1.50	9.75-10.00	1.651e-03 ± 1.148e-03	1.502e-03 ± 1.115e-03	4.980e-04 ± 3.526e-04	1.888e-03 ± 1.172e-03
1.00-1.50	10.00-10.25	1.944e-03 ± 8.249e-04	1.574e-03 ± 6.956e-04	1.255e-03 ± 6.182e-04	1.594e-03 ± 7.724e-04
1.00-1.50	10.25-10.50	1.189e-03 ± 5.925e-04	1.405e-03 ± 6.328e-04	1.646e-03 ± 7.044e-04	1.585e-03 ± 6.750e-04
1.00-1.50	10.50-10.75	1.155e-03 ± 3.870e-04	1.488e-03 ± 7.315e-04	1.668e-03 ± 7.399e-04	9.684e-04 ± 5.153e-04
1.00-1.50	10.75-11.00	3.876e-04 ± 1.463e-04	7.381e-04 ± 2.431e-04	7.341e-04 ± 2.426e-04	7.861e-04 ± 2.530e-04
1.00-1.50	11.00-11.25	2.292e-04 ± 1.203e-04	2.936e-04 ± 1.406e-04	2.699e-04 ± 1.295e-04	2.347e-04 ± 1.214e-04
1.00-1.50	11.25-11.50	6.782e-05 ± 5.295e-05	8.093e-05 ± 5.710e-05	5.427e-06 ± 5.426e-06	6.782e-05 ± 5.295e-05
1.00-1.50	11.50-11.75	...	...	...	...
1.50-2.00	9.00-9.25	...	...	...	...
1.50-2.00	9.25-9.50	...	...	...	...
1.50-2.00	9.50-9.75	...	...	...	...
1.50-2.00	9.75-10.00	...	...	...	...
1.50-2.00	10.00-10.25	...	3.746e-04 ± 3.746e-04	4.608e-04 ± 4.608e-04	7.338e-04 ± 5.356e-04
1.50-2.00	10.25-10.50	9.011e-04 ± 5.283e-04	2.730e-04 ± 2.730e-04	3.369e-04 ± 2.804e-04	...
1.50-2.00	10.50-10.75	7.769e-04 ± 3.699e-04	6.994e-04 ± 3.439e-04	8.312e-04 ± 5.648e-04	1.001e-03 ± 5.954e-04
1.50-2.00	10.75-11.00	3.766e-04 ± 1.822e-04	6.542e-04 ± 3.320e-04	7.352e-04 ± 3.417e-04	6.542e-04 ± 3.320e-04
1.50-2.00	11.00-11.25	2.639e-04 ± 1.405e-04	2.259e-04 ± 1.312e-04	3.173e-04 ± 1.599e-04	3.173e-04 ± 1.599e-04
1.50-2.00	11.25-11.50	4.034e-05 ± 2.853e-05	1.115e-04 ± 9.355e-05	2.017e-05 ± 2.017e-05	2.017e-05 ± 2.017e-05
1.50-2.00	11.50-11.75	...	2.017e-05 ± 2.017e-05	2.017e-05 ± 2.017e-05	2.017e-05 ± 2.017e-05

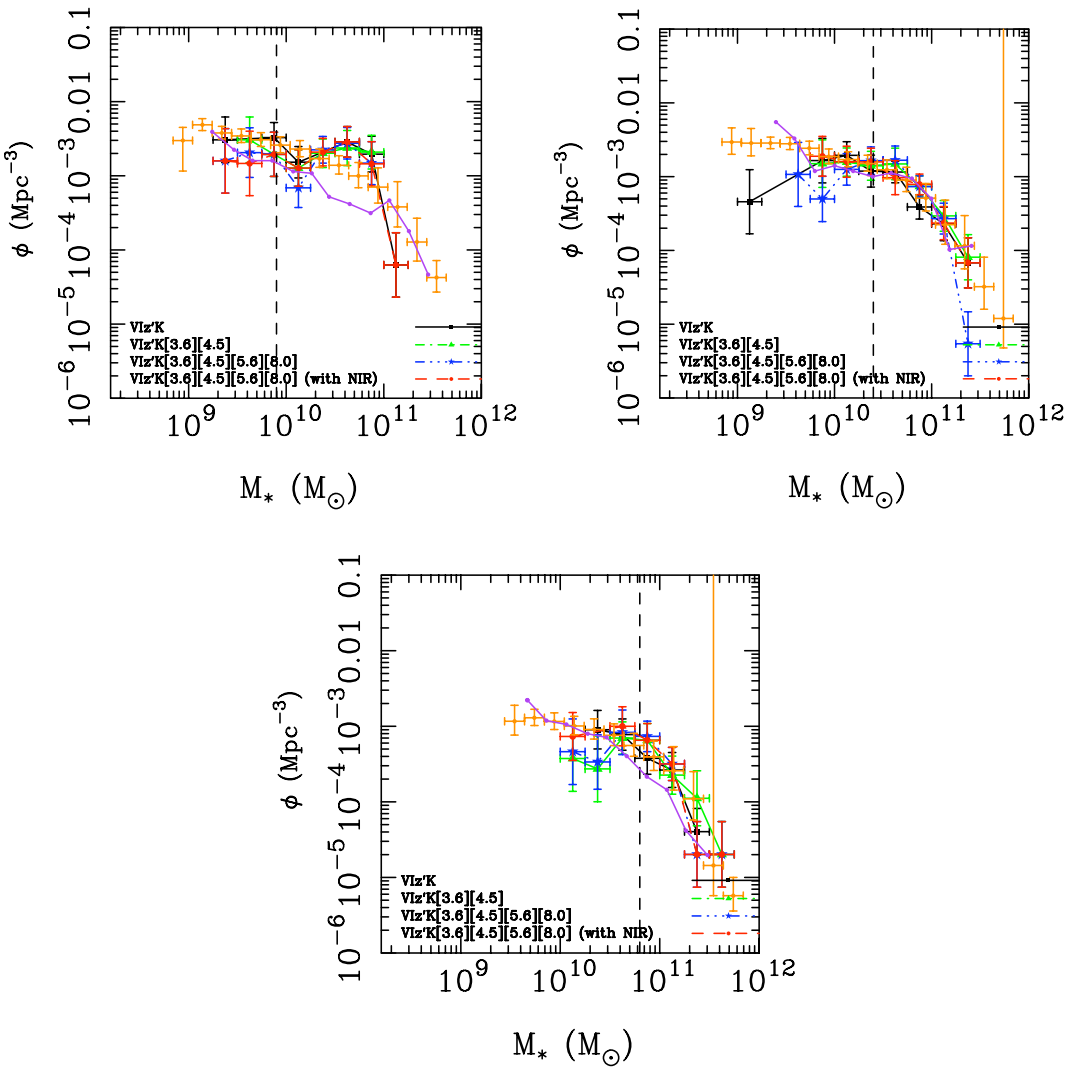

Figure 2.14 The mass function (in units of number of galaxies per unit volume) for masses calculated with the addition of IRAC photometry or the addition of a NIR SED component are consistent within the errors. Clockwise from the top-left the panels show the mass function at $z = 0.7 - 1,\ 1 - 1.5$ and $1.5 - 2$. It is also consistent with results from Pérez-González et al. (2008) (orange points) and Fontana et al. (2006) (purple points).

sample is reduced to 59 objects. For this reason, we divide the data into three, relatively large, redshift bins of 0.7-1.0, 1.0-1.5, 1.5-2.0.

The mass function at these three redshift intervals is plotted in Figure 2.14. Mass functions for the 4 different SED fitting methods are shown to illustrate the change in the measured stellar mass function given the change in derived stellar masses that can be on average 0.3 dex higher in galaxies with blue $(U-B)_{\rm rest}$ colours, while other galaxies are less affected. Masses derived from $VIz'K_s$ photometry fit to a composite SFH are shown in black squares. We augment the photometry with the IRAC [3.6] and [4.5] wavebands and plot the resulting mass function as green triangles. The addition of the longer [5.6] and [8.0] fit to a composite SFH model and a composite SFH model with a NIR emission SED component are shown in blue stars and red circles respectively. The dashed vertical line indicates the mass above which the sample is mass complete at the redshift limit of each redshift bin. Any data points for the mass function below this threshold is a lower limit.

The improvement in the measurement of stellar masses by adding IRAC photometry can potentially change the mass function in two ways, because (1) the masses have changed, in some cases increasing up to 0.3 dex and (2) because V_{max} changes as the mass changes. However, we find the overall effect is modest. *In all cases, the mass function from the different input procedures are consistent within the errors. Stellar masses most affected tended to be lower mass galaxies with blue* $(U-B)_{\rm rest}$ *colours. Since these galaxies are below the mass completeness threshold, they do not impact the mass function. But for a deeper survey, the change in the mass function due to the addition of IRAC photometry would likely be more significant.*

The values of the mass function are tabulated in Table 2.4 and illustrated in Figure 2.14. For comparison, the mass functions from Fontana et al. (2006) and Pérez-González et al. (2008) are shown as purple and orange dots respectively this figure. The Fontana et al. (2006) survey used IRAC wavebands to calculate the mass function on their 27% spectroscopic complete survey. Pérez-González et al. (2008) also used IRAC bands corresponding to $\lambda < 2\,\mu$m on their very large (28000 objects in $\sim$664 arcmin^2) survey with a spectroscopic redshift completeness of 7%, compared to the 89% spectroscopic completeness of the GDDS survey. Their mass functions, both calculated with a Salpeter (1955) IMF, are converted to the Kroupa (2001) IMF by scaling the mass function by 0.55. The mass function derived from the GDDS sample is consistent with the results from these two larger surveys.

Table 2.5. GDDS Mass Density Function ($\log M_\star/M_\odot \gtrsim 10.5$)

z	ρ (VIzK) ($M_\odot$/Mpc^3)	ρ (VIzK12) ($M_\odot$/Mpc^3)	ρ (VIzK12) ($M_\odot$/Mpc^3)	ρ (VIzK1234+GB) ($M_\odot$/Mpc^3)
0.70-1.00	6.980e+07 ± 1.439e+07	6.402e+07 ± 1.657e+07	5.720e+07 ± 1.635e+07	6.291e+07 ± 1.290e+07
1.00-1.50	2.770e+07 ± 7.509e+06	4.306e+07 ± 8.919e+06	4.117e+07 ± 8.847e+06	3.596e+07 ± 7.657e+06
1.50-2.00	2.812e+07 ± 3.884e+06	3.566e+07 ± 4.379e+06	3.456e+07 ± 5.178e+06	3.419e+07 ± 5.584e+06

The evolution of the mass function for the GDDS sample from z=2 to z=0.7 is shown in Figure 2.15, as measured from stellar masses fit with $VIz'K_s$[3.6][4.5] wavebands to a composite SFH model. The mass function shows little evolution above $10^{10.75}$M$_\odot$. At z=0.5-1, the number of galaxies from $10^{10.25}$ to $10^{10.75}$M$_\odot$ is ∼50% greater than at z=1-1.5, finding between 0.5 to 4 times (given the errors) as many galaxies in this mass range at z=0.5-1 than at z=1-1.5 . These results are consistent with those from larger surveys in which the evolution in the mass function at $M > 10^8$ $M_\odot$ is slow Fontana et al. (2006); Pérez-González et al. (2008). The large drop in the most massive galaxies in the closest redshift bin is likely due to cosmic variance as the volumes probed at closer redshifts are smaller by nature.

2.8 Mass density

The mass density, $\rho_\star(> M_{limit})$, is calculated as the weighted sum of the stellar mass in a given redshift bin:

$$\rho_\star(> M_{limit}) = \sum \frac{M_i}{w_i V_{i,max}} \tag{2.9}$$

where $V_{i,max}$ is given as Equation 2.7 and w_i is a weight to account for our spectroscopic selection bias as described and tabulated in Abraham et al. (2004). The mass density can only be integrated down to the mass-detection limit. For the GDDS, $M_{limit} = 10^{10.5}\,M_\odot$.

As with the mass function, the likelihood of the mass density function is determined through bootstrap error analysis and we divide the data into three, relatively large, redshift bins of 0.7-1.0, 1.0-1.5, 1.5-2.0.

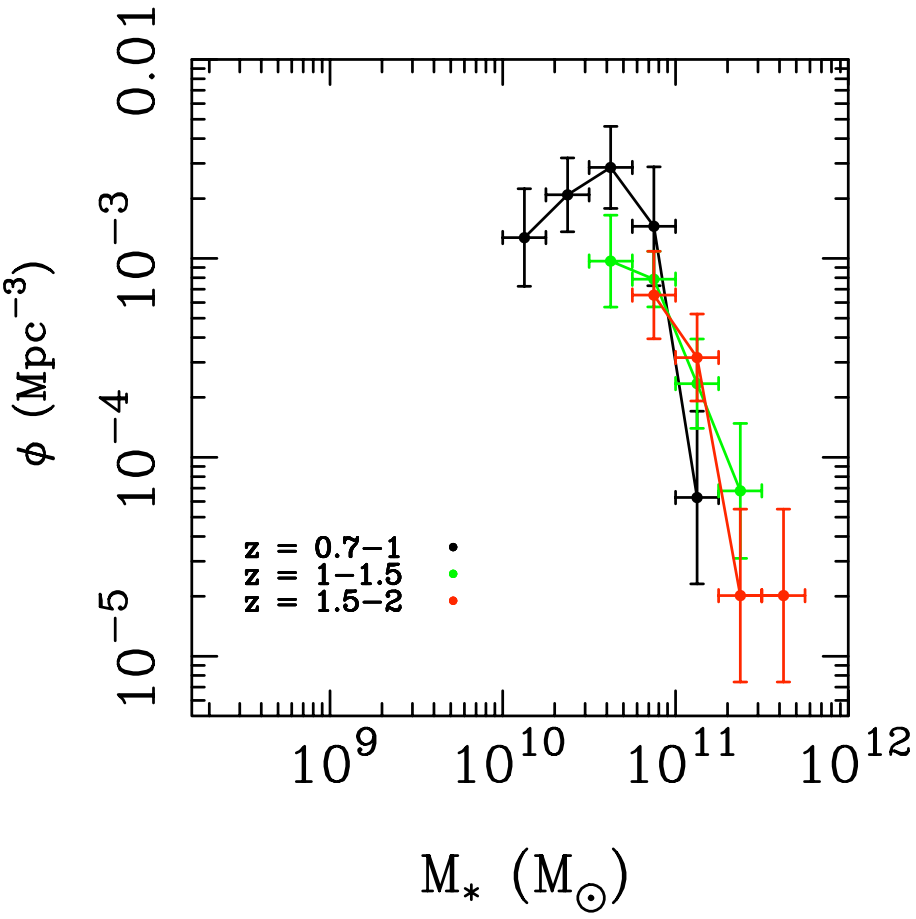

Figure 2.15 The evolution of the mass function for the GDDS sample with stellar masses computed using $VIz'K_s$[3.6][4.5] photometry fit to a composite SFH model. Evolution at $M > 10^{10.8}\ M_\odot$ is slow, but for lower masses evolution from z=1 to 1.5 is noticeable as we find from $10^{10.25}$ to $10^{10.75}\ M_\odot$, ϕ is $\sim$50% greater by $z = 0.7 - 1$ than at $z = 1 - 1.5$.

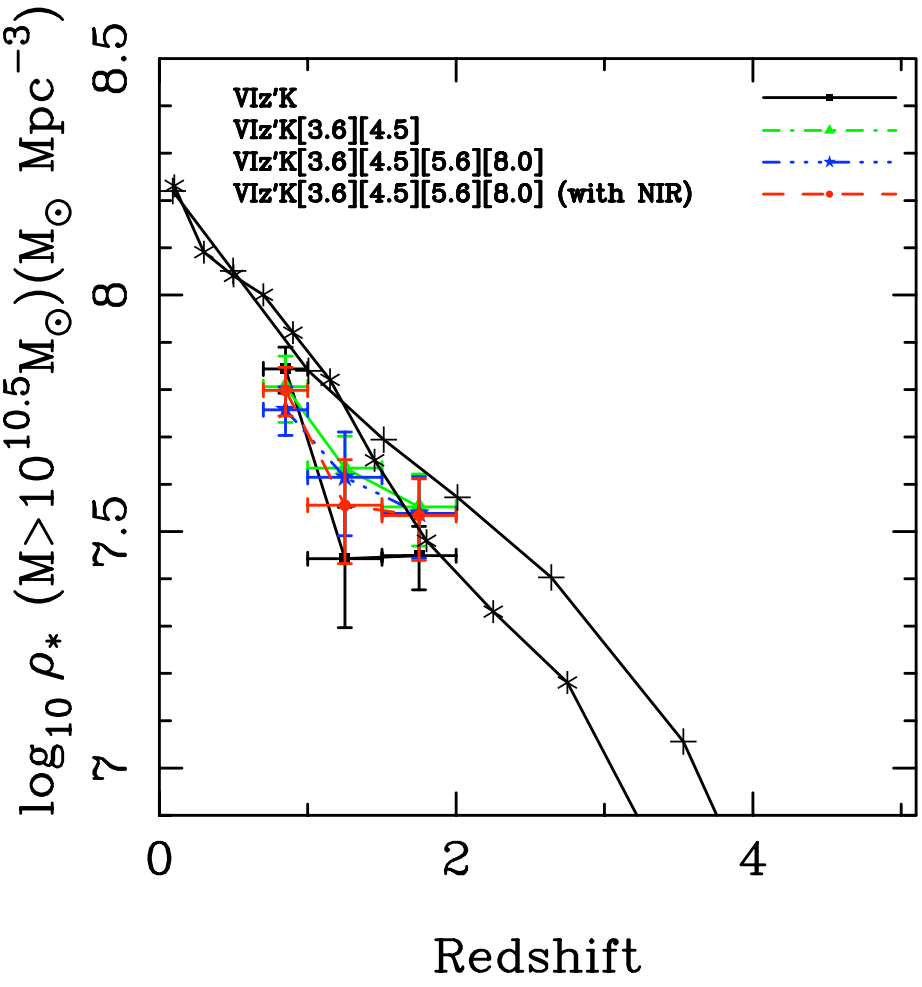

Figure 2.16 The mass density for masses calculated with the addition of IRAC photometry or an NIR emission component are shown and keyed according to the legend. The mass density is consistent for models fit to the IRAC wavebands, but the mass density computed from $VIz'K_s$ photometry is slightly underestimated at $z = 1 - 1.5$ by $\sim$50% . The mass density is slightly lower than, but consistent within errors, to those from Pérez-González et al. (2008) (black asterisks) and from Elsner et al. (2008) (black plus symbols).

Chapter 3

Detection of a near-infrared excess in observations of galaxies in the redshift desert with the *Spitzer Space Telescope*

Published as:
"A near-infrared excess in the continuum of high-redshift galaxies: a tracer of star formation and circumstellar disks?"
Mentuch, E., Abraham, R. G., Glazebrook, K., McCarthy, P. J., Yan, H., ODonnell, D. V., Borgne, D. L., Savaglio, S., Crampton, D., Murowinski, R., Juneau, S., Carlberg, R. G., Jorgensen, I., Roth, K., Chen, H.-W., & Marzke, R. O. 2009, ApJ, 706, 1020

3.1 Abstract

A broad continuum excess in the near-infrared, peaking in the rest-frame at 2-5 μm, is detected in a spectroscopic sample of 88 galaxies at $0.5 < z < 2.0$ taken from the Gemini Deep Deep Survey. Line emission from polycyclic aromatic hydrocarbons (PAHs) at 3.3 μm alone cannot explain the excess, which can be fit by a spectral component consisting of a template of PAH emission lines superposed on a modified blackbody of temperature $T \sim 850$ K. The luminosity of this near-infrared excess emission at 3 μm is found to be correlated with the star formation rate of the galaxy. The origin of the near-infrared excess is explored by examining similar excesses observed locally in mas-

sive star-forming regions, reflection and planetary nebulae, post-asymptotic giant branch stars and in the galactic cirrus. We also consider the potential contribution from dust heated around low-luminosity active galactic nuclei. We conclude that the most likely explanation for the 2-5 μm excess is the contribution from circumstellar disks around massive young stellar objects seen in the integrated light of high-redshift galaxies. Assuming circumstellar disks extend down to lower masses, as they do in our own Galaxy, the excess emission presents us with an exciting opportunity to measure the formation rate of planetary systems at cosmic epochs before our own Solar System formed.

3.2 Introduction

The spectral energy distributions (SEDs) of most normal star-forming galaxies can be well-described by a model which is simply the superposition of a component due to starlight and a component due to re-radiated dust emission. The physical details of the stellar component are well understood on the basis of many decades of observations made at visible wavelengths, but it is only recently that near (NIR) and mid-infrared (MIR) space-based observatories have revealed the richer spectral information contained in the dust component. This component is dominated by broadband thermal emission from dust grains, but emission associated with polycyclic aromatic hydrocarbons (PAHs) has also been found to be important in the NIR and MIR (Desert et al., 1990). Sensitive spectroscopic and broadband observations from the *Spitzer Space Telescope* (Werner et al., 2004) and *Infrared Space Observatory* (Kessler et al., 1996) of both the PAH emission and the warm thermal component, combined with laboratory measurements of the physical properties of interstellar dust provide a general understanding of dust in the context of galactic properties (see for example Draine et al. 2007) and can provide unique clues to our understanding of prominent dust processes such as metal enrichment and embedded star formation.

Generally, near-IR light traces stellar mass and as discussed in the previous chapter of this thesis, IRAC observations have proved essential for stellar mass measurements beyond $z \sim 1$ where the K-band rest-frame light is redshifted into the IRAC channels. However, a new result that has emerged recently is the discovery of an excess in the NIR continuum of galaxies at 2-5 μm, (Lu et al., 2003; Helou et al., 2004; Magnelli et al., 2008). This excess cannot be attributed solely to narrow emission from the 3.3 μm PAH feature and is instead due to a combination of line emission and an additional thermal

component. The emission can be significant at wavelengths around 3μm, but it is not a major contributor to a galaxy's total bolometric flux. For example, in a survey of 45 star-forming galaxies Lu et al. (2003) measure a weak excess component of continuum emission in the range of 2-5 μm that is characterized by a very high colour temperature ($\sim$ 1000 K), but is only a few percent of the far-infrared (FIR; 8-1000 μm) luminosity attributed to larger dust grains. The origin and physical mechanism of the NIR excess in galaxies is not known, although Lu et al. (2003) suggest it likely originates in the ISM.

An NIR excess continuum has also been seen locally in a range of objects. Reflection nebulae (RNae) around massive O and B-type stars have a smooth continuum feature from 1.25 to 4.8 μm that is characterized by a blackbody with a $\sim$ 1000 K temperature in addition to a narrow emission feature at 3.3 μm (Sellgren et al., 1983, 1996), attributed to the thermal emission of very small ($\sim$ 10 Å) grains (Sellgren, 1984). $JHKL$ photometry of massive stars in the $\sim 1-3$ Myr old star-forming regions NGC 3576 (Maercker et al., 2006), G305.2+0.2 (Longmore et al., 2007), and 30 Dor in the LMC (Maercker & Burton, 2005) show L-band (3.5 μm) excesses in more than half of their stars with masses $>$ 10 $M_{\odot}$ that is attributed to circumstellar disks (Lada & Adams, 1992). Excess continuum emission can also come from more diffuse sources. Observations by *Spitzer's* Infrared Array Camera (IRAC; Fazio et al. 2004) and the *Cosmic Background Explorer*/Diffuse Infrared Background Explorer *COBE*/DIRBE of the galactic cirrus (Flagey et al., 2006) reveal a continuum component in the NIR whose contribution to the IRAC [3.6 μm]-band is $50\% - 80\%$, while the PAH feature at 3.3 μm contributes the remaining flux.

The ultimate cause of $\sim$ 1000 K blackbody emission in the empirical data described above is still unknown. Large dust grains are fragile at such high temperatures, and are unlikely to be the source of the excess emission. In the canonical interstellar dust model of Desert et al. (1990), PAH molecules, unlike dust grains, can exhibit both line emission at 3.3 μm and broad continuum emission at 2-5 μm, and lead to significant NIR emission. Large PAH molecules (>1 nm) display strong broadband NIR emission and are more resilient to strong ionizing fields, while smaller PAH molecules display a larger line-to-continuum emission ratio in the NIR. This would naturally lead to broad NIR continuum emission of molecules in the vicinity of massive stars, likely contained in circumstellar disks, a mechanism for the NIR excess in galaxies not previously explored. Theoretically for local young stellar objects (YSOs), Dullemond et al. (2001) show that the puffed up inner edges of circumstellar disks can radiate at high temperatures and lead to L-band excess luminosities in the NIR of more than 1000 $L_{\odot}$ in the most massive

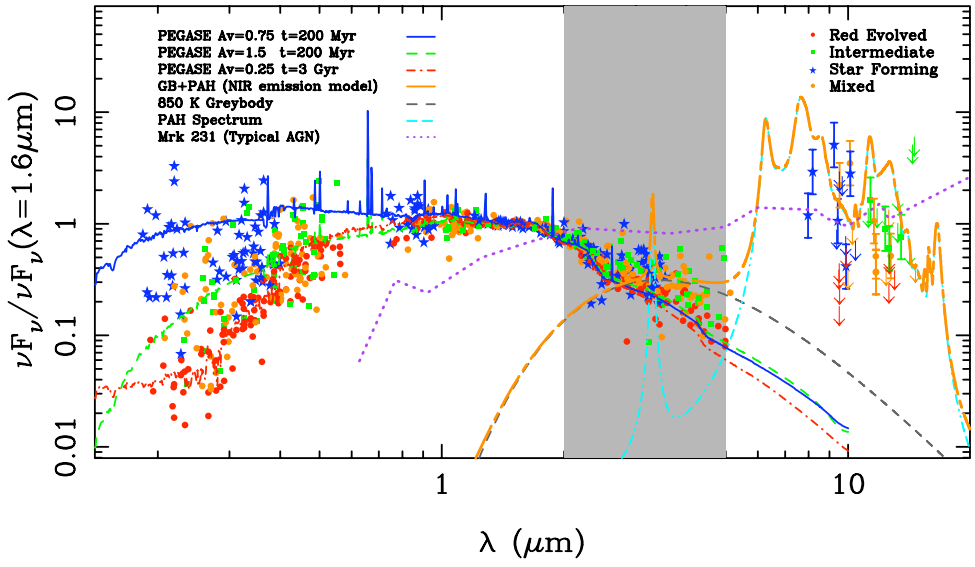

Figure 3.1 VIzK$_s$+IRAC and MIPS photometry from the GDDS normalized at $\lambda = 1.6\,\mu$m with the 2-5 μm region of NIR excess highlighted in grey. Plot symbols are keyed to galaxy spectral type, as shown in the legend and described in the text (Section 3.3.1). The blue solid curve is a stellar component model from PEGASE.2 (Fioc & Rocca-Volmerange, 1997) for a typical star-forming galaxy (t=200 Myr, A$_v$=0.75). A dusty star-forming galaxy (t=200 Myr, A$_v$=1.5) and evolved galaxy (t=3 Gyr; A$_v$=0.25) are also plotted. The orange dash-long-dashed line represents the NIR emission component model (GB+PAH) from da Cunha et al. (2008) that is supplemented in our SED modeling. An 850 K greybody emitter (grey dashed line) contributes most of the emission of this component at 2-5 μm, although the 3.3 μm PAH feature (the cyan dot-dashed curve) has some contribution ($< 20\,\%$ in a given IRAC band). For reference, an SED of an AGN (Mrk 231; purple dotted curve) is plotted. For pedagogical purposes, the GB+PAH and AGN curves have been normalized to the average MIPS flux of our sample. For those objects with MIPS detections, the AGN model is not a good representation of the photometry.

stars. In agreement with the circumstellar disk interpretation of the excess, observations presented in Arendt et al. (1994) with the *COBE*/DIRBE show that NIR continuum emission of nearby star-forming regions correlate well with bright mid-IR observations and that the dust must lie very close to the stars, as it was unresolved by the DIRBE beam. More recently, resolved excess NIR continuum emission is observed in young stars that possess circumstellar disks (see Figure 3 in Wood et al. 2008).

Whatever the cause of the emission, we will show in this chapter that it is apparently fairly easy to detect such excess emission at high redshifts, at least in an optically selected sample like the Gemini Deep Deep Survey (GDDS; Abraham et al. 2004). At first glance this seems rather surprising, since (as we have already noted) the excess emission corresponds to only a tiny fraction of a typical galaxy's bolometric flux. However, as demonstrated in Figure 3.1, the peak wavelength of a blackbody radiator emitting at $\sim 1000\,\mathrm{K}$ (grey dashed curve) falls near the global minimum in a typical galaxy's SED when modeled as a two-component system of starlight + IR emission. Therefore the contrast of even a small amount of ~ 1000 K emission seen at 2-5 μm can be significant, giving us an opportunity to probe a new component of a galaxy's flux that is ordinarily overwhelmed by either starlight or re-radiated emission from large dust grains. This new component is interesting on its own and also may be useful for calibration of the SFR. Studies of the NIR component in ultra-luminous infrared galaxies (ULIRGS; Mouri et al. 1990; Imanishi et al. 2006; Magnelli et al. 2008) suggest that the 3.3 μm emission can be used as a good indicator of the SFR in some galaxies, although further calibration and study of star-forming galaxies is needed to justify this as a useful diagnostic and is the central goal of chapter 4 of this thesis.

In this chapter, we quantify the NIR excess continuum in a spectroscopic sample of high redshift galaxies, described in Section 3.3 by performing linear least-squares fits of broadband visible+IRAC photometry to SED models. We compare two sets of SED models, the first consisting of a stellar component SED only and the second, a two component SED model consisting of both a stellar component and an additional NIR dust emission component consisting of an 850 K greybody plus PAH emission template (da Cunha et al., 2008) as described in Section 3.4. The case for an NIR excess continuum in GDDS galaxies is made through IRAC colour-colour diagrams and SED example fits in Section 3.5. We show that the luminosity of the NIR emission component is correlated with a galaxy's star-formation rate in Section 3.5.6. In Section 3.6 we speculate on the origin and potential significance of the excess, and show that the most likely candidate

is a population of heated circumstellar disks in the high redshift galaxies.

Throughout this chapter, we adopt a concordance cosmology with H_0=70 km s^{-1} Mpc^{-1}, $\Omega_M = 0.3$, and $\Omega_\Lambda = 0.7$. All photometric magnitudes are given in AB magnitudes, unless otherwise noted.

3.3 Observations

3.3.1 Summary of GDDS observations

The Gemini Deep Deep Survey (hereafter GDDS; Abraham et al. 2004) is a spectroscopically defined colour selected subset of the 1 deg^2 Las Campanas Infrared Survey (LCIRS; McCarthy et al. 2001). It consists of four $5'.5 \times 5'.5$ fields chosen from the parent sample to minimize cosmic variance. The sample consists of galaxies with $K_{s,VEGA} < 20.6$ mag and $I_{VEGA} < 24.5$ mag ($K_{s,AB} < 22.4$ mag and $I_{AB} < 24.9$ mag) in the redshift interval $0.5 < z < 2.0$. The GDDS multi-band coverage includes $UVBRIz'JHK_s$ broadband colours in addition to high-resolution Advanced Camera for Surveys (ACS) coverage of $\sim 60\%$ of the fields. For this analysis, we only select objects with high-confidence spectroscopic redshifts and those which are confidently detected in the longest IRAC channel (we required $\Delta[8.0\,\mu\mathrm{m}] < 0.3\,\mathrm{mag}$). This results in 103 galaxies from the 309 objects in the original GDDS sample.

All objects were given a spectral type classification as outlined in Table 5 of Abraham et al. (2004) and listed in Table 2.1. The classification is based on three digits that refer to young, intermediate-age, and old stellar populations. Objects showing nearly pure signatures of an evolved stellar population were assigned a GDDS class of "001" in Abraham et al. (2004). In Figure 3.1 and many figures in this chapter, we key each galaxy to their galactic spectral type. The evolved "001" galaxies are plotted as red circles. Objects showing a strong-UV continuum dominated by massive stars were classified as "100" and are plotted as blue stars. Objects with intermediate ages (e.g., strong Balmer absorption) were classified as "010" and are plotted as green squares. Some objects consist of both an evolved population plus a younger more recent star formation component. These objects are listed as mixed populations with spectral types of "110" or "101" in and are plotted as orange dots in our figures.

3.3.2 *Spitzer* IRAC photometry

Near-infrared observations are important for determining stellar masses through SED fitting, particularly at high redshift where the light from evolved stellar populations, which trace the stellar mass of a galaxy, is redshifted out of the visible. In order to determine stellar masses of GDDS galaxies, a total of 10.9 hours of *Spitzer* IRAC observations were obtained for three of the four GDDS fields (Program ID: 3554; McCarthy et al. 2004) yielding 5σ depths of 0.45, 0.9, 6 and 8 μJy in respective IRAC bands. The final field, GDDS-SA22, was observed through an existing GTO-reserved program (Program ID: 30328; Fazio et al. 2006). Mosaics were created from the archived Basic Calibration Data (BCD) images using MOPEX (Final Version 18.2), a more current and improved post-BCD mosaicing tool of the *Spitzer* Science Center to achieve better background removal and a spatial resolution of $0.6''$/pixel. The first three short-exposure BCD images were thrown away to correct for the IRAC "first-frame effect". The background was corrected, for each remaining BCD image, by subtracting the peak of a count histogram of the entire image. The resulting [5.8 μm] and [8.0 μm] images displayed noticeable gradients and in addition had to be gradient-corrected. This gradient correction was not performed in the deeper GDDS-SA22 field. The resulting BCD images were background corrected to an AB magnitude zeropoint of 21.85 and drizzle-combined to create the final post-BCD mosaics.

Objects in the post-BCD IRAC mosaics were detected by running SExtractor in dual-image mode, where a weighted-sum of [3.6 μm] and [4.5 μm] images were used as the detection image. A Mexhat filter was used instead of a Gaussian filter to better deblend and detect objects in these relatively low resolution, but deep, images. Magnitudes were then measured in each IRAC band in $4''$ diameter apertures. To extrapolate the total flux of the galaxy, aperture corrections of 0.317, 0.360, 0.545 and 0.677 mags were added to the [3.6 μm], [4.5 μm], [5.8 μm], [8.0 μm] magnitudes, respectively.

Source blending from objects on the edge of our $4''$ apertures could potentially add a flux excess. We went through our sample of 103 galaxies by eye (inspecting both our ground-based I-band and *HST* ACS [814W] images) and flagged any object that has a neighbour within a $7''$ aperture. We found 15 such objects in total and will show in Section 4 that these objects are relatively poorly fit by our SED models as a result of the photometric confusion, so we opt to exclude them from most analyses. Thus our final sample is comprised of 88 spectroscopically confirmed galaxies. This sample covers

the full GDDS redshift range of $0.5 < z < 2$, with objects ranging from $z_{\rm spec} = 0.57$ to $z_{\rm spec} = 1.97$ (32 objects from $0.5 < z < 1$, 41 objects from $1 < z < 1.5$, and 14 objects from $1.5 < z < 2$).

3.3.3 *Spitzer* 24 μm MIPS photometry

For one of our fields, GDDS-SA22, a 1320 s exposure was observed with *Spitzer's* Multiband Imaging Photometer for *Spitzer* (MIPS; Rieke et al. 2004) under a GTO reserved program (Program ID: 30328; Fazio et al. 2006). Our 24 μm MIPS imaging was reduced using a combination of the *Spitzer* Science Center's MOPEX post-processing suite and a set of custom routines developed to better remove background and artifacts. The source finding and photometry/extraction pipeline (D.V. O'Donnell et al. 2010, in preparation) employed PPP (Yee, 1991), DAOPHOT (Stetson, 1987) and additional routines for calibration. A Monte Carlo technique in which the theoretical MIPS point-spread function (PSF) was scaled, inserted into the science images and retrieved by the photometry pipeline was used to determine an aperture correction for all sources on the order of $\sim 17\%$ of the source's measured band flux.

Because a number of our objects had poor MIPS correlations, we inspected each source by eye to confirm whether they were in fact counterparts. Source confusion is a problem in some of our objects which we later flag in our analysis (Section 3.5.1). To any objects non-detected we assigned an upper limit of 70 μJy, our 1 σ detection limit computed from Monte Carlo completeness tests.

MIPS fluxes are available for 40/88 galaxies in our selected sample. The IRAC-MIPS 24 μm colour-colour plot, presented in Figure 3.2, shows the majority of objects in the GDDS-SA22 field lie in the region of starburst galaxies, left of the dashed line, as defined by Pope et al. (2008a), with a general trend of the star-forming and mixed population galaxies showing stronger S_{24}/S_8 ratios than the evolved galaxies. Non-detections (25/40) are plotted as upper limits. None of our objects have $S_{8.0}/S_{4.5} > 2$, an indication of a significant AGN component (Ivison et al., 2004; Pope et al., 2008a). We are thus confident that our optically and mass-selected sample does not have a large contamination of strong AGN. Due to selection biases between our sample and other high-z AGN samples, we cannot completely rule out contamination due to lower luminosity AGN (see later discussion in Section 3.6.1).

For comparison with other high-z galaxy samples, we also show in Figure 3.2 the

locations in the IRAC-MIPS colour-colour plane of a sample of 24 μm-selected ULIRGS at $z \sim 1-3$ (Sajina et al., 2007) and a sample of faint 24 μm-selected $z \sim 2$ dust obscured galaxies (DOGs; Pope et al. 2008b). Pope et al. (2008a) use X-ray, far-IR, sub-mm and radio observations to determine whether the DOGs have strong AGN or starburst components which we plot as separate symbols in Figure 3.2. No GDDS galaxy shows similar IRAC-MIPS colours as the class of AGN-dominated galaxies. For reference, evolutionary tracks for a typical AGN (Mrk 231) and starburst (M82) (taken from Pope et al. 2008b) are shown. It is evident that the GDDS mass-selected sample probes the less active parameter space of high-z galaxies (i.e., lower SFRs, smaller contributions from the AGN).

3.4 Spectral energy distribution fitting

We aim to understand the NIR excess by incorporating emission from dust as an additional component in each galaxy's SED. Each galaxy's stellar component is modeled using the techniques of population synthesis. In contrast to the well-worn techniques of stellar population synthesis, our modeling of dust is rather simplistic. However, we will show that even relatively crude dust models can provide interesting constraints. As astronomical facilities which explore faint galaxy populations continue to probe further into the IR (e.g., *JWST, ALMA*) it will become increasingly important to embrace dust as an essential component when modeling galaxy SEDs. Our analysis might therefore be viewed as an early attempt to move in this general direction.

3.4.1 Stellar component

To model the stellar SED component, a library of SEDs is generated consisting of a range of two component star formation histories (SFHs). We generate two sets of SED libraries, one from PEGASE.2 software (Fioc & Rocca-Volmerange, 1997) and one from Maraston (2005) (hereafter M05), whose treatment of thermally pulsing asymptotic giant branch (TP-AGB) stars is scaled to match photometry of globular clusters in the NIR. Both sets consist of a primary SFH component consisting of a monotonically evolving stellar population with a SFR $\propto \exp(-t/\tau)$, $\tau\epsilon\,[0.1, 500]$ Gyr for PEGASE.2 models and $\tau\epsilon\,[0.1, 20]$ Gyr for M05 models. The first approximates an instantaneous starburst and the last a constant SFR. A secondary SFH component models a starburst event, with

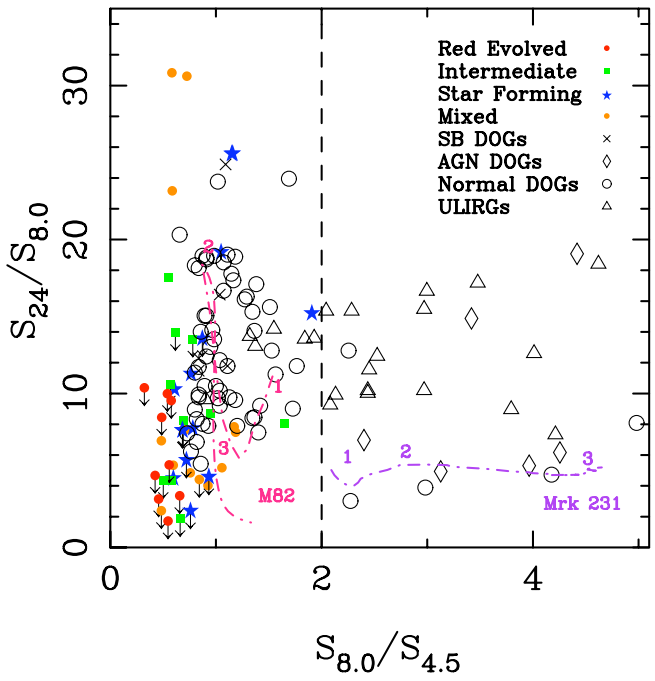

Figure 3.2 IRAC-MIPS 24 μm colour-colour plot for objects (classified by galactic spectral types as defined in Section 3.3.1) in the GDDS-SA22 field. Non-detected MIPS objects are plotted as upper limits. Evolutionary tracks for a typical AGN (Mrk 231) and starburst (M82) (taken from Pope et al. 2008b) are shown for z=1,2,3,4. Objects on the left of the dashed line are classified as starburst dominated, and those on the right of the dashed line are AGN dominated (Pope et al., 2008a). ULIRGS from Sajina et al. (2007) are plotted as open triangles, AGN-dominated, starburst-dominated and normal dust obscured galaxies (DOGs) at $z \sim 2$ as classified in Pope et al. (2008a) are plotted as open diamonds, crosses, and open circles, respectively.

a $\tau = 0.1$ Gyr exponential. In the PEGASE.2 models, this secondary component can occur at any time between z_{form} and z_{obs}, while in the M05 models it is fixed to 50 Myr before z_{obs} since the SFH is not a user input parameter in the M05 models, as it is in the PEGASE.2 models. We note here that fixing this parameter does not affect the relevant parameters (A_v, $M_\star$) derived from the SED fits. The strength of the second burst component can have a mass between 10^{-4} and 2 times the initial component. The two component stellar model allows for a more robust determination of stellar masses by correctly modeling the light from evolved populations and that from a recent star-forming episode. We opt to use the initial mass function (IMF) from Kroupa (2001).

Extinction is added to the spectra ourselves in eleven reddening bins covering $0 \leq A_{\rm V} \leq 2$ mag. We assume that nebular extinction is twice the stellar continuum and use the Small Magellanic Cloud (SMC) reddening law of Pei (1992) which provides a numerical fit to the extinction in the SMC. For the PEGASE.2 models, evolution of the stellar population assumes constant metallicity, and does not include effects due to galactic winds, infall or substellar objects. The PEGASE.2 models vary in five possible metallicity values from $0.0004 \leq Z \leq 0.02$, while the M05 models are fixed to solar metallicity.

We refer the reader to Figure 3.1 for examples of the SED model components plotted with the normalized (at $\lambda = 1.6\,\mu$m) rest-frame fluxes of our data set. The observed NIR excess region is highlighted in grey. Two examples of a young (t=200 Myr), star-forming galaxy are shown with different extinction values as the blue solid ($A_{\rm v} = 0.75$) and green dashed ($A_{\rm v} = 1.5$) curves. An evolved stellar population (t=3 Gyr; $A_{\rm v} = 0.25$) is plotted as the red dot-dashed curve. These *illustrative* SEDs, computed with PEGASE.2, are for a galaxy with an exponentially declining SFR of τ=500 Myr and $Z = Z_\odot$.

3.4.2 Additional dust component

Broadband multi-wavelength (UV, visible, and IR) empirical SED modeling performed by da Cunha et al. (2008) of galaxies from the *Spitzer* Infrared Nearby Galaxies Survey (SINGS; Kennicutt et al. 2003; Dale et al. 2005) show that emission in the NIR, from 2-5 μm, can be modeled by an additional SED component described by a PAH template spectrum superposed on an 850 K greybody modified by λ^{-1} extinction (hereafter written as GB+PAH to identify this as a single parameter SED component). The PAH template is scaled to match the NIR continuum excess (e.g., the greybody) seen in star-forming

galaxies in Lu et al. (2003) & Dale et al. (2005) and is shown to also match the relative, but not absolute, intensities of the galactic cirrus (see Figure 1 of da Cunha et al. 2008). For reference we plot the GB+PAH component as the orange dash-long-dashed line in Figure 3.1. As well, we show the separate components that comprise this model: an 850 K greybody (dark grey dashed line), and a PAH template spectrum (cyan dot-dashed line).

To investigate whether a PAH feature at 3.3 μm plus greybody component can explain the IRAC excess in our sample of star-forming galaxies we superpose our model SED with an additional component following the results of da Cunha et al. (2008) and fit an 850 K greybody modified by λ^{-1} dust extinction and add the 3.3 μm PAH emission feature using the Lorentzian profile parametrized by Verstraete et al. (2001) as $F_\nu^{\rm Lorentz} = f_{\rm o}[1+(x-x_{\rm o})^2/\sigma^2]^{-1}$, where $x = 1/\lambda$ is the wavenumber, $x_{\rm o} = 3039.1\,{\rm cm}^{-1}$ is the central wavelength of the feature and $\sigma = 19.4\,{\rm cm}^{-1}$ is its FWHM.

The 3.3 μm PAH feature is scaled to match 2.27 times the continuum emission of the greybody at 4 μm. da Cunha et al. (2008) match the amplitude of the 3.3 μm feature to 0.1 times the amplitude of the 11.3 μm PAH feature, the relative ratio found by Li & Draine (2001). They then approximate the amplitude of the greybody at 4 μm to be 0.11 times the peak amplitude of the 7.7 μm PAH feature as found in Lu et al. (2003). However, because of our spectral coverage, there is no need to account for PAH features at longer wavelengths than 4 μm. Instead we use the results of Chan et al. (2001) to relate the the ratio of the longer PAH features as $F^{\rm peak}_{\lambda=11.3\,\mu m}/F^{\rm peak}_{\lambda=7.7\,\mu m} = 0.4$. Thus relating the 3.3 μm PAH feature as 2.27 times the flux of the continuum emission at 4 μm. The contribution of the PAH line to the total PAH+greybody component in an IRAC band is at most 20%.

3.4.3 Methods

First we fit visible $VIz'K_s$ [3.6 μm] [4.5 μm] photometry to the stellar component models (both PEGASE.2 and M05). [1] We then fit all visible $VIz'K_s$ + IRAC [3.6 μm] [4.5 μm] [5.8 μm] [8.0 μm] photometry to the second model set consisting of the same library of stellar component SEDs with the additional GB+PAH component just described in Section 3.4.2 fit as a sum of linear least-squares. The normalization of this component is

[1] To justify that the longer IRAC bands are inadequately modeled by stellar component only models, we also fit all the $VIz'K_s$ [3.6 μm] [4.5 μm] [5.8 μm] [8.0 μm] photometry. This also allows us to compare the quality of fits (see 3.5.3) between the single stellar component model and the two component stellar plus NIR emission model.

thus an additional free parameter.

A grid of apparent AB magnitudes is generated by redshifting each rest-frame model to the galaxy's spectroscopic redshift and convolving this spectrum with the transmission curves for all observed filters: $VIz'K_s$ and *Spitzer* IRAC [3.6 μm], [4.5 μm], [5.8 μm], [8.0 μm]. The χ^2 for each model is calculated in flux space with the normalization of each component as a fitted parameter. We restrict the age of the model to be less than the age of the Universe at the observed redshift. To estimate errors in the fitted parameters, we consider 20 Monte-Carlo realizations of the data through a random Poisson distribution of the count rate, thus simulating the detector shot noise.

3.5 Results

3.5.1 SED fitting: the stellar component model

Figure 3.3 shows the observed-to-model flux ratios and residuals of the broadband visible+IRAC photometry fit to the two sets of models as described in Section 3.4; one consisting of a stellar component only and the other consisting of two components, a stellar and an 850 K GB+PAH SED component. Here, stellar models from M05 are shown, but the results are consistent with residuals from fits to the PEGASE.2 models. The wavelength has been blue-shifted to the rest-frame wavelength for comparison. The top panel shows the fit of the stellar component to the visible $VIzK_s$+IRAC [3.6 μm] [4.5 μm] photometry. *Spitzer* IRAC [5.8 μm] and [8.0 μm] band fluxes are also compared to the model band fluxes, although they were not used to find the best-fit SEDs. We separate the data points into their galaxy spectral types as described in Section 3.3.1. For the V-[4.5 μm] bands, the residuals are on average 0.08σ with a scatter of 2.34σ, while the residuals for the [5.8 μm] and [8.0 μm] bands have a significant offset of 3.99σ and a scatter of 4.53σ. Thus the stellar component models do a good job estimating the light blueward of 2μm where the flux is driven by the evolved population, and as a consequence galaxy stellar mass. However, redward of 2 μm, there is a significant excess in the majority of GDDS galaxies seen in the rest-frame range of 2-5 μm.

We flag points in this figure (using thin circles) to identify galaxies that are possibly contaminated by light from nearby galaxies due to blending of the IRAC PSF (see Section 3.3.2). On the whole, these systems are poorly fit by the models, and will drop them from subsequent figures and analyses, although including them changes none of our

conclusions.

A single or two-component SFH stellar population model alone is not sufficient to describe the flux generated in the NIR beyond rest-frame 2 μm. The amount of NIR excess is dependent on the galaxy spectral type as we see strong excesses of $F_{obs}/F_{model} = 3.3 \pm 2.5$ in the star-forming galaxies (blue stars), and $F_{obs}/F_{model} = 3.2 \pm 2.0$ in the mixed and intermediate populations (green squares and orange dots) and a smaller, but still noticeable excess of $F_{obs}/F_{model} = 1.5 \pm 0.6$ in galaxies dominated by an evolved stellar population (red circles). The NIR excess covers a broad spectral range indicating that a single narrow emission line such as the 3.3 μm PAH emission line is not sufficient to explain all of the excess.

3.5.2 SED fitting: additional dust component

The second set of models consists of two components: one, a stellar SED component and the other, an NIR emission component consisting of 850 K greybody emission plus a PAH spectrum (GB+PAH) that is scaled with the 850 K greybody to match NIR observations of star-forming galaxies and the galactic cirrus (da Cunha et al., 2008). The resulting ratio and residuals between observed and model band fluxes are plotted in the bottom panel of Figure 3.3 with wavelength blue-shifted to the rest-frame. The additional component matches the IRAC photometry, particularly the [5.8 μm] and [8.0 μm] bands, remarkably well. For the V-[4.5 μm] bands, the residuals are similar to the fits with just a stellar component model with a negligible offset of 0.07σ and a scatter of 2.24σ, while the residuals for the [5.8 μm] and [8.0 μm] bands no longer have a significant offset with an average value of 0.25σ and a much smaller scatter of 1.58σ.

Examples of fitting the two component SED to the visible+IRAC photometry are presented in figures 3.4 and 3.5. The black solid line represents the sum of the stellar (dashed green line) and the additional GB+PAH component (blue dotted line). We plot 10″ postage stamps from *HST* ACS images of the galaxy to show morphology of each galaxy. There is no strong correlation between the amount of NIR excess and galaxy morphology, both qualitatively or quantitatively according to the asymmetry or Gini coefficient morphological quantities as measured for the GDDS sample in Abraham et al. (2007). We also plot images from IRAC [3.6 μm] and [8.0 μm], and show the 4″ apertures used for our photometry.

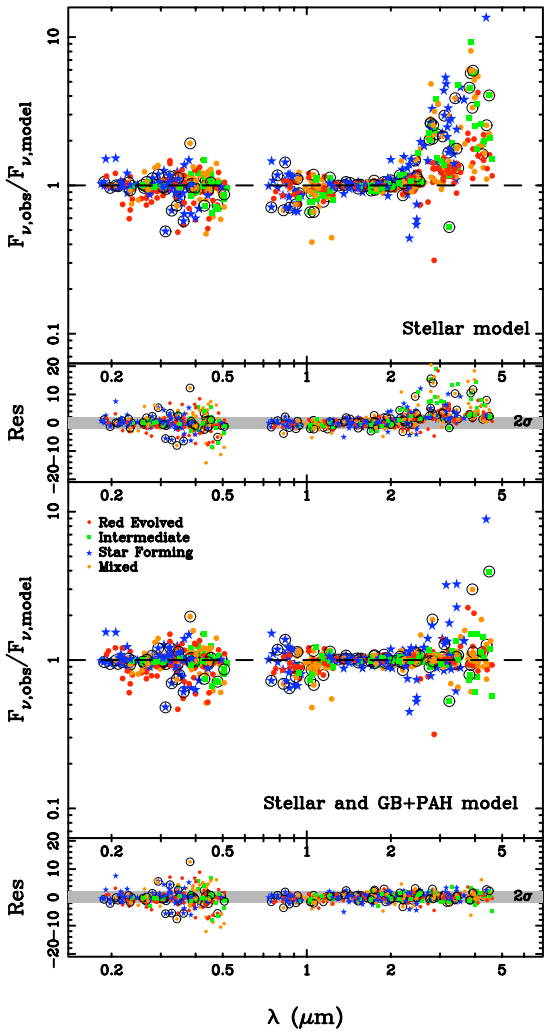

Figure 3.3 Ratios of the observed band fluxes to the best-fitting SED band fluxes for each galaxy in the sample, each blueshifted to the rest-frame wavelength. The residual between observed and model band fluxes are given as $(F_{obs} - F_{model})/\sigma$ under each panel. In both plots, we flag objects with possible contamination in the IRAC channels due to source confusion as thin open circles. *Top*: the visible (VIz'K) and *Spitzer*/IRAC [3.6 μm] and [4.0 μm] bands are fit to a stellar only SED model. *Bottom*: an additional GB+PAH component is added to the SED model as described in Section 3.4 and SEDs are fit again using all VIz'K+IRAC bands (with reasonable detections). The two component SED model fits the data much better, except for the objects with known contamination from source blending in the IRAC channels (thin open circles, Section 3.3.3). We exclude these objects in all subsequent analyses and plots.

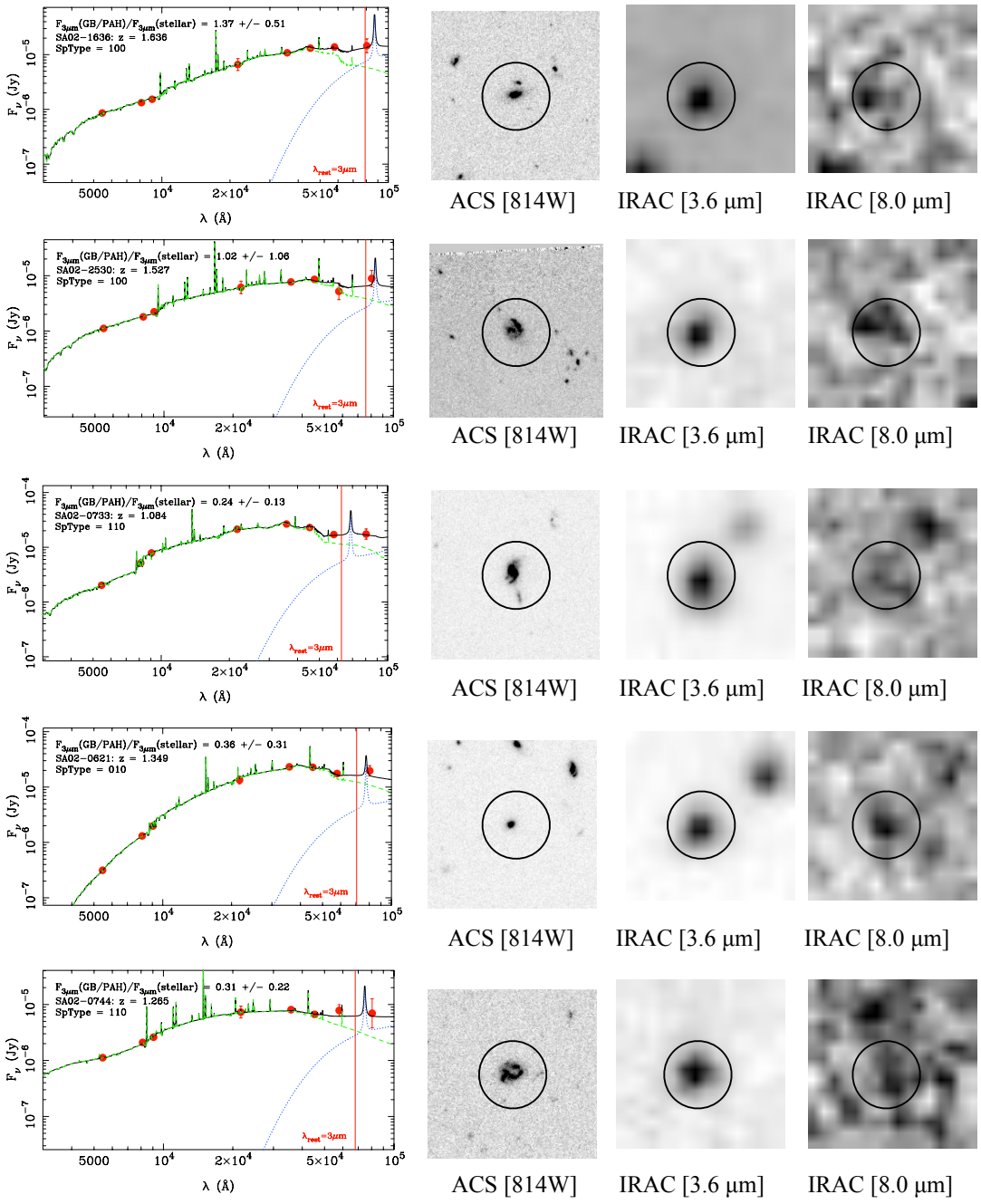

Figure 3.4 SED fit examples for objects (band fluxes shown as red dots) with SFRs $> 1\,M_{\odot}$/yr. The SED (solid black line) is composed of both a stellar component (green dashed) and an NIR emission component consisting a 850 K greybody emission and a PAH spectrum (blue dotted line). 10″postage stamps from *Hubble's* ACS [814W], IRAC [3.6 μm] and [8.0 μm] are shown for each object. The spectral type (see Section 3.3.1) of the galaxy is given in the top left corner showing the excess is seen in star-forming, intermediate, and mixed population galaxies. For reference, $\lambda_{\rm rest} = 3\,\mu$m is plotted as a red vertical line. The black circles show the 4″ apertures used to derive our photometry.

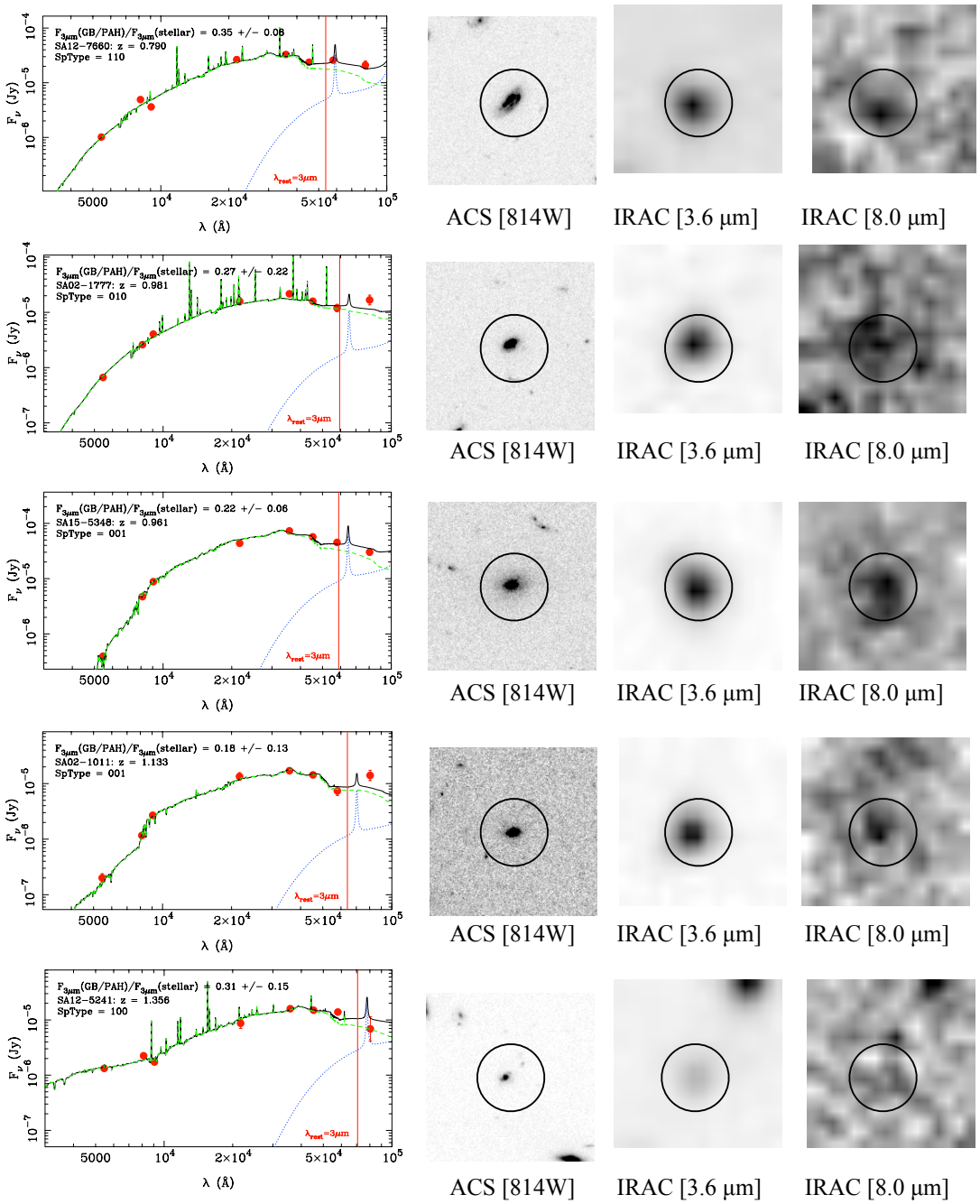

Figure 3.5 As in Figure 3.4, but for objects (band fluxes shown as red dots) with SFRs $< 1\,M_{\odot}/\mathrm{yr}$.

3.5.3 Quality of fits

Comparing the top and bottom panels of Figure 3.3, we see that the addition of a GB+PAH component greatly improves the fits qualitatively. The SED fitting routine minimizes χ^2 but we emphasize that the interpretation of the absolute value of the minimum $\chi^2_{\rm reduced}$ returned requires some careful consideration, since the number of fitted parameters exceeds the number of data points. This is a very common occurrence in broadband photometry SED fitting (e.g., Glazebrook et al. 2004), the consequence of which is that output model parameters are expected to be strongly correlated, and interpretation of statistical significance is mainly based on Monte Carlo simulations. We calculate errors and assess the statistical significance of fit improvements by refitting the photometry to randomized versions of the single best-fit SED model.

We compare $\chi^2_{\rm reduced}$ values from least-square fits with both sets of models. We fit the stellar component model two times, once with the inclusion of the two longer IRAC channels, and once with the [5.8 μm] and [8.0 μm] bands excluded. We then fit the visible and all IRAC channels to the two component model. The lowest quality SED fits are when all IRAC channels are fit to a stellar component SED model (median $\chi^2_{\rm reduced} = 2.69$). The highest quality fits are to the two component model (median $\chi^2_{\rm reduced} = 1.73$), which are just slightly better than the fits to the stellar model excluding the two longer IRAC channels (median $\chi^2_{\rm reduced} = 1.96$). The additional component improves the ensemble quality of fit by $\sim 50\%$, which our Monte Carlo simulations indicate is far above the nominal improvement expected from additional free parameters when fitting to an underlying SED with no excess flux. Thus, an SED modeled by both a stellar component and a near-infrared emission dust component represented by a 850 K GB+PAH emission spectrum is a significantly better model of a galaxy's near-infrared light than one based on stellar emission alone.

3.5.4 Greybody temperatures and other limitations of the dust model

The choice of NIR emission model is based on observations compiled by da Cunha et al. (2008). Our observations do not constrain any of the parameters in the model, such as the relative scaling between the NIR continuum and PAH emission or the temperature of the continuum emission. Due to our limited spectral coverage, we only allow its normalization to be a free parameter. Other greybody temperatures were explored and we find that the

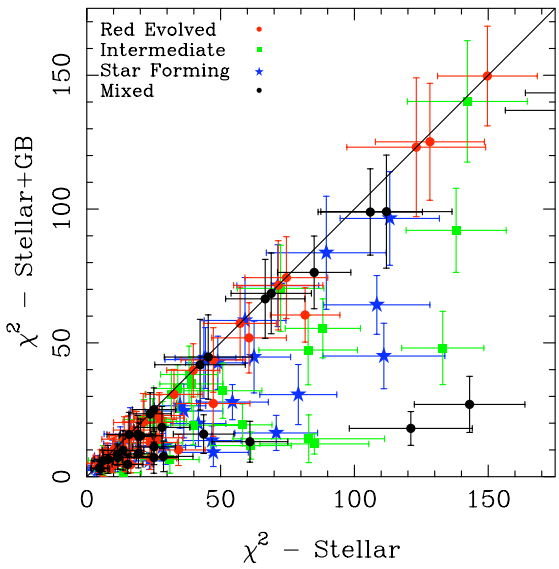

Figure 3.6 χ^2 comparison between fits of the IRAC photometry to the stellar component model to those with the stellar plus NIR emission model. Errors are determined from 100 Monte Carlo realizations of the photometry fit to the best-fit model in each scenario as described in §3.5.3. Galaxies are indicated by spectral types as star-forming (blue), evolved (red), intermediate (green) and mixed (black). In general, star-forming and intermediate population galaxies show improvements in their fit with the additional component.

continuum excess is equally fit (yielding consistent χ^2 values) by greybody temperatures ranging from 700 to 1500 K. As a comparison, Flagey et al. (2006) find that a 1100 ± 300 K works well for the galactic diffuse medium, while Lu et al. (2003) show that both a 750 K and a 1000 K greybody with λ^{-2} emissivity can match the IRAC photometry. A different extinction law (λ^{-2}) was also explored but provided no improvement in the quality of fit.

We attempted to add the temperature of the greybody as an additional parameter but found it was not possible to constrain the blackbody temperature at lower temperatures once the spectral peak of the greybody shifted outside the range of our observed photometry (for reference, an 850 K blackbody peaks at about 3.4 μm, which our IRAC observations straddle throughout $0.5 < z < 2$). Finally, fits to a model consisting solely of the 3.3 μm PAH emission feature do not succeed, showing only modest improvements to $\chi^2_{\rm reduced}$ and unrealistically high equivalent widths, as the broad wings of the line are forced to fit the broad continuum excess. The ratio of the PAH line emission to continuum emission could not be constrained by our broadband observations, but follow up with NIR spectroscopy may prove fruitful in constraining neutral to ionized PAH fractions and PAH size distributions (e.g., Desert et al. 1990; Draine et al. 2007).

3.5.5 Model consistency with MIPS photometry

Almost half (40/88) of our subset of GDDS objects with spectroscopic redshifts are found in the GDDS-SA22 field, for which archival MIPS data are available. Since MIPS data were not incorporated into any of our fits, any post-facto agreement between the MIPS observations and our model strongly supports the central idea of the NIR excess continuum being scaled to the MIR PAH spectrum. The MIPS band probes rest-frame 8-12 μm for our $z = 0.7 - 2$ galaxy sample, where PAH features are known to exist. Thus we visually compare the MIPS band fluxes with the GB+PAH SED component (orange dash-long-dashed line in Figure 3.1), using the normalization of this component derived from our two component spectral fitting. All non-detected (25/40) objects in the GDDS-SA22 field are consistent with the predicted 24 μm fluxes (< 70 μJy) from the GB+PAH component. Only 15 out of the 40 objects are detected at 24 μm with MIPS. Eleven of these 15 MIPS-detected objects show 24 μm fluxes consistent with the best-fit SED model predictions. To illustrate the degree of concordance, in Figure 3.7 we show typical fits for a range of galaxy spectral types. The figure shows NIR excesses for 3 of the 11 objects with confident 24 μm detections, as well as an example showing

a typically informative non-detection (last row in the figure). Only four galaxies do not have 24 μm fluxes consistent with the model SEDs, and three of these show obvious source blending in the *HST* ACS images as a result of the larger MIPS PSF.

Therefore only a single galaxy (SA22-2548; plotted in the 4th row of Figure 3.7) is not consistent with the stellar and GB+PAH two component model for that object (computed entirely independently of MIPS)[2]. We conclude that an additional GB+PAH model is consistent with the measured 24 μm MIPS fluxes for 97.5% of the GDDS objects observed in the only GDDS field with MIPS data.

[2]SA22-2548 is unusual in other ways: it has strong 24 μm flux slightly offset from the optical GDDS counterpart, and the ACS image shows some indication of interaction, so its 24 μm excess may be the result of a strong AGN due to merging (although its IRAC colours ([3.6 μm] - [4.5 μm] = -0.216; [5.8 μm]-[8.0 μm] = -0.426) do not seem consistent with this).

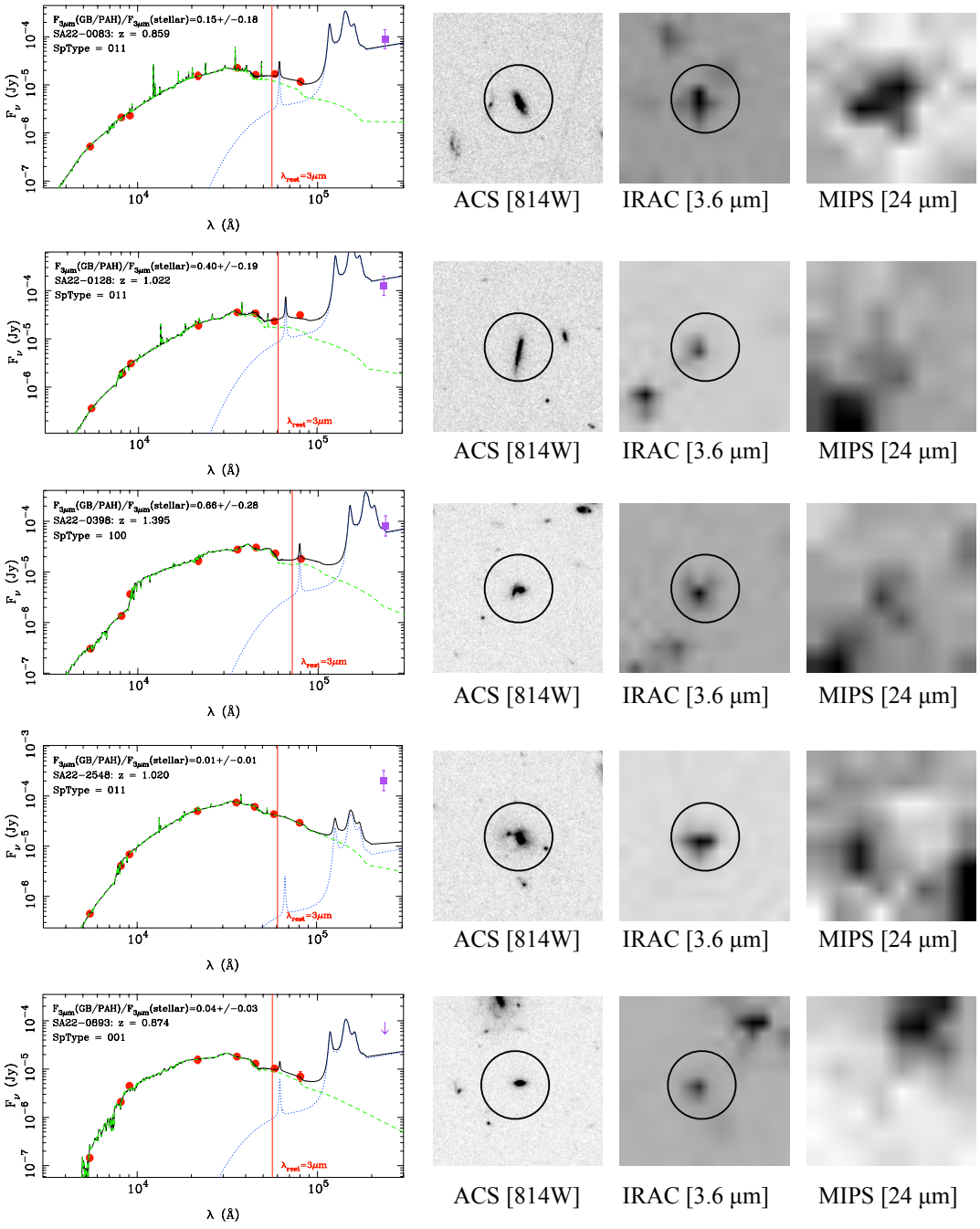

Figure 3.7 SED fit examples for objects with MIPS detections are plotted in the first three rows. The measured MIPS fluxes (purple squares) are in agreement with those fluxes predicted by the stellar and GB+PAH two component model. ACS [814W], IRAC [3.6 μm] and MIPS [24 μm] postage stamps, of 10″ wide, are shown with the photometric apertures for the visible through IRAC wavebands. We do not plot apertures on the MIPS figure which are measured as described in Section 3.3.3. SED lines are the same as in Figure 3.4, except now the wavelength range has been extended to include the MIPS data point.

3.5.6 Correlation of the near-infrared excess with the star formation rate

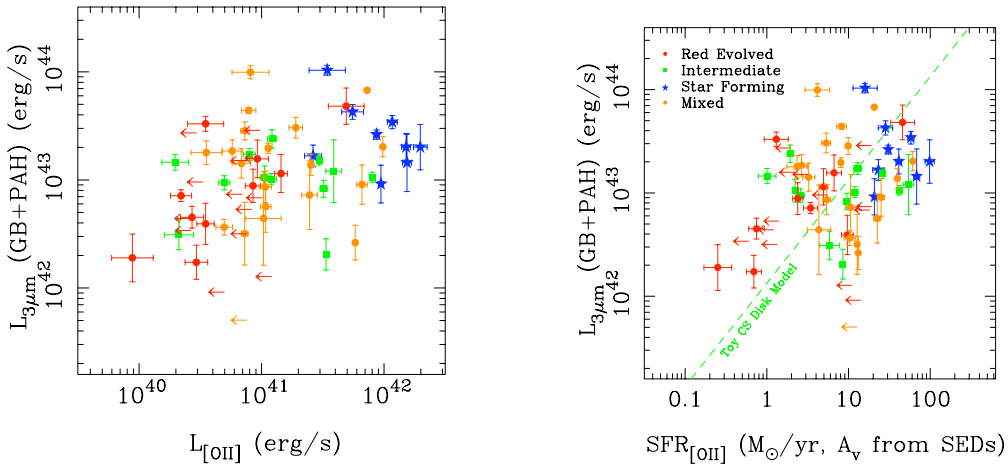

Figure 3.8 Luminosity of the GB+PAH component is correlated ($r = 0.49 \pm 0.06$) to the [O II] line luminosity (left panel) and the SFR derived from the [O II] line with dust attenuation correction as described in Section 3.5.6 (right panel). The dashed green line is the luminosity expected from an NIR excess due to circumstellar disks (that last for 1 Myr) in massive star-forming regions, assuming a simple model that scales linearly with the SFR (see Equation (3.2) in Section 3.6.2). The total luminosity of this model matches the galaxy's total luminosity in the NIR. Galaxies are indicated by spectral types as star-forming (blue stars), evolved (red circles), intermediate (green squares), and mixed (orange circles).

We quantify the amplitude of the NIR excess in our sample as the luminosity in the additional GB+PAH component at 3 μm. The stellar component determined from SED fits is subtracted from this quantity such that both the light from stars formed in the evolved population and the instantaneous burst are excluded. We find that this NIR luminosity is correlated ($r = 0.49 \pm 0.06$) with a galaxy's intrinsic [O II] line luminosity and its corresponding SFR derived from this line as demonstrated in Figure 3.8. SFRs are converted according to Juneau et al. (2005), except we apply a non-uniform dust attenuation correction using the dust attenuation given as an output parameter in the SED fitting procedure. Because the [O II] line probes the formation of massive stars, the correlation indicates that the NIR excess in these galaxies is primarily driven by star formation, and is likely powered by the radiation field provided by massive hot stars.

The correlation between the 3 μm luminosity of the GB+PAH component and the SFR is not strongly dependent on model choices. Both the PEGASE.2 and M05 models yield a similar correlation, although we have chosen to highlight the results from the M05 models which are shown to be a better representation of the NIR stellar light of globular clusters in the Magellanic Clouds due to their treatment of TP-AGB stars. However, some dependence would be expected on the choice of the dust model, in this case the GB+PAH component described in 3.4.2, as the broad continuum modeling in the NIR is different in various dust models (see Desert et al. 1990; Draine et al. 2007 for some examples of theoretical dust models). These dust components may also successfully model the NIR excess, but data at longer infrared wavelengths, combined with NIR and MIR observations, are required to correctly model the behaviour of the dust.

3.6 Interpretation of the NIR excess emission

The correlation between the NIR excess emission and the SFR is interesting for a number of reasons. As noted in the previous section, it provides us with a potentially useful mechanism for determining the instantaneous SFR from the flux density at rest-frame 2-5 μm. Unlike visible-wavelength indicators of the SFR like the UV continuum or the [O II] line, the amount of light extinguished by dust is likely to be minimal at 3-4 μm, so that the rest-frame $J - L$ colour may be useful as a sensitive and nearly extinction-free tracer of star-formation.

The further importance of the results presented in the previous section depends on the nature of the sources responsible for the excess emission. As we have already noted, the source of the emission may be a component of a galaxy that at other wavelengths is overwhelmed by either starlight or re-radiated emission from large dust grains (note in Figure 3.1 that a ~ 1000 K blackbody peaks at the minimum of these components). If, for example, it could be shown that the emission originates from protostellar or proto-planetary disk emission, then the excess emission might present us with an opportunity to probe the formation rate of planetary systems at high redshifts. On the other hand, if the emission originates in the interstellar medium (ISM) or post-AGB stars, it presents us with an opportunity to learn more about the interplay between radiation-driven winds and chemical enrichment in young galaxies. Furthermore, if low-luminosity AGNs are responsible for the excess, the correlation with the SFR indicates a connection between the growth of black holes and star-formation in our mass-selected sample.

The five best candidates for excess emission are:

1. Dust heated from low-luminosity AGNs (Daddi et al., 2007; Riffel et al., 2009)
2. The high-redshift counterpart to the interstellar cirrus emission seen in our own Galaxy (Bernard et al., 1994; Flagey et al., 2006).
3. Reflection nebulae (Sellgren et al., 1983; Sellgren, 1984; Sellgren et al., 1996).
4. Post-AGB stars/planetary nebulae (Phillips & Ramos-Larios, 2005; de Ruyter et al., 2006).
5. Protostellar/protoplanetary circumstellar disks in massive star-forming regions (Haisch et al., 2000; Maercker & Burton, 2005; Maercker et al., 2006; Longmore et al., 2007).

In the following sections we investigate whether these candidates can be responsible for the observed excess. We first consider large scale, non-stellar sources of NIR emission in Section 3.6.1 and then in Section 3.6.2 we extrapolate the NIR luminosity from dust emission around stellar candidates, to determine if it is enough to account for the total galactic NIR excess emission.

3.6.1 Non-stellar candidate sources of excess emission

Low luminosity AGN candidates

As noted in Section 3.3.2 and 3.3.3, IRAC & MIPS colours suggest that contamination of our sample from strong AGN is likely to be small. However, recent MIR spectroscopy of a survey of nearby bright galaxies from Goulding & Alexander (2009) suggests that optical spectroscopic surveys can miss up to half of the AGN population due to large dust obscuration. Indeed, NIR and MIR excesses observed in a deeper K-selected sample than ours are attributed by Daddi et al. (2007) to be due to AGN. They find that 20%-30% of their sample show MIR excesses higher than those expected from UV derived SFRs alone. On the other hand, Donley et al. (2008) show that MIR AGN detection criteria, although successful at detecting an AGN, can be significantly contaminated by star-forming galaxies and the fraction of MIR sources with an AGN is $\sim 10\%$ at MIR flux densities less than $300\,\mu$Jy (only 2/15 of our objects with MIPS detections have MIR flux densities greater than $300\,\mu$Jy). Thus, we can rule out strong AGNs as a candidate for the excess emission which is seen in the majority of our sample.

Since weak AGNs outnumber strong AGNs by a large factor (e.g., Trump et al. 2007), the degree of contamination by AGNs in any sample depends on depth and we cannot rule out contamination by weak AGNs at the $\sim 20\%$ level. It is therefore interesting to consider whether hot dust heated by a contaminating sample of weak AGN at this level could contribute significantly to the $3\,\mu$m excess seen in our observations.

We think this is implausible for a number of reasons. First, heating large quantities of hot dust to the required 800 K – 1200 K is likely to be important only for strong AGN. For example, (Riffel et al., 2009) studied the NIR spectral properties of 24 Seyfert galaxies, and they show that the NIR continuum in AGN is well-described using a three component model made up of a featureless continuum plus two hot blackbody components (Riffel et al., 2009). We can certainly exclude a dominant featureless continuum AGN component from our sample on the basis of our IRAC colours (see Figure 2.2), and based on the absence of a significant K-band excess. Figure 3.1 shows an SED for Mrk 231, a typical AGN, which has excess emission blueward of $2\,\mu$m, we do not find this type of excess in our photometry (see Figure 3.3). These authors then show that SyI and SyII samples have markedly different contributions from hot dust: 90% of SyI systems show evidence for hot dust, as opposed to only 25% for the SyII population. Therefore, even if our sample is being contaminated by a population of weak AGN, only a small subset of these is likely to be contributing significantly to the $3\,\mu$m excess. This is clearly inconsisent with Figure 3.8, which shows that the excess is a common characteristic of star-forming systems, reinforcing the view that star formation, and not an AGN, is primarily powering the NIR excess in our K-selected sample.

Galactic cirrus

Could the NIR continuum excess seen simply be a scaled up galactic cirrus component? This idea seems attractive, because after all the canonical SED being used to model the component is based on da Cunha et al. (2008)'s NIR emission model which is shown to match the observed colours of the galactic cirrus. Attributing the excess to cirrus would seem a natural interpretation, provided the energetics can be made to work.

Large-scale observations by *Spitzer* and *COBE* of the galactic cirrus reveal a continuum component in the NIR, whose field to field variations are weak and has a strong contribution to the IRAC [$3.6\,\mu$m] channel, contributing 50%-80% of the flux, while the PAH feature at $3.3\,\mu$m contributes the remaining flux (Flagey et al., 2006). Two papers

have quoted the irradiance of the galactic cirrus in the L-band and they are similar, on average, for two fields at different galactic latitudes. DIRBE measurements from Bernard et al. (1994) find $\nu F_\nu = 0.21 \times 10^{-7}\,\mathrm{W\,m^{-2}\,sr^{-1}}$ for $\lambda = 3.5\,\mu$m for two strips of the galactic plane covering $-6°$ to $-4°$ and $+4°$ to $+6°$ below and above the galactic plane. Using IRAC measurements of the galactic cirrus, at latitudes ranging from $+0°$ to $+32°$, Flagey et al. (2006) find an average intensity of $I_\nu = 0.03\,\mathrm{MJy\,sr^{-1}}$ at $\lambda = 3\,\mu$m. On the basis of these measurements, it seems that galactic cirrus has a surface brightness on the order of 5×10^{-7} Jy/arcsec^2. In an Euclidean universe surface brightness is conserved with distance, although in reality $(1+z)^4$ cosmological surface brightness dimming reduces the apparent surface brightness by a factor of around 40 at $z \sim 1.5$. The cirrus is expected to have a surface brightness on the order of several tens of nJy/arcsec^2 at $z \sim 1.5$. A typical GDDS galaxy subtends an area around 1 arcsec^2 at these redshifts, so the total flux contributed from cirrus will be around 50 nJy at a rest-wavelength of 3μm. Inspection of figures/ 5–8 makes it clear that this corresponds $< 0.1\%$ of the NIR excess. On the other hand, it may be the case that cirrus at high redshifts is far brighter than is the case in the Milky Way. Cirrus NIR emission is expected to scale linearly with the interstellar radiation field (Desert et al., 1990), so an interstellar radiation field 1000 times that in our own galaxy is needed. Given the modest SFRs in our sample ranging to a maximum of $100\,M_\odot/yr$ (at most 20–50 times that of the Milky Way), we conclude that it is unlikely that emission from cirrus dominates the NIR excess, though we cannot rule out a contribution from cirrus at the 10% level.

3.6.2 Stellar candidate sources of excess emission

In Figure 3.9, we synthesize observations from the Milky Way and the LMC in a JHL(AB) colour-colour diagram for each of the proposed stellar candidates (3-5) for the NIR excess emission. Main-sequence (MS) stars (open cyan squares) not embedded in a dust cloud occupy a region in the bottom left (Leggett et al., 2003, 2006). For dust embedded sources, both the $J-H$ and $J-L$ colours are reddened due to extinction away from the MS along the plotted vector for 10 mag of visual extinction (Indebetouw et al., 2005) .

Using Figure 3.9 as a starting point, we now consider in turn which of these local candidates seems most likely to be responsible for the bulk of the NIR excess seen in the high-redshift population. The luminosity in the NIR excess component plotted as a function of SFR in Figure 3.8 demonstrates that a useful fiducial luminosity is 10^{43} erg/s. Our simple strategy is to explore how much of each possible candidate would be needed to reach this luminosity in a typical galaxy.

Reflection nebulae

NIR excesses are commonly seen (Sellgren et al., 1983, 1996) in the diffuse emission around visual reflection nebulae (RNae) and Sturm et al. (2000) show that a scaled spectrum of NGC 7023, the archetypal RN, matches the spectrum of the starbursting galaxy M82 in the near to mid-IR. We investigate how many RNae are needed to contribute to the NIR excess seen in the GDDS galaxies. Some of the central massive stars powering visual RNae (Sellgren et al., 1996) also show NIR excess colours as plotted as purple stars in Figure 3.9. For concreteness, we adopt NGC 7023 (d=430 pc) as a reference object, and note that in this object the integrated NIR excess for the star and the nebula are similar in integrated luminosity. The central star of NGC 7023, the B2e type star HD 200755, has an L-band magnitude of $L' = 3.36$ (Sellgren et al., 1996). This leads to an intrinsic NIR luminosity of $L_{3.8\,\mu\mathrm{m}}(\mathrm{star}) = 2.52 \times 10^{35}$ erg/s. Sellgren et al. (1983) measure the intensity of the diffuse nebular region at a number of positions offset from the central star. The intensity drops off as a function of distance. To estimate the integrated flux, we opt for maximizing the potential contribution of the excess by choosing the strongest intensity measured ($S_{3.8} = 20 \times 10^{-20}\,\mathrm{W/m^2/Hz^{-1}/sr}$) and integrating the surface brightness over the nebula out to $120''$, where the surface brightness drops by a factor of 10. We find the nebular region to have a maximum integrated luminosity of $L_{3.8\,\mu\mathrm{m}}(\mathrm{nebula}) = 3.71 \times 10^{35}$ erg/s.

NGC 7023 is a special RN as the central star also exhibits strong NIR excess in addition to the diffuse NIR excess. However, the amount of integrated NIR luminosity for the diffuse region is not special for this source. NGC 2023 and NGC 2068, also relatively bright RNae measured in Sellgren et al. (1983), have similar intrinsic NIR luminosities integrated over their surfaces of $L_{3.8\,\mu\mathrm{m}}(\mathrm{nebula}) = 8.13 \times 10^{35}\,\mathrm{erg/s}$ and $L_{3.8\,\mu\mathrm{m}}(\mathrm{nebula}) = 2.11 \times 10^{35}\,\mathrm{erg/s}$, respectively. In both cases, we used the distance to the Orion Nebula (d=490 pc) and assumed the nebula covered a circular aperture in the sky of 180″ in diameter. To match the fiducial NIR excesses in GDDS galaxies of $\sim 10^{43}\,\mathrm{erg/s}$, about 10^7 RNae like NGC 7023, NGC 2023 and NGC 2068 would have to populate an average GDDS galaxy at the time of observation. Locally, RNae typically reside around stars ranging in effective temperatures from 6,800-33,000 K ($\sim 2-20\,\mathrm{M}_\odot$), but only a fraction of those surveyed (16/23) display NIR excesses (Sellgren et al., 1983, 1996). Given that only about ~ 1000 (Magakian, 2003) have been observed in our Galaxy, it is unlikely that reflection nebulae are responsible for much of the observed NIR excess, but they cannot be completely ruled out given the selection bias of the RNae surveyed locally.

Post-AGB stars/planetary nebulae

NIR excesses with spectral signatures indicative of hot ($\sim 1000\,\mathrm{K}$) continuum emission have been observed in post-AGB stars (de Ruyter et al., 2006) and planetary nebulae (Phillips & Ramos-Larios, 2005). Strong mass outflows from intermediate initial mass stars ($4-8\,M_\odot$) excites both gas and dust surrounding the luminous (100 - 1000 $\mathrm{L}_\odot$) post-AGB stars for relatively short timescales of 10^4 yrs (de Ruyter et al., 2006). Phillips & Ramos-Larios (2005) attribute K-band excesses found in a range of planetary nebula to photon heating of very small grains to temperatures on the order of $800 < T_{\mathrm{grain}} < 1200\,\mathrm{K}$. In Figure 3.9 we plot the location of several planetary nebulae as orange crosses. In a study of 51 post-AGB stars, de Ruyter et al. (2006) find that all post-AGB stars contain large IR excesses with dust excess starting near the sublimation temperature, irrespective of the effective temperature of the central star. They argue that in all systems, gravitationally bound dusty disks are present. The disks must be puffed-up to cover a large opening angle for the central star and we argue that the disks have some similarity with the disks detected around young stellar objects (see Section 3.6.2). The dust excesses of post-AGB stars are noted to be bluer with smaller mid- and far-IR

colours compared to the excesses found around Herbig Ae/Be stars and are therefore likely more compact (de Ruyter et al., 2006).

It is straightforward to show that the contribution to the NIR excess from post-AGB stars is not enough to fully account for the NIR excess seen in the integrated luminosity of high-z star-forming galaxies. About 10% of the mass formed in an episode of star formation will be in stars with masses of $4 - 8\,M_{\odot}$ that will enter the post-AGB phase within 200 Myr after a instantaneous burst of star formation (the average burst age output by our SED modeling is 247 Myr). To see a noticeable contribution from the short-lived AGB stars to the NIR excess, large-scale and high duty cycle star formation is required. We find in our SED modeling that the average amount of mass formed in an instantaneous burst of star formation is $\log M_{\rm burst}/M_{\odot} = 8.5 \pm 0.9$. In order to reach luminosities of 10^{43}erg/s, all of the $4 - 8\,M_{\odot}$ stars formed in the instantaneous burst would have to be in the post-AGB phase at the time of observation, assuming such a star has a $L_{\rm NIR} = 100\,L_{\odot}$, a conservative upper limit. This requires $10^{8.5}\,{\rm M}_{\odot}$ to be formed in just 10^4 years (de Ruyter et al., 2006), the typical timescale for the AGB phase and for all the 4-8 $\rm M_{\odot}$ stars to enter post-MS evolution at the same time, an unrealistic scenario since we know the spread in turnoff ages for the masses are larger than 10^4 years. We also note that due to the delayed response of the post-AGB phase, we would not expect a correlation between NIR excess in AGB stars and O II luminosity (the SFR indicator traces the most massive population).

Circumstellar disks around young massive stars

A number of observations (e.g., Haisch et al. 2000; Maercker & Burton 2005; Maercker et al. 2006; Longmore et al. 2007) suggest that protostellar/protoplanetary circumstellar disks in star-forming regions are attractive candidates for the NIR excess. These observations, compiled in Figure 3.9, show that the largest L-band excesses locally (up to 5 mags) are due to excesses seen in massive stars ($> 20\,M_{\odot}$) in massive star-forming complexes. Circumstellar disks are proving ubiquitous in regions of high star-formation, and the inner puffed up rims of circumstellar disks are predicted to be heated to temperatures high enough to produce prominent spectral bumps that peak at $2 - 3\mu$m.

The taxonomy used to describe such systems has grown rather large, encompassing various classes, stages, and groups, and the reader interested in the terminology used to describe young disks is referred to the 'diskionary' presented by Evans et al. (2009). For

present purposes it suffices to consider whether the IR excess we have detected could be due to any class (or classes) of circumstellar disks in a general sense, although for the sake of concreteness we will base much of our discussion on the flared disk model presented by Dullemond et al. (2001). In this particular model, the inner part of the disk is removed out to a radius (6 AU for a B2 star) of the dust evaporation temperature ($T_{evap} = 1500\,\mathrm{K}$). Unlike the top and bottom surfaces of the flared disk which receive radiation from the star at a grazing angle, the inner edge of the disk receives radiation face-on and has a large covering fraction of the central star. The result is a disk that is substantially heated to temperatures up to T_{evap} and the disk becomes puffed up, increasing the surface area of the inner rim and the NIR emission (see Dullemond et al. 2001 for schematic diagrams).

We once again refer the reader to Figure 3.9 for a summary of the local observations. The figure presents a number of data points (open stars) showing the colours of YSOs in NGC 2024 (Haisch et al., 2000), a young (0.3 Myr; Meyer 1996) massive star-forming region in the Orion molecular cloud (OMC). Haisch et al. (2000) conclude that $\geq 86\% \pm 8\%$ of NGC 2024's members exhibit NIR excesses due to circumstellar disks as indicated by their $JHKL$ colours. These excesses are seen down to quite low stellar masses, further suggesting that disks form around the majority of the stars. From their sample of 328 pre-main-sequence stars, 45 objects exhibit extremely red excesses of $K - L \geq 1.5$. They attribute these to being Class I protostars, but another possible scenario we present is that the excess NIR emission could be from disks around the more massive objects.

Moving beyond the OMC to 30 Doradus in the LMC and other large star-forming complexes in our own Galaxy, Maercker & Burton (2005), Maercker et al. (2006) and Longmore et al. (2007) have studied IR excess objects using photometry obtained in $JHKL$ and the IRAC bands. These points are also shown in Figure 3.9. Objects that have L-band IR excesses are plotted using red symbols, while those without excesses are plotted as black symbols. The non-IR excess objects roughly follow a linear trend expected due to extinction through the line of sight of the molecular clouds they are embedded in. IR-excess objects in the Maercker & Burton (2005) and Maercker et al. (2006) papers show a striking divide from typical reddening to IR-excess with a shift of $\gtrsim 1$ mag redder in L-band. This is likely because they are only reaching the more massive stars in the clusters ($\gtrsim 25\,M_{\odot}$ for 30 Dor and $\gtrsim 10\,M_{\odot}$ for NGC 3576) and in agreement with the model of Dullemond et al. (2001) this would lead to the largest L-band excess. In the OMC sample from Haisch et al. (2000), which extends down to lower

masses, the L-band excess objects are classified based on their NIR colours, however, it is apparent that there is a smooth transition away from the reddening locus, indicative of an NIR excess that increases with stellar mass also in agreement with the disk model of Dullemond et al. (2001).

Can the NIR excess due to emission from the inner puffed up rims of circumstellar disks provide enough excess flux to account for the excess seen in the integrated light of galaxies? Dullemond et al. (2001) calculate the NIR excess fluxes due to disks to be $L_{\rm NIR} = (310, 8, 0.1, 0.0035)\ L_\odot$, for stars of spectral types B2, A0, G2 and M2, luminosities of $L = (1000, 500, 1, 0.5)\, L_\odot$ and masses of $M = (10, 4, 1, 0.4)\, M_\odot$. Using the results of their Table 1, the NIR excess due to the flared disk is related to the mass of the star by

$$L_{\rm NIR}(M) = 0.0865\, L_\odot \left(\frac{M}{M_\odot}\right)^{3.48}. \tag{3.1}$$

We can integrate this over the IMF to figure out the total luminosity excess in the NIR for a given amount of mass formed during a period of star formation. Using the Kroupa (2001) IMF, we find the NIR excess due to circumstellar disks is $(L/M)_{\rm NIR,disks} = 350\, L_\odot/M_\odot$. While this seems like a high light-to-mass ratio, it is in fact very typical for very young $\lesssim 1\,$Myr star-forming regions, which output high IR luminosities.

We can then estimate the total NIR excess luminosity for a galaxy forming stars at a given SFR as:

$$L_{\rm NIR}({\rm SFR})_{\rm disk} = 350\,{\rm L_\odot/M_\odot} \left(\frac{\rm SFR}{\rm M_\odot/yr}\right) \left(\frac{\rm t_{excess}}{\rm yr}\right). \tag{3.2}$$

The cluster disk fraction drops drastically from $> 80\%$ at $t < 1\,$Myr to $< 10\%$ by $t \sim 5$ Myr (Maercker & Burton, 2005; Maercker et al., 2006) so $t_{excess} = 1\,$Myr is a good order of magnitude estimate for the timescale of circumstellar disks. We plot this simple linear relationship along with the distribution of GDDS data points in right panel of Figure 3.8. The overall normalization of the model is remarkably consistent with the data points. *We find that circumstellar disks with a puffed up inner rim can contribute enough NIR luminosity to be seen over the stellar component of a galaxy and these objects may well be responsible for the NIR excess seen in our high-redshift sample.*

We emphasize that the model presented is very simple and rather crude. Changing the viewing angle of the disks would lead to changes in the excess, and the relevant

timescales may well be shorter than 1 Myr for the most massive stars which would be provide the bulk of the light. And although we integrate the IMF down to $0.1\,M_{\odot}$, the actual contribution from stars with $M < 20\,M_{\odot}$ to the NIR excess luminosity is only $\sim 1\,\%$ of the total NIR excess luminosity for a Kroupa (2001) IMF, so we are really only seeing light from disks around massive young stars.

Given the simplicity of the assumptions in our toy model, the order of magnitude agreement with the data seems rather striking. Nevertheless, the scatter in the data clearly shows that a simple scaling of the IMF is only an approximation. Any number of physical differences in these galaxies could lead to the scatter from this simple model, such as variations in metalliticity, IMF or reddening. For example, a top-heavy IMF would result in a higher NIR excess since the fraction of the most massive stars which have the highest excesses would be greater. Alternatively lower metallicity might also lead to a smaller NIR excess for a given galaxy if the density of grains or molecules which cause the excess is smaller. And it is interesting to note that nearby, MIR and PAH emission is shown to be smaller in low-metallicity environments (Engelbracht et al., 2005; Madden et al., 2006). Another possibility is that the optical measure of the SFR upon which this diagram has been constructed may have been over-estimated, due to incorrect dust corrections which impact the most actively star-forming galaxies more than they do the quiescent galaxies. In any case, the important point is that if the IR excess is indeed due to a population of circumstellar/protostellar/protoplanetary disks, modeling the data shown in Figure 3.8 as a function of these input parameters presents us with an opportunity to determine the rate at which disks form in high-redshift galaxies as a function of basic observables, such as a galaxy's global metallicity, mass, and SFR. Furthermore, if the presence of disks around massive young stars can be extrapolated to lower mass systems which harbor the potential to form planets, then measurements of the NIR excess provide us with a chance to explore protoplanetary/protostellar disk formation in a galactic context, opening up a wide range of interesting studies. The most exciting from a cosmological standpoint might be the measurement of the volume-averaged cosmic evolution of planet formation.

3.6.3 Conclusions

In a sample of 88 galaxies from the GDDS, a near-infrared excess is detected in the observed IRAC [5.8 μm] and [8.0 μm] bands. The excess can be modeled as an additional

SED component consisting of a modified 850 K greybody augmented with a mid-IR PAH emission template spectrum (da Cunha et al., 2008). The luminosity of the excess SED component is correlated with the SFR of the galaxy, implying the possibility of using NIR luminosity as an extinction-free star formation tracer. Our exploration of the origin of the excess flux by examining NIR excesses in our own Galaxy has provided a number of tantalizing possibilities. From all of the possible NIR excess candidates seen locally, we find that circumstellar disks are the most likely candidates for the observed NIR excess. Our simple conversion of a SFR to a total NIR luminosity using locally calibrated disk timescales and intrinsic luminosities agree with the total integrated NIR luminosity excess measured in the GDDS sample of high-z galaxies. All other candidates require unrealistic abundances or extremely high duty cycle star formation. It seems natural to suppose that the presence of circumstellar disks around massive stars at high redshifts would imply also the presence of disks around less massive stars. These would be systems in which we would expect planets to form. This presents us with an opportunity to probe the formation of planets as seen in their total integrated light at high redshifts, at cosmic epochs even before our own Solar System formed.

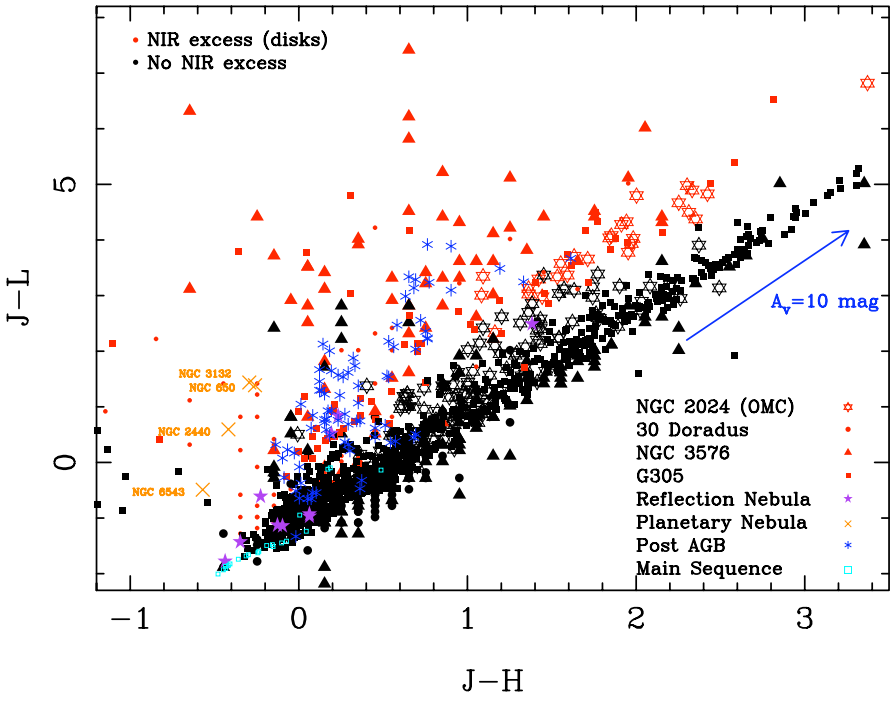

Figure 3.9 JHL(AB) colour-colour plot synthesizing local candidates for the NIR excess. MS standard stars taken from Leggett et al. (2003, 2006) occupy the bottom right of the diagram. Stars embedded in dust will show extinction extending away from the MS along the vector marked in blue. Stars classified with an infrared excess – above the excess expected from extinction– postulated by Maercker & Burton (2005); Maercker et al. (2006) to be due to circumstellar disks are indicated in red. A range of masses from NGC 2024 (Haisch et al., 2000) in the OMC are plotted as open stars. Massive O-stars in the 30 Dor starburst from Maercker & Burton (2005) are plotted as circles as well as O, B stars from star-forming regions are plotted from NGC 3576 and G305 (Maercker et al., 2006; Longmore et al., 2007). We also plot the NIR photometry of visual reflection nebula (purple stars) from Sellgren et al. (1996), planetary nebula (orange crosses) from Hora et al. (2004) and post-AGB stars (blue asterisks) from de Ruyter et al. (2006).

Chapter 4

A simple connection between the near-infrared and PAH emission of galaxies and their star formation rates

Submitted[1] to ApJ to be published as:
"A simple connection between the near-infrared and PAH emission of galaxies and their star formation rates"
Mentuch, E., Abraham, R. G. and Zibetti, S.

4.1 Abstract

We have measured the near-infrared colours of individual pixels in 68 galaxies common to the *Spitzer* Near Infrared Nearby Galaxies Survey and the Large Galaxy Atlas Survey. Each galaxy was separated into regions of increasingly red near-infrared colour using the expected colours of pure starlight as a reference. Our analysis focuses mainly on regions which are redder than expected from pure starlight. A fraction of these red-excess regions may simply be dust-extincted stellar populations, as their colours are well-modelled by the $\lambda^{-0.7}$ extinction law observed in starburst galaxies. To test this we use the observed Hα and 24 μm emission to measure the average intrinsic Hα emission and average dust

[1]Please refer to the published article for the most up to date version

extinction in each colour-selected region. Pixels with red near-infrared colours do not necessarily correspond to regions with high dust extinction, but show a tighter correlation with the intrinsic Hα emission. In regions of high star formation, the average intensity of pixels in red-excess regions (at 1.25 μm, 3.6 μm, 4.5 μm, 5.6 μm, 8.0 μm and 24 μm) scales linearly with the intrinsic intensity of Hα emission, and thus with the star formation rate within the pixel. This suggests that most NIR excess regions are not red because their light is being depleted by absorption. Instead, they are red because additional infrared light is being contributed by a process linked to star formation. This is surprising because the shorter wavelength bands in our study (1.25 μm–5.6 μm) do not probe emission from cold (10–20 K) and warm (50–100 K) dust associated with star formation in molecular clouds. However, emission from *hot* dust (700–1000 K) and/or Polycyclic Aromatic Hydrocarbon molecules can explain the additional emission seen at the shorter wavelengths in our study. The contribution from hot dust and/or PAH emission at 2 μm–5 μm and PAH emission at 5.6 μm and 8.0 μm scales linearly with warm dust emission at 24 μm and the intrinsic Hα emission. Since both are tied to the star formation rate, our analysis shows that the NIR excess continuum emission and PAH emission at $\sim 1 - 8\,\mu$m can be added to stellar population models in a very straight-forward way, by simply adding an additional component to the models that scales linearly with the star formation rate.

4.2 Introduction

The signatures of star formation are expressed across a galaxy's spectral energy distribution (SED). Ultraviolet and optical light trace the recently formed stellar populations, infrared light maps out luminous dust grains that re-emit this same starlight, and radio emission traces magnetic fields produced by short-lived, massive stars. How well these tracers can be used to determine a galaxy's star formation rate depends on the galaxy's luminosity, dust content, nuclear activity, and metallicity. At a fundamental level these tracers are highly interdependent, because energy must be conserved. For example, the energy in the UV radiation absorbed by dust must be balanced out by the re-emission of this energy at other wavelengths. This suggests that the best estimator for the star formation rate will be based on a combination of tracers which together capture the full energetics of the system.

Recent work by Calzetti et al. (2007) and Kennicutt et al. (2009) shows that a good estimator for the star formation rate emerges from the linear combination of a galaxy's

near-UV and visible-wavelength emission (either UV continuum or line fluxes, attenuated by dust) and its emission in the infrared (e.g. 8 μm, 24 μm, or total IR λ 8–1000 and also radio). The beauty of this approach is that the data itself can correct for the attenuation and emission of dust.

At near-infrared (NIR) (0.9-5 μm) and mid-infrared (MIR) wavelengths (5-30 μm), emission due to heating of very small grains (VSG) and polycyclic aromatic hydrocarbons (PAH) dominates the spectral energy distribution. UV photons excite these small molecules which emit through various vibrational/stretching/rotational modes and thus this emission should trace regions of star formation. PAH emission around 8 μm shows spatial correlation to star formation within H II regions (Calzetti et al., 2007), and can be used as a SFR indicator, particularly if used in combination with an optical SFR indicator (Kennicutt et al., 2009). Observations of nearby star-forming galaxies suggest that the spectrum of PAH line emission is expressed through constant line ratios. For example, Lu et al. (2003) found constant ratios of stellar subtracted flux densities at 4, 6.2, 7.7 and 11.3. PAH and/or dust emission at shorter wavelengths has received less attention, partly because of the stronger contribution from stellar continuum emission at these wavelengths.

Both PAH line emission and NIR continuum emission can be significant at wavelengths of 2-5 μm. High redshift star-forming galaxies, where SFRs are significantly higher than nearby, emit significant NIR excesses at this wavelength (Mentuch et al., 2009; Magnelli et al., 2008) and its emission correlates with optical SFR indicators (Mentuch et al., 2009). Nearby galaxies, studied with the *Infrared Space Observatory* also show NIR excess continuum emission (Lu et al., 2003) which scales linearly with the PAH spectrum and shows trends of increasing with increasing star formation indicators. This NIR dust emission component is seen not only in extragalactic emission, but has been found locally in galactic cirrus emission (Flagey et al., 2006), reflection nebulae (Sellgren et al., 1983, 1996), planetary nebulae (de Ruyter et al., 2006) and massive star-forming regions (Maercker & Burton, 2005; Maercker et al., 2006; Longmore et al., 2007). In the latter two cases, the NIR dust emission is linked to circumstellar disk emission (Wood et al., 2008; Touhami et al., 2010; Acke & van den Ancker, 2004) where high luminosity OB stars heat dust to its sublimation temperature (for example, a 10^5 $L_\odot$star will heat dust to 1000 K at r = 7.3 AU, while a 10^2 $L_\odot$star will heat dust to 1000 K at r = .23 AU and a $L_\odot$ star will heat dust up to 1000 K out to a radius of 0.023 AU.)

The source of extragalactic NIR dust emission, and its contribution to a galaxy's

integrated light remains uncertain. The excess seen in higher star-forming galaxies at high redshift is possibly a combination of both NIR dust emission related to star formation regions (which includes reflection nebulae and circumstellar dust emission) and NIR emission due to cirrus emission. In Mentuch et al. (2009), we show that there is a trend of increasing NIR continuum emission with star formation and show that the magnitude of NIR excess emission can be well matched if the majority of the excess NIR emission originates in hot (700 K–1000 K) thermal emission, possibly from circumstellar disks heated to their sublimation temperature. Other sources of NIR emission such as dust heated by active galactic nuclei, planetary nebula and reflection nebula can also be important, but these do not dominate the emission seen in the integrated light of a galaxy (Mentuch et al., 2009).

A central purpose of the present chapter is to test this hypothesis, using the images of nearby galaxies. Our study is primarily in the near- and mid-infrared which we define as the wavelength ranges from 1-5 μm and 5-30 μm, respectively. Additional narrow-band Hα imaging, which traces the young, massive stellar populations, complements the analysis. We perform multiwavelength pixel-by-pixel analysis on a sample of 68 nearby galaxies from the *Spitzer* Infrared Nearby Galaxies Survey (SINGS; Kennicutt et al. 2003) with complementary infrared data from the Large Galaxy Atlas (LGA; Jarrett et al. 2003). These data resolve galaxies on physical scales between 8 pc (for the closet galaxy NGC 6822 at a distance of 0.6 Mpc) and $\sim$ 400 pc (for the most distant galaxies at a distance of 30 Mpc).

This study provides synergy between studies of integrated emission for whole galaxies and studies of resolved stellar populations by grouping pixels with common near-infrared colours such that the common properties of these regions are revealed. Other resolved studies of nearby galaxies have already gained new insights on their composite stellar populations. For example, an analysis of 1800 H II regions in 38 galaxies from the SINGS sample has shown that about 4% of the H II regions are highly obscured (with attenuation of $A_{H\alpha} \gtrsim 3$; Prescott et al. 2007). Or consider the recent mapping of M33 by Verley et al. (2009) which has revealed the importance of discrete sources to 24 μm emission, and find that VSG emission, as powered by the diffuse interstellar radiation field, account for only 10% of the diffuse 24 μm emission, while unresolved AGB stars of intermediate mass (e.g. carbon stars), through their dusty circumstellar envelopes, can provide most of the diffuse 24 μm emission.

The chapter is outlined as follows. In § 4.3, we briefly summarize our sample selection

from the SINGS and LGA surveys. Our pixel-by-pixel colour selection and image processing is described in § 4.4. Results from the average intensity at Hα, 1.25 μm, 3.6 μm, 4.5 μm, 5.6 μm, 8.0 μm and 24 μm measured in each colour selected region are presented in § 4.5. Implications for studying integrated galaxies and applying our results to stellar population synthesis models are discussed in § 4.6.

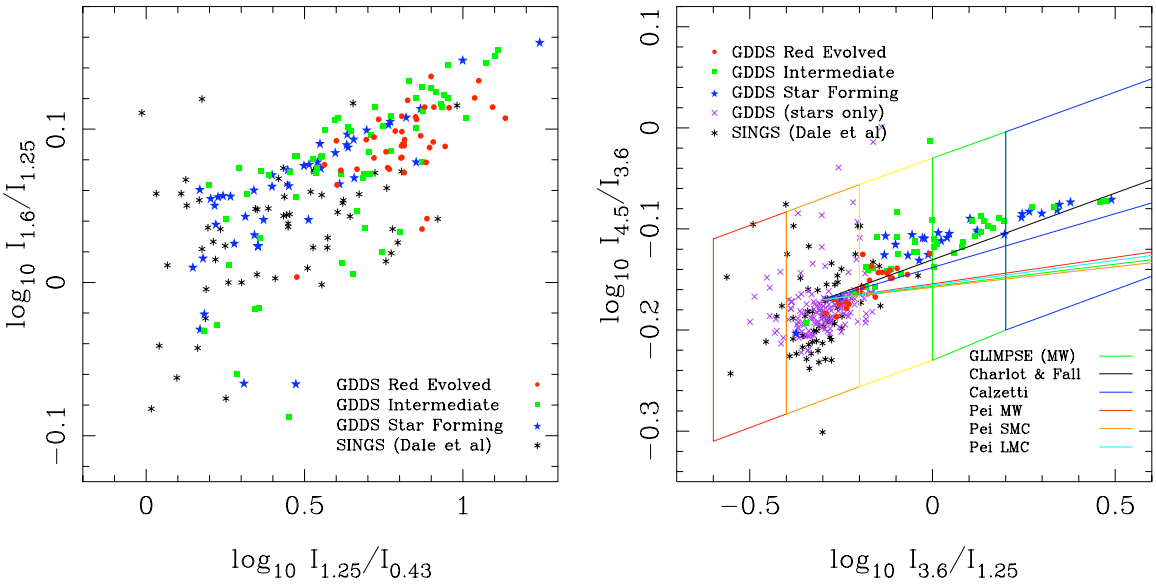

Figure 4.1 colour-colour plots in the optical/NIR (left) and the NIR (right) for the integrated SINGS photometry from Dale et al. (2007) and rest-frame colours for the GDDS high-redshift galaxy sample. Rest-frame colours are computed using best fit SEDs from Mentuch et al. (2009). The right plot shows the NIR colours for the GDDS sample extrapolated from SED fits containing only stellar emission (purple crosses) or stellar plus NIR continuum emission (points keyed to galaxy types). Extinction vectors are plotted from the colour locus of ($\log_{10}$ $I_{3.6}/I_{1.25}$, $\log_{10}$ $I_{4.5}/I_{3.6}$ = -0.30, -0.17) for various dust extinction laws. The coloured boxes indicate regions of increasing NIR colour, defined in § 4.4 and used as colour selection in the quantitative analysis presented in this chapter.

4.3 Sample Selection

Table 4.1 summarizes our sample of 68 spatially resolved nearby galaxies, with observations at 1.25 μm (J-band), 3.6 μm, 4.5 μm, 5.6 μm, 8.0 μm and 24 μm. All data come from

publicly available sources, namely the *Spitzer* Infrared Nearby Galaxies Survey (SINGS; Kennicutt et al. 2003) and the Two Micron All Sky Survey (2MASS) Large Galaxy Atlas survey (Jarrett et al., 2003, hereafter referred to as the 2MASS LGA). We used SINGS data release `2070410_enhanced_v14`. Our data is comprised of all galaxies that were observed by both surveys that meet our minimum signal-to-noise criterion (described below). As a result we excluded SINGS galaxies DDO 053, Holmberg I, Holmberg IX, M81 Dwarf A and M81 Dwarf B, which do not have NIR coverage in the 2MASS LGA. Only two SINGS galaxies, DDO 154 and DDO 165, did not contain any pixels which satisfied our signal-to-noise criterion, so only two objects were omitted for our analysis because of low signal-to-noise.

Table 4.1. Object List

Galaxy Name	Optical Morphology	Distance (Mpc)	Metallicity [O/H]	[a]AGN ?	[b]Hα ?
DDO 154	IBm	5.4	7.5	0	1
DDO 165	Im	3.5	0.0	0	1
Ho ii	Im	3.5	0.0	0	1
IC 2574	SABm	3.5	8.1	0	1
IC 4710	SBm	8.5	0.0	0	1
MRK 33	Im	21.7	0.0	0	1
NGC 0024	SAc	8.2	0.0	0	1
NGC 0337	SBd	24.7	0.0	0	1
NGC 0584	E4	27.6	0.0	0	1
NGC 0628	SAc	11.4	9.1	0	1
NGC 0855	E	9.6	0.0	0	0
NGC 0925	SABd	10.1	8.7	0	1
NGC 1097	SBb	16.9	9.0	0	1
NGC 1266	SB0	31.3	0.0	1	1
NGC 1291	SBa	9.7	0.0	1	1
NGC 1316	SAB0	26.3	0.0	1	1
NGC 1377	S0	24.4	0.0	0	1
NGC 1404	E1	25.1	0.0	0	1
NGC 1482	SA0	22.0	0.0	0	1
NGC 1512	SBab	10.4	0.0	0	1
NGC 1566	SABbc	18.0	9.0	1	1
NGC 1705	Am	5.8	0.0	0	1
NGC 2403	SABcd	3.5	8.8	0	0
NGC 2798	SBa	24.7	0.0	0	1
NGC 2841	SAb	9.8	9.3	1	1
NGC 2915	I0	2.7	0.0	0	0
NGC 2976	SAc	3.5	0.0	0	1
NGC 3031	SAab	3.5	8.9	1	1
NGC 3034	IO	3.5	0.0	0	1
NGC 3049	SBab	19.6	8.9	0	1
NGC 3184	SABcd	8.6	9.3	0	1
NGC 3190	SAap	17.4	0.0	1	1
NGC 3198	SBc	9.8	8.9	1	1
NGC 3265	E	20.0	0.0	0	1
NGC 3351	SBb	9.3	9.3	0	0
NGC 3521	SABbc	9.0	9.1	0	1
NGC 3627	SABb	8.9	9.3	1	1
NGC 3773	SA0	12.9	0.0	0	1
NGC 3938	SAc	12.2	0.0	0	1
NGC 4125	E6p	21.4	0.0	1	1
NGC 4236	SBdm	3.5	0.0	0	0
NGC 4254	SAc	20.0	9.2	0	1
NGC 4321	SABbc	20.0	9.3	0	1

Table 4.1 (cont'd)

Galaxy Name	Optical Morphology	Distance (Mpc)	Metallicity [O/H]	[a]AGN ?	[b]Hα ?
NGC 4450	SAab	20.0	0.0	1	1
NGC 4536	SABbc	25.0	8.9	0	1
NGC 4552	E	4.5	0.0	0	0
NGC 4559	SABcd	11.6	8.7	0	1
NGC 4569	SABab	20.0	9.3	1	0
NGC 4579	SABb	20.0	9.3	1	1
NGC 4594	SAa	13.7	0.0	1	1
NGC 4625	SABmp	9.5	0.0	0	0
NGC 4631	SBd	9.0	0.0	0	1
NGC 4725	SABab	17.1	9.3	1	1
NGC 4736	SAab	5.3	9.0	1	0
NGC 4826	SAab	5.6	9.4	1	1
NGC 5033	SAc	13.3	9.1	1	0
NGC 5055	SAbc	8.2	9.3	1	1
NGC 5194	SABbc	8.2	9.3	1	1
NGC 5195	SB0p	8.2	0.0	1	0
NGC 5408	IBm	4.5	8.0	0	0
NGC 5474	SAcd	6.9	0.0	0	1
NGC 5713	SABbcp	26.6	0.0	0	1
NGC 5866	S0	12.5	0.0	1	1
NGC 6822	IBm	0.6	8.1	0	1
NGC 6946	SABcd	5.5	9.1	0	1
NGC 7331	SAb	15.7	9.1	1	1
NGC 7552	SAc	22.3	9.0	1	1
NGC 7793	SAd	3.2	8.6	0	1
TOL 89	SBdm	15.0	0.0	0	1

[a]Shows spectral signatures of an active galactic nuclei (Dale et al., 2006).

[b]Indicates Hα observations

In addition to the infrared data contained in the SINGS and 2MASS LGA data releases, 45 galaxies had publicly-available Hα images, obtained from telescopes at *Kitt Peak National Observatory* (*KPNO*) or *Cerro Tololo Inter-American Observatory* (*CTIO*). We used the continuum subtracted Hα images contained within the SINGS data release. In practice, we found a small median offset in the background in the Hα subtracted images. In cases where the offset was larger than the median sky background level, we added this pedestal value to the images.

Because nuclear activity may contribute significantly to NIR and MIR flux, we took careful consideration of which systems hosted active galactic nuclei. Galaxies were differentiated based on nuclear activity using the results from Dale et al. (2006), who used

optical line diagnostics to identify which SINGS nuclei are either starburst dominated or require additional powering from an AGN, using the Liner/Starburst boundary of N II $\lambda6583/\mathrm{H}\alpha \sim 0.6$. This identification is included in Table 4.1.

4.4 Methods

4.4.1 Motivation for pixel-by-pixel analysis

An analysis of galaxy colours at the level of individual pixels is substantially more complicated than the usual approach based on integrated photometry using large apertures. It is important to establish from the outset whether such a complicated approach is really required in order to understand the underlying physics. Before embarking on a description of our methodology, we will first attempt to justify the underlying need for it.

At near-ultraviolet and visible wavelengths a galaxy's spectral energy distribution is the sum of the light from the stellar populations that make up the galaxy, modulated by dust absorption, and augmented by additional sources of emission (such as nebular lines). The different ages of the stellar populations impact the SED and the resulting colours, as young high-mass stars peak emission at shorter wavelengths and have blue visible colours, while older low-mass stars peak emission at red wavelengths and have redder visible colours. Slightly longer near-infrared wavelengths (around $\sim$1–2 μm) are ideal for probing the bulk of a galaxy's stellar mass, because starlight still dominates the overall SED and most of the light at these wavelengths comes from low-mass stars which dominate the stellar mass budget[2]. The colours of stellar populations in the near-infrared are relatively constant, probing the Rayleigh-Jeans tail of the stellar emission, where the ratio of emission in two wavebands is similar for an O-star and a K-star. Slightly longer wavelengths, say between 2 μm and 5 μm, are special. This wavelength range corresponds to a minimum in a galaxy's SED, because the Rayleigh-Jeans tail of starlight is rapidly declining but thermal emission from warm dust is not yet significant. Additional components of a galaxy that happen to emit at these wavelengths, such as hot dust, may be detectable at these wavelenghts even if they do not contribute a large fraction of a galaxy's bolometric output, simply because of contrast against the weak underlying

[2]Although an important exception occurs when the galaxies are 1–3 Gyr old, at which point light from thermally-pulsating AGB stars can dominate.

galactic SED. At wavelengths longer than 5 μm starlight starts to play a negligible role, and the physics of dust emission takes over. For example in the *Spitzer* 5.6 μm and 8.0 μm bands, molecular emission lines from Polycyclic Aromatic Hydrocarbons (PAHs) are important, while at 24 μm most of the light comes from the thermal emission of warm dust, whether it be related to stochastic heating of very small grains or intense heating of dust in the circumstellar environment.

Some of these ideas are illustrated in Figure 4.1. The left-hand panel of the figure shows a ratio of optical and near-infrared colours. Integrated photometry from Dale et al. (2007) for the SINGS sample (black asterisks) is plotted along with rest-frame colours from a high-redshift galaxy sample (data taken from the Gemini Deep Deep Survey; Abraham et al. 2004 and was analyzed in chapters 2 and 3 of this thesis). For the high-redshift data, symbols have been keyed to differing galaxy types as indicated by the spectral indicators given in Abraham et al. (2004). star-forming galaxies show spectral indicators of young stellar populations, while intermediate and evolved galaxies are mainly comprised of older stellar populations. The axes can be converted to AB magnitude colours by multiplying by 2.5.

The spread in the $I_{1.25}/I_{0.43}$ ratio (or, in magnitude space, $B-J$ colour) is over 1 dex and is much larger than the spread in the NIR intensity ratios ($J-H$ colour). star-forming galaxies tend to have bluer $B-J$ colour and evolved galaxies have redder $B-J$ colour, but the intermediate galaxies are spread throughout (dust can play a major role in this spread). In the right-hand plot, near-infrared colours are plotted for both the SINGS and GDDS rest-frame sample. The rest-frame colours of the high redshift data are interpolated from SED models fit to the observed photometry. The purple crosses are from SED models that only incorporate emission from star light and attenuation by dust. The NIR colours of these models colours occupy a compact region in the NIR colour-colour plot. However, in Mentuch et al. (2009) (and chapter 3 of this thesis), we show that these models are not a good description of the near-infrared observed photometry and find that a SED stellar population augmented with a NIR emission model better represents the observations. rest-frame colours derived from these SEDs are shown in the right panel (keyed to galaxy spectral types). These rest-frame colours of the high-redshift GDDS sample are consistent with the SINGS photometry for galaxies composed primarily of evolved populations, but for the star-forming and intermediate galaxies, the GDDS galaxies, which have higher SFRs compared to the low redshift SINGS dataset, show a large spread toward increasing $I_{3.6}/I_{1.25}$ ratios (or bluer $J-L$ colour) and $I_{4.5}/I_{3.6}$

ratios.

On the whole, Figure 4.1 makes three main points. (1) Near-infrared stellar population synthesis tracks (purple crosses) show much less variation (~ 0.2 dex) than visible-wavelength population synthesis tracks ($\sim$ 1 dex). Compared to visible-wavelength colours, near-IR colours depend little on the star formation rate or age of a galaxy. (2) In spite of the previous point, real galaxies (in particular those from the high-z sample and a couple nearby galaxies) show much greater variation (~ 1 dex) in near-infrared colour than can be encompassed by stellar population models. (3) As a result of the previous two points, the large variation in the NIR galaxy colours must be telling us quite a lot about dust or some other source of non-stellar emission. Either the starlight is being reddened by dust absorption, or dust emission must be contributing to the colours at surprisingly short wavelengths. How can we distinguish between these two possibilities?

Resolving galaxy colours can help distinguish between the latter two possibilities, because the properties of dust are known to vary from place-to-place in galaxies. Figure 4.1 shows that galaxy colours tend to scatter along the extinction vectors found in starburst regions, but *not* along the vectors appropriate for regions outside of starburst regions. The extinction curve for lines of sight through our own galaxy (obtained by the GLIMPSE survey, Indebetouw et al., 2005) is shown in green. Using the prescriptions presented in Pei (1992), we see that this extinction curve is consistent with the dust extinction law for the Milky Way (shown in red), the Small Magellanic Cloud (shown in orange) and the Large Magellanic Cloud (shown in cyan). In all these cases, teh observations demonstrate redder NIR colours. The extinction measured in starburst galaxies from Calzetti et al. (1994) is plotted in blue, and the theoretical model from Charlot & Fall (2000) is shown in black. In this figure we show all extinction vectors originating from the colours ($\log_{10}$ $I_{3.6}/I_{1.25}$, $\log_{10}$ $I_{4.5}/I_{3.6}$ = -0.30, -0.17) which we found to be the average colours of stellar emission in the NIR from the PEGASE.2 stellar SEDs[3]. The trend for NIR colours along this vector, predicted to be due to dust exinction in star burst regions, is supported by the high redshift data. The star-forming galaxies tend to have the reddest NIR colours, but we can not say for certain that dust extinction is the main culprit. Most of the GDDS galaxies have total extinction values $A_v < 1.5$ mag. The extinction vectors here suggest the extinction is in excess of $A_v > 2$ mag. What do the

[3]These colours are likely redder than that from pure stellar emission. Attenuation due to dust was included in these models.

Table 4.2. Colour key for Near-infrared colour criteria

Colour key	[a] $\log_{10}$ $I_{3.6}/I_{1.25}$	[b] $\log_{10}$ $I_{4.5}/I_{3.6}$
Red	-0.6 to -0.4	-0.19
Orange	-0.4 to -0.2	-0.17
Yellow	-0.2 to 0.0	-0.14
Green	0.0 to 0.2	-0.12
Blue	>0.2	-0.09
Purple	Manually selected	

[a]Upper and lower limits.

[b]Value in the center of the parallelogram shown in Figure 4.1.

nearby galaxies tell us about dust extinction in the NIR?

The NIR colours for the nearby sample are less scattered in the near-infrared colour plot shown in Figure 4.1. Does this small scatter remain when we resolve the galaxies on smaller spatial scales? Or do contributions from different stellar populations lead to more scatter in the NIR colours? Our methodology is to divide the galaxy into regions based on different colour-cuts motivated by both the spread in the data and the extinction curve from Charlot & Fall (2000) as indicated by the coloured parallelograms shown in Figure 4.1. The upper and lower limits of the boxes are defined as 0.1 dex above and below the extinction vector of Charlot & Fall (2000). The regions are separated in steps of increasing $\log_{10}$ $I_{3.6}/I_{1.25} = 0.2$ dex (or 0.5 mags in $L - J$ colour) from $\log_{10}$ $I_{3.6}/I_{1.25} = -0.6$. We summarize the properties of the NIR colour-selected regions in Table 4.2.

4.4.2 Image preparation

Prior to analyzing the pixel-by-pixel colours of our galaxy sample a number of steps were taken. These were:

1. All images were re-sampled to the IRAC plate scale of 1.22″/pixel using the `remap` tool in the `WCStools` library (Mink, 2002).

2. The counts in each pixel were converted to intensity units of MJy/sr.

3. Images were registered to sub-pixel accuracy using unsaturated bright stars and

500 by 500 pixel ($\sim$10.2′ by $\sim$10.2′) subsets were cut from the registered master frames.

4. Saturated regions and large galaxy neighbours on each image were manually masked.

5. All images were convolved with a gaussian kernel to match the diffraction-limited $\sim$6″ beam of the 24 μm MIPS image point-spread function. We assumed a median FWHM of 1.0″, 2.8″, 1.7″, 1.7″, 1.9″, 2.0″ and 6.0″ for the 1.25, 3.6, 4.5, 5.6, 8.0 and 24 μm images, respectively. Pixel-by-pixel image analysis requires that each pixel value be a good representation of the true intensity in the area of galaxy contained by the pixel. By convolving our images, we ensured that the distribution of intensities were matched as they were spread across the pixels by varying point-spread functions.

6. Bright foreground stars and small background galaxies were automatically removed. Foreground stars were removed in 5 pixel (6.1″) radius apertures using the the 2MASS point source catalog. Unfortunately many compact H II regions are falsely identified as point sources in the 2MASS catalog, so we attempted to identify these sources beforehand through their mid-infrared colours as in Muñoz-Mateos et al. (2009). We also did not remove any point sources with 24 μm intensity > 0.7 MJy. These two criteria result in $\sim$30% catalog point source removal, with some contaminants remaining, but we chose this approach to preserve compact H II regions and compact nuclear sources such as AGN. In addition, faint background galaxies have the potential to show up as spurious objects in our analysis. We have inspected each images carefully to note cases where contamination remains important after the steps just described, and will explicitly note these cases below.

7. We used a non-linear adaptive smoothing algorithm on the 1.25, 3.6, 4.5 μm images so that $S/N > 15$ is obtained in each pixel. This final step is non-standard and will be described below.

4.4.3 Adaptive smoothing

Much of our analysis is based on an investigation of the flux ratios of individual pixels. This required the construction of data frames obtained by dividing 1.25 μm, 3.6 μm, and 4.5 μm images against each other. To minimize the noise in the resulting divided images

we used the `Adaptsmooth` software (Zibetti, 2009) to median smooth the images so that a reasonably high signal-to-noise (S/N) threshold is first met. This trades resolution at low signal-to-noise levels for robustness in the final flux ratios (see the discussion in Zibetti et al. 2009 for details).

Our goal with `Adaptsmooth` was to obtain input data frames where $S/N > 15$ in each pixel. `Adaptsmooth` works by taking the median intensity over a smoothing aperture with a radius defined by the size needed to meet the $S/N > 15$ criterion. If the smoothing radius required is greater than 12 pixels, the algorithm is declared to have failed for that pixel, and the pixel is excluded from subsequent analysis. All results reported in this chapter in which colours were computed in individual pixels uses the smoothed then convolved images. For results described below in which the average intensity measurements were needed, we simply used the convolved images (without smoothing applied) as non-linear smoothing can sometimes lead to modest overestimates of the pixel intensities (see Zibetti et al. 2009), and our philosophy was to use adaptive smoothing only where it was really needed.

4.5 Results

The near-infrared colours in the individual pixels of the 68 galaxies in our sample were measured by performing image division with the median smoothed (and signal-to-noise optimized) then convolved images (as described in§ 4.4). The resulting pixel colours in the NIR colour space are shown for each galaxy in our sample in Figure 4.2. We find 17 galaxies to have atypical pixel distributions and these are discussed later in § 4.5.3. On the left, $10.2' \times 10.2'$ images of the galaxies are shown at IRAC 3.6 μm. Regions with saturated objects, foreground stars or neighbouring galaxies are removed. To the right of this image, we indicate the spatial location of the NIR colour-selected pixels. The colours are keyed according to the NIR colour-selection, shown in Figure 4.1 and defined in Table 4.2.

The rightmost three columns show binned colour-colour diagrams with the intensity of cells keyed to various quantities. The middle panel's intensity is keyed to the total number of pixels in that colour bin. The scatter in pixel NIR colours is larger than for the integrated colours of the SINGS galaxies shown in Figure 4.1, with some pixels containing intensity ratios at $I_{3.6}/I_{1.25} > 1$, larger than any of the integrated colours. As with the integrated colours, the majority of pixels in the galaxies are found in the orange region,

that is 0.1 dex (or 0.25 mags) above and below our canonical colour for the sample of $\log_{10}$ $I_{3.6}/I_{1.25}$, $\log_{10}$ $I_{4.5}/I_{3.6}$ = -0.30, -0.17, or (1.25]-[3.6]$_{AB}$ = -0.75 and [3.6]-[4.5]$_{AB}$ = -0.425). A smaller subset of pixels tend to scatter along the extinction vector defined by $\lambda^{-0.7}$ from empirical modeling by Charlot & Fall (2000), shown to be a good match to starburst galaxies from Calzetti et al. (1994).

Figure 4.2 allows us to map the colour-selected pixels into the spatial domain of the galaxy. The majority of pixels with NIR colours (keyed as orange regions) described by stellar emission are found throughout the galaxy. Regions with redder colours (identified as yellow then green then blue) follow the spiral structure and regions of star formation in the galaxy. A degeneracy between extinction and emission occurs at the brightest knots of star formation, where the NIR colours are their reddest. If these regions correspond to regions of high dust extinction, then the red NIR colours may be the result of dust extinction in which the light at 3.6 μm is attenuated less than the 1.25 μm emission. On the other hand, additional emission can also explain the excess continuum emission at $2 - 5\,\mu$m.

Fortunately, for 45 of the galaxies, continuum subtracted Hα images can be combined with 24 μm images to create two composite images that represent the intrinsic Hα emission and the dust extinction at Hα in each pixel. The intrinsic Hα line emission luminosity, and consequently the star formation rate, of normal star-forming galaxies and H II regions can be estimated empirically as a linear superposition of the observed Hα and 24 μm flux (Kennicutt et al., 2007; Calzetti et al., 2007). Recent work (Kennicutt et al., 2009) shows that for a sample of galaxies, including the SINGS galaxies, the dust corrected, intrinsic Hα_{int} luminosity is related to the observed Hα_{obs} and 24 μm luminosity by:

$$L(\mathrm{H}\alpha_{int}) = L(\mathrm{H}\alpha_{obs}) + 0.02 \times L(24\,\mu\mathrm{m}) \tag{4.1}$$

with the galaxies showing a rms dispersion of 0.119 dex in the fit. An important caveat to note is that this equation was inferred from integrated photometry and is only applicable over the physical scale at which interstellar radiation from stars and re-processed radiation by dust are both encapsulated. We assume, by applying this equation to each pixel, that the 24 μm PSF-matched resolution (6″) of our images covers a length larger

than this physical scale. This value can be converted to a star formation rate by a multiplicative factor (for example SFR $(M_{\odot}/yr) = 7.942 \times 10^{-42}\,\mathrm{erg\,s^{-1}}\ \mathrm{L}(\mathrm{H}_{\alpha,int})$ is commonly used from Kennicutt (1998)), which in turn can be converted to the intrinsic Hα intensity (and is thus independent of the galaxy's distance) by multiplying the second term by the ratio of wavelengths:

$$I_{\mathrm{H}\alpha,int} = I_{\mathrm{H}\alpha,obs} + 0.02 \times \frac{24.0}{0.656} \times I_{24\,\mu\mathrm{m}} \tag{4.2}$$

Similarly, the average extinction in each pixel can be derived using the intrinsic Hα intensity, $I_{\mathrm{H}\alpha,int}$, defined above and the observed Hα intensity, $I_{\mathrm{H}\alpha,obs}$. The extinction, $A(H\alpha)$ in mag, is given as:

$$A(H\alpha) = 2.5 \log_{10}\left[1 + 0.02 \times (24.0/0.656)\frac{I_{24\,\mu\mathrm{m}}}{I_{H\alpha,obs}}\right] \tag{4.3}$$

The two panels on the right of Figure 4.2 show the median intrinsic Hα intensity, $I_{\mathrm{H}\alpha,int}$, and the median dust extinction, $A(H\alpha)$, in the pixels corresponding to the given NIR colours. By spatially resolving the galaxy colours, we can see a trend emerge in the NIR colour-colour plane in the pixel plots shown in Figure 4.2. The pixels which scatter along the extinction line to the redder colour-selected regions also tend to have the highest intrinsic Hα intensities. Regions with higher intensity star formation show redder NIR colours. The dust extinction, in the far right panel, shows less variation, and tends to be $A(H\alpha) = 0 - 2\,\mathrm{mag}$. *There is no strong trend of increasingly red NIR colours with increasing dust extinction.* We now attempt to quantify this by measuring the average surface brightness in increasingly red NIR colour regions.

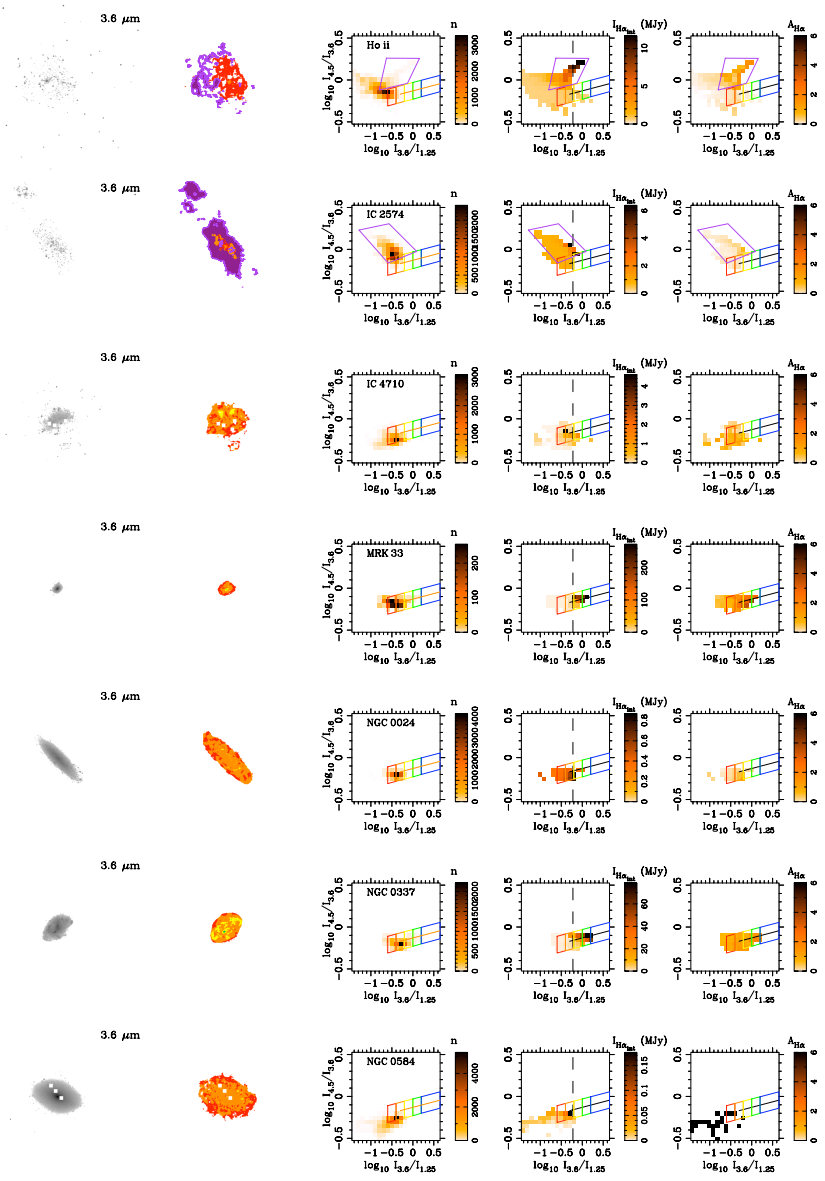

Figure 4.2 Images at IRAC 3.6 μm and the spatial locations of the NIR colour selected pixels (defined in Table 4.2) are shown for each galaxy in the sample. The three left panels plot the pixel NIR colours with the intensity levels defined as the number of pixels at each colour bin in the first of these three panels. NIR colour selection criteria is shown in coloured boxes. The last two panels show the median intrinisic Hα intensity (and consequently star formation rate) and the median $A(H\alpha)$ in mag for all the pixel in that NIR colour bin.

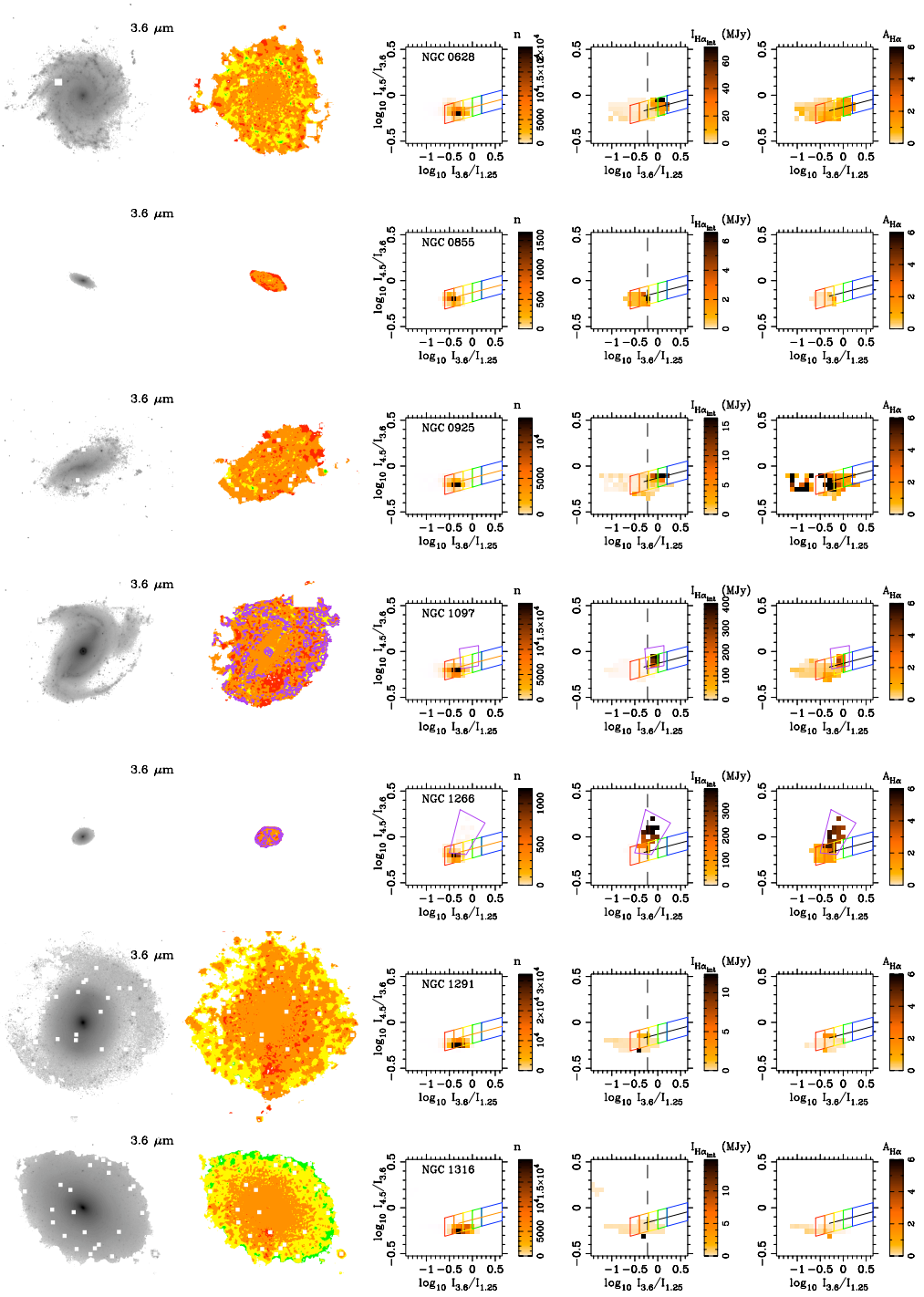

Figure 4.2 – cont'd

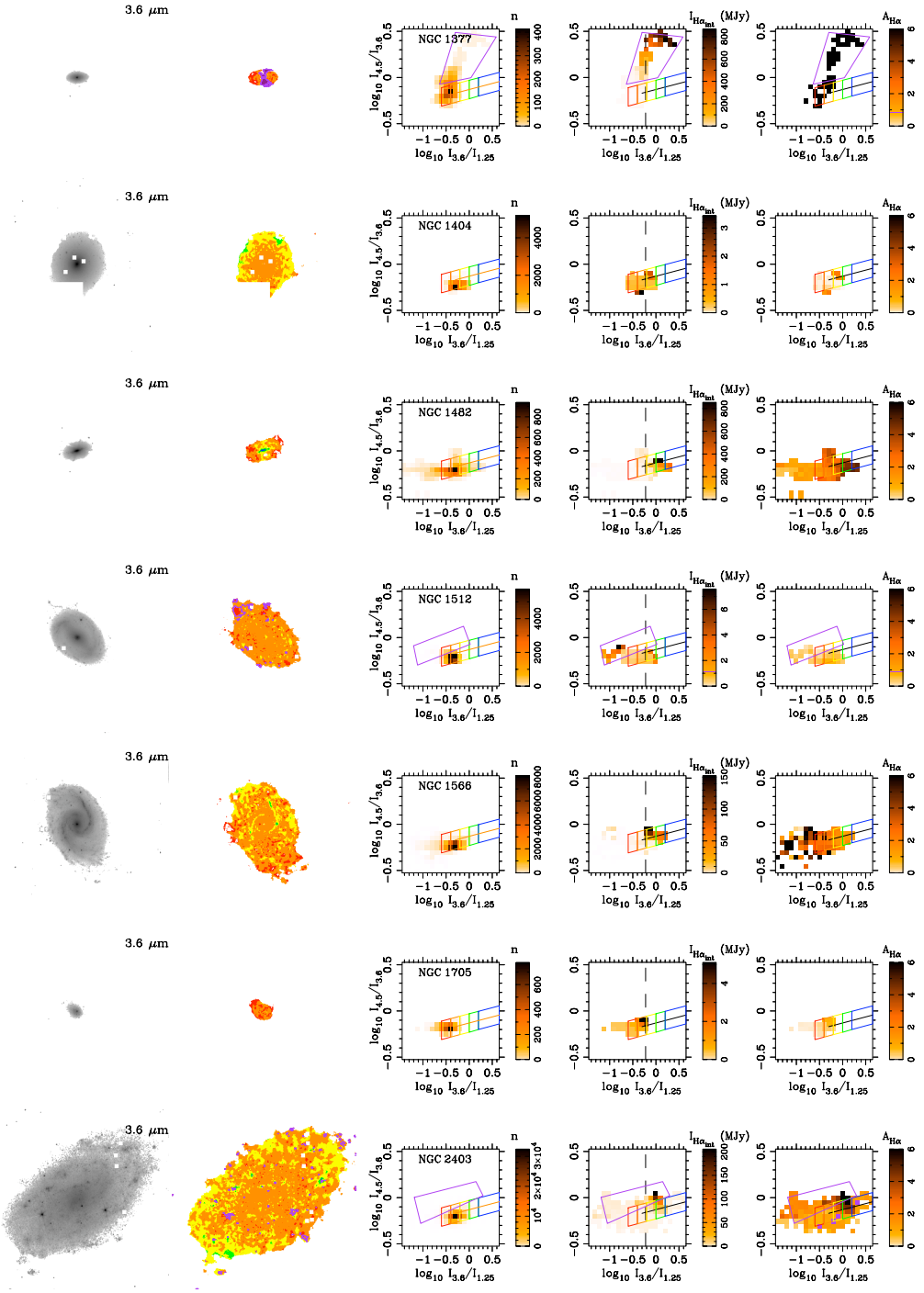

Figure 4.2 – cont'd

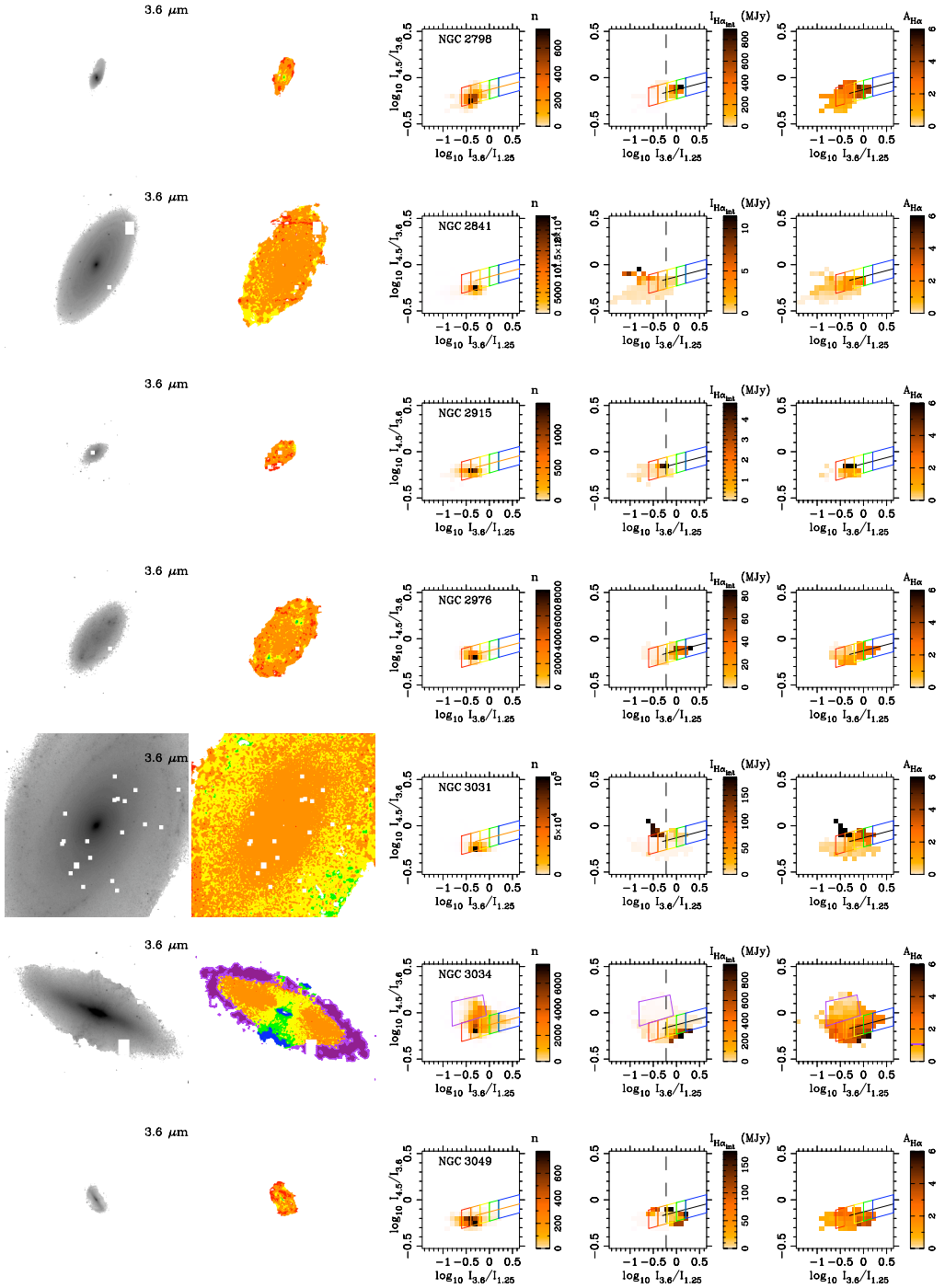

Figure 4.2 – cont'd

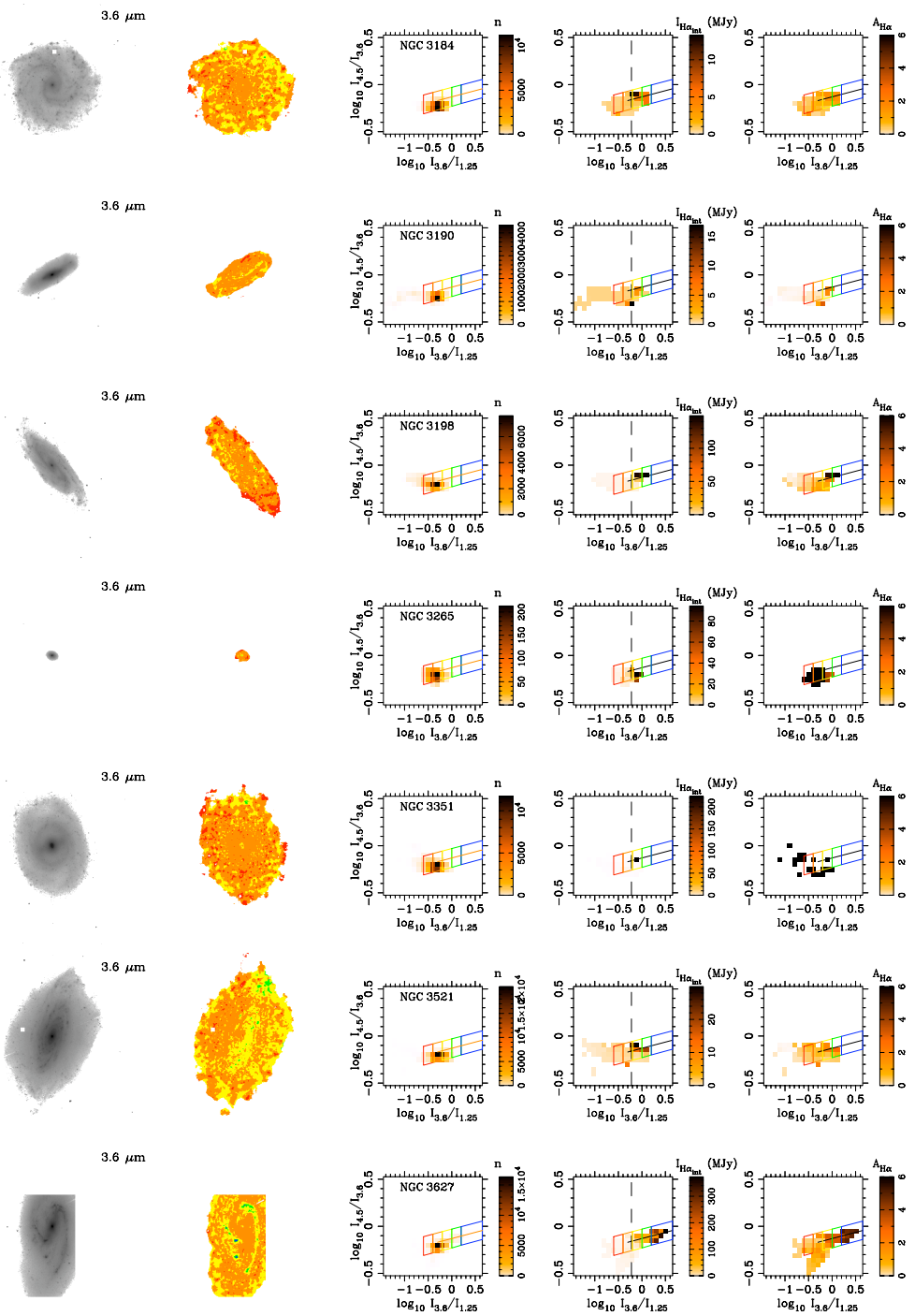

Figure 4.2 – cont'd

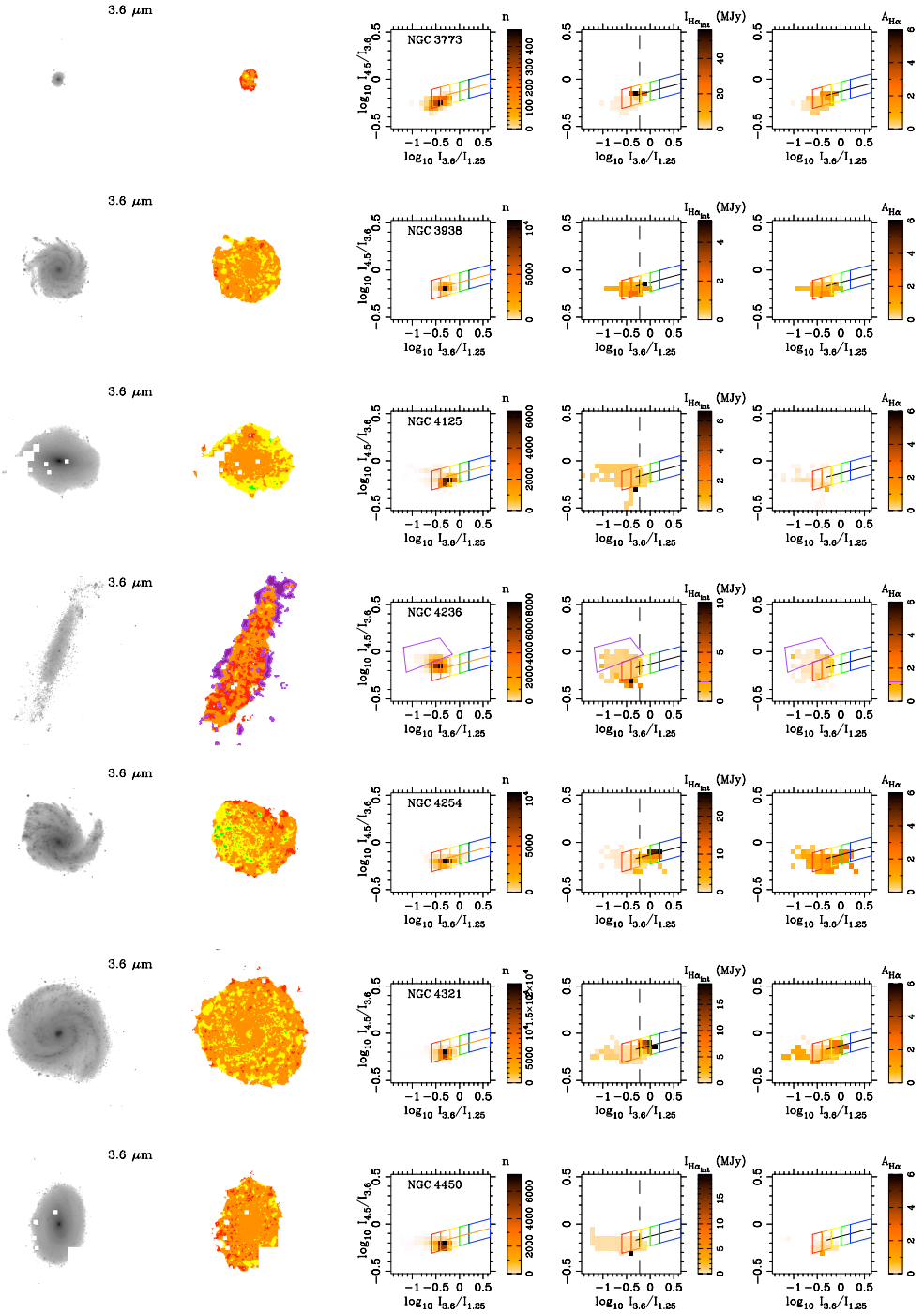

Figure 4.2 – cont'd

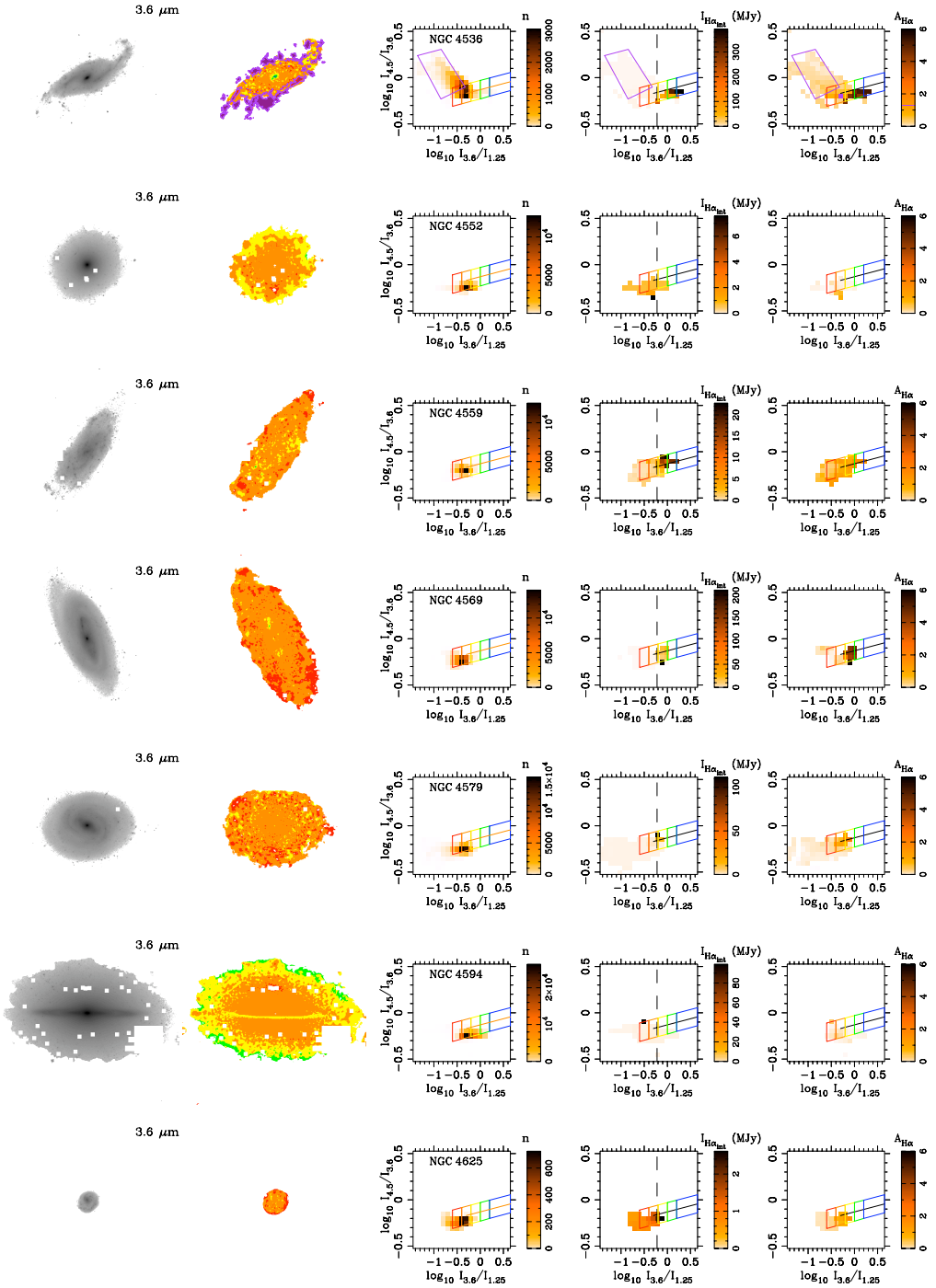

Figure 4.2 – cont'd

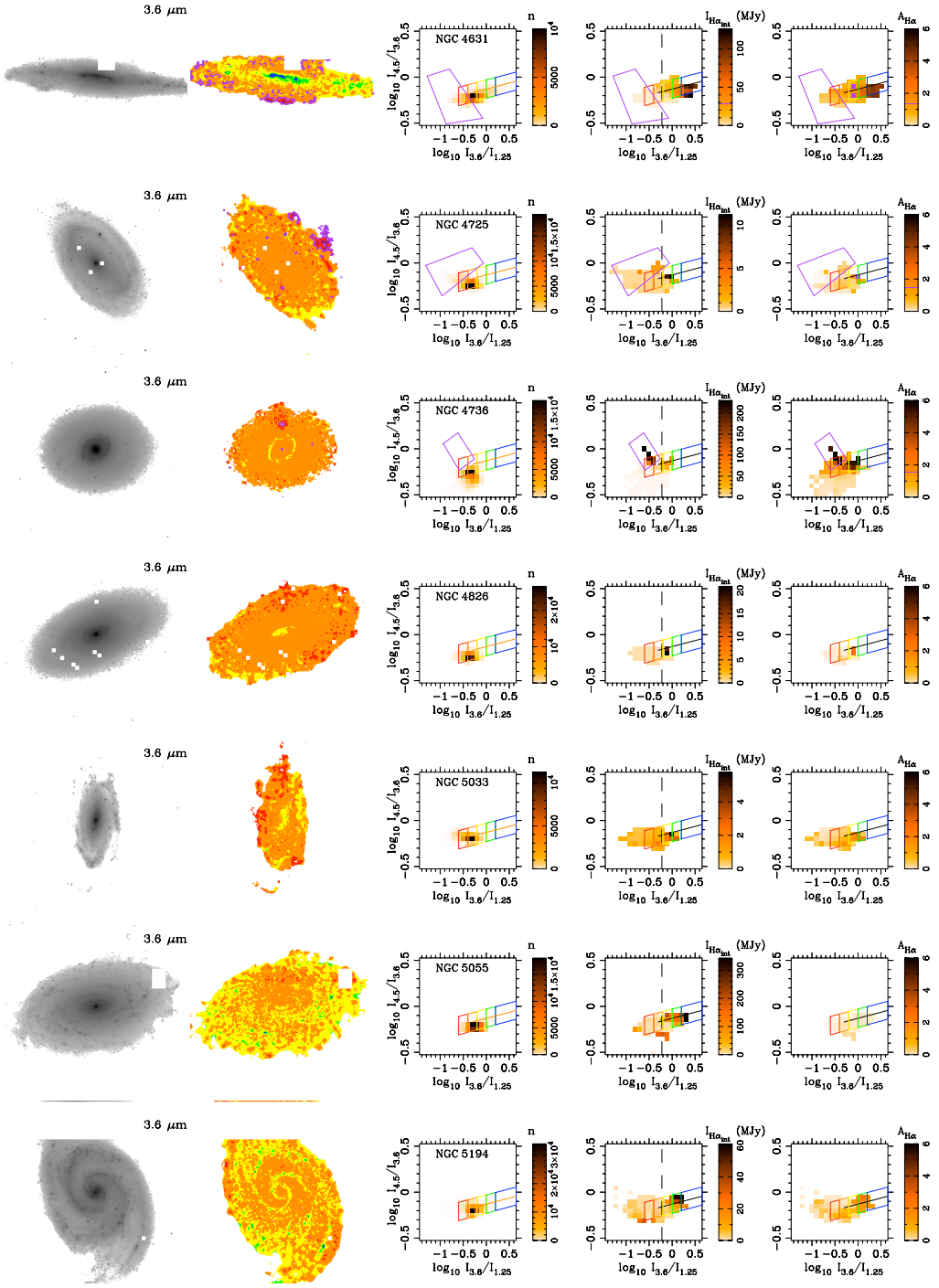

Figure 4.2 – cont'd

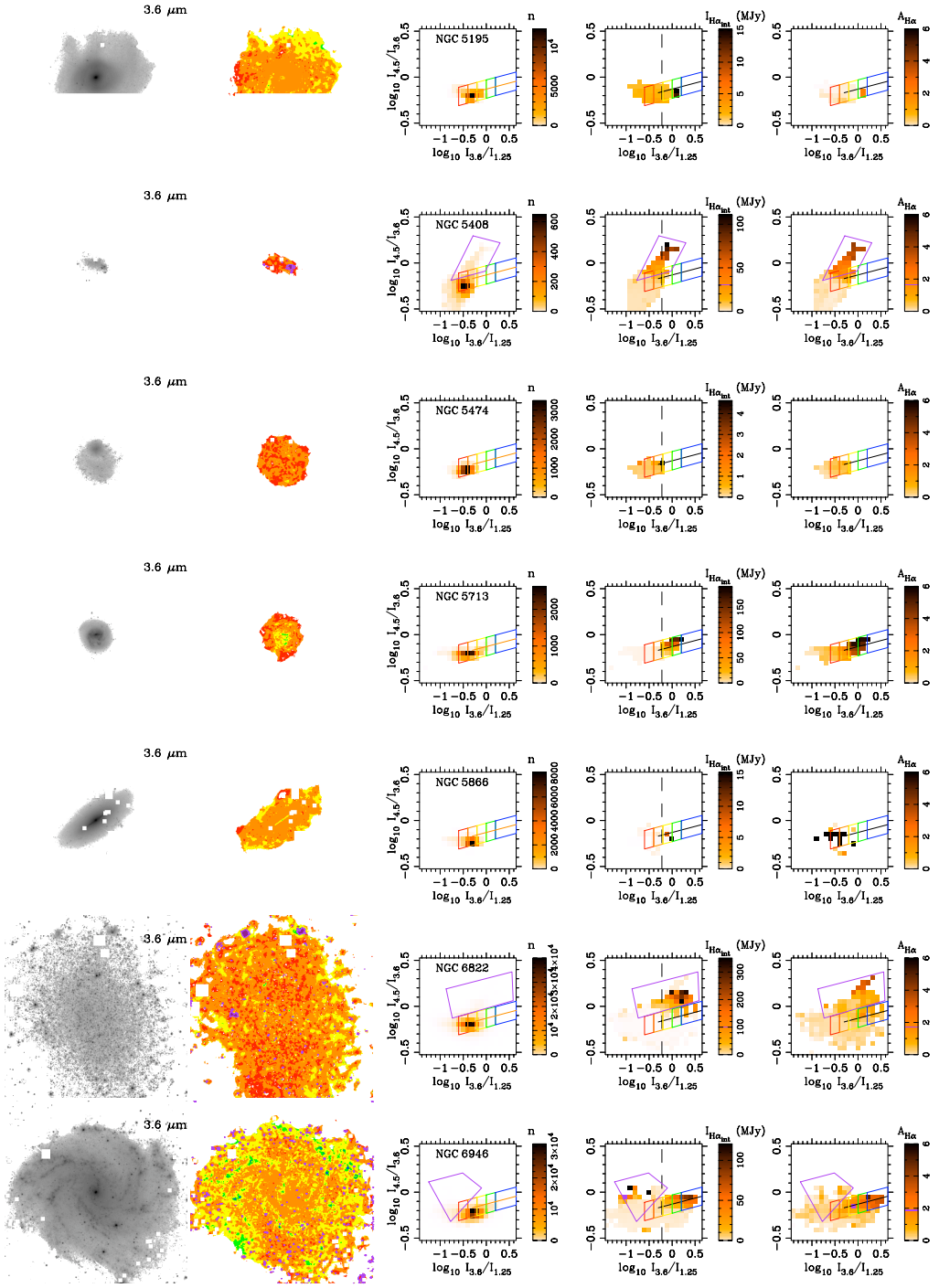

Figure 4.2 – cont'd

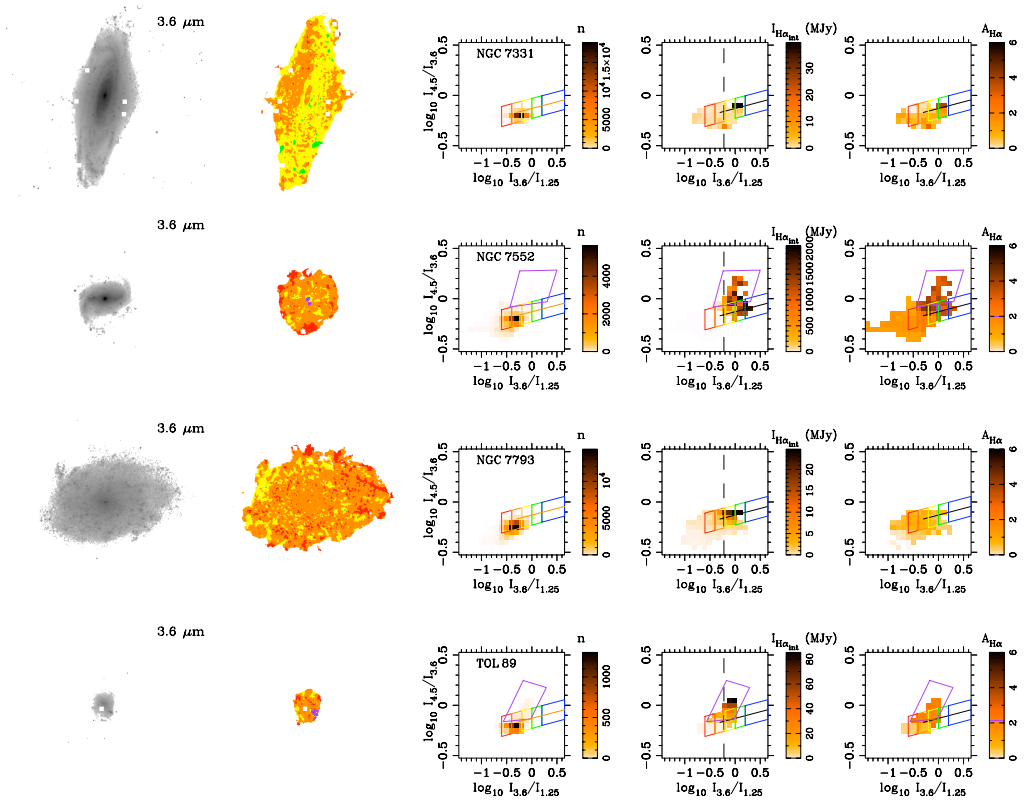

Figure 4.2 – cont'd

4.5.1 Surface brightness measurements

We measured the average intensity (i.e. surface brightness) for each galaxy in each of the NIR colour selected regions marking 0.1 dex in colour space above and below the extinction curve of $\lambda^{-0.7}$ from Charlot & Fall (2000) and defined in Table 4.2. The regions are mapped in the spatial domain and in the NIR colour plane in the second and third columns of Figure 4.2. Measurements are made at all wavelengths in this analysis (0.6563, 1.25, 3.6, 4.5, 5.6, 8.0 and 24 μm) as well as to the intrinsic Hα image defined by Equation 4.2 and the $A(H\alpha)$ dust extinction image defined by Equation 4.3.

The intensity in each region is compared for each observed waveband to the intrinsic Hα intensity (a direct measure of the average star formation rate) in Figure 4.3. There is clear correlation for increasing intensity at 5.6, 8.0 and 24 μm with intrinsic Hα intensity. These bands are dominated by PAH emission. Also evident is a correlation between emission at 1.25, 3.6 and 4.5 μm and the intrinsic Hα emission, although here the trends are more nuanced. In regions of high intrinsic Hα intensities (and high star formation rates), the emission from the young star-forming population dominates over the emission of the longer lived population. But at lower Hα intensities ($\lesssim 10$ MJy/sr), the emission at 3.6, 4.5 μm and particularly at 1.25 μm is scattered in this plane, indicating that in these regions the NIR emission from the star-forming population is lower and the emission traces the evolved stellar populations which varies from galaxy to galaxy as expected from the different star formation histories. We calculate the linear fits of each relation and tabulate the parameters in Table 4.3. The large rms scatter of the fit in log-log space leads to the large range in possible slope values for the linear relation.

Our results support the idea that very red NIR colours are due to sources of NIR emission. But the possibility that extinction may also be important needs further exploration. In particular, the trend for increasingly red NIR colours along the line predicted by extinction from the model of Charlot & Fall (2000) may suggest that the spread in NIR colours is at least partly due to dust extinction rather than any additional emission mechanism. Using the dust extinction image defined by Equation 4.3, we can measure the average dust extinction in the NIR colour-selected pixels. A trend of increasing $I_{4.5}/I_{3.6}$ colours with increasing dust extinction would give strong support for this scenario. In Figure 4.4, the average $I_{4.5}/I_{3.6}$ colour in each colour-selected region is plotted as a function of the dust attenuation, $A(H_{alpha})$. The data points are keyed to the colour selection regions. As expected (by design) the regions with higher NIR ratios are from the redder

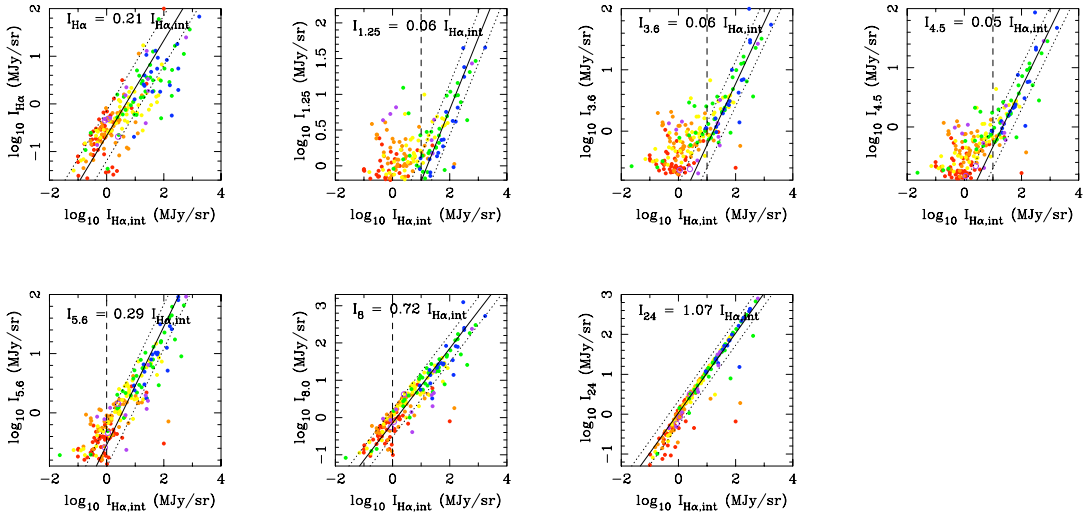

Figure 4.3 Surface brightness measurements at Hα, 1.25, 3.6, 4.5, 5.6, 8.0 and 24. μm as a function of the intrinsic Hα intensity (a direct measure of the average star formation rate per unit area). colours are keyed to increasingly red NIR colours (as defined in Table 4.2). Linear fits with zero offsets are fit to each distribution, whose slope is given in each plot. The rms of the fit is shown by the dotted curves. Only points to the right of the dashed vertical line are used for the fit to minimize the contribution of emission due to underlying evolved stellar populations. All points are used for the Hα and 24 μm fits as the Hα image is stellar subtracted and the stellar contribution at 24 μm image is assumed be negligible. The linear fit to each relation is tabulated in Table 4.3. Galaxies with anomalous NIR colours (discussed in § 4.5.3) whose pixels correspond to compact regions of star formation are shown as purple dots and those which correspond to broad distribution cirrus like emission are shown as open circles.

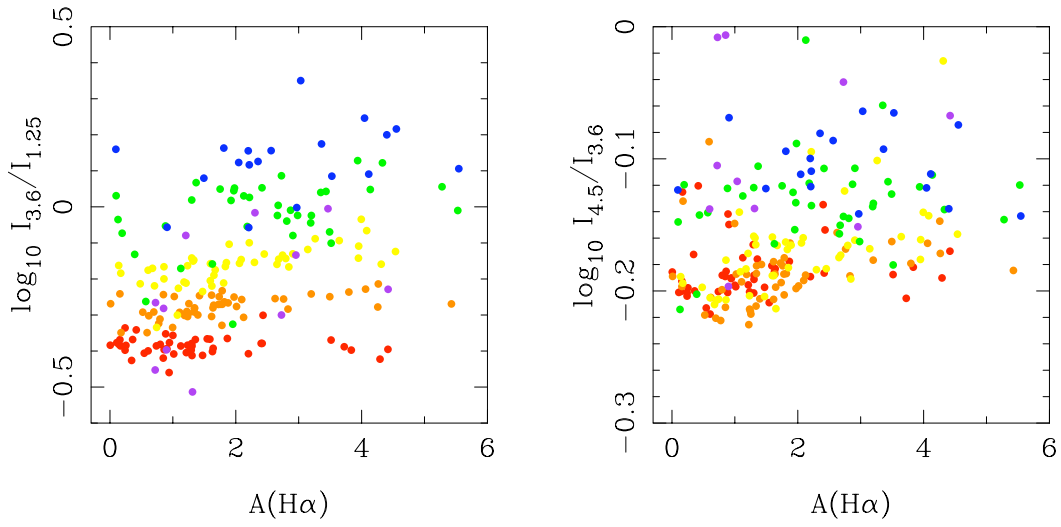

Figure 4.4 The average $I_{3.6}/I_{1.25}$ and $I_{4.5}/I_{3.6}$ colours in each of the 5 regions defined in Figure 4.2 as a function of the average dust extinction at Hα is shown in the left and right panels respectively. The colours are keyed to the NIR colour selected regions defined in§ 4.4 and described in Table 4.2. By design, the colours should change from red to blue with increasing $I_{3.6}/I_{1.25}$ and $I_{4.5}/I_{3.6}$ ratios. The Hα extinction is scattered with values ranging from 0 to 6 mags of extinction in all colour-selected regions. There is not a strong relation between dust extinction and red NIR colours.

colour-selected regions. The distribution of NIR colours versus extinction is scattered with extinction ranging from 0 to 6 mags in all colour-selected regions. There is a trend for the redder colour-selected regions having a higher median extinction value, likely a consequence of the higher star formation and dust content in these regions, resulting in slightly higher dust extinction. *However, overall, the support for a dominant trend between dust extinction and red NIR colours is not apparent.*

We further investigate any trends between average intensities at all observed wavebands and the average dust extinction in Figure 4.5. Again, the data show a correlation with the dust extinction. At 5.6, 8.0 and 24 μm larger extinction values correlate with higher intensities resulting from increased dust emission. These regions, as shown in Figure 4.3, correspond to more intense star-forming regions and as a result have the most extreme extinction values. However, the correlation with the dust extinction is weaker in all wavebands compared to the correlation between intensities and the intrinsic Hα emission shown in Figure 4.3. *In conclusion, Figures 4.3 to 4.5, indicate that the the*

NIR colour excess is due to emission and not dust extinction at wavelengths longer than 1 μm.

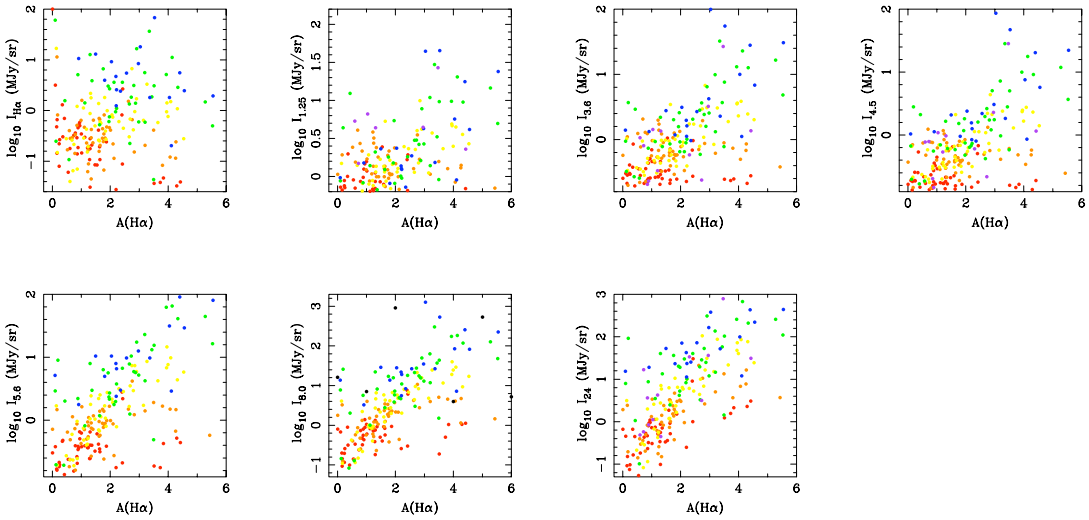

Figure 4.5 Surface brightness measurements at Hα (0.656), J (1.25), 3.6, 4.5, 5.6, 8.0 and 24. μm in relation to dust extinction derived from the ratio between the Hα and 24 μm intensities as described by Eq. 4.3. The different coloured points are keyed to the regions of increasingly redder NIR colours as defined in § 4.4 and plotted in Figure 4.2.

4.5.2 Colour-colour diagrams

We compute various colours for the average intensities measured in each NIR colour-selected region. In Figure 4.6, two IRAC colour-colour diagrams are shown for the average colours measured in the spatially resolved, colour-selected regions. In addition, the colours from the total integrated photometry from Dale et al. (2007) for the SINGS sample is plotted as black crosses. The left panel shows the $I_{8.0}/I_{4.5}$, $I_{5.6}/I_{4.5}$ ratios, the emission at 5.6 and 8.0 μm both normalized by the emission at 4.5 μm. While we have seen in Figure 4.3 that the emission linearly scales with the star formation intensity, and as a result the regions associated with the reddest NIR colours and largest star formation intensities (blue and green points) occupy the top left in this sequence. But in lower star-forming environments the ratios are lower and occupy a tight increasing red sequence in this colour space, likely due to the increasing contribution from stars at 4.5 μm and the decreasing contribution from PAH and/or NIR continuum emission at all three wavelengths.

In general, the reddest IRAC colours correspond to the higher star-forming regions, identified by their red NIR colours, but some regions with very red NIR colours (these regions are keyed as blue and green dots), have relative low $I_{8.0}/I_{4.5}$, $I_{5.6}/I_{4.5}$ ratios and also low star-forming intensities. These points correspond to regions contained within NGC 2841, NGC 4594, and NGC 6822. This emission is associated with low intensity emission on the outer edge of NGC 2841 and NGC 4594 where emission at mid-infrared wavelengths is low and may be similar to the low surface brightness cirrus emission in our own Galaxy. NGC 6822 also shows low mid-infrared emission despite having high $I_{3.6}/I_{1.25}$ and $I_{4.5}/I_{3.6}$ ratios. This galaxy is the closest member of the SINGS sample at a distance of only 0.6 Mpc and is noted for having low metallicity ([O/H] = 8.1), as well as a low PAH fraction of $q_{\rm PAH}$ = 0.7-1.0% (Draine et al., 2007). It is discuss later in more detail in § 4.5.3.

In general, the colours from full galaxy photometry are consistent with the trend in the left panel of Figure 4.6. Only one galaxy has integrated colours as red as the high star-forming regions. Spatially resolved photometry benefits from observing the full range of stellar populations within a galaxy, where integrated photometry would average over the extreme populations. In the case of red NIR colours and NIR excess emission, the brightest star-forming regions which drive the very red NIR colours are typically overwhelmed by the other stellar populations composing the galaxy.

The right panel shows another IRAC colour-colour plot. In regions of high star formation intensities, the $I_{8.0}/I_{4.5}$ becomes a constant value and corresponds to regions with the largest $I_{4.5}/I_{3.6}$ ratios. The distribution of colours is more scattered on the left part of the plot with $\log I_{4.5}/I_{3.6} < -0.15$ as a result of stellar emission dominating the $\log I_{4.5}/I_{3.6} < -0.15$ colour. A few of the integrated colours show large $I_{4.5}/I_{3.6}$. These galaxies are Holmberg I, .IC 2574, Mrk 33, NGC 0337, NGC 1291, NGC 1404, NGC 5474, NGC 5713. The purple points in these figures with low $I_{8.0}/I_{4.5}$ relative to the $I_{4.5}/I_{3.6}$ colours correspond to Holmberg II, NGC 1377, NGC 1512, NGC 1566, NGC 2403, NGC 2841, NGC 3031, NGC 4236, NGC 4536, NGC 4725, NGC 4736, NGC 6822, NGC 6946 with anomalous pixel colours are discussed in the next section.

4.5.3 Galaxies with anomalous NIR colour structures

Not all galaxies show binned pixel distributions similar to the typical ones presented in Figure 4.2. 26% show distributions with markedly different structures. To study these,

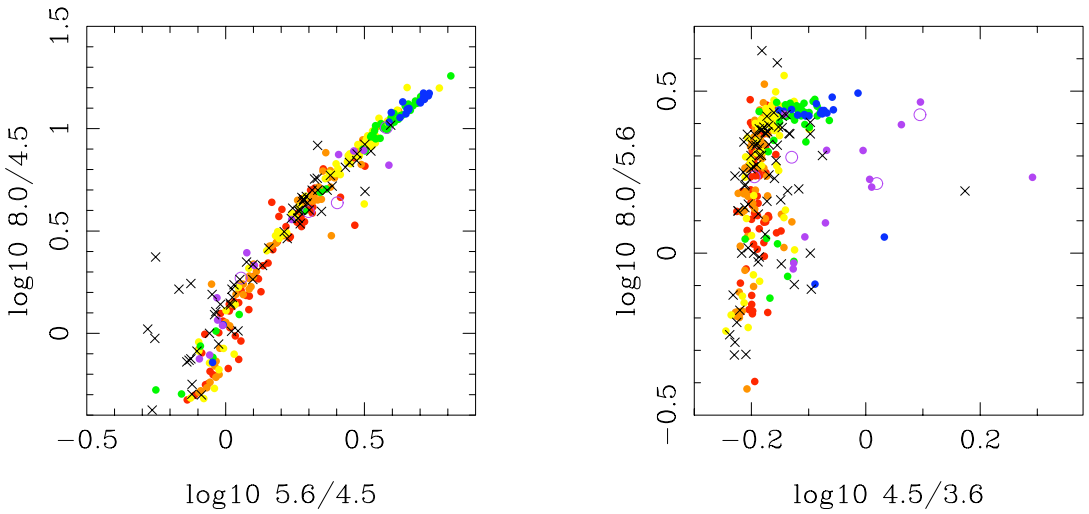

Figure 4.6 Colour-colour diagrams for the average colours in each of NIR colour selected region, keyed to the colours plotted in Figure 4.2. Additionally, colours for integrated photometry from Dale et al. (2007) are shown as black crosses and IRAC colours in regions with extremely red $I_{4.5}/I_{3.6}$ colours are plotted in purple. Open circles are for dots that are spatially related to cirrus like emission in the galaxies and solid purple circles identify regions that correspond to compact star formation.

we manually select regions in the NIR colour space to identify the spatial location of anomalous populations. Their location in pixel space and in the spatial domain are shown in purple for a subset of galaxies in Figures 4.7 and 4.8. The rest can be found in Figure 4.2. In some cases, the anomalous NIR colours are due to spurious pixels related to foreground stars not successfully removed or saturated pixels due to nearby bright neighbours. But for 18 galaxies we find that the red colours are either related to regions of clumpy star formation as indicated by compact 24 μm emission or related to extended emission, possibly analogous to cirrus emission.

Examples of the 6/13 galaxies with red NIR colours associated with star formation are shown in Figure 4.7. These galaxies (Holmberg II, NGC 1097, NGC 1266, NGC 1377, NGC 1512, NGC 2403, NGC 4725, NGC 4736, NGC 5408, NGC 6822, NGC 6946, NGC 7552, Tololo 89) generally show regions of compact star formation associated with the anomalous NIR pixel colours. In most of these cases, the NIR colours follow a vector corresponding to higher $I_{4.5}/I_{3.6}$ ratios than the $\lambda^{-0.7}$ extinction curve from Charlot & Fall (2000). For example, NGC 1377, NGC 5408 and Tololo 89 show a similar distribution of

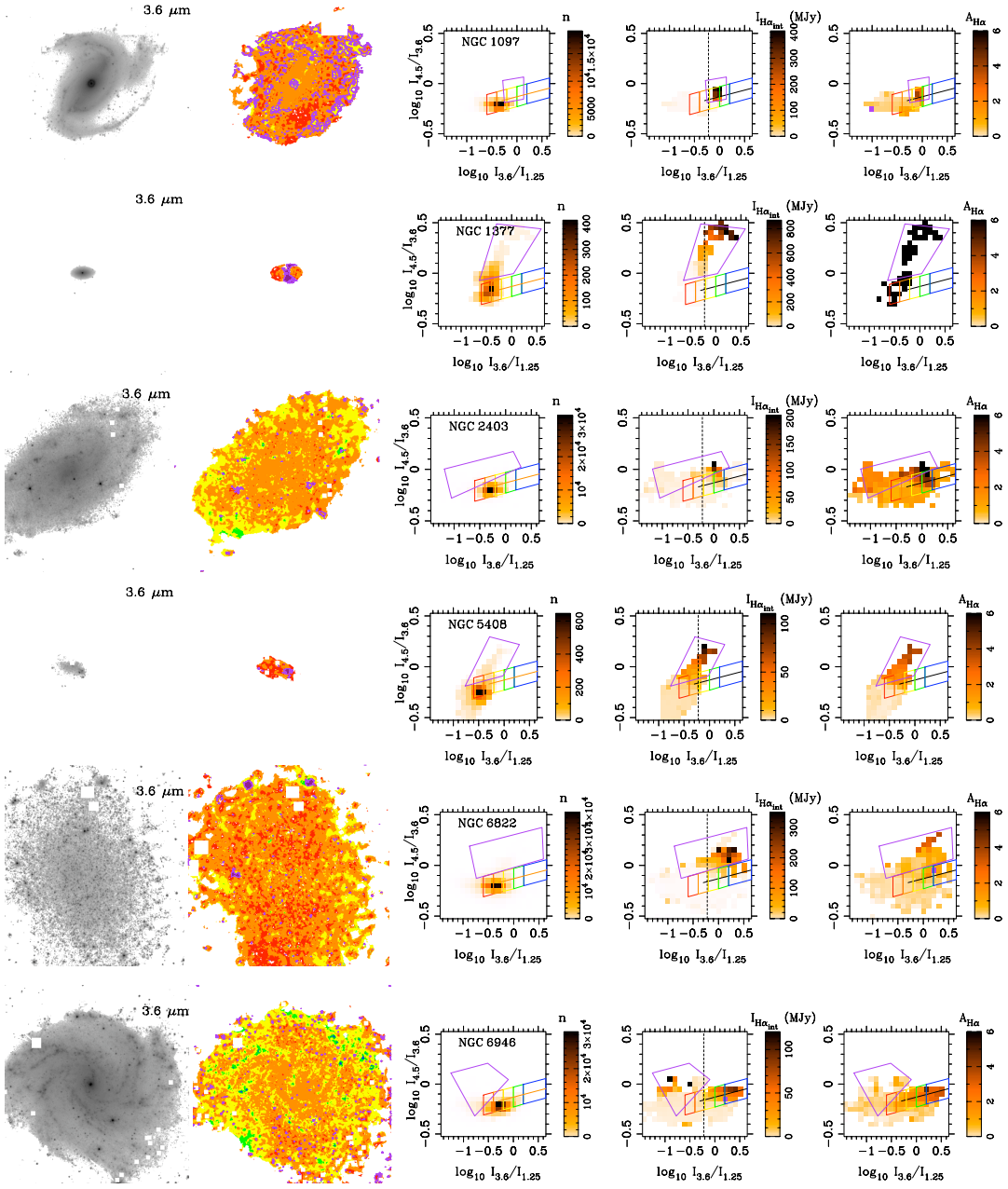

Figure 4.7 IRAC 3.6 μm images for galaxies with anomalous NIR pixel colours that correspond to bright compact regions of star formation are shown for (from top to bottom) NGC 1097, NGC 1266, NGC 1377. The second panel from the left shows the spatial location of the anomalous pixel colours (in purple). The left panel of the three pixel colour panels shows the number of pixels in each colour-colour bin. The middle panel indicates the median value of the intrinsic Hα intensity for all the pixels within that colour-colour bin. The right panel indicates the median dust extinction for the pixels.

NIR colours. The increasingly red NIR colours correspond to regions of increasing star formation (4th panel in Figure 4.7) and higher dust extinction (right panel). These regions correspond to compact regions with bright infrared emission. The emission is likely related to star formation; in many cases it corresponds to the brightest regions along a spiral arm or compact opaque star formation, as is the case for NGC 1377 which is an opaque starburst galaxy whose dust emission is optically thick (Roussel et al., 2006). In this galaxy, the emission is related to very young (< 1 Myr) starburst activity. These NIR colours are the result of either a different extinction law that manifests as an optically thick dust screen or perhaps a different dust emission law resulting from the high radiation fields produced by the starburst activity (in which the ratio of PAH emission and continuum emission from hot and warm dust is different than the typical spectrum found in normal star-forming environments found in this study).

The five galaxies (IC 2574, NGC 3034, NGC 4236, NGC 4536 and NGC 4631) with large $I_{4.5}/I_{3.6}$ ratios that correspond to more cirrus like emission are shown in Figure 4.8. The colour distribution of the pixels is unique in that the vector goes in the opposite direction that is seen in Figures 4.2 or 4.7. There is a trend of increasing $I_{4.5}/I_{3.6}$ ratios with decreasing $I_{3.6}/I_{1.25}$ ratios. These systems, have the lowest $I_{3.6}/I_{1.25}$ ratios for the entire sample of galaxies. These pixels correspond to emission found on the edges of the galaxy. In the case of IC 2574, it does correspond to bright Hα emission, but this is not the case in general. The dust extinction is not particularly high in these regions, except in NGC 3034 (M82) where dust extinction on the order of 1-2 mag is found (but this is lower than the rest of the galaxy which overall has a lot of dust extinction).

We have included the points for these 18 galaxies in the IRAC colour-colour diagrams in Figure 4.6. In the right panel, the regions have higher $I_{4.5}/I_{3.6}$ ratios than any of the normal colour-selected regions, and relatively lower $I_{8.0}/I_{5.6}$ ratios hinting at the possibility of lower PAH ratios. We also compare the average intensities (plotted as purple closed and open dots corresponding to compact and extended emission respectively) to the star formation rate intensity in Figure 4.3 and find that in most cases the values agree with the linear fits found for the standard NIR colour-selected regions. The only discrepancy is in the J-band, where very high intensities are found relative to the star formation emission indicating the possibility of a large stellar population with little to no associated dust emission as the PAH emission at longer wavelengths for these objects is low.

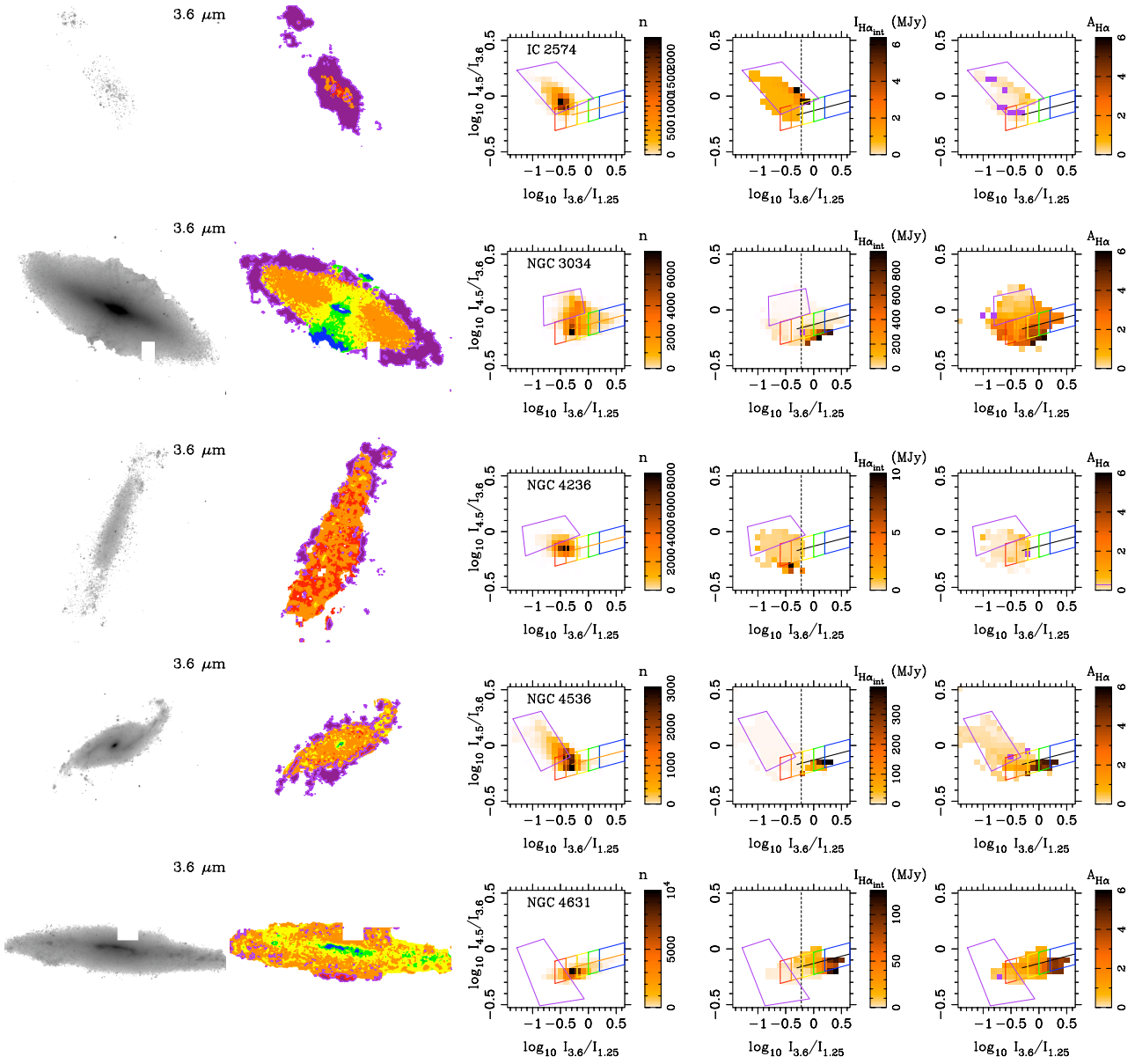

Figure 4.8 As in Figure 4.7 but for galaxies with a different spatial distribution of their extremely red NIR colours. Postage stamp images of the galaxy at IRAC 3.6 μm is shown along side the spatial location of the NIR colours for each pixel. From top to bottom: IC 2574, NGC 3034, NGC 4236, NGC 4536 and NGC 4631.

4.6 Discussion

Spatially resolved pixel-by-pixel analysis of the SINGS galaxies yields a number of insights regarding the underlying stellar populations and their resulting dust emission and extinction. In regions of negligible star formation, NIR colours occupy a small region of NIR colour space, and we have shown that the majority of pixels tend to be located in this colour space. However, younger populations, with higher Hα and 24 μm emission, tend to show colours that become increasingly red in the NIR, with both the intensity ratios of $I_{3.6}/I_{1.25}$ and $I_{4.5}/I_{3.6}$ increasing along a vector well matched by the $\lambda^{-0.7}$ extinction model from Charlot & Fall (2000). Motivated by this empirical trend in the data, we divided galaxies into different regions based on the NIR colour of each individual pixel. These regions are designed as encompassing 0.1 dex (or 0.25 mags) above and below the $\lambda^{-0.7}$ extinction curve separated into steps of 0.2 dex (0.5 mags) in $\log I_{3.6}/I_{1.25}$ colour starting at $\log I_{3.6}/I_{1.25} = -0.6$. By doing so we isolate regions with different NIR emission properties and consequently different stellar populations, revealing the relatively linear nature of emission in the near- and mid-infrared.

4.6.1 The linear scaling of the near/mid-infrared spectrum

The average intensity of NIR colour-selected regions is shown to scale with the average intrinsic Hα intensity in that region for the majority of bands in this study. The 5.8, 8.0 and 24 μm intensities scale linearly with this parameter, with scatter presumably mostly due the non-negligible contribution from the stellar population at 5.8 and 8.0 μm and also due to differences in metallicity (Calzetti et al., 2007) and possibly PAH fractions (Draine et al., 2007). Rather surprisingly, the shorter NIR wavelengths also show a linear relation to the star formation rate intensity at sufficiently high intensities where the emission is dominated by emission from the younger stellar populations (and associated dust). We find that linear fits to the data with zero offsets can fit the data in all wavebands, but limit the fits to high star formation intensities (I_{SFR} >10 MJy/sr) in the shorter bands and slightly lower star formation intensities (I_{SFR} >1 MJy/sr) at 5.8 and 8.0 μm.

The linear fit to each relation is tabulated in Table 4.3 and shown in Figure 4.9 as a canonical spectrum (black points, dotted line), normalized at 1.25 μm. For reference, three SEDs from stellar population models using PEGASE.2 are plotted for a galaxy with an exponentially declining star formation history with an e-folding time of 500 Myr at ages of 200 Myr (blue and green lines) and 3 Gyr (red line). The green spectrum is

Table 4.3. The linear scaling of I_λ with $I_{H\alpha}$

λ (μm)	slope$_{median}$	slope $_{range}$
0.656	0.214	0.064 - 0.716
1.25	0.062	0.027 - 0.140
3.6	0.059	0.026 - 0.138
4.5	0.046	0.020 - 0.107
5.6	0.286	0.121 - 0.678
8.	0.718	0.307 - 1.679
24.	1.074	0.533 - 2.163

for a 200 Myr old galaxy with dust extinction in the visible of $A_v = 0.75$, while the blue spectrum has no dust extinction applied. The older spectrum (red) is modeled with 0.25 mags of visual extinction. As emphasized in the methods section (§4.4), the stellar emission beyond 1 μm is not dependent on the star formation history of the galaxy and near-infrared colours for a galaxy that do not have emission from PAH and/or dust molecules are independent of a galaxy's age.

The canonical spectrum effectively measures the broad spectral energy distribution of a young stellar population and its surrounding dusty environment as the fits were made to minimize the contribution from emission from evolved stellar populations (except at Hα where all stellar emission is effectively removed). It is evident that beyond $\sim 2\,\mu$m the stellar SED does not provide sufficient emission to account for the observations. Although the PEGASE.2 models do not include the contribution from thermally pulsating asymptotic branch (TP-AGB) stars, which have been shown to emit significantly in this wavelength regime (Maraston, 2005), these stars would not yet have time to evolve from the main-sequence for the young stellar population modeled here. Emission due to dust heated by the young stellar population is the obvious culprit. We plot for reference dust models from (Draine & Li, 2007) for three PAH fractions of $q_{\rm PAH}$ =0.47%, 2.50% and 4.58% (these models assume $< U >_{\rm min} = 3.00$ and $u_{\rm max} = 1000$, see Draine & Li (2007) for details, and are shown for reference, not as best fits of the canonical SED).

The scaling of the near/mid-infrared spectrum with the star formation rate suggests this region of the SED for a galaxy can be incorporated into stellar population synthesis models as a spectral component that scales with the star formation rate.

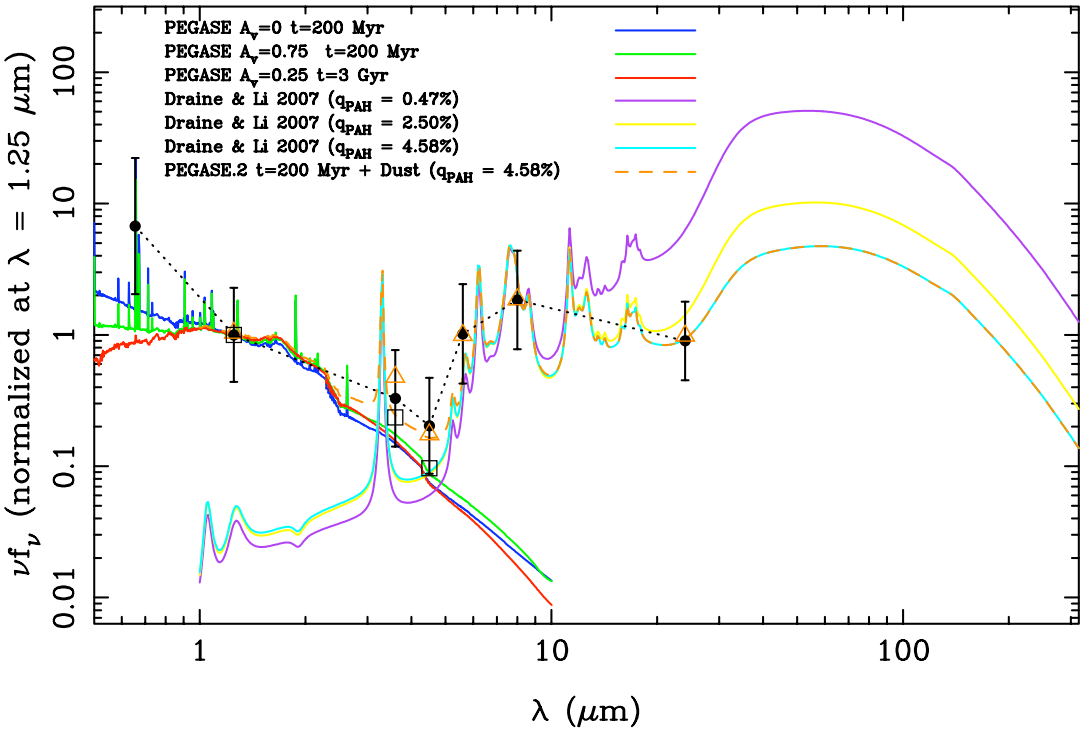

Figure 4.9 Using the linear fits from Figure 4.3 (which scale with the star formation rate), a spectrum of broadband near/mid-infrared emission is plotted as solid black points (connected by the black dotted line), normalized at 1.25 μm. This average SED is a measure of the young stellar population and its associated dusty star-forming environment as seen in the near/mid-infrared as it is shown to scale with the intrinsic Hα emission. The black open squares represent the colours ($\log_{10}$ $I_{3.6}/I_{1.25} = -0.30 \pm 0.07$ and $\log_{10}$ $I_{4.5}/I_{3.6} = -0.19 \pm 0.02$) of the majority of pixels in a galaxy (taken from the results of Figure 4.2). Shown for comparison are SEDs generated for stellar emission from PEGASE.2 models and dust emission models from Draine & Li (2007). The stellar models from PEGASE.2 are normalized at 1.25 μm, while the dust models, varying in PAH mass fraction ($q_{\rm PAH}$), from Draine & Li (2007) have been normalized at the IRAC 8 μm band. The sum of the young PEGASE model (blue) and $q_{\rm PAH} = 4.58\%$ (cyan) dust/PAH model is shown as the orange dashed curve. The open triangles represent the flux densities of this model in the 2MASS and *Spitzer*/IRAC filters and are consistent within errors to the observed average SED data points (black solid dots).

4.6.2 The NIR excess due to circumstellar (disk) emission

A hypothesis for the origin of the NIR emission we have identified was posed in Mentuch et al. (2009) (and in Ch 3 of this thesis), namely that the emission is associated with circumstellar emission of dust around massive young stars. We measure the excess NIR emission at 3.6 μm by subtracting the contribution of stellar light from the bandpass. We use the ratio for stellar emission in the near-IR of $\log \mathrm{I}_{3.6}/\mathrm{I}_{1.25} = -0.3$ ($\mathrm{I}_{3.6}/\mathrm{I}_{1.25} = 0.5$) to measure the excess emission in the NIR and plot as a function of the intrinsic Hα. A linear relation exists between the NIR excess (stellar subtracted) emission and is shown in Figure 4.10. A linear fit to the data is plotted as a solid line. The fit has a slope of 0.0435 (+0.1092/-0.0311).

We can use the quantitative model we developed in Mentuch et al. (2009) to see if the excess emission at 3.6 μm can be explained by the same model. A relationship between NIR emission from circumstellar disks from the model of Dullemond et al. (2001) was applied to the integrated light of a galaxy as:

$$L_{\mathrm{NIR}}(\mathrm{SFR})_{\mathrm{disk}} = 350\,\mathrm{L}_{\odot}/\mathrm{M}_{\odot}\left(\frac{\mathrm{SFR}}{\mathrm{M}_{\odot}/\mathrm{yr}}\right)\left(\frac{\mathrm{t}_{\mathrm{excess}}}{\mathrm{yr}}\right). \tag{4.4}$$

this equation requires a SFR in $M_{\odot}$/yr and a value for the timescale of the circumstellar disk emission, t_{excess}. The calculation assumed an Initial Mass Function from Kroupa (2001) and as a result requires the same IMF assumption when converting the intrinsic Hα intensity into a SFR.

We use the standard conversion from Kennicutt (1998), except an additional factor of 0.55 is applied to convert from an IMF from Salpeter (1955) to an IMF from Kroupa (2001).

$$\mathrm{SFR}(\mathrm{M}_{\odot}/\mathrm{yr}) = 0.55 \times 7.942 \times 10^{-42}\ \mathrm{erg\,s^{-1}}\ \mathrm{L}(\mathrm{H}_{\alpha,\mathrm{int}}) \tag{4.5}$$

The relation resulting from this model is plotted in Figure 4.10 for two timescales of 10^5 and 10^6 years, which cover the range of timescales in which circumstellar disks are found locally to survive. In general the model over predicts the emission, but is within an order of magnitude which suggests that the excess NIR emission seen in nearby young massive stars can explain the NIR colours seen in star-forming regions in the SINGS

galaxies and may be due to circumstellar dust heated to its sublimation temperature.

4.6.3 AGN activity

Do active galactic nuclei (AGN) cause red NIR colours? There is a trend for the NIR excess emission regions to be associated with regions of star formation. For many of the normal spiral galaxies in the sample, the regions of excess spatially correlate with Hα bright regions, found to be located along the spiral arms. Similar knots are seen in the irregular galaxies in the sample, but are found dispersed throughout these galaxies. In some galaxies (both irregular and spiral types), some of these regions are found in the nuclear region of the galaxy.

Table 4.1 contains a column which identifies whether a galaxy may harbor an active galactic nuclei as indicated by spectral indicators (Dale et al., 2006). We investigate each of the 24 galaxies with an AGN and find that in a third of the cases, the nuclear regions of galaxies do correspond to redder NIR colours. For 5 galaxies nuclear regions of NGC 1266, NGC 3031, NGC 3198, NGC 4736 and NGC 7552 have very red NIR colours ($I_{3.6}/I_{1.25} > 1$). The pixels in these regions have both high Hα_{int} emission and high dust extinction. The red NIR colours seen in some galaxies containing AGN may either be related to the AGN itself (or dust heated by the AGN); or could also be from optically thick dust extinction in star burst regions as the NIR colours in these nuclear regions are similar to NGC 1366, an opaque starburst galaxy (Roussel et al., 2006).

4.7 Conclusion

The near-infrared, at 1-5 μm, marks a transition in the spectral energy distribution of galaxies. At $\sim$1-2 μm, emission from longer-lived, low-mass stars from evolved populations remains bright, tracing the build up of mass in a galaxy. However, these wavelengths also trace the current star-forming population, which emits brightly in both the UV, optical and near-infrared. Near-infrared colours at 1-5 μm, if dominated by stellar emission, are predicted to be independent of the age of a stellar population. However, the contribution from Polycyclic Aromatic Hydrocarbons and dust grain emission becomes important beyond 2 μm, making the near- and mid-infrared a complicated but rich region of a galaxy's spectral energy distribution.

In this chapter, we have analyzed the pixel-by-pixel near-infrared colours for a sample

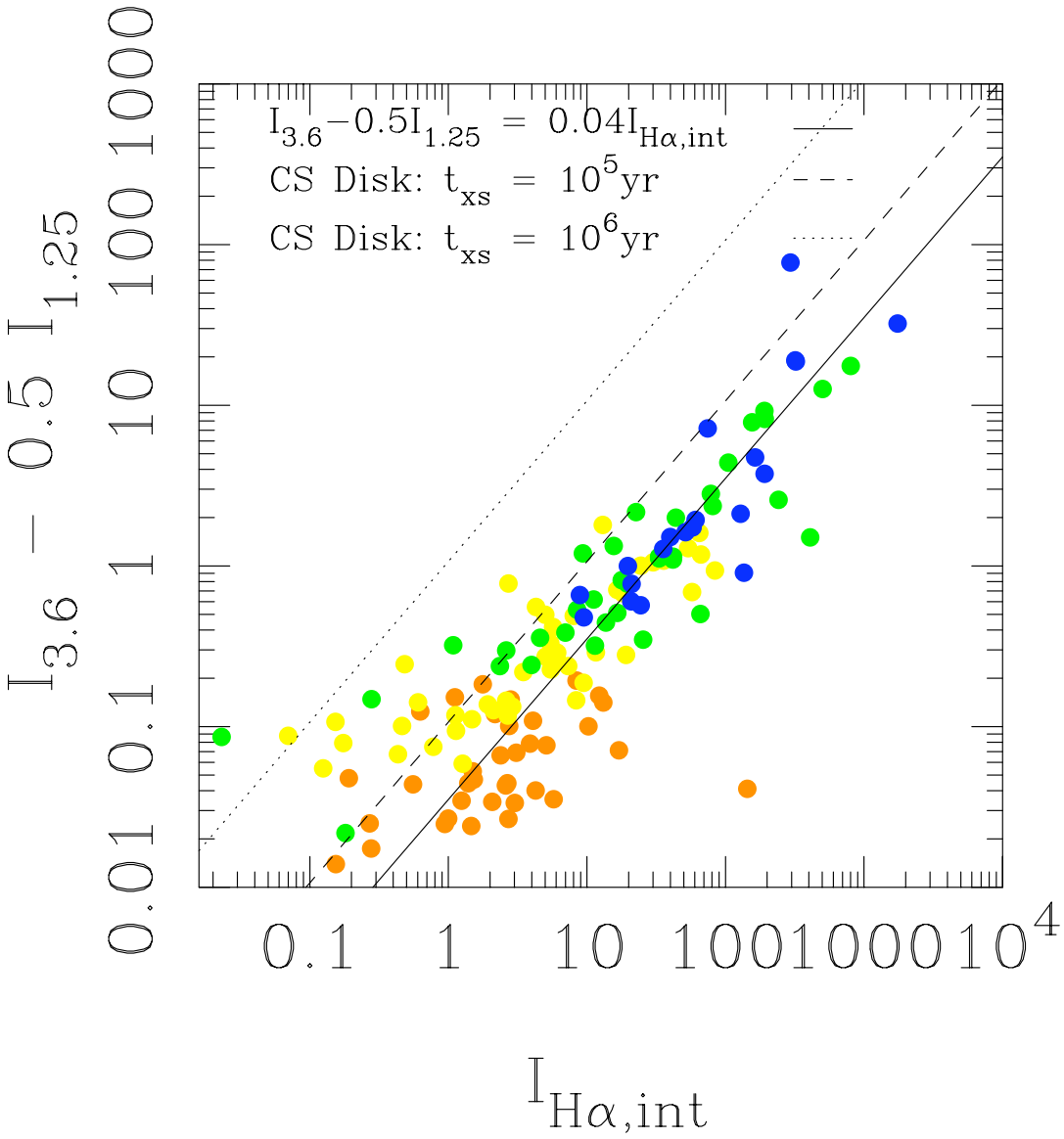

Figure 4.10 Excess NIR emission is plotted by subtracting the contribution of stellar emission at 3.6 μmusing emission at 1.25 μm. The excess emission is shown to correlate with the star formation rate with a median slope of 0.0435(+0.1092/-0.0311). The dashed and dotted lines is the equation for NIR excess emission from Mentuch et al. (2009), as applied in Eq. 4.4 and 4.5, for disk lifetimes of 10^6 and 10^5 years respectively.

of 68 galaxies from the *Spitzer* Infrared Nearby Galaxy survey (SINGS; Kennicutt et al. 2003) and Large Galaxy Atlas (LGA; Jarrett et al. 2003). Specifically we use images at 1.25, 3.6, 4.5, 5.6, 8.0 and 24 μm, as well as continuum subtracted Hα images for 45 galaxies. Using the Hα and 24 μm images, we were able to create images representing the spatially resolved dust extinction (at $A(H\alpha)$) and the intrinsic Hα intensity. The pixels in each galaxy were categorized into different regions based on a near-infrared colour selection. The majority of pixels for each galaxy in the sample are found to have constant NIR colours, as is predicted for pure stellar emission, while the reddest NIR pixels correspond to regions of star formation and trace the galaxy's spiral arms structure. Their scatter in the NIR colour plane follows a $\lambda^{-0.7}$ vector, predicted to be due to dust extinction. However, in our observations these pixels do not show unusually high dust extinction. Instead, these pixels have brighter Hα emission and are related to compact regions of star formation. Our analysis suggests that excess NIR colours are produced by emission, not dust extinction.

For each NIR colour cut, we measured the average intensities at 1.25, 3.6, 4.5, 5.6, 8.0 and 24 μm for each galaxy. We compared these to the average dust extinction and star formation rate in each region and found a linear relation between the emission at all bands from $\sim$1-8 μm and the average Hα_{int} intensity (and consequently the star formation rate). The strong relation between near-infrared and PAH emission from 1-8 μm and star formation suggests the canonical spectrum derived from this dataset can be added to stellar population synthesis models as a component directly scaled to the star formation rate of a stellar population.

Chapter 5

Observing the first stellar populations with a near-infrared tunable filter

Some work in this chapter is published as:
"Optical-mechanical operation of the F2T2 filter: a tunable filter designed to search for First Light"
Erin Mentuch, Alan Scott, Roberto Abraham, Elizabeth Barton, Matthew Bershady, Joss Bland-Hawthorn, David Crampton, Ren Doyon, Steve Eikenberry, Mike Gladders, Karl Glazebrook, Joe Jensen, Jeff Julian, Roger Julian, Jean-Paul Kneib, David Loop, Nick Raines, Neil Rowlands and JD Smith. 2008, *SPIE*, Volume 7014, pp. 701476-701476-10

5.1 Abstract

Near-infrared observations probe rest-frame optical light of distant, high-redshift galaxies and are essential for their discovery. As the sensitivity of near-infrared detectors improve, both observatories on the ground and in space are devoting large fractions of their time to discovering the deepest, most distant galaxies. From space, upgrades to the *Hubble Space Telescope* and deep re-imaging of the *Hubble* Ultra Deep Field present a number of possible candidates for galaxies at $z > 7$. From the ground, narrow and broadband searches have found thousands of galaxies at $3 < z < 7$, but beyond this, only a small number of possible candidates have been found successfully though spectroscopic slit surveys. In this chapter, we present the opto-mechanical development and commissioning

of a tunable filter designed to operate from 0.95 to 1.35 μm, and to add to the number of galaxies detected at $z > 8$. The Flamingos-2 Tandem Tunable (F2T2) filter is designed to take narrow-band images, searching for Lyman alpha emitting galaxies from $z \sim 8 - 11$. The F2T2 filter is an accessory to the infrared imaging spectrograph Flamingos-2 on the 8 m *Gemini S* telescope and will be fed through the upcoming multi-conjugate adaptive optics feed. This chapter highlights the lab work performed at COM DEV Canada as part of this thesis to digitally calibrate the closed-loop control of the opto-mechanical drive which allows the filter to be controlled at < 1 nm level precision. Software development and the optical test set up to calibrate the control are described and reflection and transmission spectra measured in the lab are presented. Once in operation, the search for high-z Lyα emitters with the F2T2 filter, undertaken by the Gemini Genesis Survey (GGS) team, will reach unprecedented flux limits from the ground by taking advantage of the magnification gain provided by strong gravitational lensing caused by intermediate redshift galaxy clusters. In this chapter, the search strategy to be implemented with the filter is presented and number count predictions for $8 < z < 11$ candidates are made by evolving the measured LAE luminosity function at $z = 5 - 7$.

5.2 Introduction

Observations have set the first constraints on the epoch of reionization, a transition from a universe filled with neutral hydrogen to one filled with ionized hydrogen, the state in which the universe now remains. Requiring high energy ionizing photons, this transition likely corresponds to the formation of the first luminous objects. Measurements of the cosmic microwave background (CMB) anisotropies suggest that the large-scale structure we see in the present universe started from small-amplitude density fluctuations. The most recent polarization measurements from the Wilkinson Microwave Anisotropy Map satellite suggest that reionization occurred at $z = 11^{+2.6}_{-2.5}$ (Page et al., 2006; Mortonson & Hu, 2008). In agreement, temperature measurements of the intergalactic medium (IGM) at $z = 2 - 4$ suggest that reionization occurred at $z < 9$ (Fan et al., 2006). On the other hand, spectral signatures of a number of distant quasars indicate that reionization was over by $z \sim 6.5$ (Fan et al., 2001). Somewhere between recombination (at $z \sim 1000$) and $z \sim 6$, a period spanning about 800 Myr, the universe changed drastically marking the period of the first stars, the assembly of the first stellar populations in galaxies, the growth of the first supermassive black holes and reionization.

The nature of the first luminous objects, referred to as *First Light*, is still unknown. The most distant object to date with a confirmed spectroscopic redshift is a gamma ray burst at $z = 8.2$ (Tanvir et al., 2009), with several objects, consisting of quasars and star-forming galaxies, spectroscopically confirmed at $z = 6 - 7$ (Fan et al., 2001; Iye et al., 2006; Vanzella et al., 2009). It is apparent that quasars, whose number density drastically decreases beyond $z \sim 2$, do not provide enough ionizing radiation to completely ionize the universe (Fan et al., 2001). However, relatively low-mass but abundant, star-forming galaxies at $z > 5$ have star formation rates (SFRs) that do produce enough ionization radiation to fully ionize the universe (Bouwens et al., 2005). Measuring the star formation rates and mass density of the most distant objects in this intermediate redshift interval will provide the missing pieces to our understanding of the epoch of reionization and the sources responsible for it.

Two distinct classes of very high redshift objects have been found using two (biased) selection techniques. The first of these are Lyman break galaxies (LBGs) and are found by looking for continuum breaks between 912 and 1216 Å. The relative efficiency in telescope time to detect LBGs has allowed for spectroscopic confirmation of about 1000 of these objects at $z \sim 3-6$ (Shapley et al., 2003). Over 500 more have been confidently detected at $\sim 6-7$, providing very high redshift measurements of the star formation history (SFH) and mass density (Eyles et al., 2007; Bouwens et al., 2006). Using NIR observations from the Infrared Array Camera (IRAC) on the *Spitzer Space Telescope*, Labbé et al. (2006) measured stellar masses and ages for these candidates allowing them to estimate the stellar mass density at z=7. As was found with high redshift quasars (Fan et al., 2001), the derived star formation density and ages suggest that these most luminous galaxies were not sufficient to reionize the universe and thus points to less massive star-forming objects providing the bulk of the ionizing photons to reionize the universe.

Beyond $z > 7$ the dropout technique becomes very inefficient from the ground. At wavelengths longer than $\sim$0.9 μm, the night sky is contaminated with a number of narrow emission lines from atmospheric hydroxyl (OH) molecules. Because of this high sky noise, it is just not feasible to detect galaxies from the ground with broadband filters on todays 8-10 m class observatories. Deep NIR observations of the *Hubble* Ultra Deep Field from space were successful at detecting $\sim$40 candidates at $z \sim 7$ (Bouwens et al., 2004) and a small number of candidates at $z \sim$8. But the numbers have jumped drastically with recent re-imaging of the *Hubble* Ultra Deep field with the new WFC3/IR camera (with about 40$\times$ increased sensitivity) on the *Hubble Space Telescope* (*HST*). The analysis of

the new data is somewhat controversial, with the number of candidates at $z \sim 8$ ranging from a conservative five candidates (Bouwens et al., 2010) to 15 candidates (Yan et al., 2009). Objects at $z \sim 9-10$, identified as J_{125}-dropouts, also vary from zero (Bunker et al., 2009) to three (Bouwens et al., 2009) to 20 (Yan et al., 2009). Depending on the numbers, these high-z dropout galaxies can provide enough photons to ionize the universe.

The other class of high-z galaxies, Lyα emitters (LAEs), are star-forming galaxies with strong Lyα ($\lambda = 1216\,$Å) emission detected through narrow-band surveys at $z \sim 3-6$ (Hu et al., 1998). Narrow-band filters, with passbands of $\sim 10\,$nm have found a number of candidates at higher redshifts of 5.6 (Shimasaku et al., 2006), 6.5 (Kashikawa et al., 2006) and 7.7 (Hibon et al., 2010; Tilvi et al., 2010). More than 30 LAE candidates found at $z \sim 6.5$ have spectroscopic confirmations (Fan et al., 2006). In theory, candidates at higher redshifts can be observed from the ground. In between the bright atmospheric OH lines are narrow atmospheric windows that can be probed with a spectral resolution greater than 500. However, narrow-band surveys beyond this redshift have yet to be successful. This is not surprising considering the surveys of with Willis & Courbin (2005), Cuby et al. (2007) and Sobral et al. (2009) were unable to reach the flux sensitivities required to probe the LF of galaxies (assuming no evolution from $z \sim 7.7$). A novel way to reach fainter galaxies is to take advantage of the magnification gain from gravitational lensing due to intermediate redshift galaxy clusters. Stark et al. (2007a) searched for high-z LAEs along critical lines of maximum magnification ($> 10-50\times$) of six galaxy clusters. This survey managed to reach flux sensitivities of $10^{41}-10^{42}\,\mathrm{erg\,s^{-1}}$ and covered a survey volume of $\sim 3-30\,\mathrm{Mpc}^3$. It detected 6 possible candidates at very high redshifts of $z = 8.5-10.4$ and conservatively measured the number density assuming only 2 of the detections are real. In both the conservative and abundant cases, the number density implies a luminosity function with a steep faint-end slope and hence a large abundance of intrinsically faint sources (Stark et al., 2007a). Comparing the results of the few high-z galaxy surveys performed thus far (Santos et al., 2004; Willis & Courbin, 2005; Cuby et al., 2007; Richard et al., 2006; Stark et al., 2007a), it is evident that the number density of massive objects is much lower at high redshifts, consistent with the standard hierarchical model of galaxy formation.

Spectroscopic slit searches probe very small spatial volumes, but have high coverage in redshift space, while traditional narrow-band filter searches can probe large spatial volumes, but not a lot of redshift space. A novel, relatively low-budget approach is to

perform a search with an instrument that can probe large volumes in both spatial and redshift space. The Flamingos 2 Tandem Tunable Filter (F2T2; Scott et al. 2006; Mentuch et al. 2008) is a tunable filter that can take narrow-band images at any wavelength within the J-band, scanning from 0.95 to 1.35 μm. Like a spectroscopic slit, a tunable filter can search for LAEs at a range of wavelengths, but unlike a spectroscopic slit, a tunable filter is able to image a large area just as a traditional narrow-band filter would. The F2T2 filter is to be used in an upcoming search for LAEs at $8 < z < 11$ on the *Gemini South* 8 m telescope in Chile. It will operate as an accessory mode instrument for the IR-optimized Flamingos-2 Imaging Spectrograph (Eikenberry et al., 2006) and will be fed by the upcoming Multi-conjugate adaptive optics (MCAO) feed.

Using the cue from spectroscopic slit surveys like Santos et al. (2004) and Stark et al. (2007a), the Gemini Genesis Survey (GGS) will expand the methodology of slit-based lensing LAE search surveys by utilizing the tunable, narrow-band F2T2 filter to image the entire plane of strong intermediate-redshift galaxy clusters, covering more volume than a spectroscopic slit and much more redshift space than a single narrow-band filter, in addition to reaching $10 - 50\times$ deeper flux limits. The instrument is described in § 5.3. The development of the opto-mechanical control of the F2T2 filter (in § 5.3.1 to § 5.3.3) and highlights from its commissioning on a 1.6 m telescope at the Mont Megantic Observatory (in § 5.3.5) are included in this chapter. In § 5.4, we present the design of a lensing survey with the tunable NIR filter F2T2 and present number count predictions from our best guess at the luminosity function of high-z LAEs. We also discuss alternative and complementary science uses of the F2T2 filter in § 5.5, including the possibility of detecting He II at lower redshift (in § 5.5.1).

5.3 The Flamingos-2 Tandem Tunable Filter (F2T2)

Fabry-Perot interferometers are variable gap etalons and operate on the same principles as narrow-band interference filters. They consist of a pair of closely separated, highly reflective transparent plates. In between the plates, light is reflective off the mirror-like surfaces resulting in transmission through the plates at well defined spectral orders corresponding to integer multiples of the phase difference across the plates. The transmission of light through a Fabry-Perot interferometer results in a comb like transmission function which is shown in Figure 5.1. They differ from narrow-band interference filters because the distance between the plates can be adjusted, resulting in the transmission of light at

variable wavelengths.

Fabry-Perot filters are not new to Astronomy. Their high resolution, tunable capabilities are useful for line-emitting, extended objects and high resolution scanning interferometers have been in use since the 1970's to measure emission lines in planetary nebula. By isolating line emission, such filters can reach much higher signal-to-noise levels against the noisy sky background, or even the continuum emission of the source itself. Because they are tunable, they also offer the ability to measure line emission from objects at different redshifts or line of sight velocities. Currently a few are operational. The Taurus Tunable Filter (Bland-Hawthorn & Jones, 1998) operates in the optical on both the *Anglo-Australian* and *William Herschel Telescopes*, the Maryland Magellan Tunable Filter (Veilleux et al., 2010) is currently in use on the 6.5 m *Magellan-Baade Telescope* and the Optical System for Imaging and Low-Intermediate-Resolution Integrated Spectroscopy (OSIRIS) instrument on the 10.4 m *Gran Telescopio Canarias* is operating the tunable imaging component of this device.

The Flamingos-2 Tandem Tunable filter (F2T2; Scott et al. 2006) is an accessory mode instrument designed for the Flamingos-2 near-IR wide field imager and multi-object spectrometer, built by the University of Florida, for use on the 8 m *Gemini South Telescope*. Although other tunable filters exist, the F2T2 filter is unlike all other tunable filters in a number of ways. First, it is the only tunable filter designed to operate in the J-band, and as a result, it is the only currently operating filter that can detect very high redshifted line emission from Lyα or He II. It is also unique in that in consists of two Fabry-Perot etalons (often also referred as Fabry-Perot interferometers) in series. In conventional devices, intermediate passband filters are used in addition to the Fabry-Perot interferometer to block out transmission at other spectral orders, but in the case of F2T2, the second etalon can effectively operate as a blocking filter. We demonstrate this in the bottom two panels of Figure 5.1. The light passing through both etalons is blocked out at all wavelengths, except at $\lambda = 1.35\,\mu$m as is seen in the total transmission in the bottom panel. The spacing between each etalon (in this case 16.04 and 14.70 μm) is tuned to allow emission at this wavelength, however the spacings are arranged so that the spectral order of transmission at this wavelength is slightly different, in this case order=23 in one etalon and order=25 in the other. A two order separation is optimal for the F2T2 filter to transmit at a single wavelength.

F2T2 is a 60 mm clear aperture, IR-optimized, air spaced, tandem-etalon tunable Fabry-Perot filter designed with the science purpose to investigate the first sources of

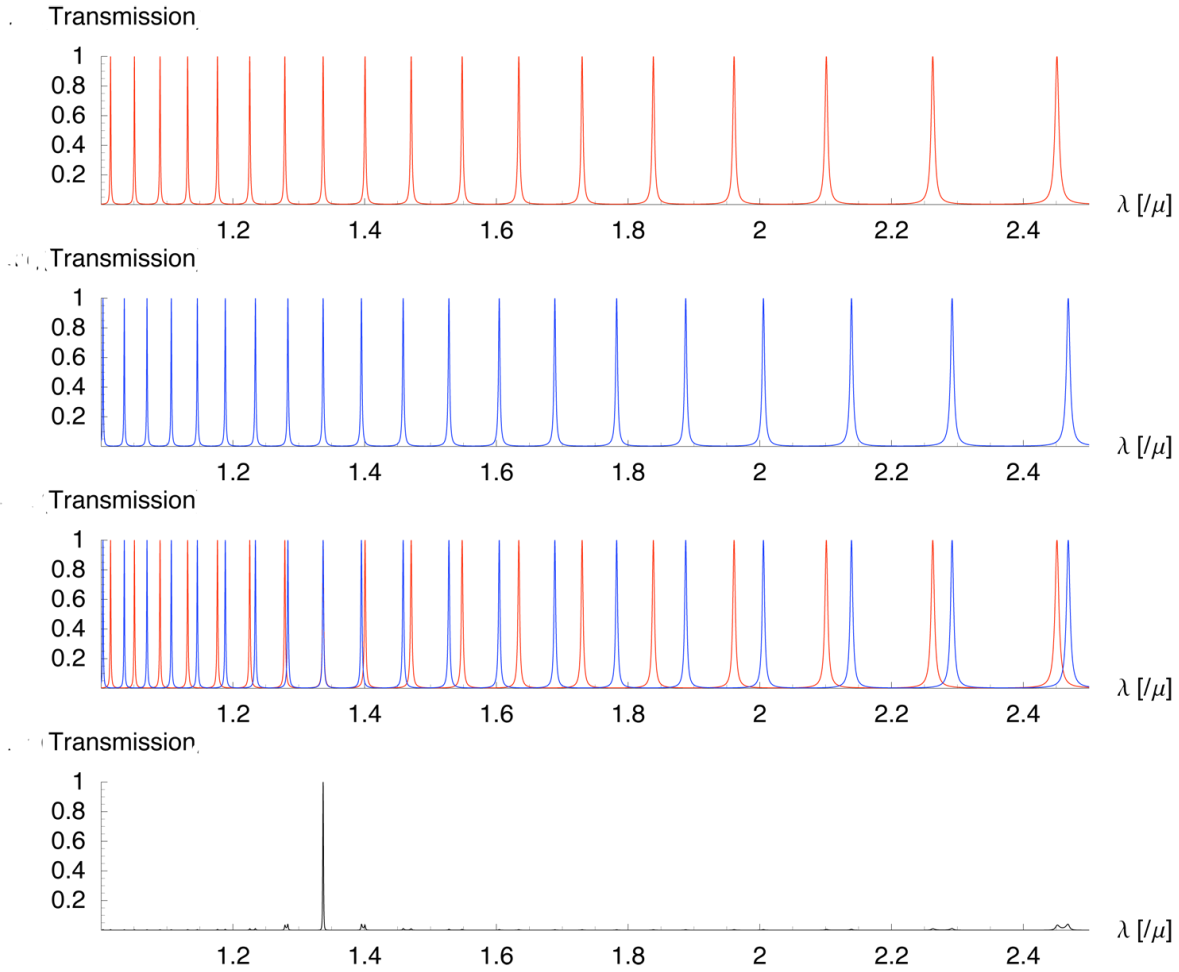

Figure 5.1 The transmission through a theoretical tandem Fabry-Perot etalon system. The top two panels shows the transmission through the first and second etalon separately. The two etalons have slightly different gap spacings (in this case 16.04 and 14.70 μm) and they are calculated such that the spectral order of transmission at 1.35 μm is two orders apart. In the third panel, the two functions are overplotted together to show that both etalons have transmission at 1.35 μm, but transmission is collectively blocked out at all other wavelengths, and the net transmission through the tandem Fabry-Perot system is shown in the bottom panel.

star formation in the Universe. The optical components and electronics for the device were designed and assembled by COM DEV Canada. Construction of the device has been funded by a Steacie Fellowship and a Canada Foundation for Innovation Career Award given to the project's Canadian-PI (R. Abraham). An image of the F2T2 filter in its optical testbed is shown in Figure 5.2. The filter is shown here without its enclosure. It will be mounted in the fore-dewar of Flamingos-2 and will be cooled to $\sim 140\,\mathrm{K}$.

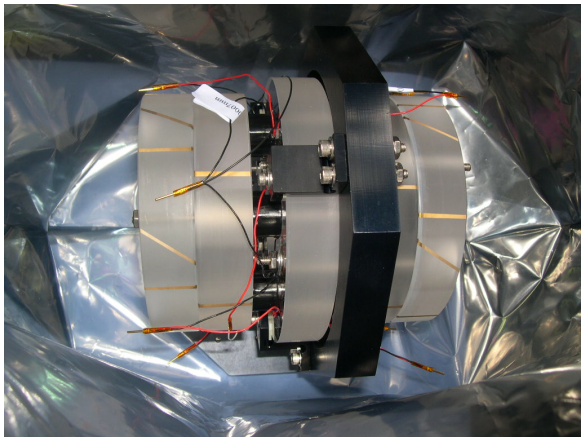

Figure 5.2 The F2T2 filter consists of two Fabry-Perot etalons in tandem. Here the instrument sits in its testbed prior to encasing. The gold ribbons are attached to the capacitors which are used for feedback in the closed loop digital control operation. The wires are attached to the piezo electric transducers.

In many aspects, the F2T2 filter is a ground-based analog to the Tunable Filter Imager (TFI, Rowlands et al. (2004)) presently being constructed as a component of the *James Webb Space Telescopes* (*JWST*) Fine Guidance Sensor Camera. The key differences are highlighted in Table 5.1. *JWSTs* TFI and *Geminis* F2T2 share key optics and electronics and like F2T2, the primary science goal of TFI is to probe star formation in the distance Universe. However, unlike F2T2, TFI is designed to withstand the challenges of space launch and flight. In addition, F2T2 is a dual etalon device operating at higher resolution than TFI, a single etalon device. The second etalon suppresses the wings of the airy transmission function, allowing F2T2 to operate with high efficiency in between contaminating OH lines, which dominate the near-IR sky background emission redward of 0.9 μm.

The gap spacings between each plate are maintained by low voltage piezo electric

Table 5.1. Key differences between the JWSTs TFI and Geminis F2T2

	Tunable Filter Imager (TFI)	Flamingos-2 Tandem Tunable Filter (F2T2)
Location in Telescope	Near the pupil of James Webb Space Telescope (JWST)	Inside Flamingos-2 imaging spectrograph near the focus of Gemini South 8m Observatory
Spectral Resolution	∼100	> 800 (wing suppressed)
Wavelength Range	1.5 μm- 5 μm	0.95 μm 1.35 μm
Field of View	$\sim 2.2'$	$\sim 50''$(with Multi-Conjugate Adaptive Optics (MCAO); $\sim 1.5''$ (without MCAO)
Image Quality	Diffraction Limited	MCAO Limited
Operating Temperature	~ 35 K	∼110 K
Principal Investigator	R. Doyon (Univ. of Montreal)	R. Abraham (Univ. of Toronto)
First Light	2015	Summer 2008 (1.6m Mont-Mgantic Observatory) Fall 2011 (8m Gemini South Observatory)

tranducers (LVPZTs) through a digitally monitored feedback system. In this section, we described the closed loop control system used to drive the etalon's opto-mechanical control, including descriptions of its operation (in § 5.3.1), calibration (in § 5.3.2) and digital control (in § 5.3.3). The optical lab design and procedure for measuring parallelism and spectral transmission are described and results from the instrument's commissioning run at the *Mont Megantic Observatory* are highlighted in § 5.3.5.

5.3.1 Etalon operation

The etalons have been polished and coated to provide a reflective finesse of > 30 over the wavelength range of 0.95 to 1.35 μm. In order to reach the required finesse, the etalons must be controlled down to a precision of < 1 nm. The system is controlled using two independently commanded Multi-Application Low Voltage Piezoelectric Instrument Control Electronic (MALICE) rack-mounted systems. The MALICE system drives low voltage piezoelectric actuators (LVPZTs) using capacitive displacement sensors (CDSs) positional feedback technology. The control software has been developed by COM DEV Canada in the C language on an Analog DSP 2191M EZKIT evaluation board using Analog Devices VisualDSP++ environment. There are 6 LVPZTs and 5 CDSs per etalon, comprising 3 capacitive bridges to provide high accuracy feedback on the gap and wedge. Two pairs are used to provide 'X' and 'Y' parallelism, while a 5th sensor is used in a 'Z' bridge with a fixed ceramic capacitor to provide an absolute gap reference.

5.3.2 Calibration routine

To calibrate the etalons, parallel plate positions are set by driving the LVPZTs with external power supplies and optical feedback. Each etalon is calibrated separately in reflection using a Fizeau interferometer optical system as described in Figure 5.3. A single laser (in our case a HeNe at 632.8 nm) can be used to parallelize the plates. Interference fringes, observed via a webcam attached with a C-mount to the beam splitter, are used to parallelize the plates in real-time with the external variable power supplies. Capacitive bridge error signals are zeroed by altering in-phase (I) and quadrature (Q) digital bridge drive setpoints via an autocalibration routine. Intermediate gap spacings can then be linearly interpolated on all three channels of each etalon. The relationship of digital setpoints to the gap size are uploaded under the 'Gap Scanning' feature of the MALICE Graphical User Interface (GUI), designed as a component of this thesis. This allows the etalon to be digitally tuned to a defined parallel gap size. [1]

5.3.3 Control methodology

The Multi-Application Low Voltage Piezoelectric Instrument Control Electronic (MALICE) software is designed to hold the plates at a parallel position for a specified length of time and accuracy. The etalon is driven to the desired parallel position using closed-loop control which minimizes the capacitive bridge errors from capacitive displacement sensor (CDS) feedback. Each plate of an etalon is supported on three equally spaced piezo electric transducers (PZTs) from a common annular baseplate, shared by both etalons. This design provides constant gap spacing from ambient down to operating temperature. The MALICE circuit has three constant current outputs with 24-bit resolution. Each output drives a pair of neighbouring PZT actuators (one PZT is attached to the bottom plate and one PZT, opposite in polarity, is attached to the top plate). To increase the gap, top PZTs raise the top platform while bottom PZTs lower the bottom platform. This results in an increase of the gap between the sense capacitor plates resulting in a decrease in capacitance which is used to measure the displacement. The inverse is performed to decrease the gap.

The LVPZTs are driven by two cascaded 12-bit digital-to-analog converters (DACs), a

[1] Calibration of the instrument required the development of new software to both the MALICE GUI and the C language control software. This was developed as part of my thesis while at COM DEV. The optical system set up for calibration was also a major component of this thesis.

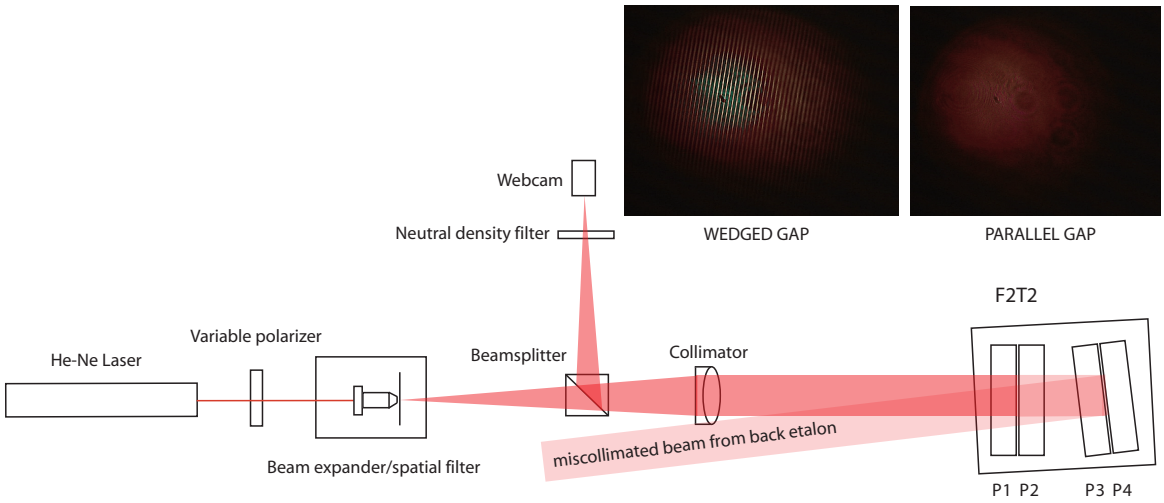

Figure 5.3 The above Fizeau interferometer schematic demonstrates the optical set up used to determine the parallelism within the plates. The light reflected through the F2T2 etalon will result in a fringe pattern if the plates are wedged, as shown in the image on the above left. If the plates are parallel, the laser emission will either be entirely opaque or transparent through the etalon (as is seen in the image in the top right) depending if the gap spacing is tuned to be an integer multiple of the HeNe laser emission.

'dynamic' DAC and a 'coarse' DAC. The dynamic DACs provide high current drive, while the coarse DACs provide current drives a factor of 1000 times smaller. The utilization of both drive levels allows for fast, high-bandwidth stepping (from the dynamic DACs) combined with high accuracy (from the coarse DACs) in a two-stage control approach. First, large feedback errors drive open loop control to a predicted position based on stored characterization data. This is done at high speed using a high current dynamic drive circuit, and thus requires a wide bandwidth. The dynamic drive with its open loop and high bandwidth allows too much noise to meet the necessary final positioning tolerances. The second stage is based on feedback from the calibrated capacitive bridge and results in small pseudo-static current adjustments using the coarse DACs to the PZTs at a very low bandwidth. The setpoint bridge drive provides a fixed frequency sine wave, and the error signal output is strongly filtered at this frequency. The resulting digital signal is synchronously demodulated to provide a very narrow error measurement bandwidth. This two-stage approach allows a very fast step over the entire PZT range, while still coming to a high accuracy final set point with a low noise bandwidth. The setpoint I and Q drive amplitudes for each bridge are set by a pair of cascaded 12-bit DACs, giving an effective 22 bit positioning precision. Calibration accuracy of the setpoint positions is limited mainly by the optical metrology.

Co-alignment of the two etalons requires monitoring in transmission under active closed-loop control. A GUI feature, we have added to the MALICE software system allows the user to scan along the parallel setpoints measured from the calibration routine described in Section 5.3.2. Tandem alignment is performed by holding one etalon at a fixed gap spacing while scanning along parallel gap spacings of the second etalon. Maximum throughput at a desired peak wavelength can be determined using spectral feedback (ideally a fast-reading Fourier Transform Interferometer (FTIR). Optimum free spectral range is achieved when the order separation between the two etalons, $\delta m = 2$. It is easier to co-align the two etalons over a larger region of the surface when the order is minimized ($m < 20$), but this results in lower spectral resolution. At room temperature, the etalon gaps scan over a range of $\sim 20\,\mu$m from ~ 5 to $25\,\mu$m absolute gap. At 140 K, this range is expected to be smaller, and the response speed will be correspondingly slower.[2]

[2]Cyrogenic testing of the F2T2 filter is planned for Fall 2010 at the University of Toronto.

5.3.4 Spectral analysis

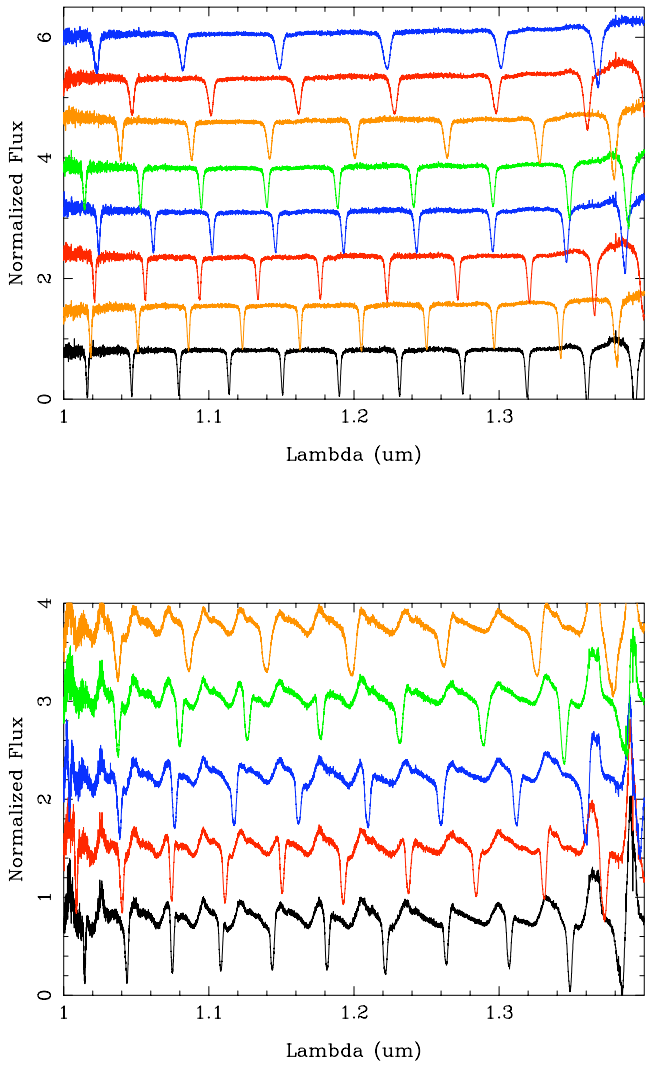

Figure 5.4 Reflection spectra for the two individual F2T2 etalons

A tandem Fabry-Perot system requires calibration of each etalon separately. Fortunately, the transmission of an etalon can be inferred from its reflection spectra, so that the F2T2 filter can be analyzed without being disassembled. We use an MIRMAT Fourier Transform Interferometer (FTIR) to measure the reflection spectra of each etalon separately. We show several examples reflections spectra in Figure 5.4 for each etalon.

The resulting spectra are analyzed with perl-based fitting software that fits a library of

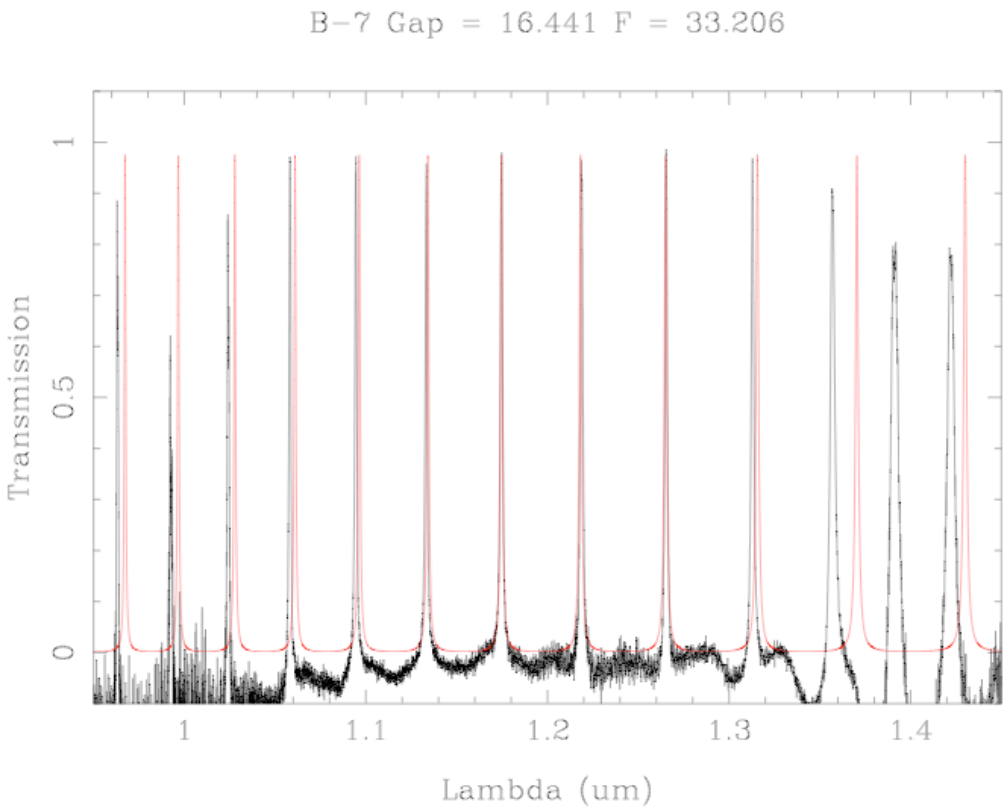

Figure 5.5 Reflection spectra of an F2T2 etalon. Fitting to a theoretical Fabry-Perot transmission spectrum (red line) reveals the gap between the etalon plates is 16.4 μm and the finesse of the etalon is 33.2.

theoretical Fabry-Perot spectra at a range of finesse and absolute gap values. Figure 5.5 shows a reflection spectrum of one of the etalons fitted to a Fabry-Perot model with a finesse of 33.2 and a gap of 16.4 μm. The gap measured in reflection for each calibrated parallel position is used to define the relationship of CDS digital setpoints to physical gap size used to align the etalons in tandem.

Tandem Operation

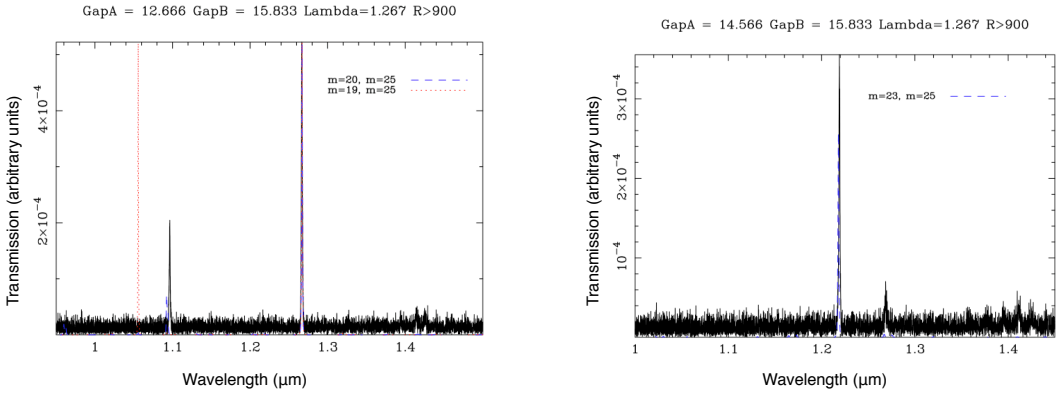

Figure 5.6 Transmission spectra of F2T2 with both etalons in tandem. In the left panel, the etalons are tuned 5 orders apart by setting the gap of Etalon A at 12.666 μm and Etalon B at 15.833 μm. Two separate tandem etalon models are plotted to show the order ratio between the two etalons. Maximum throughput at a single wavelength is achieved by tuning the etalons just two orders apart as is seen in the right panel. Etalon A has a gap of 14.566 μm and etalon B has a gap of 15.833 μm.

The relationship between absolute gap and digital setpoints can be used to align the two etalons in tandem to achieve transmission at a single wavelength by tuning the etalons to different orders at the same peak wavelength. It is found that the arrangement of a difference of two spectral order spacings results in the highest throughput at the peak wavelength and minimizes the leakage of light at nearby orders. The use of a J-band filter in the optical path of the telescope prevents light leakage at orders further away from the peak wavelength order. Figure 5.6 shows how tuning the etalon from an order difference of 5, where leakage occurs at other wavelengths, to an order difference of 2 ensures the light passing through the F2T2 filter is from the desired narrow-band spectral range.

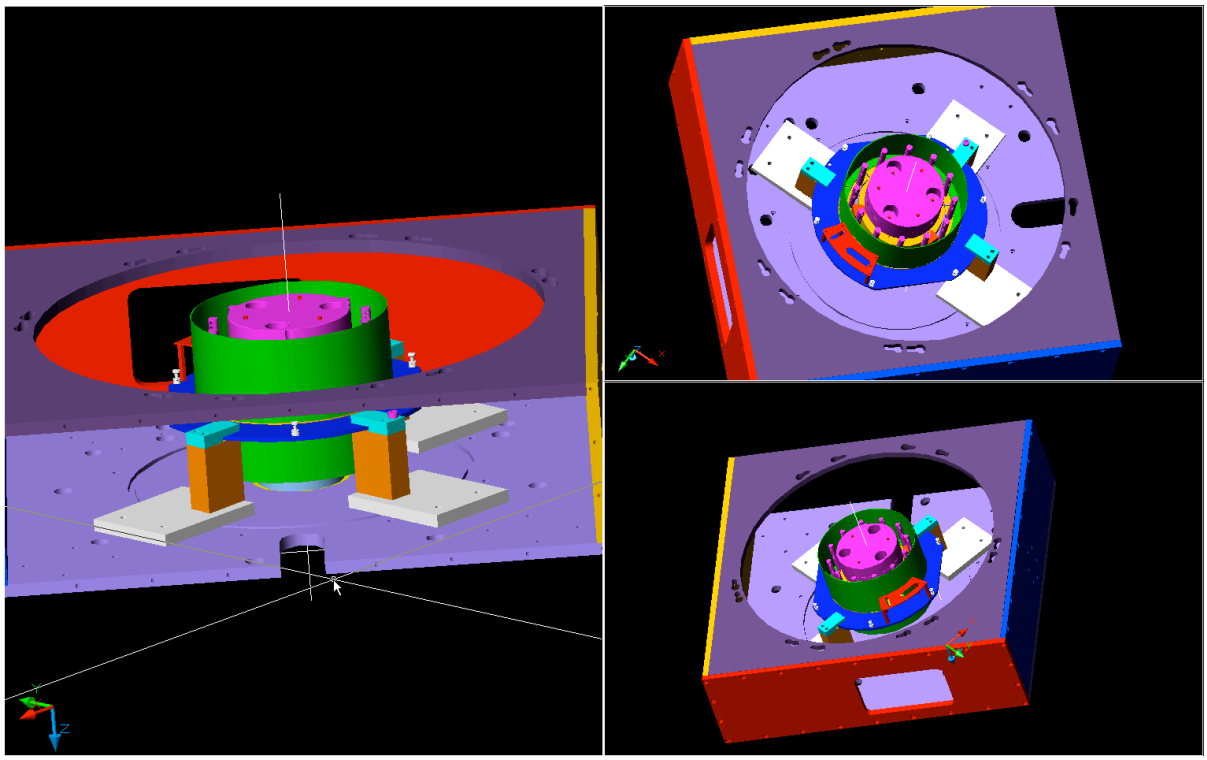

Figure 5.7 F2T2 in the filter assembly of the SIMON spectrograph at the 1.6 telescope at the *Mont Megantic Observatory*.

5.3.5 First Light at the Mont Megantic 1.6 m Telescope

Prior to its installation on Flamingos-2, F2T2 has had two engineering runs at the 1.6 m *Mont Megantic Telescope* (*OMM*) in Quebec, Canada. F2T2 was installed in place of the mask wheel of the SIMON multi-object spectrograph (Doyon et al., 2000). During three weeks of commissioning, procedures that were developed to calibrate and operate the filter were tested on the telescope and a number of instrumental capabilities were verified. Here we describe the two most advantageous operating modes of F2T2 for detecting high redshift Lyman alpha emitters.

Scanning Capabilities

As with traditional narrow-band filters, the F2T2 filter is optimized to detect line emission in objects, particularly extended objects. The F2T2 filter can scan to any wavelength in

the J-band in less than a second. As a result, it can be used as an imaging spectrograph. To test the feasibility of this mode, we scanned over the Paschen Beta line (1.2822 μm) of M57, the ring nebula. This mode has the potential of imaging ionization fronts around very high redshift quasars (if/once they are found).

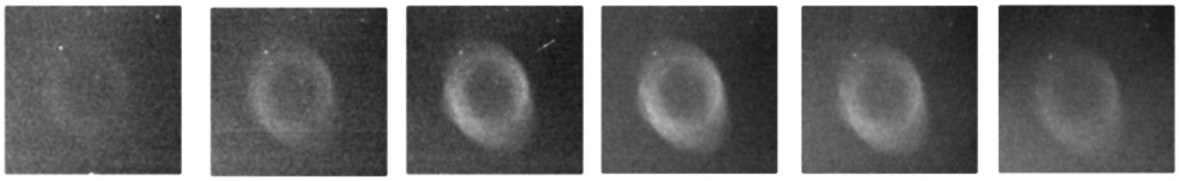

Figure 5.8 A demonstration of F2T2 scanning over the Paschen Beta line. The scan starts at 1.283 μm in the top left and then reads left to right in steps of $\Delta\lambda = 0.01\,\mu$m. The final scan is at 1.288 μm.

Signal to Noise gain with the F2T2 filter

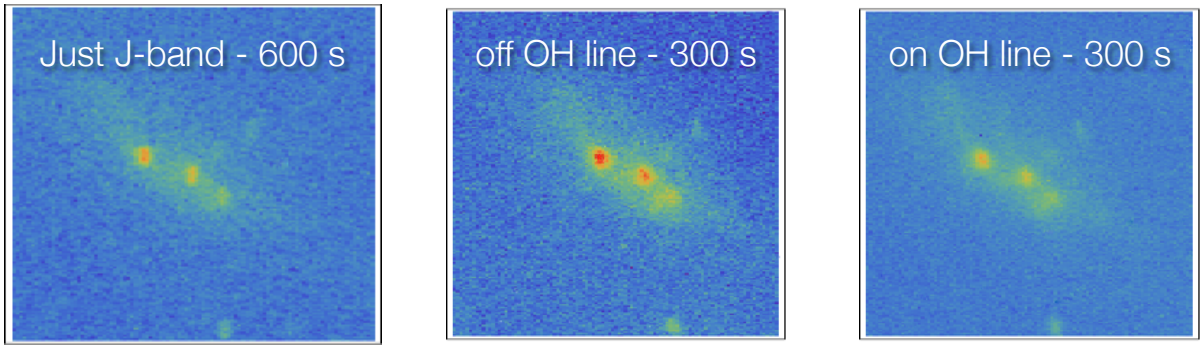

Figure 5.9 Images of NGC 1569 taken with F2T2 in SIMON at the *Mont Megantic Telescope*. The far left shows a 600 s exposure in the J-band. The two right images are 300 s exposures with F2T2 installed in SIMON. The middle image has much higher S/N because it was taken in between OH sky noise lines. The image on the far right falls on an OH line, so that the sky background is noticeably brighter and the S/N for the galaxy is lower.

The main purpose of the F2T2 filter is to take narrow-band images in between the strong OH lines that plague the NIR night sky in the J-band. By imaging where the sky is darker, F2T2 can reach signal-to-noise levels much faster than conventional

broad-band filters. This can be seen in Fig. 5.9 in the single exposure images of the star-forming dwarf galaxy NGC 1569. Without F2T2, NGC 1569, imaged on the left, is easily detected in a 600 s exposure in the J-band, but is barely visible above the sky noise at an exposure time of 300 s (not shown). The two right images also image NGC 1569, now with F2T2 installed in the SIMON imager. The middle image is taken at a wavelength where the sky has low noise levels, while the far-right image is taken in a region where the sky has relatively high noise levels due to an OH line. The middle image has much better S/N as a result. This instrumental gain in S/N, along with scanning capabilities, will allow the Gemini Genesis Survey to efficiently cover more volume and reach greater flux sensitivities than any other high redshift survey for LAEs currently being undertaken.

5.4 Gemini Genesis Survey (GGS) observing strategies

The primary science goal of the F2T2 filter is to search for high-redshift Lyman alpha (Lyα) emission in young star-forming systems. At $z > 7$, the Lyα emission line at 121.6 nm is redshifted to NIR wavelengths longer than 0.9 μm. Beyond this wavelength, the night sky is increasingly bright, about 20-50 times brighter than the optical night sky, plagued with strong hydroxyl (OH) emission lines from molecules in the atmosphere. F2T2 has been optimized to search between these narrow emission lines where the sky is much fainter (about 2000 photons/s/m^2/arcsec^2/μm). In this section we aim to predict the number of sources that a lensing search with F2T2 might find. A number of authors have developed simple star formation models to help predict the number of sources above a given flux limit that may be detected. We present our version of this prescription in § 5.4.1. Results from current high-z galaxy surveys are pointing to low-luminosity objects providing the bulk of the ionizing photons (Stiavelli et al., 2004; Stark et al., 2007b; Dijkstra et al., 2006). However, many uncertainties, discussed in detail in § 5.4.2, make this a difficult number to constrain, even given the empirical constraints provided by high-z luminosity functions of LAEs and LBGs, or the reionization limit set by CMB polarization anisotropy.

In designing the GGS, we need to decide the best searching method. For example, an instrument with the same science goal as F2T2 is undertaking a similar search. The

narrow-band imaging instrument *Dark Age Z (redshift) Lyα Explorer* (DAZLE; Horton et al. 2004) consists of a pair of interchangeable narrow-band filters which have been chosen to lie in between the contaminating atmospheric hydroxyl lines to search for high-redshift Lyα Emitters (LAEs) from $6.5 < z < 12$. Horton et al. (2004) expect DAZLE to detect LAE flux sensitivities of $\sim 1.5 \times 10^{42}\,\mathrm{erg\,s^{-1}}$ and cover a survey volume of $6900\,\mathrm{Mpc}^{-3}$. DAZLE completed its first observing run in October/November 2006 on one of the 8.2m *Very Large Telescope* (*VLT*) in Chile. No reports of successful detection have been published so far.

If the sources are relatively bright, but rare, a design similar to DAZLE is desired in which one chooses to cover more volume in exchange for less flux sensitivity. However, if, as the models and current high-z observations suggest, the sources are faint but abundant, then a better approach is to take advantage of the magnification gain due to the gravitational lensing of intermediate redshift galaxy clusters to brighten the apparent magnitude of a background high-z galaxy. Because the observations are sky-limited from the ground, the only way to reach deeper flux limits is to utilize the magnification of intermediate redshift galaxy clusters. Spectroscopic surveys, using gravitational lensing, to search for faint LAEs has helped to constrain the low-mass end of the luminosity function of LAEs at $z \sim 6$ (Santos et al., 2004) and can do the same at higher redshift, as the success of the lensing survey at $8.5 < z < 10.4$ by Stark et al. (2007a) may suggest.

5.4.1 Converting the power spectrum of the CMB to a Lyman α luminosity function

A simple prescription has been put forth in both Dijkstra et al. (2006) and Stark et al. (2007b) which relates the Lyα luminosity of a galaxy to the mass of its host dark matter halo. This allows a conversion from the mass density of dark matter halos to the observed Lyα luminosity function. Using the spectroscopically confirmed samples of high redshift LAEs in the Subaru Deep Field at z=5.6 (Shimasaku et al., 2006) and z=6.5 (Kashikawa et al., 2006), the model luminosity function can be empirically calibrated.

The model assumes that a fraction, $f_\star$, of the total baryonic mass, $(\Omega_b/\Omega_m)M_{halo}$, that is available in a given dark matter halo of mass, M_{halo}, will be converted into stars over a time scale of $t_{sys} = \epsilon_{\rm DC} t_H$. This time scale is some fraction, parameterized by the duty cycle, $\epsilon_{\rm DC}$, of the Hubble time, $t_H(z) = 2/(3H(z))$, at the redshift z. Thus the star formation rate (SFR), $\dot{M}_\star$, is related to the dark matter halo mass by:

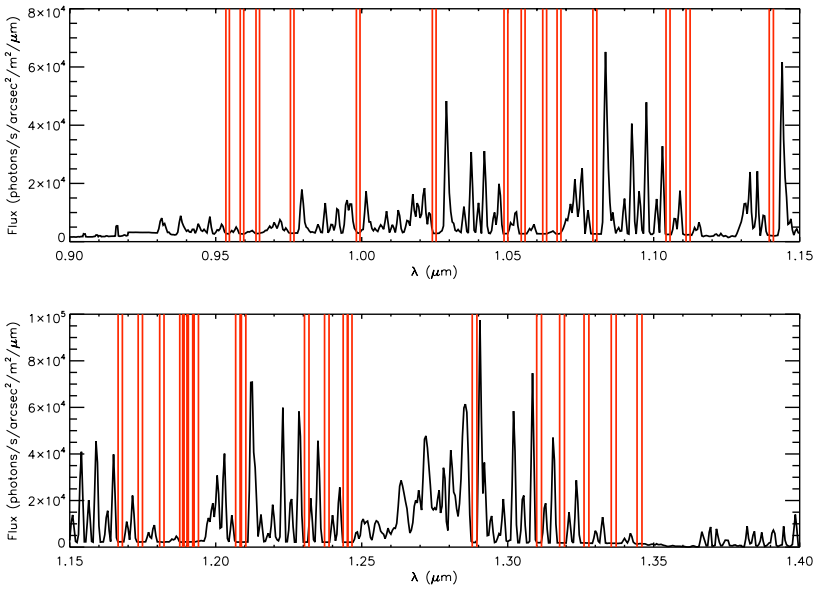

Figure 5.10 Night sky spectrum in the NIR. The vertical red lines indicate 40 possible wavelength slices of narrow transparent window in the Earth's atmosphere to probe with the F2T2 narrow-band filter. For wide spectral windows, multiple slices can be potentially probed. We avoid probing the sky where H_2O (at 0.95, 1.13 and 1.41 μm) and O_2 (at 1.27 μm) molecular absorption bands are found.

$$\dot{M}_\star = \frac{f_\star(\Omega_b/\Omega_m)M_{halo}}{t_{sys}} \tag{5.1}$$

To go from a SFR to a Lyα luminosity, the number of ionizing photons, N_γ, must be known. N_γ is dependent on the metallicity and IMF of the galaxy. For example, for a metallicity of $Z = 0.05Z_\odot$ and a Salpeter IMF, $N_\gamma = 4\times10^{53}$ photons/s/($M_\odot$/yr), but for a top-heavy IMF and $Z = 0$ galaxy, $N_\gamma = 2\times10^{54}$ photons/s/($M_\odot$/yr) (Schaerer, 2003). However, only a fraction of the ionizing photons supplied by the star-forming galaxy will be converted into observed Lyα photons. A fraction, f_{esc}, of the ionizing photons will escape into the intergalactic medium, and will consequently not be converted into a Lyα emission. A value of $f_{esc} = 0.1$ has been recently estimated by Inoue et al. (2006) for $z \sim 4-6$ galaxies. Furthermore, of those photons that do not escape, only two-thirds will result in a Lyα photon according to case B recombination, and only a fraction, $T_{\mathrm{Ly}\alpha}$, will be transmitted through the intergalactic medium which is increasingly neutral as higher redshifts are probed back to the beginning of reionization. The relation between the star formation rate, $\dot{M}_\star$, and Lyα luminosity is thus given by:

$$L_{\mathrm{Ly}\alpha} = \frac{2}{3}h\nu_{\mathrm{Ly}\alpha}N_\gamma T_{\mathrm{Ly}\alpha}(1-f_{esc})\dot{M}_\star \tag{5.2}$$

By fitting to observed luminosity functions of spectroscopically confirmed samples in the Subaru Deep Field (Shimasaku et al., 2006; Kashikawa et al., 2006), the above model can be empirically calibrated. Both Stark et al. (2007b) and Dijkstra et al. (2006) find comparable parameters with the above model fit to the Subaru field samples. They both only consider a normal Salpeter IMF ranging from $1-100$ $M_\odot$ and a metallicity of $Z = 0.05Z_\odot$.

Stark et al. (2007b) consider a mock GGS survey in which 60 clusters are observed for 5 minute exposures at 40 different wavelength regions. Figure 5.10 gives an example of some of the narrow transparent windows through the atmosphere that will be used for such a search. This would take about 200 hours of integration, but is similar in exposure time to other high-z galaxy surveys. Stark et al. (2007b) predict that the GGS could detect over 30 $z \simeq 8-10$ sources. The results of their calculation is given in Figure 5.11, which shows the GGS's ability to fall underneath the predicted luminosity function number density and thus have the potential for finding these objects. Both DAZLE and another future lensing survey, expected to start in 2009-2010 at the time of publication, with the Multi-Object Spectrograph For Infra-Red Exploration (MOSFIRE)

are shown for comparison. Given the size of the survey suggested by Stark et al. (2007b), the GGS manages to probe deep enough to detect about 30 sources. However, there are a number of parameters that can be changed in the design of the survey that can alter this number, such as the number of galaxy clusters probed, the number of different wavelength slices probed, as well as the exposure time at each wavelength slice. In addition, there are many uncertainties in the model presented in Stark et al. (2007b). The implications of the uncertainties are explored in the following section.

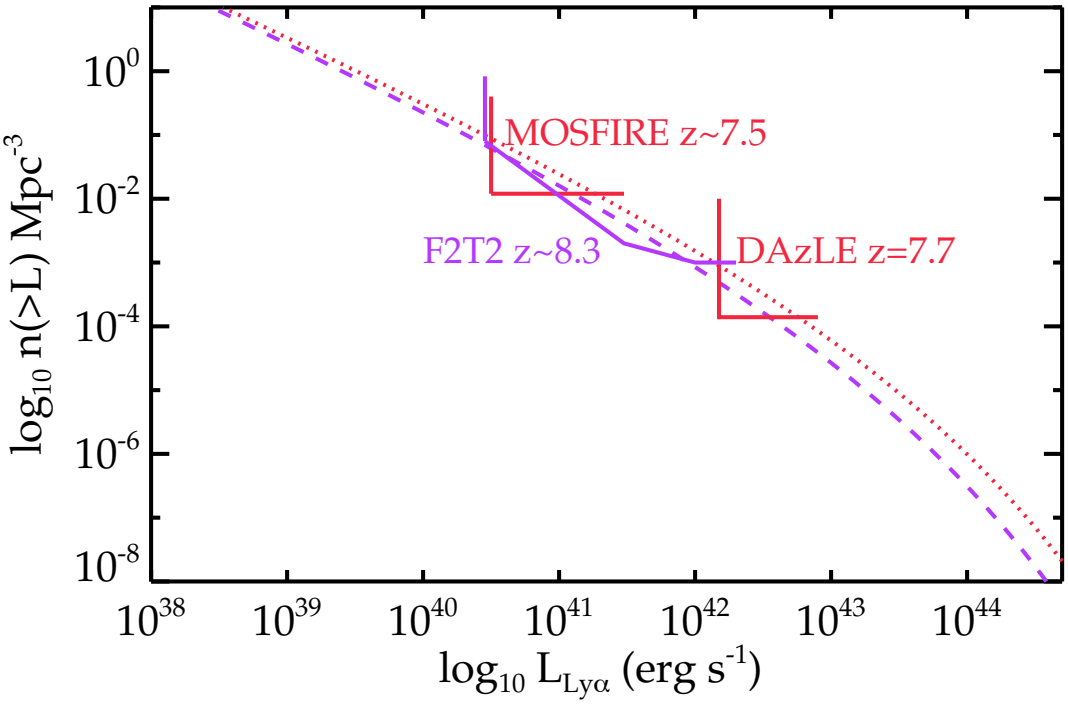

Figure 5.11 The theoretical Lyα luminosity function taken from Stark et al. (2007b) and was computed along the same principles presented in § 5.4.1. The survey limits of F2T2 (ie. GGS), DAZLE and MOSFIRE are shown in comparison. In this example, the GGS, at $z \sim 8.3$, can potentially detect about 30 sources.

5.4.2 Uncertainties in model predictions

The models that have been developed to predict the abundance of reionization sources can only be used as a guide with our current state of knowledge. The nature of the first galaxies and the transparency of the intergalactic medium to Lyα photons is extremely uncertain. Ideally, we hope to find the optimum strategy for the survey so that we find the highest number of sources and obtain the most useful information to make conclusions regarding the physical nature (number density, mass, luminosity and, if the sources are resolved, size) of primordial galaxies. Should we probe just galaxy clusters to gain in flux sensitivity in exchange for volume, or instead cover more volume by looking in blank fields as DAZLE has been designed? As we plan to use the former strategy, we might also want to consider the spatial transmission function of the filter. Possibly we will want to line up regions of higher finesse and throughput on those regions of the gravitational lens map that show the maximum magnification so that we can reach the deepest flux limits possible.

Many different elements of the model presented in Eq. 5.2 are uncertain. We consider a similar GGS survey to the one presented in Stark et al. (2007b) and choose 40 different wavelength slices and 30 galaxy clusters. We calculate the 5σ sky-limited flux sensitivity in each slice and find it to generally range from $2 - 6 \times 10^{-18}$ erg/s/cm^2 with multi-conjugate adaptive optics (MCAO) and $0.9 - 1.8 \times 10^{-17}$ erg/s/cm^2 without MCAO. The numbers change with and without an MCAO system because the spatial resolution improves by a factor of ~ 2 with MCAO, and if the sources are unresolved, then this translates directly to a gain in S/N in a given pixel. The sky noise is taken from the spectrum shown in Fig. 5.10, measured in photons/s/μm/m^2/arcsec^2, multiplied by the bandwidth of each slice ($\sim 0.001 - 0.002\,\mu$m) and the pixel area ($(0\farcs09)^2$ with MCAO, $(0\farcs18)^2$ without MCAO). We can also use this value to determine how long we will need for each exposure to be sky noise dominated over other instrumental noise. If we multiply the sky radiance by the collecting area of the Gemini South telescope (37.59 m^2), we find that the sky noise collected by the telescope is $0.16 - 0.22$ photons/s and $0.6 - 0.9$ photons/s. Assuming a read noise of 5 e^{-1} and a dark current of 0.1 e^{-1}/s/pixel, then the observations with MCAO become sky noise dominated in less than 150 s. Without MCAO, it takes only 30 s for the observations to be sky noise dominated and consequently less flux sensitive.

To calculate the number density of dark matter halos, starting with the primordial linear power spectrum of density fluctuations calculated with CMBFAST (Seljak & Zal-

darriaga, 1996), we use the fortran software package *genmf* from Reed et al. (2007). We use the mass function from Press-Schecter (Press & Schechter, 1974) with the modifications from Sheth & Tormen (1999) and Sheth et al. (2001). This mass function matches the true 'global' mass function of the N-body simulation from Reed et al. (2007) of the evolution of dark matter halos at redshifts $z = 10 - 30$. It is consistent with the mass function choice of Stark et al. (2007b) and Dijkstra et al. (2006). We use cosmological parameters from the 3 year WMAP results (Spergel et al., 2007). Specifically, we use $(\Omega_m, \Omega_\Lambda, \sigma_8, H_o) = (0.24, 0.76, 0.74, 73)$, with H_o in km/s/Mpc.

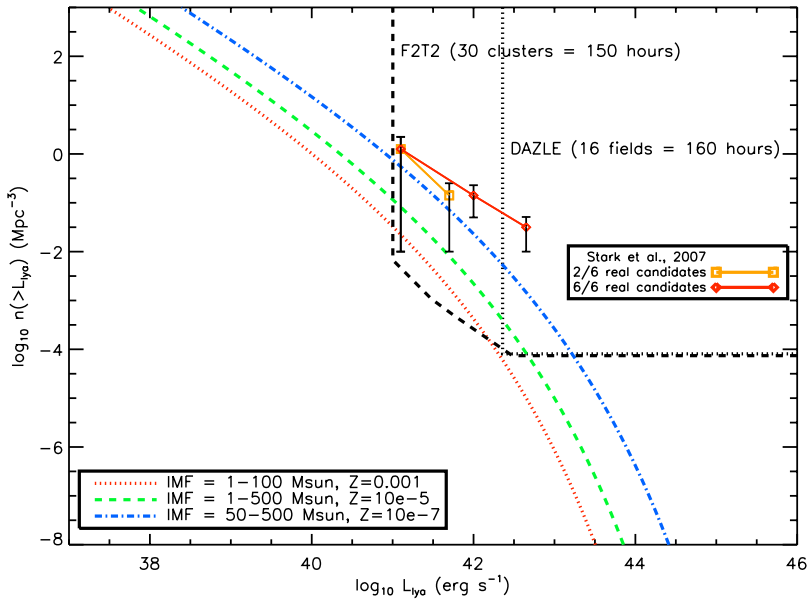

Figure 5.12 The Lyα luminosity function calculated from the initial dark matter mass function produced by Reed et al. (2007), using the conversion to Lyα luminosity prescribed by Dijkstra et al. (2006) and Stark et al. (2007b) (as in Eq.5.1 and 5.2). The survey limits for the GGS and a comparable DAZLE survey are shown. Transmission of the IGM is assumed to be the same as at $z = 6.5$ (Kashikawa et al., 2006) and each line represents the three IMF, metallicity scenarios listed in Table 5.2. For reference, the observed Lyα luminosity function found in the lensing spectroscopic slit survey of Stark et al. (2007a) is shown in the first panel.

In the following sections, we explore how the different uncertainties involved in computing the theoretical Lyα luminosity function can potentially affect the number of sources we can find. We tabulate the predicted number of sources in Table 5.2 for some of the varying parameters we now describe. Fig. 5.12 shows some of the various theoretical Lyα luminosity functions that are calculated with the varying parameters.

How many ionizing photons are produced for a given star formation rate?

The initial mass function (IMF) of these first star-forming galaxies is a major uncertainty. The number of ionizing photons for a given star formation rate depends on the IMF since a top-heavier IMF has a higher number density of massive stars which provide the bulk of the ionization radiation. For example, assuming a Salpeter IMF with a metallicity of 1/20 yields 4×10^{53} ionizing photons per second per star formation rate in $M_{\odot}/yr$, while a top-heavy IMF combined with zero metallicity produces almost an order of magnitude more ionizing photons with 3×10^{54} photons/s/$M_{\odot}$/yr (Schaerer, 2003). This value is also dependent on the metallicity of the galaxy since stars of the same mass with lower metallicity have a higher stellar temperature due to the decrease in stellar opacity.

In our model we consider three scenarios of IMF and metallicity. The first is the non-evolved scenario with a Salpeter slope IMF (Salpeter, 1955) that covers 1-100 $M_{\odot}$, and a metallicity of $Z = 0.05 Z_{\odot}$. We also consider a slightly more primordial and heavy scenario with a Salpeter slope IMF that covers 1-500 $M_{\odot}$, and a metallicity of $Z = 10^{-5} Z_{\odot}$. And finally we consider an even top-heavier IMF with a Salpeter slope and a mass range from 50-500 $M_{\odot}$ and a metallicity of $Z = 10^{-7} Z_{\odot}$.

How many of the ionizing photons produced are actually absorbed via recombination and re-emitted as Lyα photons?

Only those photons that actually get absorbed and re-emitted are measured as Lyα line emission flux. This will depend on the optical depth of the ionizing photons, primarily due to neutral hydrogen. This uncertainty is quantified by $(1 - f_{esc})$, where f_{esc} is the fraction of ionizing photons that escape the IGM and thus do not recombine and produce Lyα photons.

Inoue et al. (2006) compare the observed flux density ratio of ionizing (~ 900 Å rest-frame) to non-ionizing UV emission (~ 1500 Å rest-frame) corrected for intergalactic absorption for galaxies in the redshift range $0 < z < 6$ and find that f_{esc} increases by an

Table 5.2. Model predictions of objects with detectable Lyα emission in a GGS survey of 30 galaxy clusters in ∼150 hr of observations. Transmission, T, of Lyα through the IGM is given relative to the transmission at z=6.5.

Z	IMF	T=$T_{6.5}$	T=0.2 $T_{6.5}$	T=0.05 $T_{6.5}$	T=0.02 $T_{6.5}$	T=0.01 $T_{6.5}$
10^{-3}	1-100 $M_\odot$	12.1	0.47	0.0171	0.00126	0.000135
10^{-5}	1-500 $M_\odot$	50. 1	2.52	0.123	0.0121	0.00169
10^{-7}	50-500 $M_\odot$	407	28.9	2.09	0.299	0.0567

order of magnitude from a value less than 0.01 at $z < 1$ to about 0.1 at $z > 4$. Whether the escape fraction continues to increase is not known, but if it does, it will result in a decrease of the predicted number of sources the GGS can find.

What is the transmission of the Lyα flux through the IGM?

From the Lyα flux produced in a galaxy, what is the fraction that escapes through the intergalactic medium (IGM) and is observed? The model used in Stark et al. (2007b) and Dijkstra et al. (2006) has been calibrated with $z = 6.5$ observations from Kashikawa et al. (2006). However, as line of sight absorption from neutral gas in between high-z quasars suggests that the universe was partly neutral at $z \sim 6$ and we are thus witnessing the tail end of reionization, the observed fluxes, $F_{\rm obs}$, from Kashikawa et al. (2006) are related to the intrinsic line emission flux of the galaxy, $F_{\rm Ly\alpha}$ by

$$F_{\rm obs} = T_{6.5}(1 - f_{esc})F_{\rm Ly\alpha} \tag{5.3}$$

where $T_{6.5}$ is the transmission of the IGM at redshift 6 and f_{esc} is the escape fraction described above. Dijkstra et al. (2007) estimate the IGM transmits only $10 - 30\%$ at $z = 5.7$ and that this value is reduced by a factor of 1.2 at $z = 6.5$. It is expected that the transmission continues to decrease as the fraction of neutral hydrogen in the IGM increases with redshift.

To examine the dependency of an increasingly neutral IGM on the Lyα luminosity function model, in Table 5.2, we present how many sources we can find in the GGS survey with the transmission the same at $z = 9$ as it is at $z = 6.5$ and alternatively, at 0.2, 0.05, 0.02, and 0.01 times smaller than the transmission at $z = 6.5$. We plot the Lyα luminosity function for three of these transmission factors (1, 0.2 and 0.01)$\times$ $T_{6.5}$ in

Fig. 5.12. As expected, the decreasing transmission of the IGM greatly affects the number of sources we can see. *Probing higher redshifts, we eventually reach a point where the universe was sufficiently neutral such that that all Lyα emission is absorbed by the IGM and no sources can be observed from their Lyα line emission, from the ground or even with JWST.* As a result, the best way to search for these first star-forming galaxies is to detect their stellar continuum emission, a possibility with the Multi-Object Infrared Camera and Spectrograph (MOIRCS, Ichikawa et al. 2006) now operating on the 8.2m Subaru telescope, but more likely from space with the new WFC3/IR camera on *HST* or the future *JWST* mission.

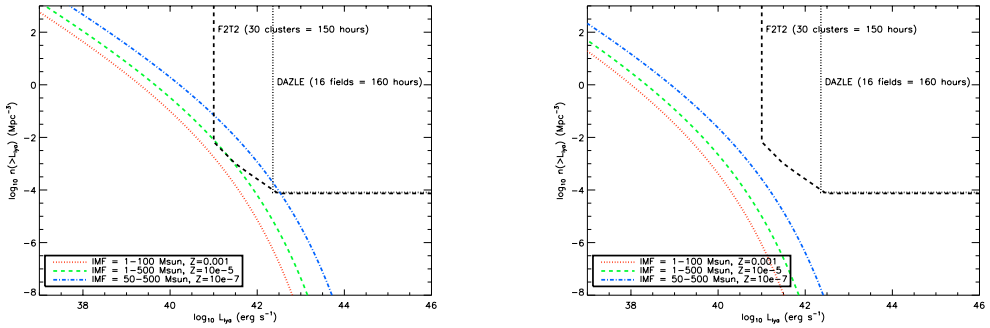

Figure 5.13 As in Figure 5.12, but for T_{IGM}=0.2 $T_{6.5}$ (right) and T_{IGM}=0.01 $T_{6.5}$ (left), where $T_{6.5}$ is defined as the transmission to Lyα radiation at $z = 6.5$. Each panel has the three IMF, metallicity scenarios listed in Table 5.2. The number of high-z galaxies that can be detected at $z > 8$ drastically decreases if the universe is neutral and opaque to Lyα emission.

Magnification by galaxy clusters used as gravitational lenses

In Stark et al. (2007b), it is found that according to the lens modeling provided by Richard et al. (2006), a typical cluster provides a magnification gain of at least $\times$5, 10, and 30 over 80%, 69%, and 33% of the F2T2 45″ field of view. For a GGS survey of 30 galaxy clusters for 40 wavelength slices, the GGS can probe a comoving volume 13 481 Mpc^3 to a flux depth of 3.0×10^{42} erg/s over the entire field of view without any magnification gain. If a galaxy cluster provides the above magnification gains, then the GGS can probe flux limits of (6.0, 3.0 and 1.0)$\times 10^{41}$ erg/s over a volume of 2157, 930.2, and 148.2 Mpc^3, respectively. We use these volume and flux limits to define the survey sensitivity of the

GGS shown in Figures 5.12 and 5.13 and to count the number of sources greater than 10^{41} erg/s that can be found with the GGS in Table 5.2.

What is the variance of our survey volume?

Interpreting and planning observations of galaxies in the reionization era requires accurate quantification of uncertainties arising from both Poisson errors and fluctuations in the large-scale distribution of galaxies. The latter can be quantified from the cosmic variance predicted by the underlying dark matter halo distribution. Over the small volumes the GGS plans to probe, it is recognized that cosmic variance is a major uncertainty and we will benefit from probing as much volume as possible.

To quantify this, we follow Somerville et al. (2004) and Stark et al. (2007b), and compute the variance of dark matter, σ^2, in a smoothing window of our survey volume as:

$$\sigma^2_{DM}(a_x, a_y, a_z) = \int P(k)\tilde{W}(\mathrm{k_x}, \mathrm{k_y}, \mathrm{k_z}; a_x, a_y, a_z)d_x d_y d_z \tag{5.4}$$

where $P(k)$ is the non-linear power spectrum of density fluctuations extrapolated to zero. To get an analytic form of $P(k)$, we apply the analytical non-linear corrections provided in Smith et al. (2003) to the linear power spectrum from CMBFAST (Seljak & Zaldarriaga, 1996) used in creating the mass function described above. Due to edge effects of our survey geometry (Kaiser & Peacock, 1991; Feldman et al., 1994), a smoothing window function, $\tilde{W}$, is chosen as the Fourier transform of a rectangular top-hat with dimensions corresponding to the survey, given by:

$$\tilde{W}(\mathrm{k_x}, \mathrm{k_y}, \mathrm{k_z}; a_x, a_y, a_z) = n_{cluster}\frac{\sin(k_x a_x/2)}{k_x ax/2}\frac{\sin(k_y a_y/2)}{k_y ay/2}\frac{\sin(k_z a_z/2)}{k_z az/2} \tag{5.5}$$

where $n_{cluster}$ is the number of galaxy clusters probed, and a_x, a_y and a_z correspond to the dimensions of the survey ($45''$ by $45\ ''$). However, these dimensions only apply to the image plane. The GGS plans to utilize the magnification gain in flux produced by galaxy clusters. But the gain in flux is balanced by a loss in survey volume. Mass models of these lensing clusters indicate that the magnification will not be isotropic, but rather strongest along lines of critical magnification. To quantify this loss in survey volume, we follow Stark et al. (2007b) and assume the dimensions are reduced by a factor of $\sqrt{\mu}$ along both the a_x and a_y directions, with μ being the magnification gain,

The clustering in dark matter halos is found by multiplying the variance in dark matter, σ^2_{DM} given by Eq. 5.4, by the large scale halo bias, $b^2(z, M)$, given in Sheth et al. (2001). From this, we can get the variance in galaxy clustering if we assume that one galaxy is formed per halo.

$$\sigma^2_{galaxy}(z, M) = b^2(z, M)\sigma^2_{DM} \tag{5.6}$$

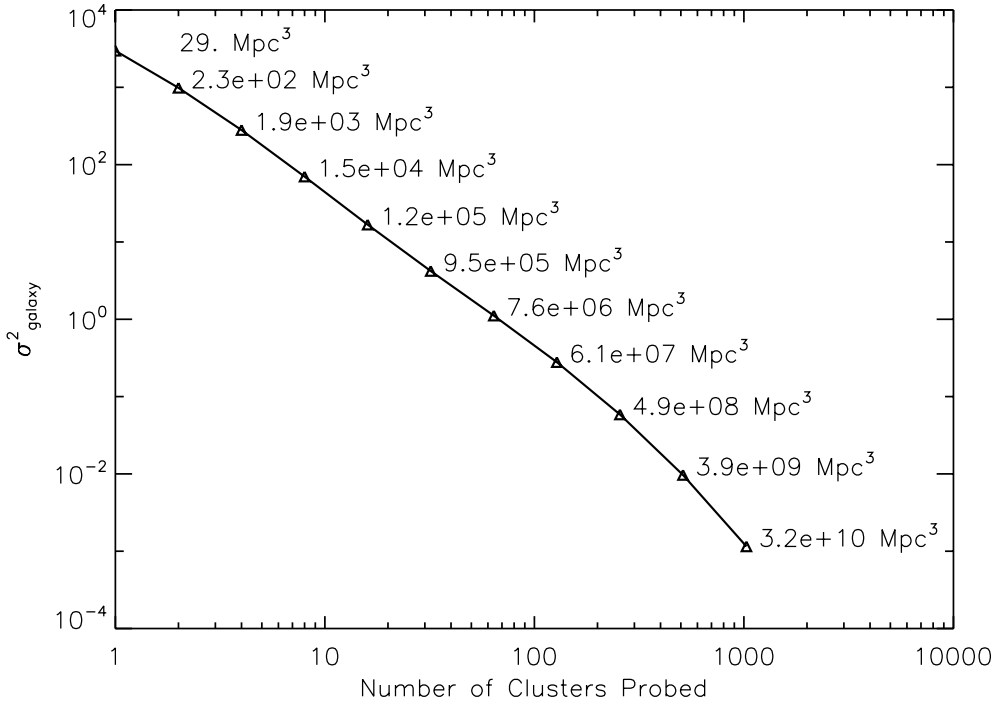

Figure 5.14 Cosmic variance in detecting galaxies at $z \sim 9$ with a Lyα luminosity of $10^{41} - 10^{42}$ erg s^{-1} as a function of the number of galaxy clusters observed. The volume probed for the given number of galaxy clusters is shown on the plot for reference. A single galaxy cluster probes a volume of 29 Mpc^3.

Fig. 5.14 shows how the cosmic variance greatly depends on the number of galaxy clusters, and consequently the survey volume, the GGS plans to probe. If we want to have $\sigma^2_{galaxy} < 1$ then at least ~ 60 galaxy clusters will have to be observed, corresponding to

a survey volume of at least 1 Million Mpc^3. This would require 300 h of observing time, if each wavelength slice is observed 3 times at 150 s each (achieving 5σ detection over the sky background).

5.4.3 Summary

There are many uncertainties in predicting the number of sources that can be potentially detected in a Lyα line emission search like the GGS. There is no real indication of the nature of the IMF of these first star-forming galaxies. A possibility of detecting Population III sources is a strong motivation for the design of the survey, especially since it is only with a top-heavy IMF that a high number of sources can be detected. Many uncertainties in the density of the IGM and the nature of reionization also make the GGS a blind, but necessary survey. For this reason, the design of the GGS is to simply go as deep as possible given sky noise background limitations. This is achieved by the design of F2T2, which can scan and provide a narrow-band imaging filter at the various windows in the NIR night sky and thus covering more survey volume than conventional fixed narrow-band surveys like DAZLE. The other way the GGS will go deeper than most surveys is by utilizing magnification gain from intermediate redshift galaxy clusters. Unlike lensing slit surveys, the GGS can cover the entire field of view of the lensing galaxy cluster. Unfortunately, the uncertainty in the observed luminosity function due to cosmic variance will be large unless a high number (> 60) of galaxy clusters are imaged.

5.5 Other high-redshift uses for the F2T2 filter

It has been demonstrated that the GGS may fail to detect Lyα sources if they are too faint for the flux sensitivity of the instrument or the IGM too neutral to allow Lyα photons to escape. However, with this unique tunable NIR filter, there are many other scientific opportunities to learn about the universe at high and very high redshifts. And in many of these cases, the implementation of the observations is very similar to a lensed Lyα search and can thus be a complementary goal. Here, we will outline a few of the possibilities and also consider observations with and without the MCAO system on the *Gemini South Telescope*.

Table 5.3. Specifications of potential deep fields

Sample	R.A.	DEC	Areal Coverage (arcmin^2)	No. of i-dropouts	No. of z_{850}-dropouts	Magnitude Limit (z_{850})
HUDF	03 32 39.0	-27 47 29.1	11	122	5	28.6
HUDFP1	03 33 03.7	-27 41 01.5	10.2	54		28.6
HUDFP2	03 33 08.2	-27 52 56.1	7	14		29.4

5.5.1 He II emission in the *Hubble* Ultra Deep Field

Before MCAO comes online, F2T2 has the potential to investigate NIR line emission of high redshift galaxies in the *Hubble* Ultra Deep Field (HUDF) and if time permits, the *Hubble* Parallel Fields as well. Table 5.3 shows the location, area and magnitude limit of these three extremely deep and well studied fields. The most direct way to detect massive stars in galaxies, and probe the heavy end of the IMF, is from their spectral signatures. Unambiguous spectral features from massive stars are most easily found in the UV part of the spectrum (e.g. He II at $\lambda = 1640$Å, Si IV at $\lambda = 1400$Å and C IV at $\lambda = 1550$ Å). In particular, there is already some indication for relatively strong He II emission in the composite spectrum of LBGs (Shapley et al., 2003), a possible indication of a top-heavy IMF (Jimenez & Haiman, 2006). If F2T2 is integrated into Flamingos-2 prior to MCAO this is an excellent opportunity to collect some interesting science and try to measure these lines in very high-z galaxies already detected in the deep fields.

Table 5.4 shows objects with known Lyα emission in the HUDF. Following the prescription of Schaerer (2003), we convert the Lyα emission into a star formation rate, assuming $T_{IGM} = 0.12$, according to Dijkstra et al. (2007). The SFR can then be converted to He II line emission flux using the constants supplied in Table 4 of Schaerer (2003) for the three metallicity, IMF scenarios listed in Table 5.2. The resulting emission flux is found in Table 5.4. As F2T2 will be sky-noise limited, it will be unable to detect emission for all three scenarios, unless we expose for much longer integration times which we could potentially do if we know the exact redshift of a He II line or some other line of interest. Of course, it is still worth observing as the model used in Schaerer (2003) is not necessarily correct.

Table 5.4. Predicted HeII line emission flux for objects in the HUDF with detectable Lyα emission.

Object ID	z	$f_{Ly\alpha}$	f_{HeII} $Z = 10^{-3}$ IMF =1-100 $M_\odot$	f_{HeII} $Z = 10^{-5}$ IMF = 1-500 $M_\odot$	f_{HeII} $Z = 10^{-7}$ IMF = 50-500 $M_\odot$
GLARE1042a	5.83	15.8	0.0165	0.0291	0.2197
GLARE1054	5.93	6.8	0.0071	0.0125	0.0946
GLARE1008	6.13	4.3	0.0045	0.0079	0.0598
GLARE3001	5.79	7.7	0.0081	0.0142	0.1071
GLARE3011	5.93	11.3	0.0118	0.0208	0.1572
BD 46	5.914	9.0	0.0094	0.0166	0.1252
BD 00	5.942	35.0	0.0366	0.0645	0.4868
GOODS i6 0	5.540	13.4	0.0140	0.0247	0.1864
UDF PFs i4	5.857	7.0	0.0073	0.0129	0.0974
UDF PFs i1	6.005	11.0	0.0115	0.0203	0.1530
UDF PFs i2	6.083	9.6	0.0100	0.0177	0.1335

All fluxes in 10^{-18}erg cm^{-2} s^{-1}

5.5.2 He II emission magnified by gravitational telescopes

We can follow a similar method to §5.4 and try to predict the amount of He II line emission as a function of the metallicity and IMF of the sources. The luminosity in an emission line of He II ($\lambda = 1640$ Å) is given by:

$$L_{\rm He} = 6 \times 10^{-11} \text{ erg s}^{-1} \; N_\gamma (1 - f_{esc}) \dot{M}_\star \tag{5.7}$$

where $\dot{M}_\star$ is given in eq. 5.1. The factor in front is analogous to the $\frac{2}{3} h\nu_{\rm Ly\alpha}$ in Eq. 5.2, but applied to the He II line. This pre-factor is taken directly from Schaerer (2003). The resulting He II luminosity function at $z = 6.5$ is shown in Fig. 5.15 along with the sensitivity limits of the GGS.

Based on this model, only 0.02 sources can be found in a volume probed by 30 clusters with the non-evolved IMF and metallicity. If we desire to detect just one source more than ~ 35 clusters must be probed. However, if we model using a top-heavier IMF with a Salpeter slope for a mass range of 1-100 $M_\odot$ and Z=10^{-5} as described in §5.4, then the number of predicted sources increases to 0.34. If we consider a much more top top-heavy IMF then 140 He II emission line sources are predicted to be found in 30 cluster GGS survey.

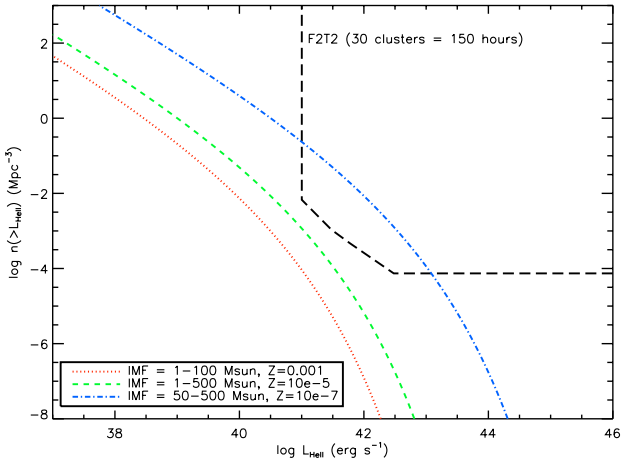

Figure 5.15 The He II luminosity function at $z = 6.5$ converted from the mass function of dark matter halos using Eq. 5.7. The survey limit of a survey of 30 galaxy clusters with F2T2 is shown for comparison.

The design of this survey for He II emission is completely identical to the search for Lyα line emission and can be carried out simultaneously. The GGS will probe He II emission for LAEs at $z \sim 5-8$. However, the confirmation of the He II line is much easier since we would expect to have a strong Lyα emission line at shorter wavelengths. These observations can be obtained from today's large ground-based facilities. The clusters probed are well studied and observed, we should expect to be able to find the corresponding Lyα emission in archived data or if necessary, we can perform a quick narrow-band search of the line since we will know which redshift range the line should be found.

5.5.3 Observability of H II reionization bubbles

At high redshift, where the universe is primarily neutral, sources of reionization are surrounded by neutral gas. As a result, the unresolved sources may not be detectable, but Stromgren Spheres of reionized hydrogen surrounded these sources might be. It is straightforward to show that for a sphere with a source of ionizing radiation in its centre, theoretical estimate of the total Lyα luminosity provided by one of these sources, scaled to $T = 10^4$ K at $z = 9$:

$$L_{\mathrm{Ly}\alpha} = 2.786 \times 10^{42}\ \mathrm{erg\ s^{-1}} \left(\frac{1+\delta}{2}\right)^2 \left(\frac{\eta}{2}\right) \left(\frac{1+z}{10}\right)^3 \left(\frac{\mathrm{R}}{5\ \mathrm{Mpc}}\right) \left(\frac{T}{10^4\ \mathrm{K}}\right)^{-3/4} \tag{5.8}$$

We investigate the ability of F2T2 to detect the flux from these sources. First, we consider how much flux is received on a single pixel. Since the luminosity of the bubble is distributed over a large volume, it will not be resolved on a single pixel or even within the entire detector area. The amount of flux that reaches a single pixel is given by

$$F = \left(\frac{\text{Pixel Area/Detector Area}}{\text{Bubble Area}}\right) L_{\mathrm{Ly}\alpha} 4\pi {\mathrm{D_L}}^2 \tag{5.9}$$

where Bubble Area $= \pi(\mathrm{R}/\mathrm{D_A})^2$, where R is the physical size of the bubble and $\mathrm{D_A}$ is the angular diameter distance. The pixel area for F2T2 without MCAO is $0.0324\,\mathrm{arcsec}^2$. The detector area is $1.5'$ by $1.5'$.

The right panel of 5.16 shows how much flux is detected over the entire detector. It seems feasible with careful image analysis and sky removal techniques that we can actually detect these bubbles, however, the possibility of detecting them on a single pixel would require hours of integration to reach a signal stronger than the sky noise.

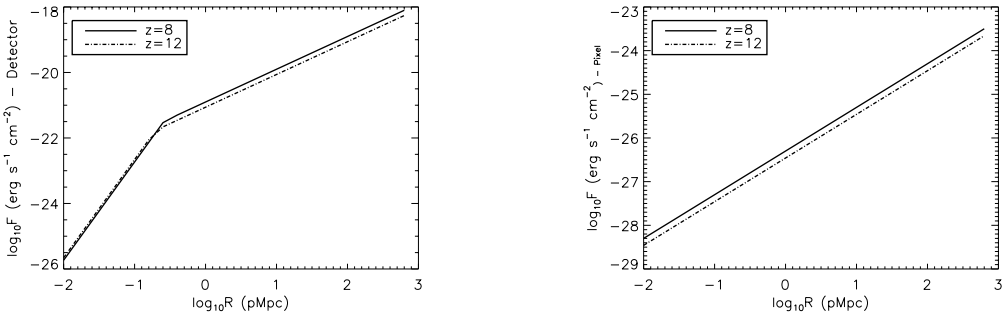

Figure 5.16 Flux sensitivity required to detect H II regions around First Light sources. We consider detecting the emission integrated over the entire detector (left) and on a single pixel (right).

5.6 Summary

The Flamingos-2 Tandem Tunable filter is an accessory mode instrument designed for the Flamingos-2 imaging spectrograph to be used with the upcoming multi-conjugate adaptive optics on the 8 m *Gemini South Telescope*. For my thesis, I have helped to develop the control software which digitally controls the two Fabry-Perot etalons that comprise the F2T2 filter. Laboratory work involved calibrating the electronics of the instrument using optical feedback from a Fizeau interferometer optical test set up. Various new software programs were written to interpolate calibration settings and perform opto-mechanical control to allow the filter to be digitally controlled down to ∼1 nm level accuracy. The filter's main science goal is to perform a search for Lyα emitting galaxies at $8 < z < 11$. The search, to be undertaken by the Gemini Genesis Survey team, requires $\sim 150-200$ h of integration, observing at least 30 galaxy clusters as $\sim 30-40$ narrow-band images corresponding to different narrow windows of transparency in the NIR night sky. Predictions for the number of possible detections are presented in this chapter, but due to the high uncertainty in the transmission of the intergalactic medium to neutral hydrogen and uncertainties related to theoretical modeling and cosmic variance, the counts can be as high as ∼400 and as low as zero.

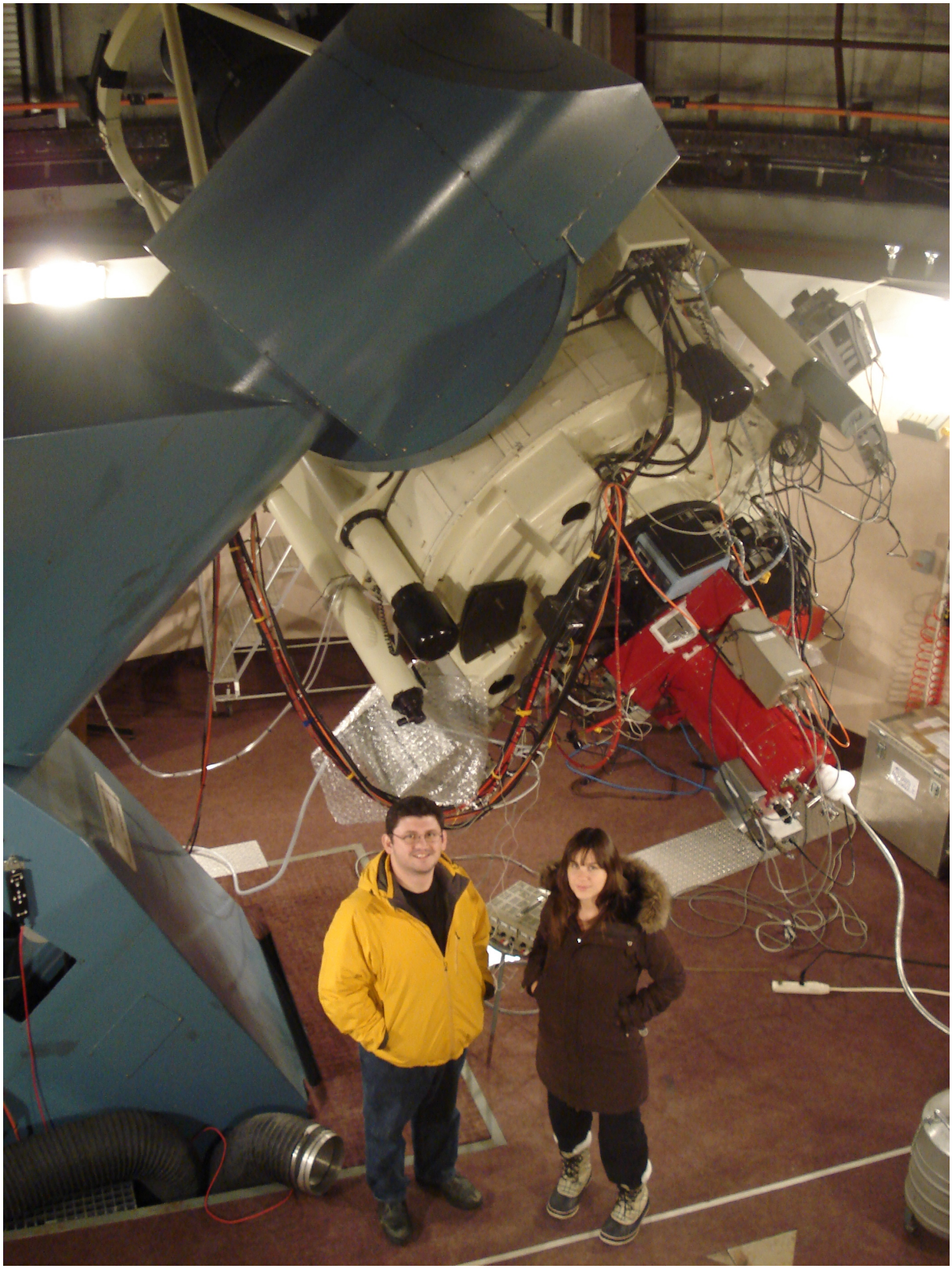

Figure 5.17 Roberto Abraham and Erin Mentuch with the F2T2 filter at the Mont Megantic Observatory. *November 2008*

Chapter 6

Conclusions

This thesis has encompassed a rather broad range of existing and potential observations of extragalactic stellar populations in the near- and mid-infrared. Some of the observations discussed in this thesis are of stellar populations that reside in nearby galaxies, while other observations are of those found in massive, star-forming galaxies at intermediate redshifts when the universe formed the bulk of its stars. This thesis also previewed future observations of extremely high redshift ($z > 7$) galaxies in the NIR with a tunable filter. Because of the broad range of observations and subject material, each chapter was presented with an independent introduction and conclusion section. Here, I briefly summarize the highlights of each chapter and discuss how this broad range of observations together form a strong extragalactic science driver for the upcoming *James Webb Space Telescope*.

6.1 Summary

In the first two chapters, *Spitzer* IRAC observations at 3.6, 4.5, 5.6 and 8.0 μm and MIPS observations at 24 μm were analyzed for a spectroscopic sample of ~ 100 galaxies at $z = 0.5 - 2$ from the Gemini Deep Deep Survey (GDDS; Abraham et al. 2004). In **chapter 2**, the galaxies were modeled using visible through mid-infrared wavelength photometry including wavebands from IRAC. I showed that the star formation history of a galaxy is more accurately determined when rest-frame UV through NIR photometry is included in the fitting analysis. Stellar masses, the evolving mass function and the resulting mass density function, previously determined with $VIz'K_s$ wavebands in Glazebrook et al. (2004), were revisited. Stellar masses for evolved, red ($U - B_{\rm rest} > 0.1$) galaxies proved

consistent with previous estimates, but galaxies with young or mixed stellar populations and bluer colours ($U - B_{\rm rest} < 0.1$), have stellar masses on average $\sim$0.2 dex higher. The largest changes, however, affect lower mass galaxies that contribute less to the resulting mass density and mass functions, and as a result the revised *Spitzer* IRAC stellar masses produce mass functions and mass densities that are consistent with those measured with the $VIz'K_s$ wavebands only. Also in chapter 2, I investigated the affect of model input parameters, such as the choice of the star formation history model, the inclusion of an NIR emission component and the treatment of TP-AGB stars, on stellar masses.

In the analysis presented in chapter 2, a surprising result emerged in the data. Although the rest-frame light short of 2 μm greatly improved stellar mass estimates through stellar population fitting, the models and observations disagreed beyond 2 μm. In **chapter 3**, I began by showing that relative to SPS models, there is a statistically significant component to a galaxy's SED that emits in the NIR above the NIR emission provided by the stellar population alone. Motivated by a correlation between the luminosity of the NIR excess emission component and the star formation rate in a sample of 88 galaxies all with high confident spectroscopic redshifts from the GDDS, I sought for objects locally that display NIR excess emission and determined how each NIR emitting candidate would stack up when seen as a galactic scaled population.

In **chapter 4**, I measured the pixel-by-pixel near-infrared colours for a sample of 68 nearby galaxies common to the *Spitzer* Infrared Nearby Galaxy survey (SINGS; Kennicutt et al. 2003) and the Large Galaxy Atlas survey (LGA; Jarrett et al. 2003) observed at Hα, 1.25, 3.6, 4.5, 5.6, 8.0 and 24 μm. I separated each galaxy into different regions based on increasingly red near-infrared colours, consisting of colours in excess of near-infrared colours due to stellar emission. The average intensities in the colour-selected regions at 1.25, 3.6, 4.5, 5.6, 8.0 and 24 μm were found to increase linearly with the star formation rate, suggesting the emission may be built into stellar population synthesis modeling as a feature tied to the input star formation rate. The spectral energy distribution (SED) resulting from the linear scaling represents the near- through mid-infrared spectrum of a star-forming population and suggests that strong PAH emission and near-infrared continuum emission is closely tied with the most massive, short lived stars and is the source of large near-infrared colours at 2-5 μm.

In **chapter 5**, I continued with the theme of near-infrared observations of stellar populations, but pushed the redshift limit and showed how a tunable near-infrared filter I have helped develop holds promise of finding bright Lyman alpha emitting galaxies at

redshifts of $8 < z < 11$. The Flamingos 2 Tandem Tunable (F2T2; Scott et al. 2006; Mentuch et al. 2008) is a tunable filter that can take narrowband images at any wavelength within the J-band, scanning from 0.95 to 1.35 μm. Like a slit spectrograph, the filter will be able to search for Lyman alpha emitting galaxies at a range of wavelengths, but more efficiently than the slit spectrograph, since the filter will be able to image a large area just as a traditional narrowband filter would. In this chapter, I presented the development of the opto-mechanical control system of the F2T2 filter and presented the results of its commissioning on a 1.6 m telescope at the *Mont Megantic Observatory*. The search strategy to be implemented with the filter is presented and number count predictions for $z = 8 < z < 11$ candidates are made by evolving the measured galaxy luminosity function at $z = 5 - 7$.

Common to all chapters is the 1-30 μm wavelength range. The increased sensitivity provided by the *Spitzer Space Telescope* has opened a new door into studying stellar populations in the near-infrared and has paved the road for future studies with new facilities such as the *Herschel Space Telescope* and upcoming facilities like the *James Webb Space Telescope*. What we have already learned and are still learning from *Spitzer* provides the fundamental tools that we will need to use to detect and understand distant extragalactic stellar populations.

6.2 The bigger picture

NIR photometry is essential for modeling stellar populations. Photometry spanning the rest-frame UV to NIR is ideal for modeling the ages of the composite stellar populations seen in the integrated light of a galaxy. UV photometry combined with visible wavelengths helps to constrain the dust extinction, while visible photometry combined with NIR measures both the underlying evolved population and the current star-forming population (as shown in Ch. 2 of this thesis), providing the most accurate mass-to-light measurements and resulting stellar mass estimates. Even without visible wavelength information, the NIR alone can offer relatively robust stellar mass measurements because of the smaller variation of the mass-to-light ratio at NIR wavelengths as a function of the age of a stellar population.

At wavelengths longer than $\sim$2 μm, emission from non-stellar sources (dust and PAHs) contributes to the SEDs of galaxies. The emission at 2–5 μm can be modeled as a hot ($\sim$ 1000 K) greybody whose luminosity correlates with the star formation rate (as seen

for our sample of high-z galaxies in Ch. 3). In addition to this, work shown in this thesis (Ch. 4) suggests the NIR and MIR SED of a stellar population is also tied its age, as it is with the visible SED of a stellar population. Although the nuances of this model, particularly those concerned with metallicity and variations in dust composition, are yet to be addressed, the tight linear relationship of the SED to the star formation rate indicates heating from the stellar populations (specifically massive young stars) results in emission from PAHs and/or dust; at least if the emission is averaged over large enough scales ($\sim$500 pc worked well for the SINGS sample). If the NIR through MIR broadband photometry of a stellar population can be well described as a function of its age, then just as with the optical combined with NIR, the NIR combined with MIR observations of galaxies may improve our understanding of their composite stellar populations. From this modeling, the infrared mass-to-light ratio and stellar mass estimates offered from a combination of NIR and MIR photometry may be just as robust as those provided by a combination of NIR and visible photometry.

The *James Webb Space Telescope* (*JWST*) will be launched in just a few years (2014 is the earliest expected launch date). This infrared facility will operate from 0.6 to 28 μm. Its 6.5 m mirror and improved detectors will provide deeper sensitivity and over 7$\times$ better resolution than *Spitzer*. *JWST* will be able to detect fainter, more distant galaxies than we have ever seen before. The work in this thesis shows we can now begin to create the tools to determine the redshift, stellar mass and star formation rate of a galaxy in a manner optimized for the superior data provided by *JWST*. The additional constraints provided by *JWST* will increase the precision of the modeled parameters and will be particularly useful for faint surveys of distant galaxies where visible wavelength data may not be available or is not sensitive enough.

6.3 Future work

In closing this thesis, a number of exciting possibilities are open for further investigation. Some of these I hope to accomplish as a postdoctoral researcher for Professor Christine Wilson at McMaster University, and others will continue at University of Toronto in collaboration with my PhD thesis supervisor Professor Bob Abraham.

PAH emission as a tool for measuring star formation rates

Previous work (Lu et al., 2003; Smith et al., 2007) on nearby galaxies has suggested a universal scaling of the PAH spectrum for typical star-forming galaxies, but the tight linear relation to the intrinsic Hα emission (i.e. ionized hydrogen gas) that is found in this thesis is a surprising new result. If Hα, especially intrinsic Hα, is used as a proxy for a galaxy's star formation rate, can the luminosity of PAH emission also be used? Theoretical models of PAH emission (see for example Draine et al. 2007) are complex and shown to depend on a number of parameters, like the ionization states of the PAH molecules, the strength and spectrum of ionizing radiation and the local interstellar environment. And indeed resolved studies show PAH emission is not universally mapped to atomic or molecular gas emission, nor are the line ratios comprising the spectrum as constant, on the scales in our own galaxy. However, the results of a linearly scaled near- and mid-IR spectrum for a large number of stellar environments shows that on large enough scales, the details are glossed over and the SED can be used to gain insight on the galaxy and even measure its star formation rate. But this was found by isolating the "normal" pixels of galaxies, those pixels containing stellar populations with standard NIR colours. Studying galaxies with atypical properties such as low metallicity, low stellar mass or those containing a strong active galactic nuclei is a necessary next step to determine how well the PAH luminosity is a proxy for the star formation rate.

Spatially resolved PAH emission spectrum

The broad colours of the PAH emission spectrum are constant for a large number of resolved stellar populations in nearby galaxies. Is this the result of constant line and/or continuum emission ratios? Do these ratios remain the same over different fields? *JWST's* mid-infrared camera MIRI will offer low and high resolution observing modes to explore the SED of PAH emission at higher spectral resolution for observations greater than 5 μm, while its near-infrared spectrograph, NIRI, or NIR tunable filter, TFI, can probe wavelengths from 1-5 μm.

Infrared emission and stellar populations

The total infrared luminosity of a galaxy is often used as a proxy for the star formation rate. How well does this assumption of a strong link between total IR emission and the SFR apply for nearby resolved stellar populations? Using the tools I have developed in

my thesis, an obvious next step is to study the broad spectral energy distribution at a pixel-by-pixel level and verify this assumption as well as calibrate the use of NIR and MIR line emission or NIR colours as a measure of the star formation rate. In the Fall of 2010 I begin a postdoctoral research position at McMaster University working with Professor Christine Wilson. Professor Wilson has extensive experience studying molecular and gas emission in nearby galaxies and its relation to star formation. She is the principal investigator of the *Herschel* key program *"Physical Processes in the Interstellar Medium of Very Nearby Galaxies"* survey and a member of another key program entitled *"Key Insights on Nearby Galaxies: A Far-Infrared Survey with Herschel (KINGFISH)"* survey. Both surveys plan to augment a rich suite of ancillary data (ranging from broadband imaging in the UV through Infrared, as well as atomic and molecular gas mapping) with high resolution infrared imaging with *Herschel* for the closest galaxies and are ideal laboratories for resolved stellar population synthesis studies and their connection to star formation.

Galaxies at $z > 8$

The F2T2 near-infrared tunable filter still awaits use on a $\sim$10 m class telescope. In its conception in 2004, the filter was expected to be installed within the Flamingos-2 imaging spectrograph on Gemini South in Fall 2007. Flamingos-2 is four years late and as is the case with many astronomical instruments, the delay was never expected to be this long. Although the refurbished *HST* has found a number of candidate galaxies at $z > 8$, our understanding of these galaxies and their implications for reionization is still uncertain and F2T2 still stands to offer new insights before *JWST*. These *HST* galaxies have yet to be spectroscopically confirmed. The F2T2 filter could confirm these systems if they emit Lyα emission. The candidates also represent the most massive galaxies at the time, but apparently they do not provide enough ionizing radiation to reionize the universe. F2T2, by utilizing the gain of intermediate galaxy clusters, can probe smaller, fainter galaxies and determine whether low-mass, but high star-forming galaxies at $z > 8$ could have caused reionization. If F2T2 fails to do so, its counterpart in space, the Tunable Filter Imager (TFI) on *JWST* stands the best chance of doing so, offering unprecedented sensitivity at very high spatial resolution from $1 - 5\,\mu$m.

Bibliography

Abraham, R. G., Glazebrook, K., McCarthy, P. J., Crampton, D., Murowinski, R., Jørgensen, I., Roth, K., Hook, I. M., Savaglio, S., Chen, H.-W., Marzke, R. O., & Carlberg, R. G. 2004, The Astronomical Journal, 127, 2455, (c) 2004: The American Astronomical Society

Abraham, R. G., Nair, P., McCarthy, P. J., Glazebrook, K., Mentuch, E., Yan, H., Savaglio, S., Crampton, D., Murowinski, R., Juneau, S., Borgne, D. L., Carlberg, R. G., Jørgensen, I., Roth, K., Chen, H.-W., & Marzke, R. O. 2007, The Astrophysical Journal, 669, 184, (c) 2007: The American Astronomical Society

Acke, B. & van den Ancker, M. E. 2004, Astronomy and Astrophysics, 426, 151

Althaus, L. G. & Benvenuto, O. G. 1997, Astrophysical Journal v.477, 477, 313

Arendt, R. G., Berriman, G. B., Boggess, N., Dwek, E., Hauser, M. G., Kelsall, T., Moseley, S. H., Murdock, T. L., Odegard, N., Silverberg, R. F., Sodroski, T. J., & Weiland, J. L. 1994, Astrophysical Journal, 425, L85

Baldry, I. K. & Glazebrook, K. 2003, The Astrophysical Journal, 593, 258, (c) 2003: The American Astronomical Society

Bernard, J. P., Boulanger, F., Desert, F. X., Giard, M., Helou, G., & Puget, J. L. 1994, Astronomy and Astrophysics (ISSN 0004-6361), 291, L5

Bessell, M. S., Brett, J. M., Wood, P. R., & Scholz, M. 1989, Astronomy and Astrophysics Supplement Series (ISSN 0365-0138), 77, 1

Bland-Hawthorn, J. & Jones, D. H. 1998, Proc. SPIE Vol. 3355, 3355, 855

Borgne, J.-F. L., Bruzual, G., Pelló, R., Lançon, A., Rocca-Volmerange, B., Sanahuja, B., Schaerer, D., Soubiran, C., & Vílchez-Gómez, R. 2003, Astronomy and Astrophysics, 402, 433

Bouwens, R. J., Illingworth, G. D., Blakeslee, J. P., & Franx, M. 2006, ApJ, 653, 53

Bouwens, R. J., Illingworth, G. D., Labbe, I., Oesch, P. A., Carollo, M., Trenti, M., van Dokkum, P. G., Franx, M., Stiavelli, M., Gonzalez, V., & Magee, D. 2009, arXiv, astro-ph.CO

Bouwens, R. J., Illingworth, G. D., Oesch, P. A., Stiavelli, M., Dokkum, P. V., Trenti, M., Magee, D., Labbé, I., Franx, M., Carollo, C. M., & Gonzalez, V. 2010, The Astrophysical Journal Letters, 709, L133

Bouwens, R. J., Illingworth, G. D., Thompson, R. I., & Franx, M. 2005, ApJ, 624, L5

Bouwens, R. J., Thompson, R. I., Illingworth, G. D., Franx, M., van Dokkum, P. G., Fan, X., Dickinson, M. E., Eisenstein, D. J., & Rieke, M. J. 2004, ApJ, 616, L79

Bressan, A., Fagotto, F., Bertelli, G., & Chiosi, C. 1993, Astronomy and Astrophysics Supplement Series (ISSN 0365-0138), 100, 647

Broadhurst, T. J., Ellis, R. S., & Shanks, T. 1988, Royal Astronomical Society, 235, 827

Bruzual, G. & Charlot, S. 2003, Monthly Notices of the Royal Astronomical Society, 344, 1000

Bunker, A., Wilkins, S., Ellis, R., Stark, D., Lorenzoni, S., Chiu, K., Lacy, M., Jarvis, M., & Hickey, S. 2009, arXiv, astro-ph.CO

Calzetti, D., Kennicutt, R. C., Engelbracht, C. W., Leitherer, C., Draine, B. T., Kewley, L., Moustakas, J., Sosey, M., Dale, D. A., Gordon, K. D., Helou, G. X., Hollenbach, D. J., Armus, L., Bendo, G., Bot, C., Buckalew, B., Jarrett, T., Li, A., Meyer, M., Murphy, E. J., Prescott, M., Regan, M. W., Rieke, G. H., Roussel, H., Sheth, K., Smith, J. D. T., Thornley, M. D., & Walter, F. 2007, The Astrophysical Journal, 666, 870

Calzetti, D., Kinney, A. L., & Storchi-Bergmann, T. 1994, The Astrophysical Journal, 429, 582

Chabrier, G. & Baraffe, I. 1997, Astronomy and Astrophysics, 327, 1039

Chan, K.-W., Roellig, T. L., Onaka, T., Mizutani, M., Okumura, K., Yamamura, I., Tanabé, T., Shibai, H., Nakagawa, T., & Okuda, H. 2001, The Astrophysical Journal, 546, 273

Charlot, S. & Fall, S. M. 2000, The Astrophysical Journal, 539, 718

Cole, S., Norberg, P., Baugh, C. M., Frenk, C. S., Bland-Hawthorn, J., Bridges, T., Cannon, R., Colless, M., Collins, C., Couch, W., Cross, N., Dalton, G., Propris, R. D., Driver, S. P., Efstathiou, G., Ellis, R. S., Glazebrook, K., Jackson, C., Lahav, O., Lewis, I., Lumsden, S., Maddox, S., Madgwick, D., Peacock, J. A., Peterson, B. A., Sutherland, W., & Taylor, K. 2001, Monthly Notices of the Royal Astronomical Society, 326, 255

Colless, M., Ellis, R. S., Taylor, K., & Hook, R. N. 1990, Royal Astronomical Society, 244, 408

Contursi, A., Lequeux, J., Cesarsky, D., Boulanger, F., Rubio, M., Hanus, M., Sauvage, M., Tran, D., Bosma, A., Madden, S., & Vigroux, L. 2000, Astronomy and Astrophysics, 362, 310

Cowie, L. L., Songaila, A., Hu, E. M., & Cohen, J. G. 1996, Astronomical Journal v.112, 112, 839

Cuby, J., Hibon, P., Lidman, C., Le Fèvre, O., Gilmozzi, R., Moorwood, A., & van der Werf, P. 2007, A&A, 461, 911

da Cunha, E., Charlot, S., & Elbaz, D. 2008, Monthly Notices of the Royal Astronomical Society, 388, 1595, (c) Journal compilation © 2008 RAS

Daddi, E., Dickinson, M., Morrison, G., Chary, R., Cimatti, A., Elbaz, D., Frayer, D., Renzini, A., Pope, A., Alexander, D. M., Bauer, F. E., Giavalisco, M., Huynh, M., Kurk, J., & Mignoli, M. 2007, The Astrophysical Journal, 670, 156, (c) 2007: The American Astronomical Society

Dale, D. A., Bendo, G. J., Engelbracht, C. W., Gordon, K. D., Regan, M. W., Armus, L., Cannon, J. M., Calzetti, D., Draine, B. T., Helou, G., Joseph, R. D., Kennicutt, R. C., Li, A., Murphy, E. J., Roussel, H., Walter, F., Hanson, H. M., Hollenbach,

D. J., Jarrett, T. H., Kewley, L. J., Lamanna, C. A., Leitherer, C., Meyer, M. J., Rieke, G. H., Rieke, M. J., Sheth, K., Smith, J. D. T., & Thornley, M. D. 2005, The Astrophysical Journal, 633, 857, (c) 2005: The American Astronomical Society

Dale, D. A., Paz, A. G. D., Gordon, K. D., Hanson, H. M., Armus, L., Bendo, G. J., Bianchi, L., Block, M., Boissier, S., Boselli, A., Buckalew, B. A., Buat, V., Burgarella, D., Calzetti, D., Cannon, J. M., Engelbracht, C. W., Helou, G., Hollenbach, D. J., Jarrett, T. H., Kennicutt, R. C., Leitherer, C., Li, A., Madore, B. F., Martin, D. C., Meyer, M. J., Murphy, E. J., Regan, M. W., Roussel, H., Smith, J. D. T., Sosey, M. L., Thilker, D. A., & Walter, F. 2007, The Astrophysical Journal, 655, 863

Dale, D. A., Smith, J. D. T., Armus, L., Buckalew, B. A., Helou, G., Kennicutt, R. C., Moustakas, J., Roussel, H., Sheth, K., Bendo, G. J., Calzetti, D., Draine, B. T., Engelbracht, C. W., Gordon, K. D., Hollenbach, D. J., Jarrett, T. H., Kewley, L. J., Leitherer, C., Li, A., Malhotra, S., Murphy, E. J., & Walter, F. 2006, The Astrophysical Journal, 646, 161

Damjanov, I., Mccarthy, P. J., Abraham, R. G., Glazebrook, K., Yan, H., Mentuch, E., Borgne, D. L., Savaglio, S., Crampton, D., Murowinski, R., Juneau, S., Carlberg, R. G., Jørgensen, I., Roth, K., Chen, H.-W., & Marzke, R. O. 2009, The Astrophysical Journal, 695, 101

de Ruyter, S., van Winckel, H., Maas, T., Evans, T. L., Waters, L. B. F. M., & Dejonghe, H. 2006, Astronomy and Astrophysics, 448, 641

Desert, F.-X., Boulanger, F., & Puget, J. L. 1990, Astronomy and Astrophysics (ISSN 0004-6361), 237, 215

Dickinson, M., Papovich, C., Ferguson, H. C., & Budavári, T. 2003, The Astrophysical Journal, 587, 25

Dijkstra, M., Lidz, A., & Wyithe, J. S. B. 2007, MNRAS, 377, 1175

Dijkstra, M., Wyithe, S., & Haiman, Z. 2006, ArXiv Astrophysics e-prints

Donley, J. L., Rieke, G. H., Pérez-González, P. G., & Barro, G. 2008, The Astrophysical Journal, 687, 111

Doyon, R., Nadeau, D., & Vallée, P. 2000, Imaging the Universe in Three Dimensions. Proceedings from ASP Conference Vol. 195. Edited by W. van Breugel and J. Bland-Hawthorn. ISBN: 1-58381-022-6 (2000), 195, 548, iSBN: 1-58381-022-6

Draine, B. T., Dale, D. A., Bendo, G., Gordon, K. D., Smith, J. D. T., Armus, L., Engelbracht, C. W., Helou, G., Kennicutt, R. C., Li, A., Roussel, H., Walter, F., Calzetti, D., Moustakas, J., Murphy, E. J., Rieke, G. H., Bot, C., Hollenbach, D. J., Sheth, K., & Teplitz, H. I. 2007, The Astrophysical Journal, 663, 866, (c) 2007: The American Astronomical Society

Draine, B. T. & Li, A. 2007, The Astrophysical Journal, 657, 810

Dullemond, C. P., Dominik, C., & Natta, A. 2001, The Astrophysical Journal, 560, 957, (c) 2001: The American Astronomical Society

Eikenberry, S., Elston, R., Raines, S. N., Julian, J., Hanna, K., Hon, D., Julian, R., Bandyopadhyay, R., Bennett, J. G., Bessoff, A., Branch, M., Corley, R., Eriksen, J., Frommeyer, S., Gonzalez, A., Herlevich, M., Marin-Franch, A., Marti, J., Murphey, C., Rashkin, D., Warner, C., Leckie, B., Gardhouse, W. R., Fletcher, M., Dunn, J., Wooff, R., & Hardy, T. 2006, in Society of Photo-Optical Instrumentation Engineers (SPIE) Conference Series, Vol. 6269, Society of Photo-Optical Instrumentation Engineers (SPIE) Conference Series

Elsner, F., Feulner, G., & Hopp, U. 2008, Astronomy and Astrophysics, 477, 503

Engelbracht, C. W., Gordon, K. D., Rieke, G. H., Werner, M. W., Dale, D. A., & Latter, W. B. 2005, The Astrophysical Journal, 628, L29

Evans, N., Calvet, N., Cieza, L., Forbrich, J., Hillenbrand, L., Lada, C., Merín, B., Strom, S., & Watson, D. 2009, eprint arXiv, 0901, 1691

Eyles, L. P., Bunker, A. J., Ellis, R. S., Lacy, M., Stanway, E. R., Stark, D. P., & Chiu, K. 2007, MNRAS, 374, 910

Fan, X., Carilli, C. L., & Keating, B. 2006, ARA&A, 44, 415

Fan, X., Narayanan, V. K., Lupton, R. H., Strauss, M. A., Knapp, G. R., Becker, R. H., White, R. L., Pentericci, L., Leggett, S. K., Haiman, Z., Gunn, J. E., Ivezić, Ž., Schneider, D. P., Anderson, S. F., Brinkmann, J., Bahcall, N. A., Connolly, A. J.,

Csabai, I., Doi, M., Fukugita, M., Geballe, T., Grebel, E. K., Harbeck, D., Hennessy, G., Lamb, D. Q., Miknaitis, G., Munn, J. A., Nichol, R., Okamura, S., Pier, J. R., Prada, F., Richards, G. T., Szalay, A., & York, D. G. 2001, AJ, 122, 2833

Fazio, G., Ashby, M., Barmby, P., Huang, J., Rigopoulou, D., Webb, T., Willner, S., Wilson, G., & Yamada, T. 2006, Spitzer Proposal ID #30328, 30328

Fazio, G. G., Hora, J. L., Allen, L. E., Ashby, M. L. N., Barmby, P., Deutsch, L. K., Huang, J.-S., Kleiner, S., Marengo, M., Megeath, S. T., Melnick, G. J., Pahre, M. A., Patten, B. M., Polizotti, J., Smith, H. A., Taylor, R. S., Wang, Z., Willner, S. P., Hoffmann, W. F., Pipher, J. L., Forrest, W. J., McMurty, C. W., McCreight, C. R., McKelvey, M. E., McMurray, R. E., Koch, D. G., Moseley, S. H., Arendt, R. G., Mentzell, J. E., Marx, C. T., Losch, P., Mayman, P., Eichhorn, W., Krebs, D., Jhabvala, M., Gezari, D. Y., Fixsen, D. J., Flores, J., Shakoorzadeh, K., Jungo, R., Hakun, C., Workman, L., Karpati, G., Kichak, R., Whitley, R., Mann, S., Tollestrup, E. V., Eisenhardt, P., Stern, D., Gorjian, V., Bhattacharya, B., Carey, S., Nelson, B. O., Glaccum, W. J., Lacy, M., Lowrance, P. J., Laine, S., Reach, W. T., Stauffer, J. A., Surace, J. A., Wilson, G., Wright, E. L., Hoffman, A., Domingo, G., & Cohen, M. 2004, The Astrophysical Journal Supplement Series, 154, 10

Feldman, H. A., Kaiser, N., & Peacock, J. A. 1994, ApJ, 426, 23

Fioc, M. & Rocca-Volmerange, B. 1997, Astronomy and Astrophysics, 326, 950

Flagey, N., Boulanger, F., Verstraete, L., Deschênes, M. A. M., Crespo, A. N., & Reach, W. T. 2006, Astronomy and Astrophysics, 453, 969

Fontana, A., Donnarumma, I., Vanzella, E., Giallongo, E., Menci, N., Nonino, M., Saracco, P., Cristiani, S., D'Odorico, S., & Poli, F. 2003, The Astrophysical Journal, 594, L9

Fontana, A., Salimbeni, S., Grazian, A., Giallongo, E., Pentericci, L., Nonino, M., Fontanot, F., Menci, N., Monaco, P., Cristiani, S., Vanzella, E., de Santis, C., & Gallozzi, S. 2006, Astronomy and Astrophysics, 459, 745

Gillett, F. C., Forrest, W. J., & Merrill, K. M. 1973, Astrophys. J., 183, 87, a&AA ID. AAA010.133.001

Glazebrook, K., Abraham, R. G., McCarthy, P. J., Savaglio, S., Chen, H.-W., Crampton, D., Murowinski, R., Jørgensen, I., Roth, K., Hook, I., Marzke, R. O., & Carlberg, R. G. 2004, Nature, 430, 181, (c) 2004: Nature

Glazebrook, K., Ellis, R., Colless, M., Broadhurst, T., Allington-Smith, J., & Tanvir, N. 1995a, Monthly Notices of the Royal Astronomical Society, 273, 157

Glazebrook, K., Peacock, J. A., Miller, L., & Collins, C. A. 1995b, Monthly Notices of the Royal Astronomical Society, 275, 169

Goulding, A. D. & Alexander, D. M. 2009, Monthly Notices of the Royal Astronomical Society, 1045, (c) Journal compilation © 2009 RAS

Haisch, K. E., Lada, E. A., & Lada, C. J. 2000, The Astronomical Journal, 120, 1396, (c) 2000: The American Astronomical Society

Helou, G., Lu, N. Y., Werner, M. W., Malhotra, S., & Silbermann, N. 2000, The Astrophysical Journal, 532, L21

Helou, G., Roussel, H., Appleton, P., Frayer, D., Stolovy, S., Storrie-Lombardi, L., Hurt, R., Lowrance, P., Makovoz, D., Masci, F., Surace, J., Gordon, K. D., Alonso-Herrero, A., Engelbracht, C. W., Misselt, K., Rieke, G., Rieke, M., Willner, S. P., Pahre, M., Ashby, M. L. N., Fazio, G. G., & Smith, H. A. 2004, The Astrophysical Journal Supplement Series, 154, 253

Hibon, P., Cuby, J.-G., Willis, J., Clément, B., Lidman, C., Arnouts, S., Kneib, J.-P., Willott, C. J., Marmo, C., & McCracken, H. 2010, Astronomy and Astrophysics, 515, 97

Hora, J. L., Latter, W. B., Allen, L. E., Marengo, M., Deutsch, L. K., & Pipher, J. L. 2004, The Astrophysical Journal Supplement Series, 154, 296, (c) 2004: The American Astronomical Society

Horton, A., Parry, I., Bland-Hawthorn, J., Cianci, S., King, D., McMahon, R., & Medlen, S. 2004, Ground-based Instrumentation for Astronomy. Edited by Alan F. M. Moorwood and Iye Masanori. Proceedings of the SPIE, 5492, 1022

Houck, J. R., Roellig, T. L., Cleve, J. V., Forrest, W. J., Herter, T. L., Lawrence, C. R., Matthews, K., Reitsema, H. J., Soifer, B. T., Watson, D. M., Weedman, D., Huisjen,

M., Troeltzsch, J. R., Barry, D. J., Bernard-Salas, J., Blacken, C., Brandl, B. R., Charmandaris, V., Devost, D., Gull, G. E., Hall, P., Henderson, C. P., Higdon, S. J. U., Pirger, B. E., Schoenwald, J., Sloan, G. C., Uchida, K. I., Appleton, P. N., Armus, L., Burgdorf, M. J., Fajardo-Acosta, S. B., Grillmair, C. J., Ingalls, J. G., Morris, P. W., & Teplitz, H. I. 2004, Optical, 5487, 62

Hu, E. M., Cowie, L. L., & McMahon, R. G. 1998, ApJ, 502, L99+

Ichikawa, T., Suzuki, R., Tokoku, C., Uchimoto, Y. K., Konishi, M., Yoshikawa, T., Yamada, T., Tanaka, I., Omata, K., & Nishimura, T. 2006, in Society of Photo-Optical Instrumentation Engineers (SPIE) Conference Series, Vol. 6269, Society of Photo-Optical Instrumentation Engineers (SPIE) Conference Series

Imanishi, M., Dudley, C. C., & Maloney, P. R. 2006, The Astrophysical Journal, 637, 114, (c) 2006: The American Astronomical Society

Indebetouw, R., Mathis, J. S., Babler, B. L., Meade, M. R., Watson, C., Whitney, B. A., Wolff, M. J., Wolfire, M. G., Cohen, M., Bania, T. M., Benjamin, R. A., Clemens, D. P., Dickey, J. M., Jackson, J. M., Kobulnicky, H. A., Marston, A. P., Mercer, E. P., Stauffer, J. R., Stolovy, S. R., & Churchwell, E. 2005, The Astrophysical Journal, 619, 931

Inoue, A. K., Iwata, I., & Deharveng, J.-M. 2006, MNRAS, 371, L1

Ivison, R. J., Greve, T. R., Serjeant, S., Bertoldi, F., Egami, E., Mortier, A. M. J., Alonso-Herrero, A., Barmby, P., Bei, L., Dole, H., Engelbracht, C. W., Fazio, G. G., Frayer, D. T., Gordon, K. D., Hines, D. C., Huang, J.-S., Floc'h, E. L., Misselt, K. A., Miyazaki, S., Morrison, J. E., Papovich, C., Pérez-González, P. G., Rieke, M. J., Rieke, G. H., Rigby, J., Rigopoulou, D., Smail, I., Wilson, G., & Willner, S. P. 2004, The Astrophysical Journal Supplement Series, 154, 124, (c) 2004: The American Astronomical Society

Iye, M., Ota, K., Kashikawa, N., Furusawa, H., Hashimoto, T., Hattori, T., Matsuda, Y., Morokuma, T., Ouchi, M., & Shimasaku, K. 2006, Nature, 443, 186

Jarrett, T. H., Chester, T., Cutri, R., Schneider, S. E., & Huchra, J. P. 2003, The Astronomical Journal, 125, 525, (c) 2003: The American Astronomical Society

Jimenez, R. & Haiman, Z. 2006, Nature, 440, 501

Johnson, H. L. 1962, Astrophysical Journal, 135, 69

Juneau, S., Glazebrook, K., Crampton, D., McCarthy, P. J., Savaglio, S., Abraham, R., Carlberg, R. G., Chen, H.-W., Borgne, D. L., Marzke, R. O., Roth, K., Jørgensen, I., Hook, I., & Murowinski, R. 2005, The Astrophysical Journal, 619, L135, (c) 2005: The American Astronomical Society

Kaiser, N. & Peacock, J. A. 1991, ApJ, 379, 482

Kashikawa, N., Shimasaku, K., Malkan, M. A., Doi, M., Matsuda, Y., Ouchi, M., Taniguchi, Y., Ly, C., Nagao, T., Iye, M., Motohara, K., Murayama, T., Murozono, K., Nariai, K., Ohta, K., Okamura, S., Sasaki, T., Shioya, Y., & Umemura, M. 2006, ApJ, 648, 7

Kauffmann, G., Heckman, T. M., White, S. D. M., Charlot, S., Tremonti, C., Brinchmann, J., Bruzual, G., Peng, E. W., Seibert, M., Bernardi, M., Blanton, M., Brinkmann, J., Castander, F., Csábai, I., Fukugita, M., Ivezic, Z., Munn, J. A., Nichol, R. C., Padmanabhan, N., Thakar, A. R., Weinberg, D. H., & York, D. 2003, Monthly Notice of the Royal Astronomical Society, 341, 33, (c) 2003 RAS

Kennicutt, R. C. 1998, Annual Review of Astronomy and Astrophysics, 36, 189

Kennicutt, R. C., Armus, L., Bendo, G., Calzetti, D., Dale, D. A., Draine, B. T., Engelbracht, C. W., Gordon, K. D., Grauer, A. D., Helou, G., Hollenbach, D. J., Jarrett, T. H., Kewley, L. J., Leitherer, C., Li, A., Malhotra, S., Regan, M. W., Rieke, G. H., Rieke, M. J., Roussel, H., Smith, J.-D. T., Thornley, M. D., & Walter, F. 2003, The Publications of the Astronomical Society of the Pacific, 115, 928, (c) 2003: The Astronomical Society of the Pacific

Kennicutt, R. C., Calzetti, D., Walter, F., Helou, G., Hollenbach, D. J., Armus, L., Bendo, G., Dale, D. A., Draine, B. T., Engelbracht, C. W., Gordon, K. D., Prescott, M. K. M., Regan, M. W., Thornley, M. D., Bot, C., Brinks, E., de Blok, E., de Mello, D., Meyer, M., Moustakas, J., Murphy, E. J., Sheth, K., & Smith, J. D. T. 2007, The Astrophysical Journal, 671, 333

Kennicutt, R. C., Hao, C.-N., Calzetti, D., Moustakas, J., Dale, D. A., Bendo, G., Engelbracht, C. W., Johnson, B. D., & Lee, J. C. 2009, The Astrophysical Journal, 703, 1672

Kessler, M. F., Steinz, J. A., Anderegg, M. E., Clavel, J., Drechsel, G., Estaria, P., Faelker, J., Riedinger, J. R., Robson, A., Taylor, B. G., & de Ferrán, S. X. 1996, Astron. Astrophys., 315, L27

Kroupa, P. 2001, Monthly Notices of the Royal Astronomical Society, 322, 231, (c) 2001 The Royal Astronomical Society

Kroupa, P., Tout, C. A., & Gilmore, G. 1993, Royal Astronomical Society, 262, 545

Kurucz, R. L. 1979, Astrophysical Journal Supplement Series, 40, 1, a&AA ID. AAA026.064.004

Labbé, I., Bouwens, R., Illingworth, G. D., & Franx, M. 2006, ApJ, 649, L67

Lada, C. J. & Adams, F. C. 1992, Astrophysical Journal, 393, 278

Leger, A. & Puget, J. L. 1984, Astronomy and Astrophysics (ISSN 0004-6361), 137, L5

Leggett, S. K., Currie, M. J., Varricatt, W. P., Hawarden, T. G., Adamson, A. J., Buckle, J., Carroll, T., Davies, J. K., Davis, C. J., Kerr, T. H., Kuhn, O. P., Seigar, M. S., & Wold, T. 2006, Monthly Notices of the Royal Astronomical Society, 373, 781

Leggett, S. K., Hawarden, T. G., Currie, M. J., Adamson, A. J., Carroll, T. C., Kerr, T. H., Kuhn, O. P., Seigar, M. S., Varricatt, W. P., & Wold, T. 2003, Monthly Notices of the Royal Astronomical Society, 345, 144, (c) 2003 RAS

Leitherer, C., Schaerer, D., Goldader, J. D., Delgado, R. M. G., Robert, C., Kune, D. F., de Mello, D. F., Devost, D., & Heckman, T. M. 1999, The Astrophysical Journal Supplement Series, 123, 3

Lejeune, T., Cuisinier, F., & Buser, R. 1997, A & A Supplement series, 125, 229

Li, A. & Draine, B. T. 2001, The Astrophysical Journal, 554, 778

Lilly, S. J., Tresse, L., Hammer, F., Crampton, D., & Fevre, O. L. 1995, Astrophysical Journal v.455, 455, 108

Longmore, S. N., Maercker, M., Ramstedt, S., & Burton, M. G. 2007, Monthly Notices of the Royal Astronomical Society, 380, 1497

Lu, N., Helou, G., Werner, M. W., Dinerstein, H. L., Dale, D. A., Silbermann, N. A., Malhotra, S., Beichman, C. A., & Jarrett, T. H. 2003, The Astrophysical Journal, 588, 199, (c) 2003: The American Astronomical Society

Madden, S. C., Galliano, F., Jones, A. P., & Sauvage, M. 2006, Astronomy and Astrophysics, 446, 877

Maercker, M. & Burton, M. G. 2005, Astronomy and Astrophysics, 438, 663

Maercker, M., Burton, M. G., & Wright, C. M. 2006, Astronomy and Astrophysics, 450, 253

Magakian, T. Y. 2003, Astronomy and Astrophysics, 399, 141

Magnelli, B., Chary, R. R., Pope, A., Elbaz, D., Morrison, G., & Dickinson, M. 2008, The Astrophysical Journal, 681, 258, (c) 2008: The American Astronomical Society

Maraston, C. 2005, Monthly Notices of the Royal Astronomical Society, 362, 799, (c) 2005 RAS

McCarthy, P., Abraham, R., Chen, H.-W., Crampton, D., Glazebrook, K., Savaglio, S., & Yan, L. 2004, Spitzer Proposal ID #3554, 3554

McCarthy, P. J., Carlberg, R. G., Chen, H.-W., Marzke, R. O., Firth, A. E., Ellis, R. S., Persson, S. E., McMahon, R. G., Lahav, O., Wilson, J., Martini, P., Abraham, R. G., Sabbey, C. N., Oemler, A., Murphy, D. C., Somerville, R. S., Beckett, M. G., Lewis, J. R., & MacKay, C. D. 2001, The Astrophysical Journal, 560, L131

Mentuch, E., Abraham, R. G., Glazebrook, K., McCarthy, P. J., Yan, H., O'Donnell, D. V., Borgne, D. L., Savaglio, S., Crampton, D., Murowinski, R., Juneau, S., Carlberg, R. G., Jørgensen, I., Roth, K., Chen, H.-W., & Marzke, R. O. 2009, The Astrophysical Journal, 706, 1020

Mentuch, E., Scott, A., Abraham, R., Barton, E., Bershady, M., Bland-Hawthorn, J., Crampton, D., Doyon, R., Eikenberry, S., Gladders, M., Glazebrook, K., Jenson, J., Julian, J., Julian, R., Kneib, J.-P., Loop, D., Raines, N., Rowlands, N., & Smith,

J. D. 2008, Ground-based and Airborne Instrumentation for Astronomy II. Edited by McLean, 7014, 236

Meyer, M. R. 1996, Thesis (PH.D.)–UNIVERSITY OF MASSACHUSETTS, 3, thesis Advisor: Stephen E. Strom

Millan-Gabet, R., Monnier, J. D., Berger, J.-P., Traub, W. A., Schloerb, F. P., Pedretti, E., Benisty, M., Carleton, N. P., Haguenauer, P., Kern, P., Labeye, P., Lacasse, M. G., Malbet, F., Perraut, K., Pearlman, M., & Thureau, N. 2006, The Astrophysical Journal, 645, L77

Mink, D. J. 2002, Astronomical Data Analysis Software and Systems XI, 281, 169, iSBN: 1-58381-124-9

Monnier, J. D., Millan-Gabet, R., Billmeier, R., Akeson, R. L., Wallace, D., Berger, J.-P., Calvet, N., D'Alessio, P., Danchi, W. C., Hartmann, L., Hillenbrand, L. A., Kuchner, M., Rajagopal, J., Traub, W. A., Tuthill, P. G., Boden, A., Booth, A., Colavita, M., Gathright, J., Hrynevych, M., Mignant, D. L., Ligon, R., Neyman, C., Swain, M., Thompson, R., Vasisht, G., Wizinowich, P., Beichman, C., Beletic, J., Creech-Eakman, M., Koresko, C., Sargent, A., Shao, M., & van Belle, G. 2005, The Astrophysical Journal, 624, 832

Mortonson, M. J. & Hu, W. 2008, The Astrophysical Journal, 686, L53

Mouri, H., Kawara, K., Taniguchi, Y., & Nishida, M. 1990, Astrophysical Journal, 356, L39

Muñoz-Mateos, J. C., Paz, A. G. D., Zamorano, J., Boissier, S., Dale, D. A., Pérez-González, P. G., Gallego, J., Madore, B. F., Bendo, G., Boselli, A., Buat, V., Calzetti, D., Moustakas, J., & Kennicutt, R. C. 2009, The Astrophysical Journal, 703, 1569

Murakami, H., Baba, H., Barthel, P., Clements, D. L., Cohen, M., Doi, Y., Enya, K., Figueredo, E., Fujishiro, N., Fujiwara, H., Fujiwara, M., Garcia-Lario, P., Goto, T., Hasegawa, S., Hibi, Y., Hirao, T., Hiromoto, N., Hong, S. S., Imai, K., Ishigaki, M., Ishiguro, M., Ishihara, D., Ita, Y., Jeong, W.-S., Jeong, K. S., Kaneda, H., Kataza, H., Kawada, M., Kawai, T., Kawamura, A., Kessler, M. F., Kester, D., Kii, T., Kim, D. C., Kim, W., Kobayashi, H., Koo, B. C., Kwon, S. M., Lee, H. M., Lorente, R., Makiuti, S., Matsuhara, H., Matsumoto, T., Matsuo, H., Matsuura, S., Müller, T. G.,

Murakami, N., Nagata, H., Nakagawa, T., Naoi, T., Narita, M., Noda, M., Oh, S. H., Ohnishi, A., Ohyama, Y., Okada, Y., Okuda, H., Oliver, S., Onaka, T., Ootsubo, T., Oyabu, S., Pak, S., Park, Y.-S., Pearson, C. P., Rowan-Robinson, M., Saito, T., Sakon, I., Salama, A., Sato, S., Savage, R. S., Serjeant, S., Shibai, H., Shirahata, M., Sohn, J., Suzuki, T., Takagi, T., Takahashi, H., Tanabé, T., Takeuchi, T. T., Takita, S., Thomson, M., Uemizu, K., Ueno, M., Usui, F., Verdugo, E., Wada, T., Wang, L., Watabe, T., Watarai, H., White, G. J., Yamamura, I., Yamauchi, C., & Yasuda, A. 2007, Publications of the Astronomical Society of Japan, 59, 369

Muzerolle, J., Calvet, N., Hartmann, L., & D'Alessio, P. 2003, The Astrophysical Journal, 597, L149

Muzzin, A., Marchesini, D., van Dokkum, P. G., Labbé, I., Kriek, M., & Franx, M. 2009, The Astrophysical Journal, 701, 1839

Page, L., Hinshaw, G., Komatsu, E., Nolta, M. R., Spergel, D. N., Bennett, C. L., Barnes, C., Bean, R., Doré, O., Dunkley, J., Halpern, M., Hill, R. S., Jarosik, N., Kogut, A., Limon, M., Meyer, S. S., Odegard, N., Peiris, H. V., Tucker, G. S., Verde, L., Weiland, J. L., Wollack, E., & Wright, E. L. 2006, ArXiv Astrophysics e-prints

Papovich, C., Moustakas, L. A., Dickinson, M., Floc'h, E. L., Rieke, G. H., Daddi, E., Alexander, D. M., Bauer, F., Brandt, W. N., Dahlen, T., Egami, E., Eisenhardt, P., Elbaz, D., Ferguson, H. C., Giavalisco, M., Lucas, R. A., Mobasher, B., Pérez-González, P. G., Stutz, A., Rieke, M. J., & Yan, H. 2006, The Astrophysical Journal, 640, 92, (c) 2006: The American Astronomical Society

Peeters, E., Mattioda, A. L., Hudgins, D. M., & Allamandola, L. J. 2004, The Astrophysical Journal, 617, L65

Pei, Y. C. 1992, Astrophysical Journal, 395, 130

Pérez-González, P. G., Rieke, G. H., Villar, V., Barro, G., Blaylock, M., Egami, E., Gallego, J., de Paz, A. G., Pascual, S., Zamorano, J., & Donley, J. L. 2008, The Astrophysical Journal, 675, 234

Phillips, J. P. & Ramos-Larios, G. 2005, Monthly Notices of the Royal Astronomical Society, 364, 849

Pope, A., Bussmann, R. S., Dey, A., Meger, N., Alexander, D. M., Brodwin, M., Chary, R.-R., Dickinson, M. E., Frayer, D. T., Greve, T. R., Huynh, M., Lin, L., Morrison, G., Scott, D., & Yan, C.-H. 2008a, The Astrophysical Journal, 689, 127, (c) 2008: The American Astronomical Society

Pope, A., Chary, R.-R., Alexander, D. M., Armus, L., Dickinson, M., Elbaz, D., Frayer, D., Scott, D., & Teplitz, H. 2008b, The Astrophysical Journal, 675, 1171, (c) 2008: The American Astronomical Society

Popesso, P., Dickinson, M., Nonino, M., Vanzella, E., Daddi, E., Fosbury, R. A. E., Kuntschner, H., Mainieri, V., Cristiani, S., Cesarsky, C., Giavalisco, M., Renzini, A., & Team, G. 2009, Astronomy and Astrophysics, 494, 443

Prescott, M. K. M., Kennicutt, R. C., Bendo, G. J., Buckalew, B. A., Calzetti, D., Engelbracht, C. W., Gordon, K. D., Hollenbach, D. J., Lee, J. C., Moustakas, J., Dale, D. A., Helou, G., Jarrett, T. H., Murphy, E. J., Smith, J.-D. T., Akiyama, S., & Sosey, M. L. 2007, The Astrophysical Journal, 668, 182

Press, W. H. & Schechter, P. 1974, ApJ, 187, 425

Reed, D. S., Bower, R., Frenk, C. S., Jenkins, A., & Theuns, T. 2007, MNRAS, 374, 2

Richard, J., Pelló, R., Schaerer, D., Borgne, J.-F. L., & Kneib, J.-P. 2006, A&A, 456, 861

Rieke, G. H., Young, E. T., Engelbracht, C. W., Kelly, D. M., Low, F. J., Haller, E. E., Beeman, J. W., Gordon, K. D., Stansberry, J. A., Misselt, K. A., Cadien, J., Morrison, J. E., Rivlis, G., Latter, W. B., Noriega-Crespo, A., Padgett, D. L., Stapelfeldt, K. R., Hines, D. C., Egami, E., Muzerolle, J., Alonso-Herrero, A., Blaylock, M., Dole, H., Hinz, J. L., Floc'h, E. L., Papovich, C., Pérez-González, P. G., Smith, P. S., Su, K. Y. L., Bennett, L., Frayer, D. T., Henderson, D., Lu, N., Masci, F., Pesenson, M., Rebull, L., Rho, J., Keene, J., Stolovy, S., Wachter, S., Wheaton, W., Werner, M. W., & Richards, P. L. 2004, The Astrophysical Journal Supplement Series, 154, 25

Riffel, R., Pastoriza, M. G., Rodríguez-Ardila, A., & Bonatto, C. 2009, Monthly Notices of the Royal Astronomical Society, 400, 273

Roussel, H., Helou, G., Smith, J. D., Draine, B. T., Hollenbach, D. J., Moustakas, J., Spoon, H. W., Kennicutt, R. C., Rieke, G. H., Walter, F., Armus, L., Dale, D. A.,

Sheth, K., Bendo, G. J., Engelbracht, C. W., Gordon, K. D., Meyer, M. J., Regan, M. W., & Murphy, E. J. 2006, ApJ, 646, 841

Rowlands, N., Evans, C., Greenberg, E., Gregory, P., Scott, A., Thibault, S., Poirier, M., Doyon, R., Hutchings, J. B., & Alexander, R. 2004, in Society of Photo-Optical Instrumentation Engineers (SPIE) Conference Series, Vol. 5487, Society of Photo-Optical Instrumentation Engineers (SPIE) Conference Series, ed. J. C. Mather, 676–687

Sajina, A., Yan, L., Armus, L., Choi, P., Fadda, D., Helou, G., & Spoon, H. 2007, The Astrophysical Journal, 664, 713

Salpeter, E. E. 1955, Astrophysical Journal, 121, 161

Santos, M. R., Ellis, R. S., Kneib, J.-P., Richard, J., & Kuijken, K. 2004, ApJ, 606, 683

Schaerer, D. 2003, Astronomy and Astrophysics, 397, 527

Schmidt, M. 1968, Astrophysical Journal, 151, 393

Scott, A., Javed, M., Abraham, R., Eikenberry, S., Barton, E., Bershady, M., Bland-Hawthorn, J., Crampton, D., Doyon, R., Julian, J., Julian, R., Kneib, J., Loop, D., Raines, N., Rowlands, N., & Smith, J. D. 2006, in Society of Photo-Optical Instrumentation Engineers (SPIE) Conference Series, Vol. 6269, Society of Photo-Optical Instrumentation Engineers (SPIE) Conference Series

Seljak, U. & Zaldarriaga, M. 1996, ApJ, 469, 437

Sellgren, K. 1984, Astrophysical Journal, 277, 623

Sellgren, K., Werner, M. W., & Allamandola, L. J. 1996, Astrophysical Journal Supplement v.102, 102, 369

Sellgren, K., Werner, M. W., & Dinerstein, H. L. 1983, Astrophysical Journal, 271, L13

Shapley, A. E., Steidel, C. C., Adelberger, K. L., Dickinson, M., Giavalisco, M., & Pettini, M. 2001, The Astrophysical Journal, 562, 95

Shapley, A. E., Steidel, C. C., Pettini, M., & Adelberger, K. L. 2003, ApJ, 588, 65

Sheth, R. K., Mo, H. J., & Tormen, G. 2001, MNRAS, 323, 1

Sheth, R. K. & Tormen, G. 1999, MNRAS, 308, 119

Shimasaku, K., Kashikawa, N., Doi, M., Ly, C., Malkan, M. A., Matsuda, Y., Ouchi, M., Hayashino, T., Iye, M., Motohara, K., Murayama, T., Nagao, T., Ohta, K., Okamura, S., Sasaki, T., Shioya, Y., & Taniguchi, Y. 2006, PASJ, 58, 313

Smith, J. D. T., Draine, B. T., Dale, D. A., Moustakas, J., Kennicutt, R. C., Helou, G., Armus, L., Roussel, H., Sheth, K., Bendo, G. J., Buckalew, B. A., Calzetti, D., Engelbracht, C. W., Gordon, K. D., Hollenbach, D. J., Li, A., Malhotra, S., Murphy, E. J., & Walter, F. 2007, The Astrophysical Journal, 656, 770

Smith, R. E., Peacock, J. A., Jenkins, A., White, S. D. M., Frenk, C. S., Pearce, F. R., Thomas, P. A., Efstathiou, G., & Couchman, H. M. P. 2003, MNRAS, 341, 1311

Sobral, D., Best, P. N., Geach, J. E., Smail, I., Kurk, J., Cirasuolo, M., Casali, M., Ivison, R. J., Coppin, K., & Dalton, G. B. 2009, Monthly Notices of the Royal Astronomical Society: Letters, 398, L68

Somerville, R. S., Lee, K., Ferguson, H. C., Gardner, J. P., Moustakas, L. A., & Giavalisco, M. 2004, ApJ, 600, L171

Spergel, D. N., Bean, R., Doré, O., Nolta, M. R., Bennett, C. L., Dunkley, J., Hinshaw, G., Jarosik, N., Komatsu, E., Page, L., Peiris, H. V., Verde, L., Halpern, M., Hill, R. S., Kogut, A., Limon, M., Meyer, S. S., Odegard, N., Tucker, G. S., Weiland, J. L., Wollack, E., & Wright, E. L. 2007, ApJS, 170, 377

Stark, D. P., Ellis, R. S., Richard, J., Kneib, J.-P., Smith, G. P., & Santos, M. R. 2007a, The Astrophysical Journal, 663, 10

Stark, D. P., Loeb, A., & Ellis, R. S. 2007b, The Astrophysical Journal, 668, 627

Steidel, C. C., Giavalisco, M., Pettini, M., Dickinson, M., & Adelberger, K. L. 1996, Astrophysical Journal Letters v.462, 462, L17

Stern, D., Eisenhardt, P., Gorjian, V., Kochanek, C. S., Caldwell, N., Eisenstein, D., Brodwin, M., Brown, M. J. I., Cool, R., Dey, A., Green, P., Jannuzi, B. T., Murray, S. S., Pahre, M. A., & Willner, S. P. 2005, The Astrophysical Journal, 631, 163, (c) 2005: The American Astronomical Society

Stetson, P. B. 1987, Astronomical Society of the Pacific, 99, 191

Stiavelli, M., Fall, S. M., & Panagia, N. 2004, ApJ, 600, 508

Sturm, E., Lutz, D., Tran, D., Feuchtgruber, H., Genzel, R., Kunze, D., Moorwood, A. F. M., & Thornley, M. D. 2000, Astronomy and Astrophysics, 358, 481

Tanvir, N. R., Fox, D. B., Levan, A. J., Berger, E., Wiersema, K., Fynbo, J. P. U., Cucchiara, A., Krühler, T., Gehrels, N., Bloom, J. S., Greiner, J., Evans, P. A., Rol, E., Olivares, F., Hjorth, J., Jakobsson, P., Farihi, J., Willingale, R., Starling, R. L. C., Cenko, S. B., Perley, D., Maund, J. R., Duke, J., Wijers, R. A. M. J., Adamson, A. J., Allan, A., Bremer, M. N., Burrows, D. N., Castro-Tirado, A. J., Cavanagh, B., de Ugarte Postigo, A., Dopita, M. A., Fatkhullin, T. A., Fruchter, A. S., Foley, R. J., Gorosabel, J., Kennea, J., Kerr, T., Klose, S., Krimm, H. A., Komarova, V. N., Kulkarni, S. R., Moskvitin, A. S., Mundell, C. G., Naylor, T., Page, K., Penprase, B. E., Perri, M., Podsiadlowski, P., Roth, K., Rutledge, R. E., Sakamoto, T., Schady, P., Schmidt, B. P., Soderberg, A. M., Sollerman, J., Stephens, A. W., Stratta, G., Ukwatta, T. N., Watson, D., Westra, E., Wold, T., & Wolf, C. 2009, Nature, 461, 1254

Tilvi, V., Rhoads, J. E., Hibon, P., Malhotra, S., Wang, J., Veilleux, S., Swaters, R., Probst, R., Krug, H., Finkelstein, S. L., & Dickinson, M. 2010, eprint arXiv, 1006, 3071, submitted to ApJ, 3 figures

Touhami, Y., Richardson, N. D., Gies, D. R., Schaefer, G. H., Boyajian, T. S., Williams, S. J., Grundstrom, E. D., McSwain, M. V., Clemens, D. P., & Taylor, B. 2010, arXiv, astro-ph.SR

Trump, J. R., Impey, C. D., McCarthy, P. J., Elvis, M., Huchra, J. P., Brusa, M., Hasinger, G., Schinnerer, E., Capak, P., Lilly, S. J., & Scoville, N. Z. 2007, The Astrophysical Journal Supplement Series, 172, 383, (c) 2007: The American Astronomical Society

Vanzella, E., Giavalisco, M., Dickinson, M., Cristiani, S., Nonino, M., Kuntschner, H., Popesso, P., Rosati, P., Renzini, A., Stern, D., Cesarsky, C., Ferguson, H. C., & Fosbury, R. A. E. 2009, The Astrophysical Journal, 695, 1163

Veilleux, S., Weiner, B. J., Rupke, D. S. N., McDonald, M., Birk, C., Bland-Hawthorn,

J., Dressler, A., Hare, T., Osip, D., Pietraszewski, C., & Vogel, S. N. 2010, The Astronomical Journal, 139, 145

Verley, S., Corbelli, E., Giovanardi, C., & Hunt, L. K. 2009, Astronomy and Astrophysics, 493, 453

Vermeij, R., Peeters, E., Tielens, A. G. G. M., & van der Hulst, J. M. 2002, Astronomy and Astrophysics, 382, 1042

Verstraete, L., Pech, C., Moutou, C., Sellgren, K., Wright, C. M., Giard, M., Léger, A., Timmermann, R., & Drapatz, S. 2001, Astronomy and Astrophysics, 372, 981

Verstraete, L., Puget, J. L., Falgarone, E., Drapatz, S., Wright, C. M., & Timmermann, R. 1996, Astronomy and Astrophysics, 315, L337

Vinković, D., Ivezić, Ž., Jurkić, T., & Elitzur, M. 2006, The Astrophysical Journal, 636, 348

Werner, M. W., Roellig, T. L., Low, F. J., Rieke, G. H., Rieke, M., Hoffmann, W. F., Young, E., Houck, J. R., Brandl, B., Fazio, G. G., Hora, J. L., Gehrz, R. D., Helou, G., Soifer, B. T., Stauffer, J., Keene, J., Eisenhardt, P., Gallagher, D., Gautier, T. N., Irace, W., Lawrence, C. R., Simmons, L., Cleve, J. E. V., Jura, M., Wright, E. L., & Cruikshank, D. P. 2004, The Astrophysical Journal Supplement Series, 154, 1

Willis, J. P. & Courbin, F. 2005, MNRAS, 357, 1348

Wood, K., Whitney, B. A., Robitaille, T., & Draine, B. T. 2008, The Astrophysical Journal, 688, 1118, (c) 2008: The American Astronomical Society

Yan, H., Windhorst, R., Hathi, N., Cohen, S., Ryan, R., O'Connell, R., & McCarthy, P. 2009, arXiv, astro-ph.CO

Yee, H. K. C. 1991, Astronomical Society of the Pacific, 103, 396

Zibetti, S. 2009, eprint arXiv, 0911, 4956